UNIVERSITY OF SOUTHAMPTON

FACULTY OF ENGINEERING AND THE ENVIRONMENT

National Centre for Advanced Tribology (nCATS)

Volume 1 of 1

Investigation of wear and corrosion products released from the CoCrMo tapers and cement-stem interface in total hip replacements

by

Alina Mariana Crainic

Academic Supervisory Team

Dr. Richard B. Cook

Prof. Martin R. Palmer

Thesis for the degree of Doctor of Philosophy

July 2018

UNIVERSITY OF SOUTHAMPTON

ABSTRACT

FACULTY OF ENGINEERING AND THE ENVIRONMENT

National Centre for Advanced Tribology

Thesis for the degree of Doctor of Philosophy

INVESTIGATION OF WEAR AND CORROSION PRODUCTS RELEASED FROM THE COCRMO TAPERS AND CEMENT-STEM INTERFACE IN TOTAL HIP REPLACEMENTS

Alina Mariana Crainic

Adverse local tissue reactions (ALTRs) to solid and soluble debris released from cobalt-chromium-molybdenum (CoCrMo) alloy metal-on-metal (MoM) hip replacements have been raising numerous concerns and currently represent the main reason for MoM revision surgery. The introduction of modularity at the femoral components has further contributed to the increasing incidence of body responses to the implant, due to the wear and corrosion of the metallic tapers. Products originating from the secondary metallic interfaces, such as tapers or cement-stem interfaces, were suggested to elicit more severe body responses to the implant than the equivalent dose of debris from the bearing surfaces. Body responses are dictated by the interaction of the particles with the biological environment, and highly depend on the particle size, morphology, aggregation state, chemical composition and speciation.

Despite the increasing evidence of ALTRs to metal debris originating from the tapers or cement-stem interfaces, little is known about these products and their characteristics. There have been numerous reports of black and flaky deposits of debris around the revised tapers or cement-stem interfaces, which were confirmed to be metallic by analytical techniques. The speciation of CoCrMo taper debris has only been reported for debris in periprosthetic tissue or spread at distant organs, which may have been altered by the specific biological environments at these sites.

The present study reveals the nature of debris released *in vivo* from the mixed (CoCrMo/Ti alloy) and matched (CoCrMo/CoCrMo alloy) tapers and CoCrMo cement-stem interfaces. The implants used in this study have been retrieved from patients at the time of revision

surgery and have been forensically examined to understand the main wear and corrosion processes responsible for their failure. The wear and corrosion flakes were comprehensively characterised from the micro scale down to the nano level, to understand their structural and chemical features and reveal the constituent building blocks. Two different methods were used to clean the debris and their effects on the particle characteristics were assessed. The study is the first to reveal the size, elemental composition and speciation of debris from the mixed and matched material tapers and cement-stem interfaces, by using complementary state-of-the-art characterisation techniques. The study compared the physicochemical characteristics of debris released from CoCrMo tapers and stems, and debris from mixed and matched material taper junctions, and revealed significant size differences which may influence the adverse body responses to the implant. The speciation analysis revealed chemical species whose effects on the cells have not been previously assessed and may be linked to the increased *in vivo* reactivity of the CoCrMo debris from tapers and cement-stem interfaces.

Table of Contents

`

Table of Tables

Table of Figures

Table of Figures

Academic Thesis: Declaration of Authorship

I, Alina Mariana Crainic

Declare that this thesis and the work presented in it are my own and has been generated by me as the result of my own original research.

Investigation of wear and corrosion products released from the CoCrMo tapers and cement-stem interface in total hip replacements

I confirm that:

1. This work was done wholly or mainly while in candidature for a research degree at this University;
2. Where any part of this thesis has previously been submitted for a degree or any other qualification at this University or any other institution, this has been clearly stated;
3. Where I have consulted the published work of others, this is always clearly attributed;
4. Where I have quoted from the work of others, the source is always given. With the exception of such quotations, this thesis is entirely my own work;
5. I have acknowledged all main sources of help;
6. Where the thesis is based on work done by myself jointly with others, I have made clear exactly what was done by others and what I have contributed myself;
7. Parts of this work have been published as:

   Investigation of nano-sized debris released from CoCrMo secondary interfaces in total hip replacements: Digestion of the flakes
   Alina M. Crainic, Mauro Callisti, Martin R. Palmer, Richard B. Cook
   J Biomed Mater Res Part B, 2018:00B:000–000
   https://doi.org/10.1002/jbm.b.34134

   A comparison between debris from CoCrMo tapers, cement-stem interfaces and CoCrMo/Ti tapers
   Alina M. Crainic, Mauro Callisti, Arjen van Veelen, Martin R. Palmer, Richard B. Cook
   Orthopaedic Research Society (ORS) Annual Meeting, New Orleans, Louisiana (US)
   10-13 March 2018. Contribution: Poster Presentation

Characterisation of wear and corrosion products from around a retrieved CoCrMo taper junction

Alina M. Crainic, Mauro Callisti, Martin R. Palmer, Richard B. Cook

Orthopaedic Research Society (ORS) Annual Meeting, San Diego, California (US)

19-22 March 2017. Contribution: Poster Presentation

Investigation of wear and corrosion products from the cement-stem interface of explanted hip replacements

Alina M. Crainic, Mauro Callisti, Agnes Michalik, James A. Milton, Martin R. Palmer, Richard B. Cook

British Hip Society (BHA) Annual Meeting, London (UK)

1-3 March 2017. Contribution: Oral Presentation

Characterisation of wear and corrosion products released from CoCrMo hip replacements

Alina M. Crainic, Mauro Callisti, Agnes Michalik, James A. Milton, Martin R. Palmer, Richard B. Cook

Northern Retrieval Registry (NRR) Inaugural Conference, Newcastle (UK)

3rd May 2017. Contribution: Oral Presentation

Isolation and characterisation of wear and corrosion products from CoCrMo hip replacements

Alina M. Crainic, Mauro Callisti, Martin R. Palmer, Richard B. Cook

ATEM Users Annual Meeting, Oxford (UK)

7th December 2016. Contribution: Oral Presentation

Signed: Alina Mariana Crainic

Date: 2nd July 2018

Acknowledgements

My first thoughts go to my supervisor, Dr. Richard Cook, who has been supporting me during the whole journey of my PhD and believed in myself and in the potential of this project. During the four years, Richard has been both an academic advisor and a friend, who helped me in the most difficult times. I would like to thank him for giving me the chance to be part of his team and for teaching me the best research practices. I am grateful for his advice, the time and energy he invested in this project, and for helping me get access to the state-of-the-art techniques, so necessary for completing this study. Finally, I would like to thank him for his contagious optimism which kept my moral up and helped me get to end of this difficult, but pleasant journey.

I would also like to thank my second supervisor, Prof. Martin Palmer, who has been very supportive during these years and shared his experience with us. I am grateful to him for taking the time to carefully read our manuscripts, grant proposals, conference abstracts and for providing us with great advice which improved the quality of our work.

I am also grateful for having the chance to closely work with Dr. Mauro Callisti who was my mentor and shared with me his knowledge and expertise in electron microscopy. I thank him for his patience when teaching me how to align and operate the high-resolution microscope in Oxford, process the data and get the best out of it. Following his advice, the quality of our manuscripts, posters and conference abstracts has definitely reached the maximum and contributed to them being successful.

I would also like to thank Patricia Goggin for teaching me how to operate the TEM and SEM equipment at the Biomedical Imaging Unit, Agnes Michalik and James A. Milton for the ICP-MS work presented in this study, Dr. Arjen van Veelen for helping us grant access to the synchrotron facility at Diamond and for all his support with the XANES work, and Dr. Richard Cook for analysing the retrievals with RedLux. I would also like to thank Dr. Russ Alberts for all his support with the hip simulator work at the very beginning of my PhD.

I would like to gratefully acknowledge the funding sources which made my PhD work possible. The project was partly funded by the University of Southampton and EPSRC (Biomet grant), and was awarded with a £50 000 research grant from Arthroplasty for Arthritis Charity, UK. I would also like to acknowledge the 'South of England Analytical Electron Microscope' supported by EPSRC (EP/K040375/1) which provided us access to the high-resolution electron microscope in Oxford. I am grateful to Dr. Neil Young and Dr. Ian Griffith from the University of Oxford for all their support with the electron microscopy work.

My thoughts also go to my friend, Dr. Vlad Niste, who advised me to apply for this PhD position and has supported me all the way since I submitted the application. I appreciate his advice and unconditioned support ever since I met him.

Acknowledgements

I would also like to thank all my PhD colleagues, especially Alex, Behrad, Florence, Charlie, Nan, Mike and Ma Dina for being so nice, helpful and patient with me, and for making the whole PhD experience better. Thank you all for the great time we had together here in Southampton and more recently in Romania.

Lastly, I would like to thank my family and my extended family for all their support during these years. Thank you all for being so patient and for understanding when I couldn't join you at important family events. Special thanks to my mom and dad who taught me to be brave and take risks in life, work hard and wait patiently for the rewards. Thanks to my brother who always encouraged me not to give up and made efforts to call and check on me. Finally, I would like to thank my beloved husband, Claudiu, who encouraged me to take this PhD opportunity and left behind his life in Romania to follow me and pursue my dreams. I am grateful for you being so supportive all these years and for looking after both of us. Thank you for your little jokes which helped me take breaks and disconnect for moments from the work or thesis writing. I could not have made this without you and your love. Thank you.

'*Aș dori să mulțumesc întregii mele familii pentru tot sprijinul acordat pe parcursul celor 4 ani de studii doctorale. Vă mulțumesc pentru răbdarea de care ați dat dovadă și pentru că ați înțeles de fiecare dată lipsa noastră de la evenimentele importante de familie. Doresc să mulțumesc în primul rând părinților mei care m-au învățat că munca e întotdeauna răsplătită și că rezultatele bune se obțin numai cu trudă, răbdare și efort. Vă mulțumesc pentru că mi-ați insuflat curajul și spiritul independent și m-ați făcut să înțeleg că satisfacțiile sunt nemărginite atunci când lupți să obții ceea ce-ți dorești prin forțele proprii. Conștient sau nu, m-ați crescut după zicala 'Dă-i omului un pește și va avea de mâncare o zi. Învață-l cum să pescuiască și va avea de mâncare toată viața'. Pentru aceasta vă mulțumesc! Îi mulțumesc și fratelui meu, Sorin, care m-a sunat de nenumărate ori doar ca să se asigure că sunt bine și care m-a încurajat de câte ori am fost pe punctul de a renunța la tot. Nu în ultimul rând, gândurile și mulțumirile mele se îndreaptă către soțul meu, Claudiu, care m-a încurajat sa mă înscriu la doctorat și mi-a acordat sprijin nemărginit, renunțând la tot și urmându-mă pentru a-mi îndeplini visul. Îți mulțumesc pentru răbdarea de care ai dat dovadă în cei 4 ani de zile și pentru că ai avut grijă să am parte de liniște acasă și te-ai asigurat că nu-mi lipsește nimic. Îți mulțumesc că m-ai învățat să mă bucur de micile plăceri ale vieții și m-ai ajutat să mențin un echilibru aproape perfect între muncă și viața personală. Fără tine mi-ar fi fost greu să duc la bun sfârșit acest proiect, iar o mare parte din merite o datorez ție. Vă mulțumesc tuturor.*'

List of Abbreviations

A	area
AAS	atomic absorption spectroscopy
ABG II	design of hip replacement
AFM	atomic force microscopy
ALTR	adverse local tissue reactions
ALVAL	aseptic lymphocyte vasculitis associated lesions
APL	average particle length
AR	aspect ratio
ARMD	adverse responses to metal debris
ASR	design of hip replacement
BSA	bovine serum albumin
CoB	cylinder on bar
CoC	ceramic on ceramic
CoCrMo	cobalt-chromium-molybdenum alloy
CoM	ceramic on metal
CoP	ceramic on polyethylene
CPT	design of hip replacement
DIW	deionised water
DLS	dynamic light scattering technique
DNA	deoxyribonucleic acid
E	elongation
ECD	equivalent circle diameter
EDTA	ethylene-diamine-tetra-acetic acid

EDX	energy dispersive X-ray analysis
EELS	electron energy loss spectrometry
EFTEM	filter transmission electron microscopy
EMPA	electron microprobe analysis
ESKA	design of hip replacement
FAAS	flame atomic absorption spectroscopy
FCC	face centred cubic
FEA	finite element analysis
FEG-SEM	field emission gun scanning electron microscopy
FEM	finite element method
FL	fibre length
FTIR	fourier transform infrared spectroscopy
FW	fibre width
GFAAS	graphite furnace atomic absorption spectrometry
GMS	Gatan Microscopy Suite
HA	hip aspirate
HAADF	high-angle annular dark field
HCP	hexagonal close packing
HRA	hip resurfacing arthroplasty
HRTEM	high resolution transmission electron microscopy
HS	hip simulator
ICP-MS	inductively coupled plasma mass spectrometry
IR	infrared spectroscopy
ISO	International standard organisation
KOH	potassium hydroxide

L	length
LM	light microscopy
LYDIA	lymphocyte dominated immunological answer
MACC	mechanically assisted crevice corrosion
Mc	million cycle
MD	maximum diameter
MHRA	medicines and healthcare products regulatory agency
MMD	mean maximum diameter
MoM	metal on metal
MoP	metal on polyethylene
MOPS	three-(N-morpholino)propanesulfonic acid
NCS	new-born calf serum
OA	osteoarthritis
P	perimeter
PBS	phosphate buffer saline
PMMA	poly(methylmethacrylate/methylacrylate), the matrix of the bone cement
PR	post revision
PRG4	proteoglycan 4
PSD	particle size distribution
R	roundness
RA	rheumatoid arthritis
RNA	ribonucleic acid
ROS	reactive oxygen species
RPM	rotations per minute

SAED	selected area electron diffraction
SDS	sodium dodecyl sulphate
SEM	scanning electron microscopy
SF	synovial fluid
SS	stainless steel
STEM	scanning transmission electron microscopy
STXM	scanning transmission X-ray microscopy
TCR	tribochemical reactions
TEM	transmission electron microscopy
THA	total hip arthroplasty
THR	total hip replacement
UHMWPE	ultrahigh molecular weight polyethylene
W	width
XANES	X-ray absorption near edge structure
XPS	X-ray photoelectron spectroscopy
XRD	X-ray diffraction

Chapter 1 Introduction

1.1 Background

Hip arthroplasty is one of the most successful orthopaedic procedures, routinely performed to relieve pain and restore the functionality of the joints, following arthritis or violent trauma. Despite a wide selection of bearing couples, fixation techniques and designs available nowadays, the rate of revision surgery is still of concern. With an increasing number of primary operations mainly caused by an aging population with increased life expectations, the number of revision surgery is also expected to rise. This translates in an immense financial burden for the NHS and surgery associated pain and risks for the patients.

Of all types of hip prostheses, CoCrMo metal-on-metal (MoM) articulations are raising the most serious concerns, due to their potential to trigger local and systemic body reactions to wear and corrosion products[1]. With the introduction of modularity at the head-stem connection, the number of sites susceptible to wear processes has increased. The taper junction and cement-stem interface can contribute to the release of metal debris independently of the bearing surfaces. There have been reports of adverse local tissue reactions (ALTRs) to metal debris released from the secondary metallic interfaces in patients implanted with metal-on-polyethylene (MoP), (MoM) or ceramic-on-metal (CoM) bearing surfaces[2–4]. The pseudotumour or bursae has often been associated with signs of corrosion at the modular tapers or evidence of micromotion at the cement-stem interface. The body's reactions to particulate debris depend on their characteristics such as size, morphology, chemical composition and speciation[5]. Depending on their origin, the particles can have distinct physicochemical characteristics which can initiate different types of adverse body reactions. It has been suggested that debris released from taper junctions can trigger more severe adverse body reactions, compared to the equivalent dose of particles originating from the bearings[6,7]. The cause, however, remains unknown, although it is believed that the particular physicochemical conditions at the taper interface may have an influence on the *in vivo* particle reactivity. It is therefore important to understand the characteristics of particulate debris in relation to the origin, be it bearing surfaces, taper junction or cement-stem interface.

The conventional material used for metallic bearings or stems in many hip replacements is CoCrMo alloy. Under normal conditions, CoCrMo alloys demonstrate good tribological properties and corrosion resistance, representing an attractive alternative to other materials. Compared to MoP, the normal volumetric wear rate of the MoM articulations is almost two orders lower[8], but the total number of particles can be up to 100 times more, with the majority in the nanometre size range[9]. The introduction of modularity at the head-stem interface aimed to simplify the process of primary and revision surgery, but it introduced a new metallic interface which can contribute to the overall

metallic ion and debris release, by fretting and crevice corrosion[2,10]. Moreover, pairing different metals (e.g. CoCrMo head and Ti alloy neck) can initiate galvanic corrosion and thus accelerate the release of material from the taper[11]. There is also more and more evidence demonstrating that cement-stem interface can represent an alternative source of wear and corrosion products in cemented total hip replacements (THR). At the interface, the bone cement and metallic stem are held together by mechanical interlock which can debond under physiological loading, allowing for low amplitude micro-motion between the surfaces, resulting in material being removed[12].

CoCrMo wear particles released from the bearing surfaces are significantly smaller than polyethylene debris and can easily enter the blood circulation, spreading within the body. The analysis of biopsy from patients with failed MoM hip prostheses has confirmed wear debris in distant organs, such as liver, heart or brain[13,14]. The reduced size of the particles also increases their solubility in the body fluids, resulting in high ions in the bloodstream[15]. The relative proportion of ions in serum and synovial fluid is believed to depend upon the site of wear and several authors[2,4] reported much higher levels of Co compared to Cr, following the failure at the taper. In several cases, the abnormally high Co serum level has been associated with visual impairment, hearing loss and various neurological and cardiologic issues[1,16]. These manifestations are usually referred to as arthroprosthetic cobaltism or cobalt toxicity and can disappear after the removal of the metal source[1]. The long term effects of the patients' exposure to high Co and Cr ions are still not known, but there are concerns regarding their potential genotoxicity and cytotoxicity[17,18]. Adverse local tissue reactions to wear debris, described in the literature as fluid collections or solid masses around the hip, can be a cause of pain and inflammation, potentially altering the surrounding tissue and bone. Significant damage to the periprosthetic environment can further affect the outcomes of the inevitable revision surgery[19].

With so many potential sources of wear and such a broad spectrum of adverse reactions to the implant, it is imperative to understand the origin, characteristics and subsequent health implications of the particles. Most of the previous studies have investigated metallic debris generated from the bearings and isolated from artificial lubricants used in hip simulators[20–23], while others have reported debris from synovial aspirates[24,25] or periprosthetic tissue, retrieved at revision time[26]. Most of the studies have employed various electron microscopes for imaging and chemical analysis. Particles size distribution varies between the studies and covers the 10 nm-10 µm size range, with the majority in the nanometre scale[9,27]. Previous energy dispersive X-ray (EDX) data suggested that the small particles are mainly Cr_2O_3[28] while the larger particles can consist of the bulk alloy elements. The techniques, however, failed to provide definitive evidence of this. The literature is still scarce in clear evidence of individual nanoparticles generated from hip implants *in vivo* and this could be mainly due to the technical limitations of the older generations of microscopes. To our knowledge, no study to date has reported the characteristics of particles released from around the tapers or cement-stem interface, which have a significant contribution to the total amount of debris and adverse body reactions in patients. Some authors have characterised the black corrosion flakes on retrieved

CoCrMo stems[29], and demonstrated they consisted of densely packed Cr_2O_3 nanoparticles (~50 nm length) surrounded by organic material, potentially formed by tribochemical reactions at the cement-stem interface. At increased magnification, the particles consisted of smaller entities joined together by biological debris, but the study failed to provide a more in-depth structural characterisation of the potential agglomerate.

Despite increasing evidence of the debilitating effects of metal debris generated in the body, little is known about the characteristics and structural changes they suffer after being released. *In vivo*, particles are susceptible to oxidisation, dissolution and release of ions, or can migrate within the body and interact with the biological matrix in their attempt to achieve a more stable configuration. The sequence of transformations the particles undergo depend on their characteristics which reflect in the particle reactivity. Most of the previous studies have characterised debris in periprosthetic tissue and internalised in macrophages. These phagocytic cells are highly specialised in capturing and destroying foreign bodies, such as metal debris, which are subject to a highly aggressive chemical milieu, inside the lysosomes. These treatments, therefore, can alter the size and chemistry of the particles entrapped in periprosthetic tissue and macrophages, and the reported physicochemical characteristics may not be representative of the native properties of debris. It is therefore imperative to characterise particles which have had minimal contact with tissue, body fluids and their protection mechanisms, to understand the original properties of the particulate debris in relation to their origin.

Different metal particles have different surface properties, which affect things such as free-radical generation. Through knowledge of the composition of the particles, how they differ from the original metal, and link this to the site and their method of release, one can be more specific about what ions are being released into the body and how the release varies between the sites of origin (taper or stem-cement interface). By understanding the relation between the particle characteristics, their origins and adverse reactions, the designs of the future implants could be improved, by mitigating the release of the most health threatening particles. A better understanding of the particle nature, in the context of the present knowledge about debris reactivity, could explain why at equal doses, taper debris triggers worse ALTRs compare to the bearings debris[6,7].

Although the popularity of MoM hip replacements has considerably decreased in the last years due to the abnormal revision rates, many people around the world are still implanted with prostheses that contain at least one CoCrMo interface, be it the bearing couple, the taper junction (head-neck, neck-stem) or stem-cement interface. Besides hip replacements, other medical devices, such as spine, knee or wrist implants, contain metallic components that can release material. Understanding the origins and the nature of the particles generated, in partnership with the body's reaction to it, means future designs can minimise the generation of particles which can compromise the health, or medical solutions can be developed to inhibit the reactive pathways the particles initiate. The study, therefore,

outlines the importance of using clinically relevant particles for a realistic interpretation of the adverse effects associated with the implant related debris.

Besides the important contribution to understanding the nature of particles released *in vivo* from hip replacements, the cleaning protocol and the characterisation techniques used in this study can be successfully applied in other scientific areas, such as materials sciences, chemistry or life sciences. The study provides a step-by-step guidance on how to isolate, clean and characterise synthetic or natural nanoparticles, be it debris or drug carriers.

1.2 Aims and Objectives

The main objective of the present study is to characterise the wear and corrosion products released *in vivo* from the tapers and cement-stem interfaces of total hip replacements. By understanding the physicochemical characteristics of the particles and debris, in relation to their origin, solutions can be found to mitigate the incidence of ALTRs triggered by implant related debris.

The specific objectives of the study are:

- To characterise the structure and chemical composition of the as-retrieved wear and corrosion flakes (no treatment applied) released from tapers and cement-stem interfaces;
- To digest the wear and corrosion products to reveal the constituent building blocks and understand their formation;
- To assess the efficiency and the effects of the cleaning treatments on the particle morphology and chemical composition;
- To reveal the physico-chemical characteristics of the nanoparticles released from tapers and cement-stem interface;
- To compare the physico-chemical characteristics of debris released from CoCrMo tapers and cement-stem interface;
- To compare the physico-chemical characteristics of debris released from mixed (CoCrMo/Ti alloy) and matched (CoCrMo/CoCrMo alloy) material taper interface;
- To compare debris released from a toggling and a non-toggling taper, to assess the influence of the failure modes on the particle characteristics;
- To reveal the chemical species released from the secondary metallic interfaces of total hip replacements.

Chapter 2 Literature Review

2.1 The Health Implications of Solid and Soluble Debris from CoCrMo Hip Replacements

2.1.1 Introduction

The popularity of MoM articulations has decreased due to the numerous concerns regarding the adverse reactions to solid and soluble debris[30]. A wide spectrum of local and systemic manifestations has been reported in the literature in patients with CoCrMo contacts subjected to wear and corrosion[2,4,31–33]. Pain and inflammatory responses to metal debris can lead to damage to the periprosthetic tissue and bone, further impacting the post-revision outcomes. Studies have emphasised the importance of early identification and good management of the failing metallic prostheses, which are linked to a successful revision surgery. The integrity of the periprosthetic bone and tissue are important factors to the mechanical fixation of the newly inserted device which can impact the fate of the prosthesis as well as the time required for the patient to start performing simple domestic tasks.

Systemic reactions have often been correlated with high cobalt in blood or serum[34] which might have escaped from the joint area or been released by dissolution from the particles spread to distant sites by the circulatory system[35]. A particular characteristic of the debris generated from CoCrMo hip replacements is the reduced size range, with most in the nanometre domain[27,36–39]. This means increased mobility and larger surface area exposed to the highly corrosive body fluids, leading to particle accumulation at distant organs and cobalt systemic toxicity[13,14,40,41]. Arthroprosthetic cobaltism is sometimes difficult to identify, especially when the clinical and radiological signs are missing, due to the multiple potential causes of symptoms such as hearing loss, visual impairment or mood changes[34]. Researchers came to the help of the clinicians and provided guidance on the management of the patients and tried to identify ion safety levels, over which deeper investigations or revision should be considered[19,42].

The immunological implications of ions as well as the long term exposure to Co and Cr ions have also raised concerns. To date, there is no clear evidence of an increased risk of developing cancer among the individuals with metallic devices, despite the fact that Co and Cr have been introduced on the list of compounds with potential carcinogenic effects to humans[43]. However, the cytotoxicity of Co and Cr ions has been investigated by different *in vitro* studies and demonstrated dose dependent toxic effects[17,44,45]. The health impact of the long term exposure to ions is still not known, but some of the systemic manifestations are reversible and improve when the source of metal is removed[34]. More research is necessary for a better understanding of the wide spectrum of adverse reactions and

early identification of signs of failing prostheses, to avoid the onset of pain and extensive damage to the surrounding tissue.

2.1.2 Local Adverse Biological Effects

Metal related pathology, including periprosthetic soft tissue reactions, account for almost 40% of the MoM hip revisions[46]. ALTRs, described as fluid collections or cystic/solid aseptic masses around the hip, normally present with clinical, radiological or histopathological signs of inflammation[46] and are denominated pseudotumours[47] mainly because of their potential to cause alterations to the surrounding tissue or bone, through necrosis or osteolysis. Various terms have been used in the literature to describe these manifestations, including aseptic lymphocyte vasculitis associated lesions (ALVAL), bursae, metallosis or adverse reactions to metal debris (ARMD)[48]. They may lead to pain and tissue or bone destruction, culminating with poor outcomes for the resultant revision surgery[19]. This outlines the importance of early diagnosis of both symptomatic and asymptomatic adverse reactions and a good management of the patients, aiming to improve the function of the newly introduced hips, following revision.

The concerns raised by the reports of *pseudotumours* after implantation of MoM orthopaedic devices, has led to different studies which aimed to identify the risk factors to the development of soft tissue masses. The incidence of pseudotumours was found to be greater in female patients and a possible reason could be the difference in the native anatomy and bone size[48]. Large diameter MoM THA has also been associated with higher risk of developing soft tissue masses, potentially due to the enhanced risk of damage and corrosion at the taper[2,33]. Wear and corrosion products from around the trunnions can contribute to the total amount of wear debris and have been shown to trigger ALTRs, similar to the spectrum of reactions normally reported with debris originating from bearings[31,49]. Another predictor could be the Co and Cr levels measured in blood samples[19,48]. Pseudotumour formation has been associated with abnormal ion concentrations, which exceeded several recently proposed safe levels. According to the Medicines and Healthcare products regulatory (MHRA) agency, 7 µg/L represents the level for both Co and Cr concentrations in blood, over which the patients should be considered for investigations[48]. Another study proposed Cr 4.6 µg/L and Co 4 µg/L as the upper ion limits in well-functioning unilateral implants and Cr 7.4 µg/L and Co 5 µg/L for bilateral HRA[50]. More recently, a threshold cutoff of ≥1.0 ng/ml Co, ≥0.15 ng/ml Cr, and a Co/Cr ratio of 1.4 were proposed to indicate ALTRs due to corrosion at the taper interface of MoP hip replacements[51]. There are still debates concerning the safe ion levels over which the patients should be closely monitored, as various researchers and agencies advised on different thresholds, without setting a generally agreed limit[42,48,50,51].

Metallosis, or the black discoloration of periprosthetic tissue due to metal infiltration, has been reported by several studies[16,52–54] in patients with MoP implants introduced after the fracture of a ceramic femoral head. The low elasticity and plasticity of ceramic components sometimes can result in brittleness and fracture, followed by the release of numerous sharp particles which are difficult to retrieve. The small ceramic particles left inside the joint cavity can migrate towards the newly introduced bearing surfaces where they promote third body abrasive wear, as shown in **Figure 2.1**. The ceramic particles found in polyethylene liners and the signs of severe wear on the retrieved metal heads, support this hypothesis[16,52–54]. These studies support the replacement of failed ceramic components with other CoC hip implants rather than MoP or MoM prostheses. The different hardness values possessed by metal, polyethylene and ceramics make the first two materials more vulnerable to third-body abrasive wear, with potentially dramatic consequences for the patient[52].

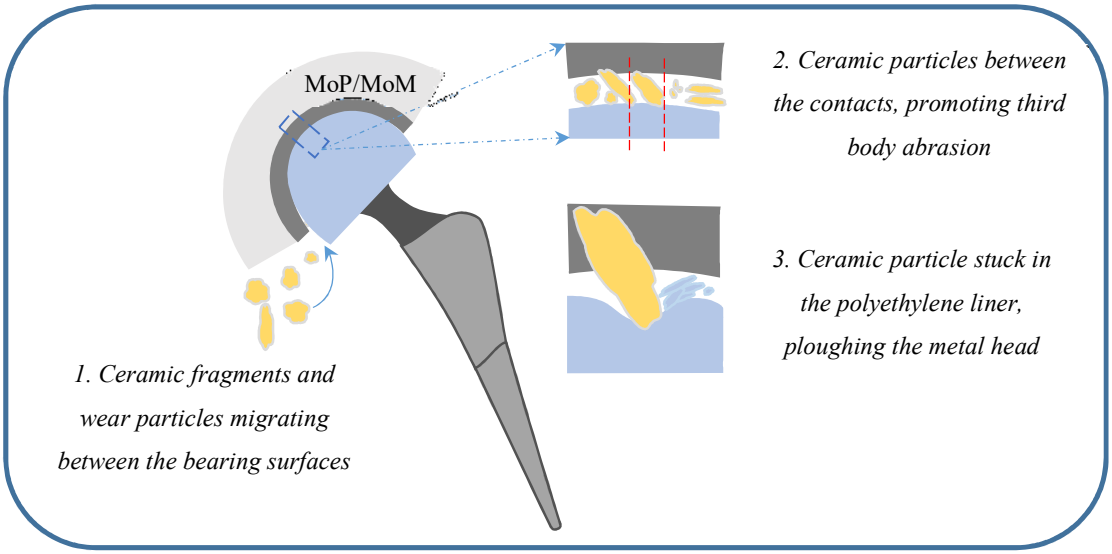

Figure 2.1 Entrapment of ceramic particles between MoP or MoM bearings with subsequent third body abrasion and release of material.

Although they are normally below the critical size required to induce an osteolytic response by polyethylene in macrophages[55,56], metallic particles can also stimulate osteolytic cytokines production, and thus *osteolysis*[57–59]. Several studies reported osteolysis in patients with MoM hip replacements, following abnormal[60,61] or moderate wear[57,59,62] and it is believed to have a multifactorial cause, including cell-mediated delayed-type hypersensitivity reactions[59]. Others analysed periprosthetic tissue retrieved from patients implanted with metal bearings between 5 and 11 years and revealed no sign of bone resorption or osteolysis[63]. Another long term follow-up study and investigation of tissue samples identified the presence of macrophages, but could not see multinucleated giant cells normally found in polyethylene induced osteolytic tissue[64]. These studies confirm that not only the size, shape and composition of particles but also the amount can influence the subsequent local reactions[56]. Wear rates are highly dependent on implant design and material properties, such as the radial clearance, head diameter, sphericity, heat treatment and content of

carbon in the alloy should be carefully selected so that the impact on the general health of the patients is minimised[56].

The clinical and histological features of soft tissue reactions to metal debris were firstly reported in 2005 by Willert et al.[65]. Perivascular infiltration of T and B lymphocytes, the presence of macrophages, plasma cells and giant cells, tissue necrosis and cellular death are all histological signs of adverse reactions to solid or soluble debris[38]. These manifestations resemble T lymphocyte mediated type IV hypersensitivity and have been denominated aseptic lymphocytic vasculitis associated lesions (ALVAL) or lymphocyte dominated immunological answer (LYDIA)[65]. These histological features are classified based on the ALVAL score, which aims to assess the integrity of the synovial lining, the extent of lymphocyte infiltration, number of macrophages and level of tissue organisation[66]. Depending on the ALVAL score, two types of immunological reactions could be identified.

Metal reactivity is an innate immunological reaction, manifested as a non-specific foreign body response to large amounts of metal debris, usually released from poorly functioning prostheses[67]. Significant tissue damage has been reported even with moderate amounts of metal debris from the large diameter MoM THA, therefore other factors such as the low pH and highly toxic corrosion products released from the taper, might play an important role as well[32]. Histologically, metal reactivity is characterised by a low ALVAL score, few lymphocytes and more abundant macrophage infiltration, as well as a grey coloration of tissue due to the massive infiltration of metal debris[66].

Metal sensitivity or *metal allergy* is an abnormal immunological reaction to metal debris which normally occurs in people with genetic predisposition even in the presence of small amounts of metal debris. The histological features are similar to metal reactivity, however some specific characteristics, such as higher ALVAL score, more abundant lymphocytic infiltrates and synovial ulceration, can be used to distinguish between the two manifestations[66]. Metal allergy as a response to hip prosthesis has been rarely reported, considering the relatively high number of metallic orthopaedic devices implanted to date. The symptoms, such as swelling and unexplained pain or local rashes, usually occur shortly after implantation (1-2 years post operatively) and patients do not necessarily exhibit high systemic ions[68]. In most cases, revision to a non-metal bearing is recommended (CoC or ceramic on polyethylene (CoP)), reducing the exposure to wear and corrosion products and thus mitigating the symptoms of metal toxicity.

The most common metal sensitizer is nickel (Ni)[59] which is found mainly in the stainless steel used in coronary stents[69] and dental implants[70], followed by cobalt (Co), and chromium (Cr) usually found in CoCrMo hip implants[71]. Titanium (Ti) and vanadium (V), as well as some components of bone cement could also lead to the sensitisation of patients, and eventually to allergic reactions. Although metal sensitivity is usually associated with contact dermatitis, studies are contradictory[72,73] and there is still no clear evidence of any correlation between dermal metal allergy and the risk of developing

adverse reactions to MoM hip prostheses. Studies have shown that female patients are more prone to develop metal allergy, potentially due to the more frequent use of metal jewellery, which can enhance their sensitivity to metals[74]. Although the mechanism is not clearly understood, it is assumed that metal ions released *in vivo* bond to host proteins and form organometallic complexes able to trigger immune responses that as a consequence release cytokines, which further activate macrophages[56]. This chain of reactions can end up with rapid osteolysis and subsequent implant failure. There are still no reliable procedures for the diagnosis of metal ion sensitivity of patients, which could be used to decide on an appropriate type of implant design and material[56].

2.1.3 Systemic Adverse Biological Effects

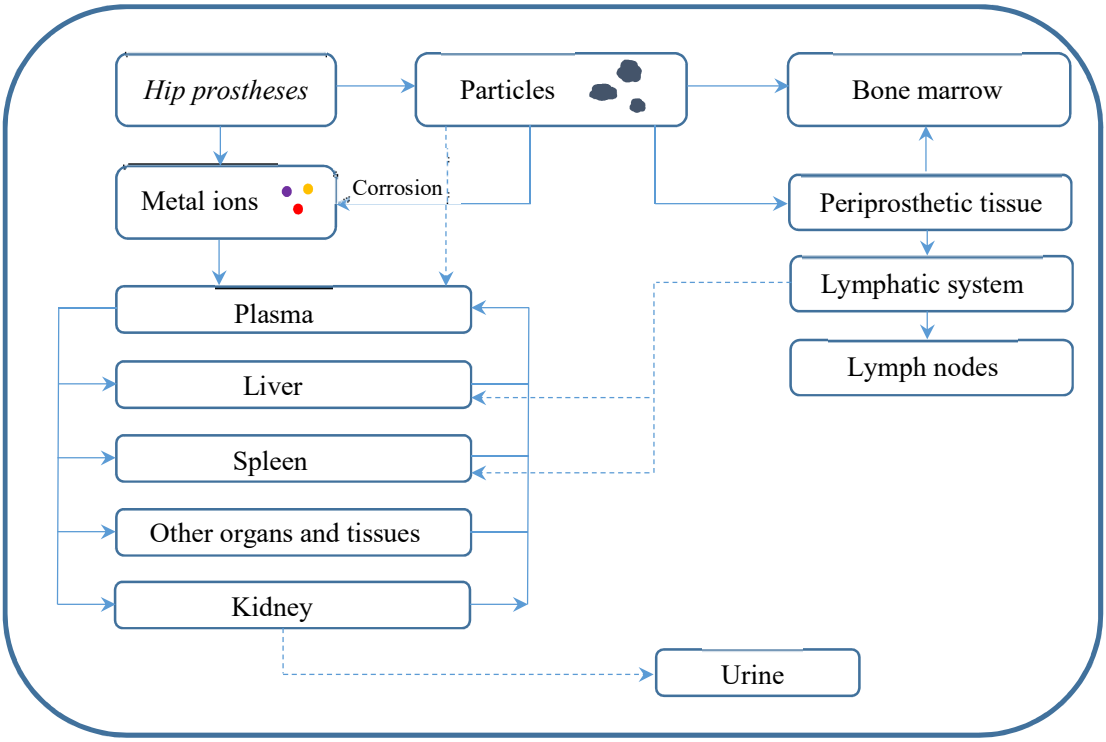

Figure 2.2 Systemic dissemination of wear debris and corrosion products released from metallic implants.

Dissemination of wear particles from the joint area to distant sites around the body has been reported in several post mortem studies on individuals with artificial bearings[13,14,40,75,76]. The pathway is normally via the body fluids which link the synovial cavity, where the particles are generated, with the distant organs, where evidence of wear debris has been found (**Figure 2.2**). Under normal wear conditions, the material removed from the implant is released in the synovial fluid, where the macrophages capture the particles and further enter the lymphatic system. The lymph nodes filter the foreign bodies from the lymphatic fluid in a similar manner to the spleen, which filters the blood[77]. When the wear of the joint is excessive, synovial macrophages cannot capture all the material released and part of it can directly enter the plasma or infiltrate in the periprosthetic tissue or bone,

triggering abnormal immunological reactions and inflammation[35]. When the lymphatic fluid is saturated with macrophages engulfed with metal, it can bypass the lymph nodes, releasing debris at distant sites, such as liver and spleen. The free circulation between organs is probably the cause of the widespread accumulation of metal reported by the previous studies[13,40,41,75]. The journey can stop at kidneys, where part of the solid and dissolved metal can be eliminated through urine[35].

Systemic reactions to metal debris have been described in several case reports and the entire spectrum of manifestations is thought to be linked to the abnormal serum concentrations of Co[16,52–54,78–82]. A review study in 2014 summarised the clinical manifestations of arthroprosthetic cobaltism as they occurred in 18 patients and were previously reported in a total of 26 journal papers[34]. The symptoms of cobalt intoxication varied from one case to another and occurred at different times after implantation[34]. The relevant data about the patients such as age, gender, pre and post revision Co and Cr serum levels and hip replacement types, are all summarised in **Table 2.1**.

The whole spectrum of reactions is comprised in three main categories, suggestively called neuro-ocular toxicity, cardiotoxicity and thyroid toxicity[34]. Each main group can be further divided into more specific subcategories, all represented in **Figure 2.3**.

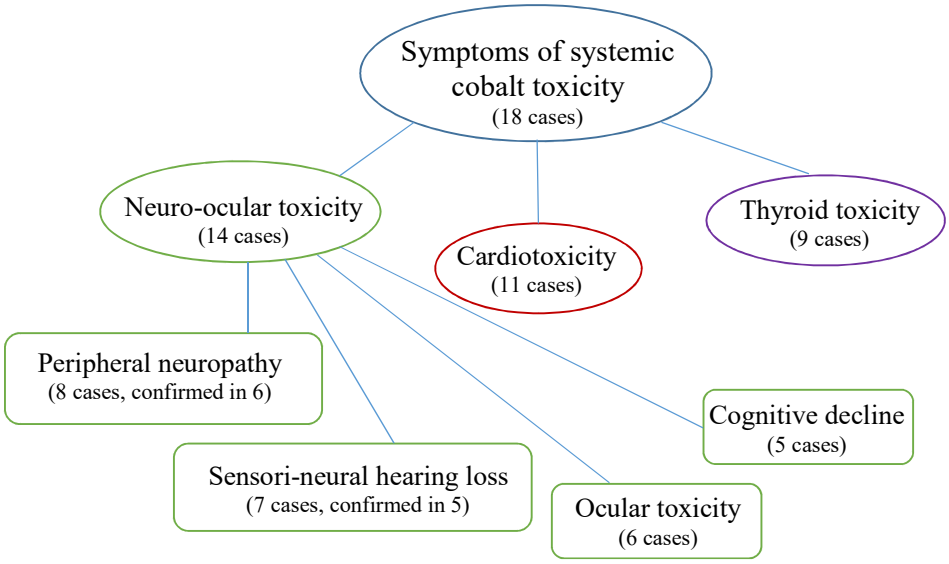

Figure 2.3 Main categories and subcategories of systemic cobalt toxicity manifestations.

Most of the patients described in these studies presented with peripheral neuropathy which was confirmed in 6 patients out of 8. Cobalt level in all patients exceeded 250 µg/L, which is an abnormal value compared to the acceptable limit of 4 µg/L, proposed by Van Der Straeten et al.[50]. Most of the patients complaining of hearing loss also had high serum Co, reaching 885 µg/L in a patient implanted with MoP after a fractured ceramic component. In some cases, the hearing alteration was accompanied by unexplained mood changes, but these symptoms were difficult to link to arthroprosthetic cobaltism, as they were also reported in patients with non-metallic bearings[83] or with normal Co levels[34].

Table 2.1 Information about patients identified with systemic manifestations of arthroprosthetic cobaltism[34].

Case No	Age (years)	Gender	Bearings	Brand	Co pre revision or at operation (µg/L)*	Co post revision (µg/L)*	Cr pre revision or at operation (µg/L)*	Cr post revision (µg/L)*	Systemic adverse effects to metal debris
1	61	Female	MoM	Not stated	254.3	10	91	35	Profound numbness with evidence of central demyelinating neuropathy
2	52	Male	MoP after fractured CoC	Not stated	6521	2618 (two weeks post revision)	23.6	Not stated	Fatigue, anorexia, weight loss, hypothyroidism, dyspnoea, dilated cardiomyopathy, pericardial effusion, polycythaemia and hepatic failure
3	53	Male	MoC after fractured CoC	Not stated	398	< 1 (six months post revision)	56	12.2 (six months post revision)	Visual and hearing impairment (optic atrophy and retinopathy), paraesthesia
4	49	Male	MoM THR after MoM hip resurfacing	ASR XL	23	11 (two days post revision)	Not stated	Not stated	Memory loss, vertigo, hearing loss, groin pain and breathlessness
5	49	Male	MoM THR	ASR XL	32-122	1.2 (ten months post revision)	28-63	7.5 (ten months post revision)	Cognitive, behavioural and mood disturbances, hip pain, dyspnoea, tinnitus, hearing loss, sleep apnoea, diastolic dysfunction, tremor and incoordination, optic nerve atrophy

Case No	Age (years)	Gender	Bearings	Brand	Co pre revision or at operation (µg/L)*	Co post revision (µg/L)*	Cr pre revision or at operation (µg/L)*	Cr post revision (µg/L)*	Systemic adverse effects to metal debris
6	58	Female	MoP after fractured CoC	Not stated	549	~270	54	Not stated	Visual and hearing impairment, sensori-motor peripheral neuropathy
7	56	Female	MoP after fractured CoC	Not stated	>400	39 (two years PR)	22	19 (two years post revision)	Hypothyroidism, distal sensory neuropathy, hearing loss
8	57	Male	MoP after fractured CoP	Not stated	625	34 (five months PR)	81	13 (five months post revision)	Hypothyroidism, peripheral neuropathy, concentration disorder, fatigue, headaches, seizure, hearing loss, weight loss and tachycardia
9	59	Male	MoP after fractured CoC	Not stated	506	270 (two weeks PR)	14.3	25.8 (two weeks post revision)	Distal paraesthesia of legs, weight loss, hearing loss, pericardial effusion, cardiomegaly, hypothyroidism, sensori-motor polyneuropathy
10	65	Male	MoC after fractured CoC	Not stated	446.4	Not stated	46	Not stated	Visual impairment, malaise, cardiomyopathy, bulbar palsy, hypothyroidism, motor axonopathy
11	39	Female	Bilateral MoM hip resurfacing	ASR	44.7	Remained stable	30.9	Remained stable	Paracentral scotoma, ocular discomfort, nausea and metallic taste
12	47	Male	MoP after fractured CoP	Not stated	Not stated	Not stated	Not stated	Not stated	Hypothyroidism, sensori-motor peripheral neuropathy, pericardial effusion

Case No	Age (years)	Gender	Bearings	Brand	Co pre revision or at operation (µg/L)*	Co post revision (µg/L)*	Cr pre revision or at operation (µg/L)*	Cr post revision (µg/L)*	Systemic adverse effects to metal debris
13	75	Male	MoM hip resurfacing	ASR	13.6	4.5	4.1	Not stated	Dyspnoea, chest tightness, dilated cardiomyopathy, limited coronary artery disease
14	73	Female	MoM THR	ASR XL	24.2	3.5 (two months PR)	12.5	Not stated	Cognitive decline, memory loss, depression, anorexia, weight loss, metallic taste, stroke
15	60	Male	MoM THR	ASR XL	12.6-15.2	2.5 (two months PR)	4.6	Not stated	Muscle fatigue, cramp, dyspnoea, cognitive decline
16	75	Male	MoM after fractured CoC	Not stated	352.6	49.3 (six month PR)	67.9	51.7 (six month post revision)	Hip pain, weakness, dilated hypokinetic left ventricle
17	59	Female	Bilateral MoM THR	ASR	398.6	11.8 (three months PR)	Not stated	Not stated	Cough and exertional dyspnoea, biventricular cardiac failure, global hypokinesia, moderate circumferential pericardial effusion and echocardiography
18	55	Male	MoP after fractured CoC	Not stated	885	86.1 (fourteen months PR)	49	Not stated	Heart failure, hypothyroidism, visual loss and hearing impairment

*Normal serum Cr range, µg/L: <0.4;

Normal serum Co range, µg/L: <0.45[79]; PR: post revision

Ocular toxicity is a group of systemic reactions to metal debris, manifested mainly as visual impairment, correlated with high serum Co, following the wear of the bearings after fractured ceramic devices. Less serious sight issues have been reported in patients with lower Co concentrations, with symptoms which persisted even after the removal of the metal sources and are believed to have other causes[16]. Cardiologic issues as a reaction to excessive Co have been described in 11 patients, of which 7 had previously had a failed ceramic implant and 4 had had ASR MoM replacements, a design recalled in 2010 due to unexpected high wear rates[84]. The abnormal values of the serum Co, registered after the fractured ceramic components, have been correlated with other symptoms of systemic toxicity, while two of the ASR patients had questionable association with Co toxicity, supported by the lack of other manifestations[16,85]. Another patient with bilateral ASR prostheses developed progressive cardiologic issues, which eventually required implantation of an artificial ventricular device and subsequent heart transplant[86].

Thyroid toxicity, manifested mainly as hypothyroidism, was reported in 9 patients with revised ceramic components and in one with MoM prosthesis. The association of Co with hypothyroidism and goitre has been known for a long time[87,88]. Cobalt intake is believed to reduce the iodine uptake by the thyroid gland, resulting in clinical manifestations such as those described in this study[34].

In most of the cases, systemic toxicity initiated several months or years after the primary MoM hip replacement, and was clinically confirmed usually after longer times. The high systemic Co levels in some patients followed the revision of fractured ceramic components with new metal or polymer bearings, which were subject to abnormal wear due to third body abrasion. The serum Co and Cr levels[89] as well as the wear tracks of the retrieved implants and periprosthetic metallosis[32,79,89], support this scenario and justify the abnormal release of material[79]. These, however, are extreme and rare situations. The clinical improvement of the symptoms has been noticed in most cases only after the removal of the metal source, when the serum Co levels dropped down to acceptable levels[34].

The correlation between the frequency of systemic toxicity and serum ion levels in patients with metallic hip prostheses has been demonstrated by Van Der Straeten et al.[50]. The study found increased incidence of systemic manifestations in patients with serum Co levels >20 μg/L, which is considered the limit over which the patients are at high risk of developing systemic reactions and a revision surgery is recommended. The same upper limit was independently proposed by other researchers[16], as a sign of increased wear at the bearing component. The overall spectrum of reactions and severity of the symptoms is believed to depend on the blood/serum ion levels and fall into four categories, as shown in **Table 2.2**.

Table 2.2 The symptoms of metallosis specific to serum cobalt levels (www.drugwatch.com, 4th July 2018).

Cobalt level in blood (µg/L)	Possible symptoms
1-5	Heart and memory issues
>7	Hip pain, tissue, necrosis, pseudotumours
>23	Hip pain, mental problems (concentration, memory), vertigo, deafness
>66	Blindness, hip pain, deafness, seizure, tremor, heart failure, goitre, rashes, abnormal blood pressure, depression, weakness

Most of the systemic reactions reported in this chapter have been attributed to Co toxicity, which is the major element of the orthopaedic CoCrMo alloy. Although the percentage of Mo is considerably lower and the serum level has not been reported to increase following metallic prostheses[90,91], little is known about the toxicity of Mo ions or compounds to humans[92]. Acute toxicity is believed to require high doses and the most affected organs are the liver and kidneys, which normally present increased concentrations of Mo, compared to other organs. To our knowledge, the consequence of the long term exposure to low amounts of Mo, which might be the case of the patients implanted with CoCrMo alloy, has not been investigated, but the moderate cytotoxicity of Mo has been demonstrated on bone marrow stroma cells, with irreversible effects initiated between 3 and 6 hours from the exposure[93].

2.1.4 Molecular and Immune Toxicity of Metal Debris

Local and systemic adverse reactions to metal debris are all related to the fate of solid and soluble metal *in vivo* and the interactions established with the surrounding cells and molecules[48,94]. Understanding these mechanisms means solutions can be proposed to inhibit the pathways responsible for adverse reactions.

Under optimal wear conditions, hip simulators predict a low wear rate for MoM prostheses, usually under 1 mm^3/ million cycle (Mc)[95,96]. Most of the particles are released from the tribolayer and are predominantly in the nanometre size range (10-80 nm)[28,36,97,98]. Improper conditions, such as edge loading, normally lead to higher wear rates, generating considerably more debris and favouring the onset of pseudotumours and ALTRs[99]. Lubrication, among other factors, plays an important role in the performance of the implants. Well-performing prostheses allow for the formation of a lubricating

film between the two articulating surfaces, protecting them from excessive wear, as shown in **Figure 2.4**.

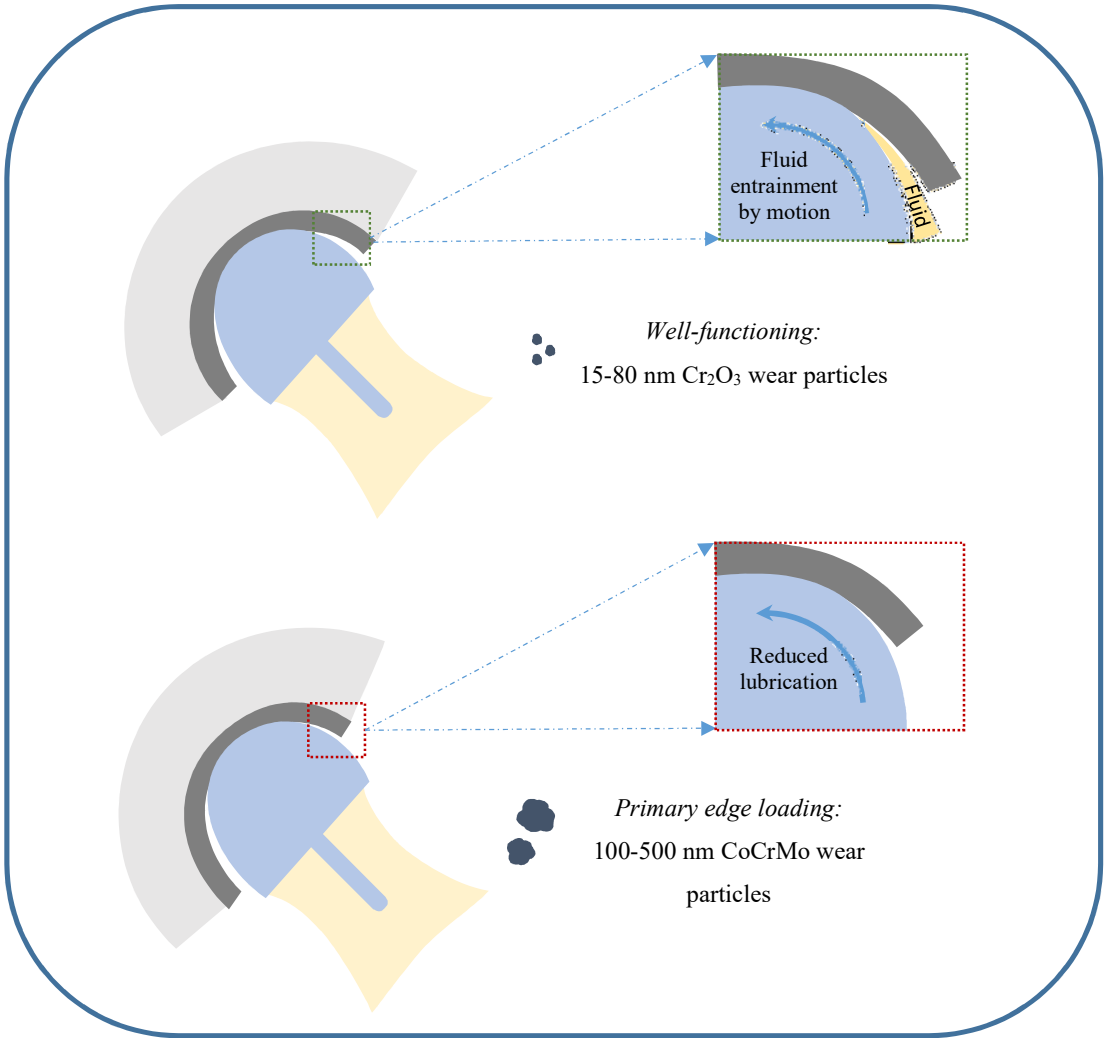

Figure 2.4 Schematic representation of well-functioning and primary edge loading conditions for MoM hip implants, the implication on fluid film formation and general wear particles characteristics.

Edge loading reduces the potential for fluid entrainment disturbing the lubrication and thus leading to more aggressive wear and large particles being released[48]. In the case of CoCrMo bearings, small particles are usually generated from the superficial nanocrystalline layer, while larger particles are released under severe wear conditions and have a more similar composition to the bulk material, containing Cr, Co and Mo in various proportions[28].

During the process of wear, both particles and ions are released in the joint cavity. Most of the body fluids represent a highly corrosive milieu which favours the corrosion of solid debris, and further release of ions[9,15,40]. Cobalt has an increased solubility compared to Cr and is present in the form of

divalent ion Co^{2+}, while Cr is mostly found as Cr^{3+} [38,100], which is the most thermodynamically stable form, but Cr^{6+} was also reported in a previous study[14]. Of the two Cr valence states, the hexavalent Cr has a well-documented toxicity[101] and Co ions are thought to be responsible for the systemic reactions, commonly referred to as arthroprosthetic cobaltism[34,102–104]. Because of their reduced size, wear particles can escape from the joint cavity, spreading all over the body, releasing ions and corrosion products both locally and at distant sites. Urban et al. investigated the dissemination of wear particles and found solid metal in lymph nodes, bone marrow, liver and spleen[13,40]. At these sites, wear particles and ions can enter the cells, where they can exert their harmful effects.

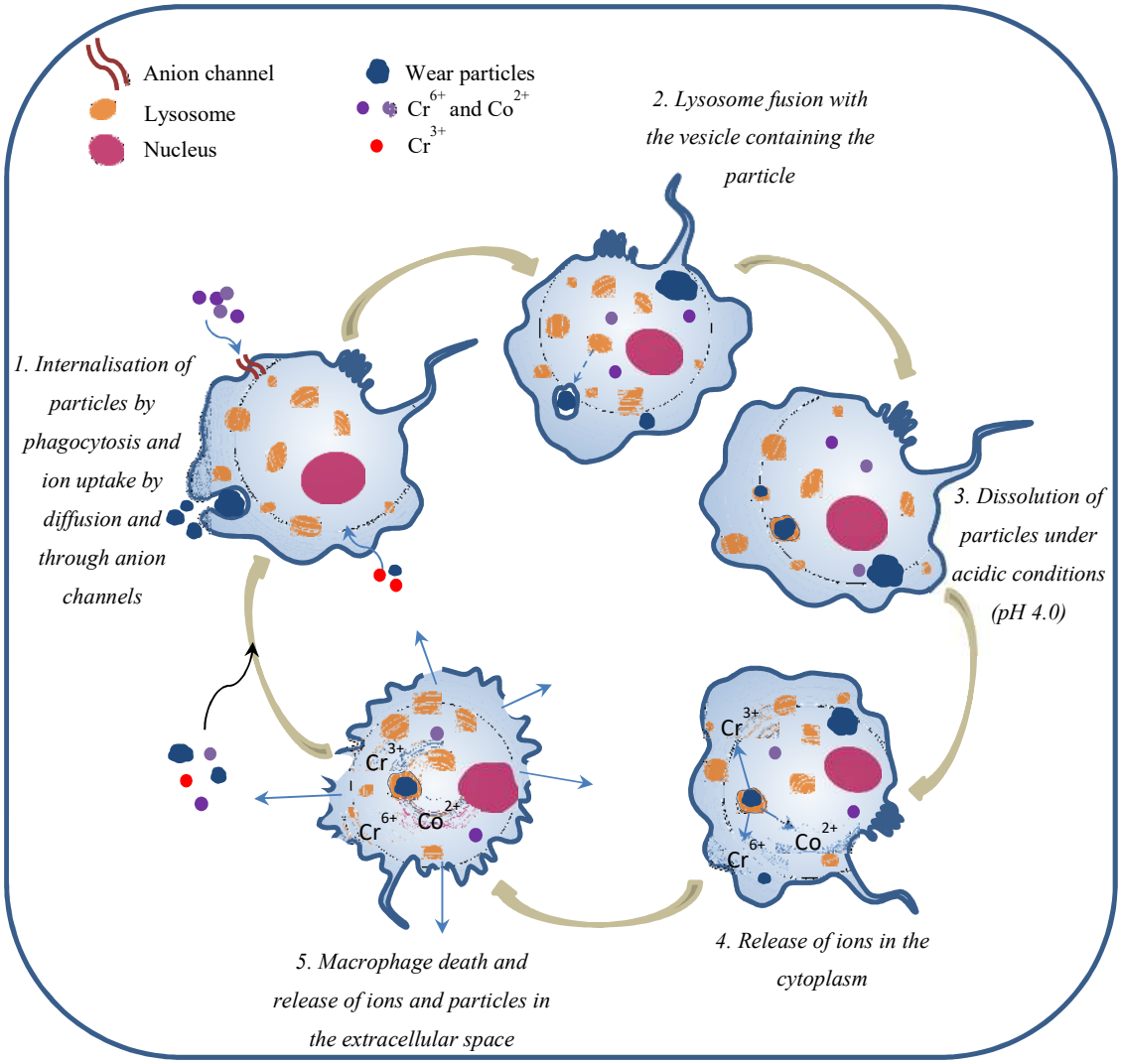

Figure 2.5 Microphage uptake of wear debris, the transformations occurring after internalisation and the impact on the cellular structure and function.

The uptake routes of both ions and particles has been previously investigated by others[38,71,105] and are schematically represented in **Figure 2.5**. The particle size, shape and surface chemistry are important characteristics which are responsible for most of the interactions and affinity levels exerted by

different cellular structures[106]. Most of the biological membranes contain negatively charged phospholipids which are permeable for positively charged structures and restrict the transport of negatively charged entities. Similarly, the interactions with nucleic acids strongly depend on the chemical make-up of particles and ions internalised by cells[106]. Cobalt Co^{2+} and Cr^{6+} enter the cells through non-specific anion channels, while Cr^{3+} has very low permeability and can only pass the phospholipid membrane by diffusion in small amounts[48,105]. In biological environments, Cr exists mainly in the form of chromate ions $[CrO_4]^{2-}$ which can easily pass the cell membrane via non-specific anion channels, being rapidly internalised[105]. Inside of the cell, $Cr^{6+}$is reduced to Cr^{3+} which cannot pass back through the membrane and thus accumulates in the cell[107]. The cellular uptake of metal particles has been investigated as well[38,105]. Phagocytic cells, such as macrophages, are responsible for the internalisation of micrometre sized particles by phagocytosis. They are further corroded under the action of lytic enzymes and peroxides following the fusion with the lysosomes. In addition, nanoparticles are believed to pass through the cellular membrane via passive diffusion and receptor mediated endocytosis and pinocytosis[108,109]. These mechanisms allow for the uptake of nanoparticles even by non-phagocytic cells, such as leukocytes or fibroblasts[48]. Once internalised, particles accumulate in the cytoplasm, where they can corrode under the action of the biological environment, releasing ions[110]. Nanoparticles are the most exposed, as they possess a larger specific area compared to big particles. Intracellular accumulation of ions can lead to cellular death and an entire avalanche of adverse reactions.

The cytotoxic effects of ions and nanoparticles has been demonstrated by numerous *in vitro* studies[17,44,111,112]. Of particular interest is the effect of metal debris on lymphocytes and macrophages, as these cells are commonly found with pseudotumors and have recognised roles in the development of soft tissue reactions[113]. Studies demonstrate a dose dependent toxicity of Co ions and nanoparticles on macrophage viability, whereas Cr^{3+} fails to exert any change even when incubated at higher concentrations[44,111]. Viability of lymphocytes was significantly reduced by both Cr and Co ions and an increase in cellular apoptosis was noticed at high ion concentrations[17]. Cell proliferation and function was also affected even by non-toxic levels and the impact of Co compared to Cr ions was more significant.

Genotoxicity of Co and Cr has been raising concerns since Co ions and Cr^{6+} compounds have been classified as potentially carcinogenic to humans[43]. Cobalt ions can promote mutagenesis by altering the DNA structure through bond breaking reactions, cross-linking or by interrupting the DNA repair mechanisms. On the other hand, the intracellular reduction of Cr^{6+} to Cr^{3+} can lead to highly reactive oxygen species (ROS) which can neutralise through reactions with nucleic acids[18,48]. The cytoplasmic accumulation of Cr^{3+} can also contribute to the genotoxic effects by promoting cross linking, single and double strand breaks[114] and the formation of stable Cr-DNA adducts[115]. Despite these findings, the incidence of cancer among the patients implanted with MoM hips was similar to that of the

normal population[116–118], but the long term effects associated with prolonged exposure to metal debris still needs to be investigated.

2.1.5 Summary

Body reactions to wear and corrosion products from CoCrMo contacts represent the major cause of revision surgery, considerably reducing the lifetime of metallic implants[46]. The wide spectrum of reactions ranges from local pain and inflammation to systemic manifestations, such as hearing loss or mood alterations, with no apparent association with the artificial joint[34]. Metal sensitivity seems to have an increased incidence in certain groups of patients, such as women[48] or individuals with genetic predisposition, while metal reactivity is normally initiated by large amounts of debris and corrosion products, often correlated with severe systemic effects. Osteolysis has been reported with wearing metallic components, but the incidence is significantly lower compared to polymeric bearings[59].

The nature of the particles released from CoCrMo (i.e. reduced size and high surface area) favours their dissemination within the body and localisation at distant sites[13,40,76], where they can dissolve under the action of body fluids and cells. Cobalt toxicity is believed to be responsible for most of the systemic reactions and their severity depends on the Co blood/serum levels[16,80,81]. Several authors have tried to correlate the intensity of adverse reactions with circulatory Co and Cr concentrations and proposed different safety levels, which vary from one study to another[42,50]. Little attention has been given to Mo and its health implications, which along with Co and Cr, demonstrated dose dependant toxicity on osteogenic cells[93], potentially contributing to the overall tissue damage. Despite no clear evidence of increased incidence of cancer in patients implanted with CoCrMo prostheses, Co and Cr are listed among the carcinogenic chemicals to humans[43] and this raises even more concerns regarding the release of debris in humans.

The mechanism and the site of wear and corrosion dictates the properties of particles as well as the amount of systemic ions[32], influencing the body responses. It has been suggested that the failure at the taper interface was associated with more debilitating health effects[6,7], due to the nature of the particles and different electrochemical environment in which they are generated. The fate of the particles *in vivo* depends on their chemistry, size, morphology and aggregation state[5,119], thus a better understanding of the particles originating from different contacts, be it bearings, taper junctions or stem-cement interface, could provide more insight into their associated adverse reactions and solutions to mitigate their onset could be found.

2.2 Elements of Tribology

2.2.1 Introduction

Tribology is the study of interacting surfaces in relative motion, which has numerous applications among the engineering sciences and more recently in interdisciplinary fields[120]. New areas of tribology have emerged in the last 20-30 years which apply the principles of tribology to study and control the friction, wear and lubrication at the nanoscale (nanotribology) or to provide eco-friendly alternatives to the conventional lubricants (green tribology). Other fields have aimed to understand the tribology of the natural systems which found intelligent solutions to decrease or increase friction and provide self-lubrication (biomimetics). These could have important applications in our lives and could solve many engineering problems. Human joints are an example of self-lubricating systems which can reduce friction by the natural production of synovial fluid (SF) and by the contribution of the cartilage[121–124]. The lubrication might become a problem after the replacement of the joint following trauma or disease (osteoarthritis (OA) or rheumatoid arthritis (RA)) as the new artificial bearings cannot produce surface active compounds and cannot provide the cushion effect of the collagen fibres in the natural cartilage[125]. The tribology of the joint prosthetics as well as of other medical devices falls under the field of bio tribology.

2.2.2 Wear mechanisms

The relative motion between two contacting surfaces can be slowed down by friction. This is a force that opposes the motion between the surfaces and depends on the materials in contact, surface roughness and lubrication[126] and can result in the wear of the bearings. Wear can be described as the loss or transfer of material which can cause damage and alter the geometries of the surfaces. There are four major types of wear which can damage the articulating surfaces. Abrasive wear normally occurs between surfaces with different hardness, when the asperities of the harder surface removes material from the softer counter face (**Figure 2.6 a**). This can further lead to third body abrasion which can initiate the loss of material due to the entrapment of wear debris between the moving surfaces (**Figure 2.6 b**). Abrasive wear is the main type of wear acting at the bearings of the hip replacements and is responsible for the main material loss. Adhesive wear results from the local welding or interaction of two contacting surfaces under high mechanical load which forms a transient bonding and leads to the release of debris from the softer material (**Figure 2.6 c**). MoM contacts are susceptible to adhesion when the oxide film is removed from the surfaces and the bulk material is exposed. However, the high energies stored in the deformed metal and defect density lead to a rapid passivation, impeding adhesion[127]. Surface fatigue results in weakened mechanical properties due to cyclic loading and high contact pressures which eventually end up with material torn off[28]. This particular type of wear can be encountered with hip prostheses when the femoral head consists of a hard material (ceramic, metals) which articulates against a softer, polyethylene liner. Polyethylene

liners can experience oxidative degradation during shelf ageing or following sterilisation by gamma irradiation. This can result in free radicals in the polymeric chain which can react with atmospheric oxygen, providing weak mechanical properties and susceptibility to wear[128].

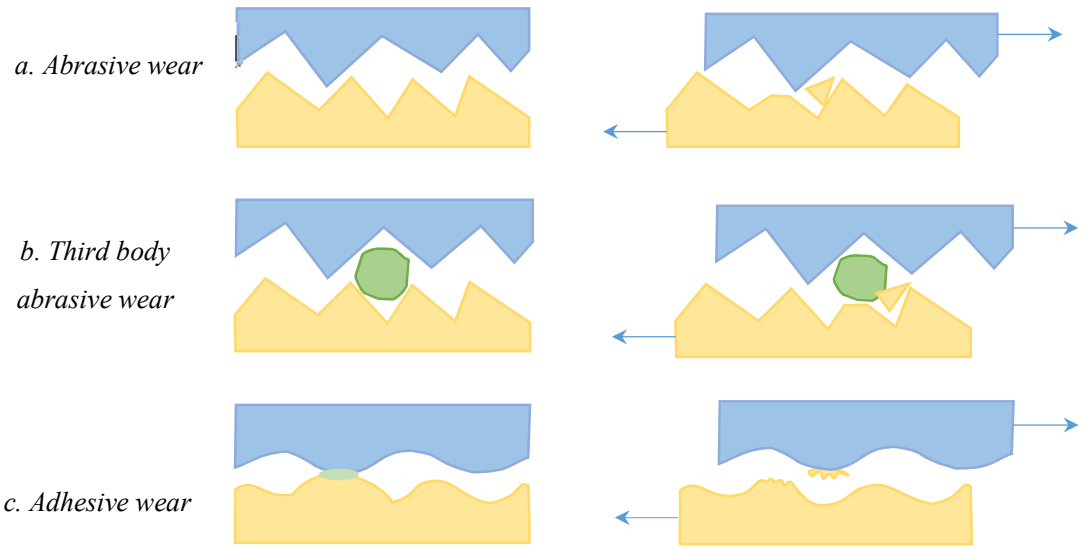

Figure 2.6 The main types of wear mechanism which can occur with the hip prostheses.

Tribochemical reactions (TCR) represent the fourth type of wear which can occur at the MoM contacts as a result of the interactions between the metal surfaces and the organic compounds in the lubricant (SF, bovine serum)[108,127,129–131]. In theory, the phenomenon occurs within or adjacent to the contact area as a result of the mechanical load and friction[127]. This can lead to an increase of temperature at the contact, which can exceed the value at which the proteins in the lubricant denature. Wimmer et al.[127] reported the formation of a carbon-rich solid layer adhered to the metal surfaces, which was suggested to result from protein denaturation, due to mechanical shear, high temperatures, local changes in pH and the catalytic assisted dehydration in the presence of dissolved ions[129]. This carbonaceous layer, also known as *tribolayer/tribochemical layer*, can incorporate wear particles released from the oxide film or subsurface material, as well as dissolved metal ions, generating a metallo-organic composite formed by mechanical mixing. In the absence of biological material (aqueous lubricant) tribochemical layers were suggested to form by a sequence of events which include particle agglomeration (due to their high surface energy), compaction and cold sintering[131]. The presence of tribolayers was suggested to smooth the surfaces, by filling the wear grooves[131] and also provide improved corrosion resistance[132]. Furthermore, the presence of tribolayers between the articulating surfaces was suggested to act as a solid lubricant, impeding the direct contact between the bearings and thus providing them with an ultra-low wear regime[133]. It is believed that a combination of mechanically assisted wear and TCR are responsible for the release of material from the bearings. It is not clear yet the exact sequence of events which initiate and propagate the wear

process, but signs of abrasion, fatigue and TCR were reported with both *in vitro*[127,131] and *in vivo* studies[129].

2.2.3 Lubrication

The release of material from the articulating surfaces can be mitigated by lubrication[126]. In engineering systems, various lubricants are used to reduce friction and wear by interposing between the surfaces and reducing their contact area. Lubricants can be liquid, solid and semisolid, and their selection is made according to the conditions in which they are expected to perform (vacuum, high temperatures, low temperatures etc.).

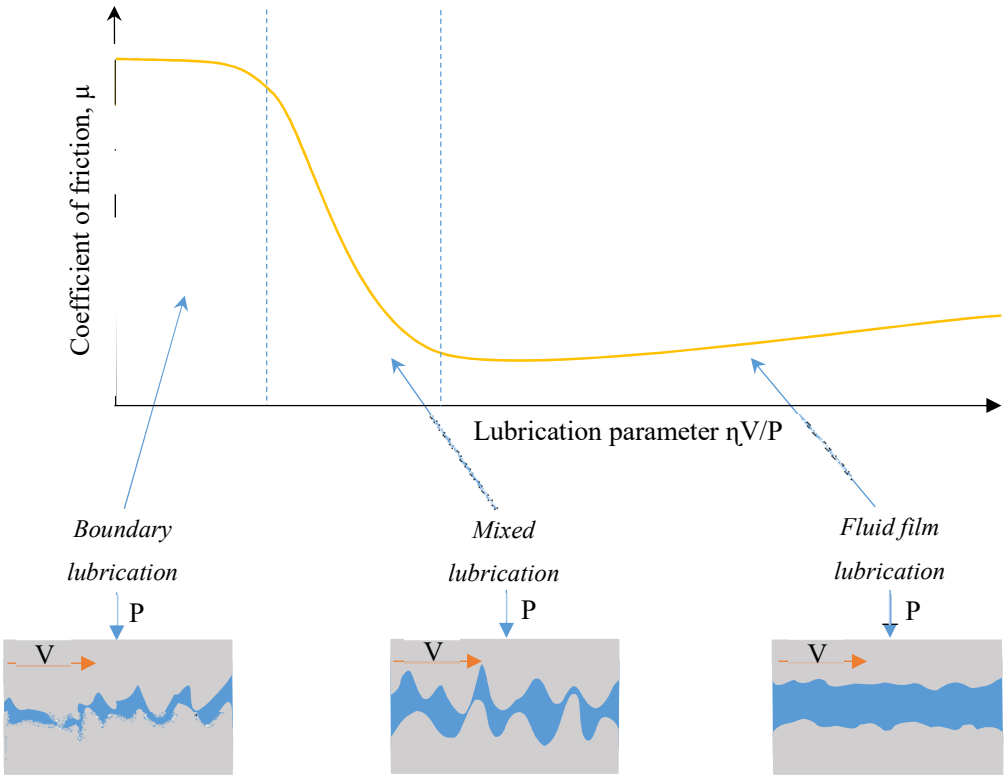

Figure 2.7 Stribeck curve and the main lubrication regimes.

In the case of natural and artificial joints, the lubrication is provided by SF[121–124,126]. There are three main lubrication regimes which can occur. These are described by the Stribeck curve, shown in **Figure 2.7**, and represents the relationship between the coefficient of friction μ and the lubrication parameter ηV/P (or Sommerfield Number), where η is the viscosity of the fluid, V is the average sliding speed and P represents the average surface load[126]. *Hydrodynamic* or fluid film lubrication is characterised by a complete separation of the surfaces by a pressurised, non-compressible fluid film which normally occurs from the relative motion of the bearings at high speeds. In this case, the applied load is held by the fluid and the surfaces do not come in contact, resulting in minimised or non-existent wear. This type of lubrication is an ideal case which is difficult to achieve and maintain

in real situations. *Boundary lubrication* occurs when the surfaces are separated by a thin fluid film which allows the asperities of the contacting surfaces to rub against each other, resulting in high friction and wear. In this case, the surface active biomolecules found in lubricants (particularly in the SF) engage in physical and chemical interactions with the surfaces, creating a protective molecular film which reduces the friction coefficient compared to dry lubrication. The third type is the *mixed lubrication* regime which is a condition between the ideal hydrodynamic lubrication and boundary regime. In this regime, the surfaces are partly separated by the fluid film which provides improved friction coefficient compared to boundary lubrication. However, some of the asperities of the opposite surfaces (those higher than the thickness of the fluid film) will come into contact, resulting in wear and material loss. The predominant lubrication modes in artificial joints are boundary and mixed lubrication[126,134,135]. MoP and CoP hip replacements operate mainly in the boundary and mixed regimes, independently of their size, while mixed lubrication is the prevailing mode of MoM joints, although they can pass through all types of regimes[126,134]. The lubrication of MoM articulations was found to be the most dependant on the implant geometry, design and loading conditions, with the best lubricating conditions being achieved with large heads and reduced clearance, defined as the distance between the inner diameter of the cup and the diameter of the femoral head[136–138]. The estimation for CoC hips using empirical formula and numeric simulations[126], as well as experimental results suggested they can achieve fluid film lubrication[134]. Despite the low film thickness characteristic to ceramic bearings, they possess high surface finishing (low surface roughness, wettability) which altogether provide proper conditions for hydrodynamic regime[126,139]. As with MoM, CoC designs also require a proper selection of clearance. High values can lead to boundary lubrication, while too low clearances can result in edge contact and lubricant starvation.

The hip bearings have a conformal spherical geometry (ball-in-socket) in which the two components are manufactured with a clearance[126]. Normally, this clearance is in the order of tens or hundreds of microns and has an important role in the lubrication of artificial joints and contact pressures[136]. The contact area and stress distribution at the hard-on-hard hip bearings is frequently estimated using the Hertz theory, which was initially developed for non-conformal geometries and assumed that the contact area between two external spheres under load can be reduced to a plane circle[126]. This and other approaches, such as the finite element method (FEM) which can be applied to more complex geometries and material behaviours, are estimations considering the contact at the macro scale. In reality, the contact occurs between the surface asperities which experience high stresses and strains, resulting in damage at the micro level. In the case of conformal geometries, such as the femoral ball and cup, the nominal contact surfaces are part of spheres. The load is distributed across the entire contact, which means that a small area will result in higher stresses and wear. Polar loading is a typical case of reduced contact area provided by a large diametrical clearance between the head and the cup (**Figure 2.8 a**), whereas a small clearance can result in surfaces not fitting together geometrically and achieving equatorial contact (**Figure 2.8 b**). Both situations are associated with high contact stresses and increased wear. The optimal clearance allows for the formation of a

wedge between the head and the cup (**Figure 2.8 c**) which favours the entrainment of the fluid during motion, providing lubrication and reduced friction or wear[126].

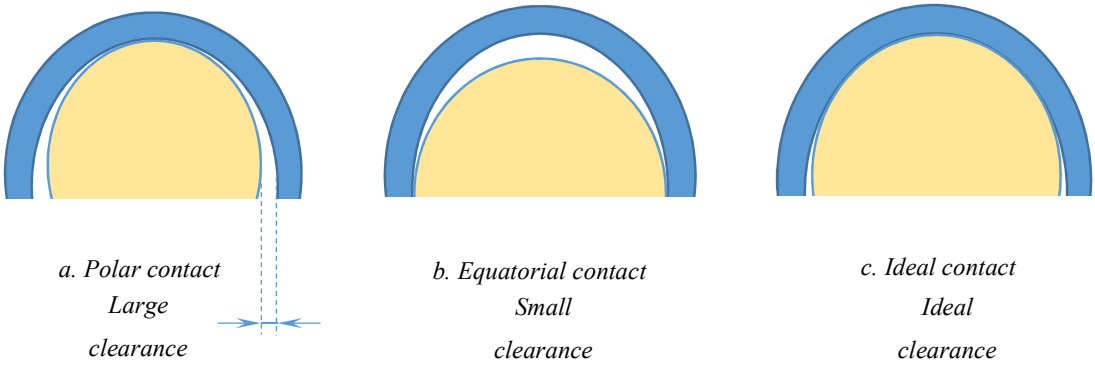

Figure 2.8 Schematic representation of polar contact (a), equatorial contact (b) and the ideal contact (c).

Together with clearance, head diameter is an important parameter which can influence the tribological behaviour of hip replacements[126]. Smaller heads and larger clearances (less conformal surfaces) were suggested to provide the highest contact pressures. A comparison between MoM and MoP with the same femoral head size, showed a contact pressure 10 times higher for the MoM design, although its contact width was 4 times lower than that of MoP [126]. This means that larger areas are worn with MoP compared to MoM couplings. The coefficient of friction was suggested to be the lowest for CoC and the highest for MoM designs, with a small difference between total MoM and resurfacing MoM (the latter showed lower values)[126].

2.2.4 Wear and Corrosion of the CoCrMo Hip Bearings

MoM bearings experience a biphasic wear, characterised by a short period of high wear during which the bearing surfaces undergo a self-polishing process which results in more conformal geometries of the head and cup[140,141]. This area of conformance reduces the contact pressures and improves the lubrication of the bearings. The 'bedding in' or 'running in' phase is followed by a low steady-state wear phase, in which the wear is reduced. The cup inclination was suggested to influence the formation of the critical conformance area[141]. Steep cup inclinations are associated with edge loading which prevent the formation of the conformal patch and extend the contact area over the cup rim, experiencing high contact pressures[142]. The reduction of the film thickness at the cup rim[143], in association with high contact pressures resulted in high wear rates, commonly reported with large heads and resurfacing MoM hips[144–147].

The material released from the CoCrMo bearing surfaces is believed to originate from the tribochemical layers and mechanically mixed zones at the subsurface[28,130,148]. Tribochemical layers are generated from the mechanical and chemical interactions between the contacting surfaces and the compounds found in the lubricant, interposed between the bearings[127,129]. The sliding motion and friction at the bearings can result in high temperature and energy in the deformed metal which enhance the oxidation. Partially oxidised islands can flake off when they reach a critical thickness which results in the exposure of the bulk material to the lubricating fluid. This facilitates the corrosion and the release of ions. It is believed that the proteins from the lubricant can form ogano-metallic complexes with the ions in the proximity of the bearing surfaces[149], which facilitates their adhesion to the metal[150]. These regions of oxides and adhered organic material can be incorporated into the metallic matrix by a process known as mechanical mixing.

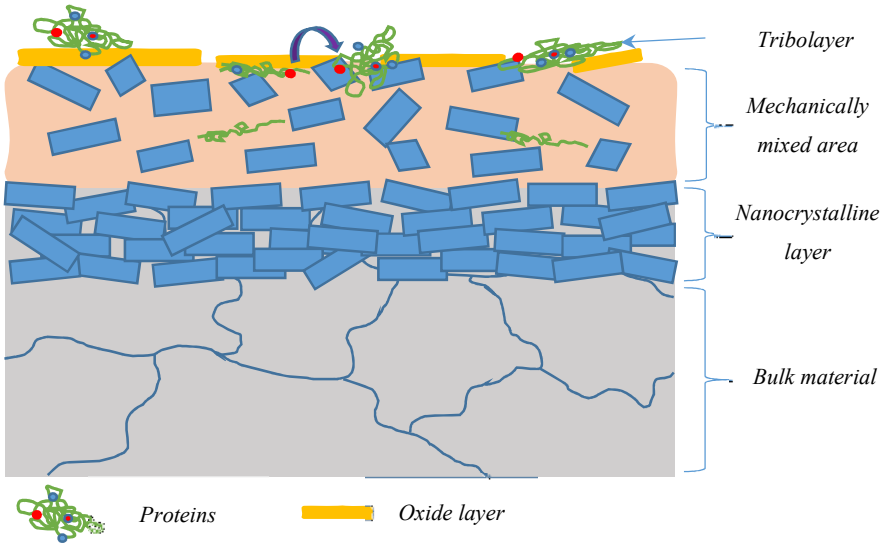

Figure 2.9 Schematic representation of a mechanically mixed area and tribolayer, believed to be the source of wear debris.

Wimmer et al.[130] explained the mechanical mixing process which was found to change the structure of the uppermost layers of the CoCrMo alloy, which is schematically represented in **Figure 2.9**. The formation of a nanocrystalline structure below the surface of the CoCrMo alloy from explanted hips and pin on disc tribological tests was reported by Büscher et al.[131]. In these regions, the size of the grains was between 50 and 80 nm and the nanocrystalline layer was observed to a depth of 500 nm below the surface of the retrieved bearings. It was suggested that the nanocrystals are a consequence of the mechanical polishing involved in the implant's manufacturing, which promotes plastic deformation, causing mechanical milling and dynamic recrystallization[131]. At the surface, the crystals can rotate under the action of shear stresses, engaging the C rich tribolayers and oxide patches in motion resulting in their migration deep into the metallic matrix. This contributes to the formation of a mechanically mixed zone of nanocrystalline metal and organic constituents, with a structure

which varies from purely metal to a metallo-organic composite. Wimmer et al.[130] showed than the upper 50 nm of the contact area is formed mainly of C, N and O, while the composition starts to change between 50 nm and 200 nm depth. In this region the proportion of C gradually decreases while the proportion of the metal elements (Co, Cr and Mo) gradually increases. The presence of nanocrystals was demonstrated by transmission electron microscopy (TEM) which found mainly hexagonal close packing (HCP) crystals, suggesting the strain induced phase transformations (from face centred cubic (FCC) to HCP), also reported by others[130,131,151,152]. The size of the nano crystals correlates to the size of the particles released from the CoCrMo MoM hip joints and tribotests[28,131] which support the hypotheses that wear debris can originate from the mechanically mixed regions and nanocrystalline microstructure of the CoCrMo bearings. It was suggested that the round particles are released from the nanocrystalline layer, while the needle shaped particles are fragments of the ε-martensite bands which form in the subsurface[131].

The nature of debris released from MoM hip replacements in hip simulator studies was found to depend on the choice of the lubricant. In general, the tests performed in water resulted in higher wear rates[153,154] and the release of larger CoCr particles (more Co over Cr), believed to originate from the alloy matrix[20]. The studies using serum lubricants (bovine serum or solutions of bovine serum) reported reduced wear rates and mainly small Cr, O and C containing debris, potentially from the passivation layer[20]. The more aggressive wear conditions observed when the bearings are lubricated by water can be the consequence of the lack of tribolayers, which do not form in the absence of proteins and biological compounds. Moreover, the thickness of the passivating oxide layer formed by CoCrMo bearings when immersed in water is of only 3-3.5 nm, compared to ~85 nm in serum[155,156]. The removal of the thin superficial oxide film reveals the alloy material which either repassivates[157,158] or contributes to the release of debris in the form of CoCrMo particles.

The main problems associated with metallic bearings is the release of metals and ions, which can trigger severe ALTRs. It is not clear yet if the body responses are a consequence of the particles, ions or both, but the level of systemic ions was correlated to the frequency of adverse reactions[50]. Metal ions result from the electrochemical reactions involved in the corrosion of metal surfaces and particulate debris. Mechanical wear leads to the removal of the oxide film and the exposure of the bulk material which is susceptible to corrosion.

However, the dissolution and reformation of the oxide film can occur even in the absence of wear[157]. Under proper electrochemical conditions (the presence of oxygen), the oxide film is spontaneously formed, mitigating the dissolution of ions from the subsurface (**Figure 2.10**)[50,157].

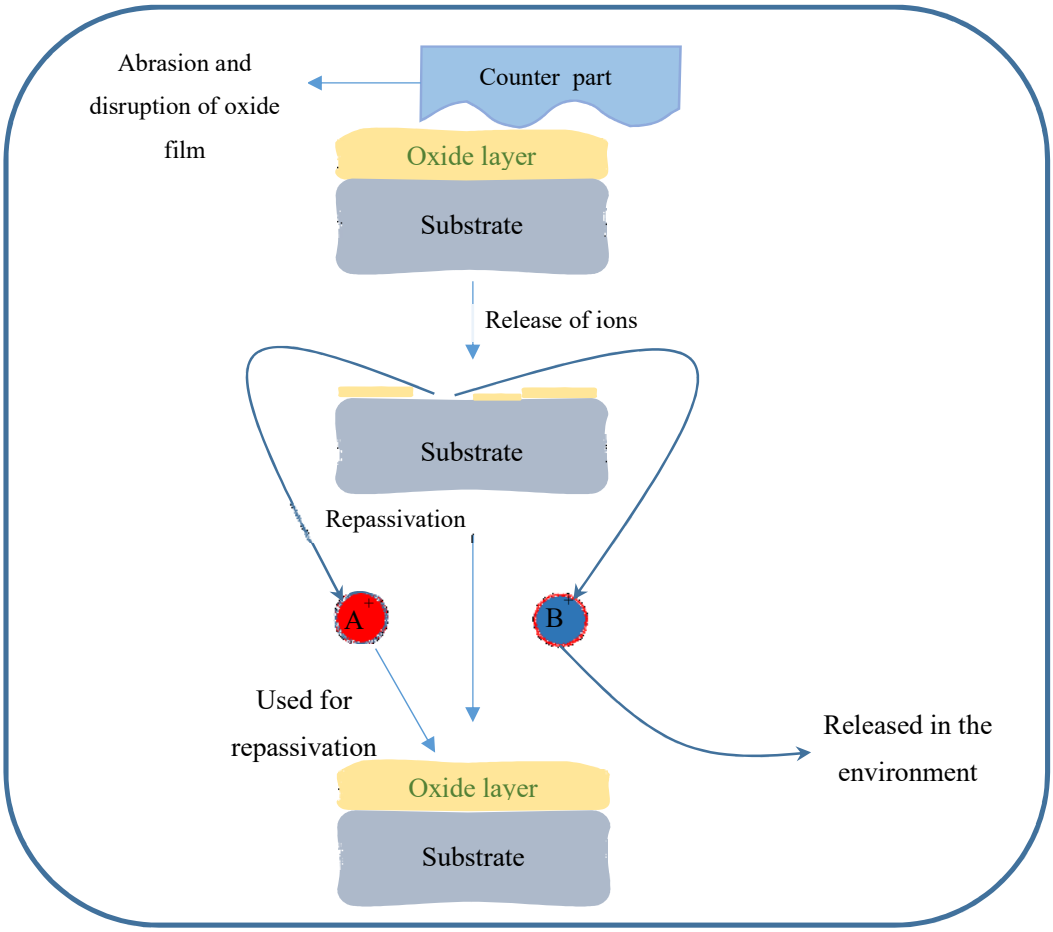

Figure 2.10 Schematic representation of the rupture and reformation of the oxide film.

Crevice corrosion is a particular type of corrosion which occurs in confined spaces which allow the ingress and stagnation of fluids[159] and is commonly found at the taper-trunnion interface, associated with severe ALTRs[2,32,160]. The electrochemical environment in crevices is characterised by a reduced concentration of dissolved oxygen and high concentrations of corrosion products. The lack or the low concentration of dissolved oxygen, promotes the cathodic reaction which results in even more ions and a lower pH[161]. This further enhances the corrosion and metal dissolution potentially creating a highly toxic environment.

In the case of CoCrMo alloy, the passivating layer consists mainly of chromium (III) oxide (Cr_3O_2) with fewer Mo oxides, while Co is mainly dissolved into the body[157]. The exposure of the subsurface material means that the bulk alloy is in contact with the surrounding fluid and biomolecules, which

facilitate the release of ions. Of these, some will be used in the regeneration of the oxide layer (Cr in the case of CoCrMo alloy) while other will be released in the environment as shown in **Figure 2.10**.

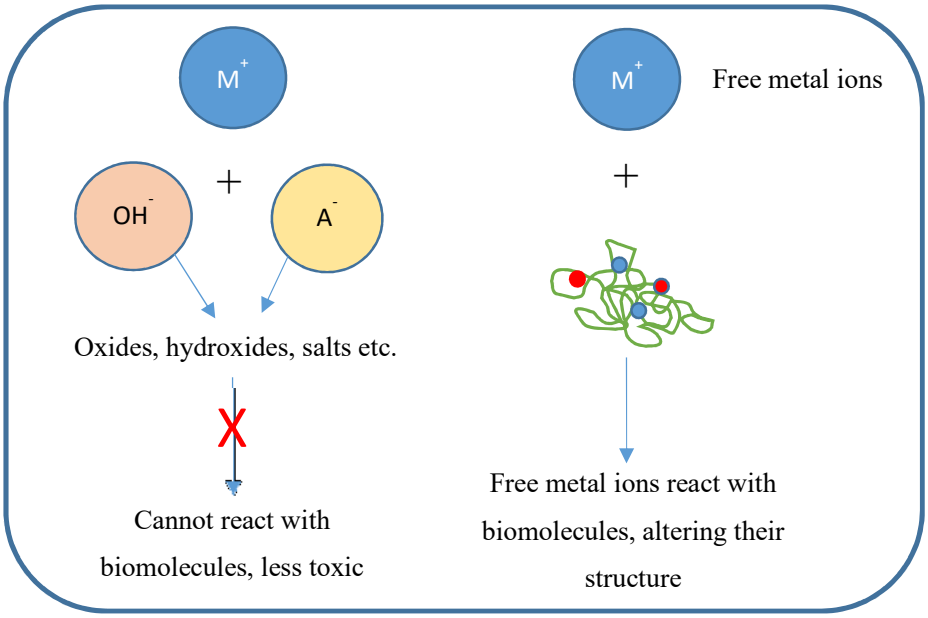

Figure 2.11 The possible pathways of ions in the body.

The free metal ions can further engage in reactions with anions from the fluid, forming oxides, salts or hydroxides (**Figure 2.11**)[157]. Under this form, the ions cannot react with the biomolecules, such as DNA, RNA, and thus they are considered less toxic. However, some ions can enter the cells where they can bind to proteins and nucleic acids, changing their structure and function. This results in altered function of the cells and the onset of ALTRs.

Wear particles can undergo similar reactions. The increased number of particles of very small sizes makes them susceptible to corrosion due to the large surface area exposed to the corrosive environment. It was suggested that one third of the total amount of ions released from MoM bearings result from the corrosion of metal debris[162,163] which means that solution to mitigate the wear and release of particles should be found.

2.2.5 Wear and Corrosion of Tapers

Modularity at the femoral head and stem in total hip arthroplasty was introduced around 1970s as an alternative to conventional monoblock femoral components and aimed at simplifying the primary and revision procedures by allowing the exchange of the worn out bearings while retaining the well-fixed stems[4]. This results in an overall reduction of the surgery time, blood loss and tissue/bone exposure and a shortening of the recovery of patients[10,161]. Modular stems can accommodate a wider range of femoral heads (i.e. different sizes or materials) leading to more customised fit prostheses, personalised to every patient's needs. This allows for a better adjustment of the leg length and lateral offset, as well as enabling a proper soft tissue balance around the hip[4,161]. Dual modular stems aim to provide even more intra-operative options for surgeons, at the price of an additional metallic interface[164]. An aspect of modularity was also cost saving as the hospitals needed fewer components in their inventory, particularly for the modular neck joints.

Despite the clear advantages, modularity means more interfaces and the increased potential to produce wear and corrosion debris, contributing to the overall release of material[4,31,49]. The issue is not entirely new and it was first described in the early 1980s in a study aiming to verify the susceptibility to galvanic corrosion of mixed material couplings in total hip replacements[165]. The literature is now rich in studies presenting the wear and corrosion at the modular contacts in total hip implants[2,31,49,166–169], and more research is needed to better understand the process and identify solutions to mitigate the release of material. Like the head-stem interface, the neck-stem junction is susceptible to wear and corrosion, releasing material which has been reported in association with ALTRs[4,49,160,169]. These junctions are subjected to higher stresses compared to the head-neck tapers, due to eccentric loading and cantilever-type bending stresses[32,164], increasing the damage to the oxide layer[169,170]. In addition, fracture[171,172] and dislocation[173] at the modular stem-neck have also been reported.

Metal debris from tapers can trigger a similar spectrum of reactions as the material originating from CoCrMo bearings. Revision surgery revealed pseudotumours and tissue necrosis in patients with modular MoM[31,49,169,174,175], CoP[3,32,176] or MoP bearings[2,4,49,169,177], with evidence of wear and corrosion on the retrieved tapers, in both matched[4] and mismatched (mixed) material combinations[31,178]. The incidence and severity of taper damage varies from one study to another[4,10,179] and retrieval analyses usually revealed higher incidence and more severe damage associated with dissimilar combinations of metals[167,180–182]. The contribution of modular designs to MoM failures has resulted in higher revision rates for total hip replacements (THR), in relation to matched resurfacing systems[183,184], even when edge wearing exists[145,146]. The wear and corrosion at the taper has been acknowledged as an important source of metal debris and more importance has been given to the study of this particular interface.

The exact mechanism of trunnionosis (i.e. failure due to taper wear and corrosion) is still not well understood, but it is believed to have a multifactorial cause[179]. Taper design, material combination and the size of the femoral head are among the factors which can influence the tribology and corrosive behaviour of the tapers[10]. To understand their contribution, it is important to know how the junction works and how the modularity is provided. The femoral components are joined together by the bore of the head and trunnion of the stem (**Figure 2.12**)[10,161]. They are mechanically stabilised by the impaction force applied by the surgeon at implantation time, resulting in force-fit connection exerted by radial stresses from the male taper (trunnion) to the wall of the female side (bore)[185]. Tapers are cylindrical structures with uniformly decreasing diameters towards the proximal end, with important geometrical and material properties, such as length[186], diameter and stiffness[182], angle and clearance[187], surface texture and roughness[185,186], which can influence the distribution of stresses and the stability against motion[188].

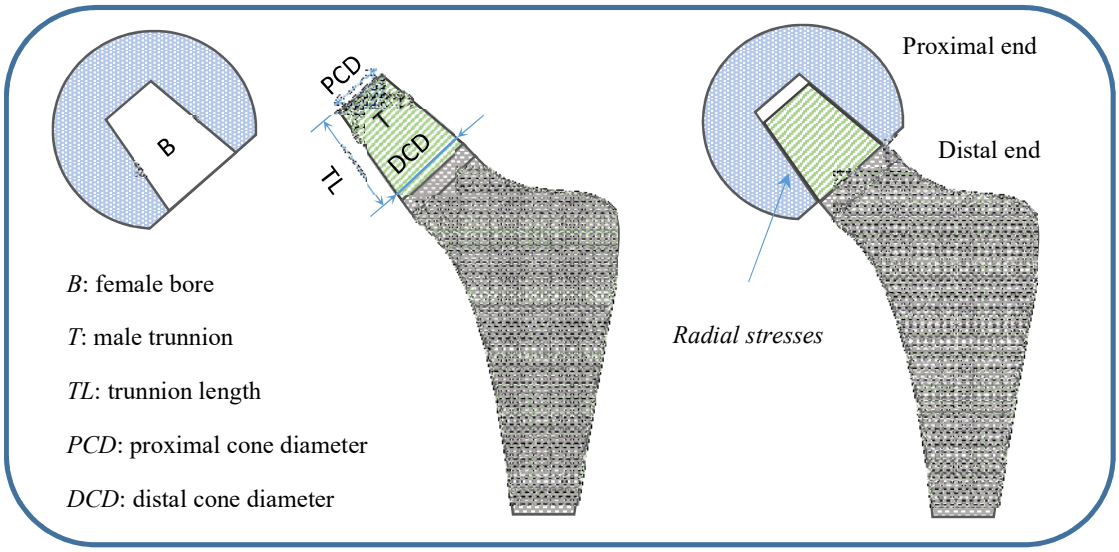

Figure 2.12 Schematic representation of the bore of the head and trunnion of the stem.

The initiation of damage at the tapers is believed to occur due to cyclic loading conditions which can generate oscillatory motion between the surfaces and can disrupt the oxide layer releasing particulates, by a mechanism known as fretting wear and further exposing the sub surface material[2,4,189]. Under proper electrochemical conditions (i.e. oxygen-rich environment) the superficial layer can reoxidise, and thus protect the native material from dissolution[10]. When the taper design allows the formation of crevices, the amount of fluid entering the cavity is limited, with a continuously changing chemistry and increasing corrosion capacity. The metal surface in the crevice can play an anodic function, resulting in the release of cations (positively charged ions) by dissolution[161]. The cation-rich environment can trigger hydrolysis, which decreases local pH, and leads to accumulation of anionic species, such as Cl^-. The crevice corrosion is then accelerated following the cyclic pathway[32]. The combination of fretting and crevice corrosion is known as mechanically assisted crevice corrosion (MACC) and has an important contribution to the release of

material from the taper[2]. The presence of fluid in the crevice can also promote erosion corrosion, due to impaction of the wear particles and proteins found in the bathing fluid, to the wall of the crevice. The consequence is the release of increasing levels of ions in the SF and serum[2], typically with much higher Co compared to Cr[2,4,160,169,190] and subsequent onset of ALTRs, similar to those reported after the failure of metallic bearings[2,4,31,49].

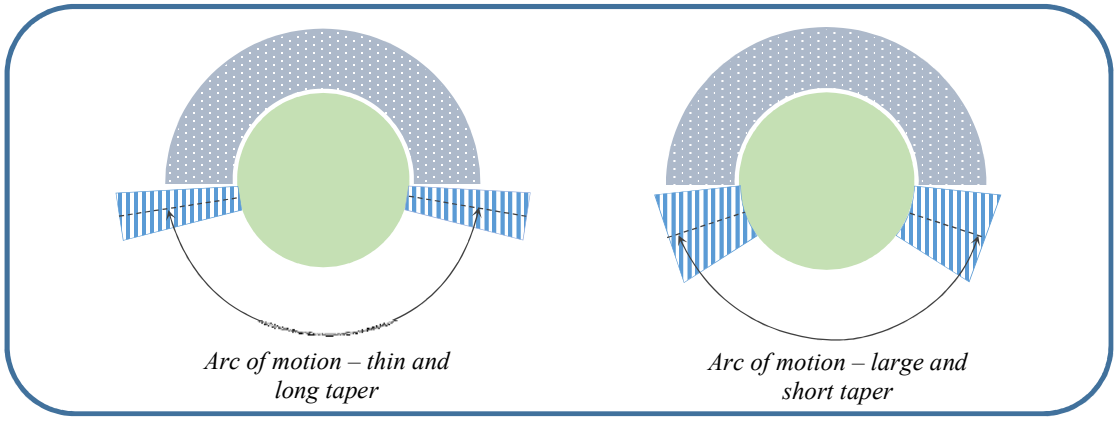

Figure 2.13 The effect of a taper diameter and length on impingement and arc of motion.

Taper geometry is among the factors believed to influence the wear and corrosion at the modular interfaces and studies have been conducted[186,191–194] to identify how the diameter, length, angle and contact length impact on the performance of the tapers. Large diameters and long tapers with circular necks offer a bigger contact area between the bore and trunnion and are believed to promote better interlock and mitigate the range of motion[191]. However, Nassif et al. identified higher fretting and corrosion scores associated with larger tapers and longer contact length, suggesting that the larger the engagement area between the bore and the trunnion, the greater the area susceptible to fretting[192]. Narrow trunnions can mitigate the risk of dislocation by increasing the head-neck ratio, and providing a higher range of motion free of impingement (**Figure 2.13**)[195]. At the same time, shorter tapers fully sit within the bore and increase the risk of mechanical loading at the base of the trunnion[161,194]. Tan et al. reported increased damage around the base area in a retrieval study, and concluded that this particular region of the short tapers is subjected to higher stresses, resulting in enhanced damage[193]. Furthermore, a comparison between mini and standard neck tapers showed increased surface roughness and evident change in the surface profile on the head tapers articulated with mini necks, which was attributed to the reduced contact area[186]. Large metal heads matched with threaded short stem tapers (10-12 mm long) were reported to migrate onto the stem[184], resulting in imprinted marks on the originally smooth head inner surface, following a screwing like motion pattern, believed to occur from the combined action of the joint force and increased torque moments, observed with the large MoM bearings[196]. Panagioutidou et al. reported similar findings on the head bore matched with mini neck tapers, and observed the loss of material from the circumferential groves, which were deeper and more widely spaced than the originally machined surface finish, and showed marks of

pitting and corrosion[186]. There are debates concerning the importance of taper dimensions, as Higgs et al. found no correlation between the wear and corrosion and the size of the male taper, but it implied that other factors such as the head offset, implantation time, patient's weight and taper's flexibility might have more implication to the phenomenon[197]. Regarding the distribution of wear across the taper interface, most of the retrieved MoM modular components presented either uniform or circumferential wear, with more emphasised damage in the distal region of the contact[182,192,198] suggesting toggling of the head[2,198].

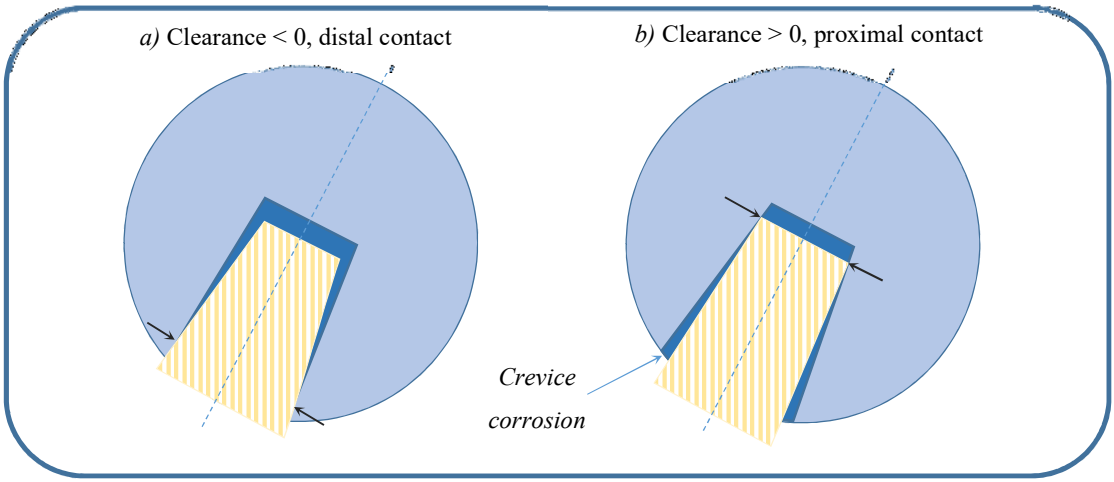

Figure 2.14 Representation of angular mismatch between head and trunnion, impacting the contact stresses and promoting micromotion and crevice corrosion (MACC).

The taper angles vary between manufacturers and although there is no correlation between angle and the extent of taper corrosion, it has been suggested the importance of angular match between the bore and trunnion, as emphasised in **Figure 2.14**[32,199,200]. An angular mismatch over 0.075° was found to increase micromotion[199] and promote crevice corrosion (**Figure 2.14 b**). Kocagöz et al. investigated the correlation between the taper angle clearance (difference between the head taper angle and trunnion angle of the stem) of 50 ceramic and 50 metal heads and trunnions and the associated visual fretting-corrosion scores [187]. All ceramic pairs in this study had exclusively positive clearances, indicating proximal contact which was supported by the evidence of metal transfer on the ceramic head taper in the proximal overlapping region. The cohort of metal heads had both positive and negative taper angle clearances, suggesting either proximal or distal contacts, confirmed by the surface topography of the investigated regions with signs of material loss. However, the study did not find any correlation between the taper angle clearance or geometrical contact and the visual corrosion scores for any of the head-stem cohorts. A limitation of this work, as outlined by the authors, was the use of matched head-stem pairs, designed to work together, with expected low clearances and thus moderate damage[187].

Studies suggest that ceramic heads matched with metal stems mitigate the fretting and corrosion at the tapers compared to MoM couplings[201–203]. The trunnions designed to pair with ceramic femoral heads are manufactured with fine parallel ridges which were originally introduced to soften the interface and reduce the local stress concentration caused by mismatched taper angles[184,188]. This can be detrimental for the ceramic heads, due to their susceptibility to burst fracture[204,205], as the impaction force required to insert the trunnion into the bore, flattens the threads and provides a uniformly distributed load within the periodical contact points[185]. It has been suggested that fracture can originate at the taper interface[206–209], where the surface roughness and the microscopic irregularities cannot smooth out the stresses[210]. The risk of fracture is believed to be reduced by the proximal contact of the ceramic head and trunnion, which transfers the load to the strongest part of the ceramic component, closer to the centre of the femoral head[187,210]. This provides the largest cross-sectional area to resist the tensile hoop stresses and prevents the burst fracture.

Although the threaded trunnions with smaller angles were initially introduced to mitigate the fracture risk of the ceramic heads, the design has been adopted by most of the taper manufacturers and they are now mated with either ceramic or metal heads. The proximal contact is not a requirement for metal heads, which are much tougher than ceramic components and can adopt a full contact at the interface[188]. If the taper angle is not of such a concern as it can be easily manufactured to match the two counterparts, several studies have suggested that mating metal heads with threaded trunnions can result in increased wear[184,187,194] and corrosion[186] at the taper interface. Despite the groves being machined only on the trunnion surface, a similar pattern has been identified on the inner taper of the retrieved metallic heads[184,187,194] or following *in vitro* testing[211,212]. In their experiments, Panagiotidou et al. observed that the circumferential pattern was more prominent, in regions with high loading, decreased contact area and rougher surface finish on the male taper[186]. The authors implied that the wear tracks are generated by the high frictional torque experienced by the large femoral heads[196] in combination with rougher trunnion surface finish, originally designed for pairing with ceramic heads. These findings raise concerns about mating metal heads with stems specially designed for ceramic heads, as the particular geometric and surface features required by ceramic components might not work so well for metallic heads, increasing the risk of material release.

Although in contradiction with the initial purpose of modularity, there are concerns regarding the replacement of a worn-out head while preserving a well-fixed stem. Insertion and removal of a femoral head may result in disruptions of the oxide film from the trunnion surface[185]. The damaged areas are seen as potential stress raisers which could initiate the fracture of the new ceramic head[206,209,213] or enhance wear due to compromised interlock or micromotion at the interface. Furthermore, the offset of the head may change and the contact will not occur at the same regions across the junction[10]. Hothi et al. and Matthies et al. support the retention of well-fixed and well-positioned stems only when the trunnions are minimally damaged or not damaged and the Co and Cr serum levels are negligible[175,214].

From a material point of view, dissimilar combinations of head and stem (CoCrMo alloy head on Ti alloy stem) have been associated with higher rates and more severe damage at both the bore and trunnion[10,166,180–182], potentially due to the contribution of galvanic corrosion. The stem taper topography, however, was found to affect differently the mixed and matched material tapers, with the CoCrMo/CoCrMo junctions being more affected and more prone to severe damage[215]. Generally, the retrieval studies have revealed higher corrosion and more material loss at the head taper than at the trunnion[2,180,182,184,203], and different corrosion processes were suggested to dominate the damage of the neck tapers made of either CoCrMo or Ti alloy[180,216]. Intergranular corrosion occurred only on CoCrMo trunnions and it was correlated with the sintering process of the porous coating, while mechanically assisted crevice corrosion prevailed on both CoCr and Ti alloy tapers[216].

Despite the advantages of larger femoral heads (reduced risk of impingement and dislocation), they are believed to enhance taper damage due to higher torque[145,184,198,211] experienced by the trunnion adjacent to the base of the head[194,217]. Lavernia et al. developed a Finite Element Analysis (FEA) model to investigate the effects of the large femoral heads on the stresses at the full contact taper junction and observed a significant rise with increasing femoral heads, close to the distal head-neck contact area[217]. The authors concluded that the elevated stresses at the trunnions, coupled with micromotion at the interface can promote tribocorrosion and the release of ions from the contact. An *in vitro* study also suggested the increase of corrosion with the head size, due to the reduction of the ratio between the head size and the actual contact area[211]. The friction moment at the taper junction is believed to contribute to fretting corrosion[218] and it was suggested to increase with the femoral head size and in conditions of poor lubrication at the bearings[145,198] or following third body abrasion after the entrapment of metal particles in the polyethylene liner[219]. Several retrieval studies[189,194,219,220] support these statements and found a positive correlation between the head size and frequency of taper damage. Triantafyllopoulos et al. investigated retrieved femoral heads ranging from 22 to 44 mm, and included 8 heads larger than 38 mm, of a total of 154. The fretting scores of both taper and trunnions were found to increase with the time *in vivo*, and dissimilar material combinations[221]. The study, however, did not find any association between the head size and the extent of corrosion or fretting in a cohort of MoP prostheses[221].

The impaction force applied by the surgeon to assemble the head onto the stem is also believed to affect the corrosion at the taper junction[188,222]. A higher force will normally ensure a better bond and a greater friction resistance at the interface, which will reduce the risk of micromotion and fretting corrosion[223]. Furthermore, a higher impaction force provides improved sealing, impeding the fluid ingress at the contact and mitigating the corrosion of the exposed surfaces. The correlation between the increasing assembly force and decreasing corrosion rate at the taper interface was demonstrated by Moczkowski et al. with mismatched CoCrMo heads and Ti alloy stems[222].

With so many factors which can contribute to the overall damage at the taper, it is expected that a combination of wear and corrosion mechanisms are often responsible for the release of material from

the interface. High rates of revision due to corrosion and fretting had been reported with several neck designs (Stryker's Rejuvenate and ABG II systems)[32,160], which led to their recall in 2012. The alert raised awareness of the potential of these stem systems to generate excessive wear debris from the modular junctions, potentially resulting in ALTRs. The retrospective analysis of patients implanted with ABG II dual modular hip systems (titanium stem and cobalt-chrome neck) revealed elevated Co levels, signs of metallosis, bone and tissue necrosis and pseudotumour formation[160]. Similar results have been reported by Cooper et al. after the investigation of a cohort of double modular Rejuvenate femoral components, consisting of mixed Ti alloy stem and CoCrMo alloy neck[32]. Pseudotumour has been demonstrated in 8 of 9 patients and serum Co level was elevated compared to Cr or Ti. Surgical findings included soft tissue necrosis and histological signs of ALTRs as well as evidence of fretting corrosion and black flaky deposits around the retrieved neck-body junction[32]. The study also reported evidence of fretting and pitting corrosion at the CoCrMo neck mated with ceramic femoral heads, contrary to the belief that ceramic head-stem junctions are less prone to taper damage[201,202]. The failure of more Rejuvenate CoCrMo dual neck THRs has been presented by Werner et al.[190] in a case report. The scenario was similar and included elevated Co levels, fluid collections and corrosion products accumulated around the femoral stem-neck junction. Gill et al. reported the failure of three ESKA dual modular short stem systems (CoCrMo femoral stem, neck and head) due to fretting and corrosion at the stem-neck junction and pseudotumour formation[169]. The ion serum level was compared to a group of patients implanted with an identical prostheses and bearing couple, but without any modularity at the stem. The Co level in the dual modular group was almost 10 times higher than in the reference cohort and the retrieved neck trunnions presented evidence of marked fretting and corrosion, with no signs of damage at the neck-head junction. This emphasises the contribution of modular interfaces to the overall release of ions, especially Co. Following the study of Gill et al., the ESKA dual modular short term system has been withdrawn from the Australian market[169].

It has been suggested that the increased micromotion at the neck-stem junction and the different loading conditions (eccentrically vs centrally through the head) compared to the head-neck interface favour the wear and corrosion at the neck-stem interface, as it was reported in most of the above studies[160,169]. The high serum found in most of the patients, might be justified by the preferential dissolution of Co under favourable corrosive conditions[180], from the Co rich CoCrMo alloy. At the same time, some of the soluble Cr can be precipitated as chromium phosphate, and stored locally rather than disseminated in the form of organometallic complexes with proteins[32]. This results in higher systemically Co levels, characteristic to wear originating at modular junctions.

In order to understand the structure of the site of wear and corrosion, Zeng et al. investigated the near surface layers found on the head taper of a CoCrMo head and reported differences between the original surfaces and overlapping head-stem interface[224]. The original surface was found to consist of a carbonaceous layer (80-100 nm), believed to originate from the adsorption of proteins from the

SF, a porous oxide layer (50-100 nm), which does not share the stoichiometry of Cr_2O_3, and a nanocrystalline substrate (~5 μm) with grains of ~50 nm diameter. In the area where the tapered surfaces started to overlap, the carbonaceous layer got thicker (200-500 nm) and contained C and traces of N and Ca, suggesting that different chemical and electrochemical conditions (pH, oxygen levels) might be implicated in its formation. The Cr oxide layer in this region was thinner (10-50 nm) and it was believed to be removed and reformed by the successive wear and repassivation processes, leading to variable thicknesses across the surface. Interestingly, the overlapping region consisted of a unique superficial layer which appeared to be made of C, O and Cr, potentially formed by mechanical mixing between the carbonaceous layer, Cr oxide and metal particles from the underneath substrate. These findings are in agreement with Wimmer et al.[130] and Bryant et al.[225] who have demonstrated similar structural organization at the bearings and stem surface respectively. The nanocrystalline organisation of the surface has been also reported by others[131,226,227] and it is believed to originate from the machining process. The thickness of this particular layer varies between the non-overlapping (~5 μm) and overlapping regions (1-2 μm) and it was suggested to be reduced in the overlapping region due to the wear and corrosion processes, responsible for the release of ions and particles[224].

Most revisions of modular components revealed black, flaky corrosion products[4,169] accumulated around the taper[190], accompanied by visible signs of metallosis and ALTRs as well as evidence of wear and corrosion at the retrieved tapers. These reports present a different mechanism of failure which has been acknowledged to have a significant contribution to the overall burden of revisions. The debris originating from tapers was suggested to provoke more aggressive reactions, at lower wear volumes compared to metallic bearings[6,7]. This might be explained by the different processes responsible for their generation which can impact the properties of the particles, as well as their surface energy and reactivity within the body. More research is necessary to fully understand the differences between particles released at different sites and their associated body reactions.

2.2.6 Wear and Corrosion at the Cement-Stem Interface

Cemented femoral stems represent an alternative to press fit fixation, aiming to provide mechanical stability for individuals with either good or poor bone stock, by interposing a cement mantle between the host bone and prosthesis (**Figure 2.15**). Although their popularity has slightly decreased over the last few years, they remain the second most preferred option in the UK[30]. Cemented THRs have good cost effectiveness and are expected to perform well *in vivo* for up to 15-20 years[228,229]. At implantation, the cement fills in the bone cavity drilled by the surgeon and fits around the cancellous bone, providing mechanical fixation (**Figure 2.15**). The fixation is gained by initial and physiological loading, which causes the stem to sink into the mantle and get stabilised by the effects of the hoop stresses[230]. The migration of the stem into the mantle continues after implantation and can sink between 0.32 and 1.2 mm over a two years period. This can initiate damage at the cement-stem interface, by a combination of abrasion[231], metallic shedding and tribocorrosion[29,232,233], releasing debris and triggering body reactions[29]. Bone resorption and aseptic loosening are recognised as the main reasons for failure of cemented femoral prostheses and have a significant contribution to the overall burden of THR revisions[12,228]. The issue has been described in association with bone-cement local defects for decades[234,235].

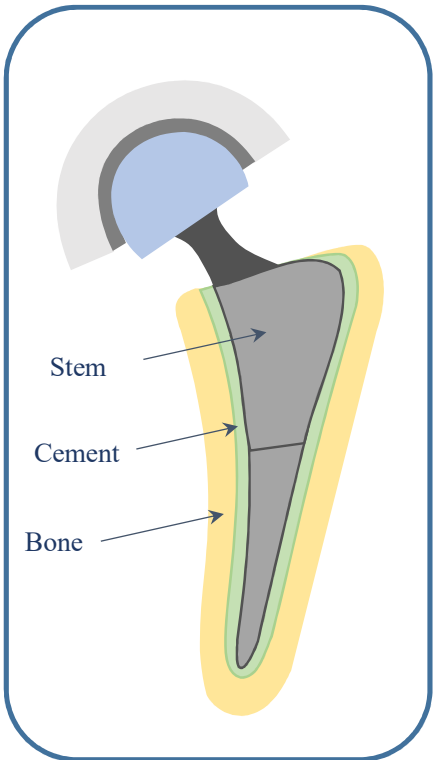

Figure 2.15 Schematic representation of cemented THR.

The cement interface acts as an intermediate zone between two materials with quite different properties, such as stiffness, hardness and elastic modulus, and has been regarded as a weak link in the THRs[236,237]. Numerous studies[220,230,232,233,238,239] have previously reported damage at the cement-stem interface and acknowledged its importance to the overall release of material, adding to the total debris originating from the bearings and taper[2,4]. Particularly high early revision rates have been associated with some types of cemented titanium stems[240–242], whose use with this fixation technique has been questioned by some researchers[243]. The retrieval analysis of 16 proximally cemented Ti femoral stems demonstrated signs of abrasive wear at the stem surface and Ti particles embedded in all the investigated cement mantles[244], initiated by the debonding at the proximal cement-stem interface, which led to proximal bone-cement and distal bone-implant loosening.

The mechanism and the exact sequence of events initiating and propagating the damage at the cement-stem interface is not entirely known and authors have proposed different theories to explain

the process[230,232,233,245–247]. A number of previous studies[235,248] reported mirror like finishes on certain regions of explanted matt femoral stems which coincided with the regions of high torsional stresses[249], which led to the release of both cement and metal debris by abrasion and fatigue. The removal of material from the inner side of the mantle can result in larger clearance between the stem and cement, further facilitating the rotational forces at the interface[235]. It has been suggested that several factors, including the surface finish of the stem[249] as well as the composition and preparation technique of the cement[12] prior to implantation can influence the tribology at the cement stem-interface.

Bone cement is polymeric in nature and is available in different formulations, usually consisting of a poly(methyl methacrylate/methyl acrylate) (PMMA) base and various amounts of antibiotics[232] and radiopacifiers, such as ZrO_2 or $BaSO_4$ [230,233]. The radiopacifiers are added to allow the investigation of the mantle after implantation, using X-ray imaging, but it has been suggested to be involved in both the wear of the stem-cement interface[230,247,248] and articulating surfaces in THRs, following third body abrasion. Antibiotics have been integrated into bone cement formulations since 1970s in order to prevent and treat periprosthetic infections. Nevertheless, the release mechanism of antibiotics is still not well understood and there have been questions about their efficacy[250–252]. Furthermore, their presence in the cement mantle has been suggested to affect the initiation and propagation of crevice corrosion at the stem interface as well as the mechanical properties of the cement[247]. Bryant et al.[247] reported a reduction of the breakdown potential of 316L SS with the addition of antibiotics and radiopaque agents, which means increased susceptibility to the initiation of corrosion. Although the integrity of the Cr oxide layer on CoCrMo alloy provides a better protection against corrosion, once initiated it can be accelerated by the addition of both antibiotics and radiopacifiers[247]. The increased susceptibility to localised corrosion identified with sulphate containing antibiotics and radiopacifiers, has been hypothesised to be related to the enriched sulphate content within the interface and crevice. This is regarded as an aggressive anion, known to affect the corrosive behaviour of materials[253] by inhibiting pitting corrosion but also by propagating it once initiated[254,255]. An analysis of data reported by the Norwegian Arthroplasty Register on revision of cemented THRs showed different failure rates of the same implant designs inserted with different types of cement[256]. Also, different stem designs fixed with the same cement formulation provided different outcomes[257], suggesting that a better attention should be given to the choice of the stem-cement pairs.

Stem material can also have implications on the tribological behaviour of the stem-cement interface. The comparison between Ti and CoCrMo alloy stems with the same type of surface finish, subjected to similar testing conditions, demonstrated more wear at the CoCrMo stem compared to Ti. However, other factors such as the ingress of SF[243] combined with the lower stiffness of Ti can result in increased micromotion and higher stresses at the cement interface[258], generating more Ti debris and triggering more aggressive body reactions, which eventually require revision surgery. This might explain the high rates of early loosening experienced with certain Ti stems *in vivo*[240–242], compared

to CoCrMo stems, despite the results of the *in vitro* simulations which showed more material release from the latter design. A comparison between the corrosion of retrieved SS and CoCrMo cemented stems also revealed significantly greater corrosion scores in the CoCrMo stem cohort and higher blood Co/Cr ratio despite similar volumetric wear at the CoCrMo MoM articulations and trunnion interfaces in both cohorts[214]. This implies that CoCrMo stems release more Co ions, increasing the overall concentration, added to the amount originating at bearings and tapers. The correlation between the *in vivo* service duration and initiation of fretting wear at the cement stem interface has been investigated by Zhang et al. by an *in vitro* simulation which demonstrated that the disruption and transfer of material from the stem surface to the cement mantle occurred after a certain loading time, between 5 and 10 years of usage[228].

The cement is relatively soft compared to its metallic counterparts (0.32 GPa vs 6.0 GPa for CoCrMo alloy)[259]. Studies have suggested that the mechanical properties can differ from one cement formulation to another[223,248] and they can be altered by the addition of radiopacifiers. Despite these findings, the evaluation of the effect of three different cement formulations on the fretting of the same design of femoral stem, showed no significant difference between the types of cement tested[12]. From the surface finishing point of view, it has been suggested that different wear mechanisms contribute to the damage of the polished and matt stem components[249]. Polished surfaces, which have a reduced surface roughness, are mainly characterised by fretting wear, exhibiting unidirectional pitting and retention of wear debris at the interface, while matt surfaces are more prone to abrasive wear, releasing material from both metal and cement surfaces and showing polishing changes[249]. The increased abrasive wear at the rough stems and cement mantle interface compared to smooth surfaces has been demonstrated by Bader et al.[248], while Crowninshield et al. concluded from their *in vitro* testing that the abrasion of the cement stem depends on the surface roughness of the metal articulating counterpart[262]. Howell et al. also postulated that all stems with a surface roughness higher than 0.4 μm are very likely to release debris by abrasive wear[249]. A study by Duffy et al.[263] on proximal macrotextured stems further supported these findings and suggested increased risk of debonding at the cement-stem interface, which facilitates micromotion and release of debris.

Nevertheless, both polished and matt surfaces have a certain degree of surface roughness, interposing harder asperities at the contact with the cement mantle[12,230]. During the walking cycle, the alternating loading of the joint can result in micromotion at the cement-stem interface which can engage the asperities into abrasion, removing material from the cement surface[264]. Following the wear of the PMMA matrix, the radiopacifiers, harder in nature, protrude from the cement surface, forming asperities which come in contact with the metallic stems. The abrasive nature of these protrusions means micromotion at the interface can also result in material being ploughed from the stem surface and then transferred to the cement mantle[230,246]. This theory has been proven by Shearwood-Porter et al. in a study on 12 CPT polished stem retrievals, which were forensically examined to understand the mechanism of damage at the cement-stem interface[230]. The localisation of agglomerated ZrO_2 at

the surface of the cement mantle was confirmed by scanning electron microscopy (SEM) and EDX and corresponded to the highly damaged areas on the stem surfaces. The flattened morphology of these agglomerates further suggested their involvement in the process of wear at the interface and the presence of Cr and Mo on the cement mantle indicated the transfer of material from the CoCrMo surface to the cement mantle. In a previous study, Zhang et al. demonstrated by SEM/EDX and 2D profile analysis the accumulation of metal debris around and inside the voids at the cement surface, further supporting the transfer of metal at the interface[12]. Most of the studies reported highly damaged areas with signs of fretting wear, predominantly at the proximal contact between the stem and cement, and islands of polishes regions with unaltered morphology[230,246,265]. Shearwood-Porter et al. reported a unidirectional alignment of the wear tracks at ~45° from the long axis of the stem, trend observed on both the worn out stems and the corresponding regions on the cement counterparts[230].

Shrinkage bumps of ~ 50 μm width and 1-2.5 μm height can form at the cement surface following the polymerisation process and have been proposed to contribute to the initiation and propagation of wear at the interface[228]. These oscillations of the surface level were believed to influence the contact area and distribution of the load, but Blunt et al. later postulated that the contribution of bumps to the initiation of wear is relatively insignificant[266]. Zhang et al.[12] suggested that the micropores at the cement surface can influence the mechanical properties of the cement mantle and alter the bonding process by reducing the contact area at the cement-stem interface. This in turn can result in micromotion, with subsequent fretting wear and release of material. The implication of micropores in the relative micromotion and fretting wear of polished cemented stems has been postulated by others[266]. The study has concluded that larger micropores might promote more severe damage at the interface, due to increased micromotion, and methods to reduce porosity and the effective size of the pores might mitigate the fretting wear of the polished stems[266]. Zhang et al. identified damaged areas in the posteromedial region of several stems, subjected to *in vitro* testing, which alternated with isolated islands of undamaged areas, corresponding to the micropores on the opposite cement mantle[12,245,246]. The optical and interferometric investigations of the stem regions with incipient damage, suggested that the fretting is initiated at the contact between the stem and the edge of the voids, where the differential distribution of stresses across the variable thickness of the margins can promote micro-cracks. The SEM images revealed the presence of micro-cracks around the voids, which appeared to originate at the edge of the micropores, spreading towards the bulk material[245,246]. Micromotion can lead to fretting at the contact between the stem and the micropores edges, which further extends to the proximal area across the posteromedial region. This results in highly worn out surfaces with regions of unaltered finishing, corresponding to the voids. Zhang et al.[246] demonstrated the transfer of metal from the stem to the cement mantle in the proximity of the voids, using EDX analysis. The spectra also confirmed the presence of radiopacifiers inside and around the voids, which is in agreement with the findings of Shearwood-Porter et al.[230]. This evidence along with the fact that the mechanical fixation of the stem is provided by hoop stresses rather than adhesive forces, support the hypothesis that the radiopaque agents distributed in and around the pores are actually

involved in the initiation and propagation of wear at the cement-stem interface and could justify the worn and unworn alternating islands reported by others[12,245,246].

In their attempt to understand the mechanism and the nature of tribocorrosion products generated at the cement-stem interface, Bryant et al.[29] compared the nature of the surface of an unworn, uncemented femoral stem, with the deposits at the retrieved, damaged stems. The surface of the unworn femoral stem consisted of a nanocrystaline layer at the upper most 200 nm. SEM analysis of the retrieved stems, showed ploughing tracks and metal debris in the valleys formed by fretting wear, and deposits of corrosion products comprising of smooth overlaid plaques. The EDX mapping suggested the deposits contained Cr, C, O and N, with diffuse evidence of Mo and limited amount of Co. Cross-sectional TEM analysis demonstrated that the Cr and O rich corrosion layer on top of the damaged stems is actually made of densely packed chromium oxides nanocrystals mixed with air voids and organic material. High magnification TEM images demonstrated that some of the investigated particles were actually composed of smaller ellipsoidal particles of ~ 50 nm long, held together by biological material, which according to their diffraction pattern corresponded to Cr_2O_3 d-spacing[29]. The Cr and O enriched layer demonstrated evidence of C and traces of Mo and Co indicating the deposits originated from the TCR occurring at the interface.

The sequence of events is initiated by the wear at the interface (**Figure 2.16 a-b**), when mechanical loading can exceed the yield stress of the passivated Cr_2O_3 layer, resulting in the disruption of the film[29], as shown in **Figure 2.16 c**. When the loading is ceased, the two surfaces can separate (**Figure 2.16 d**) and the SF can bathe the worn surfaces[267]. This can favour the repassivation of the exposed surfaces (**Figure 2.16 e**) and the corrosion of the particulate debris. When loading is applied again, debris from the previous cycle and organic material from the fluid are all entrapped in the contact and subjected to mechanical mixing (**Figure 2.16 a**). The repeated cycle can eventually lead to the tribochemical layer consisting of closely packed Cr_2O_3 and organic compounds, as reported by Bryant et al.[29]. These findings are in agreement with others which demonstrated the TCR at the bearings[97,129] and their implications on the tribology and the release of material from the interfaces. Furthermore, these results support the increased dissolution of Co and repassivation of the Cr rich surface, with subsequent formation of Cr_2O_3, as implied by Hodgson et al.[158,268]. Cobalt has an increased solubility and is very likely to escape into the biological environment, resulting in increased serum levels and ALTRs such as tissue necrosis and aseptic loosening. According to Goldberg et al. the repassivation occurs from the edges of the initial oxide layer towards the centre of the exposed region, while oxides nucleated in the middle will expand towards the margins, eventually creating a

new compact passive film[269]. The crevice formation at the debonded interface can also result in localised pits, as reported by Hothi et al. with CoCrMo and SS retrieved stems[214].

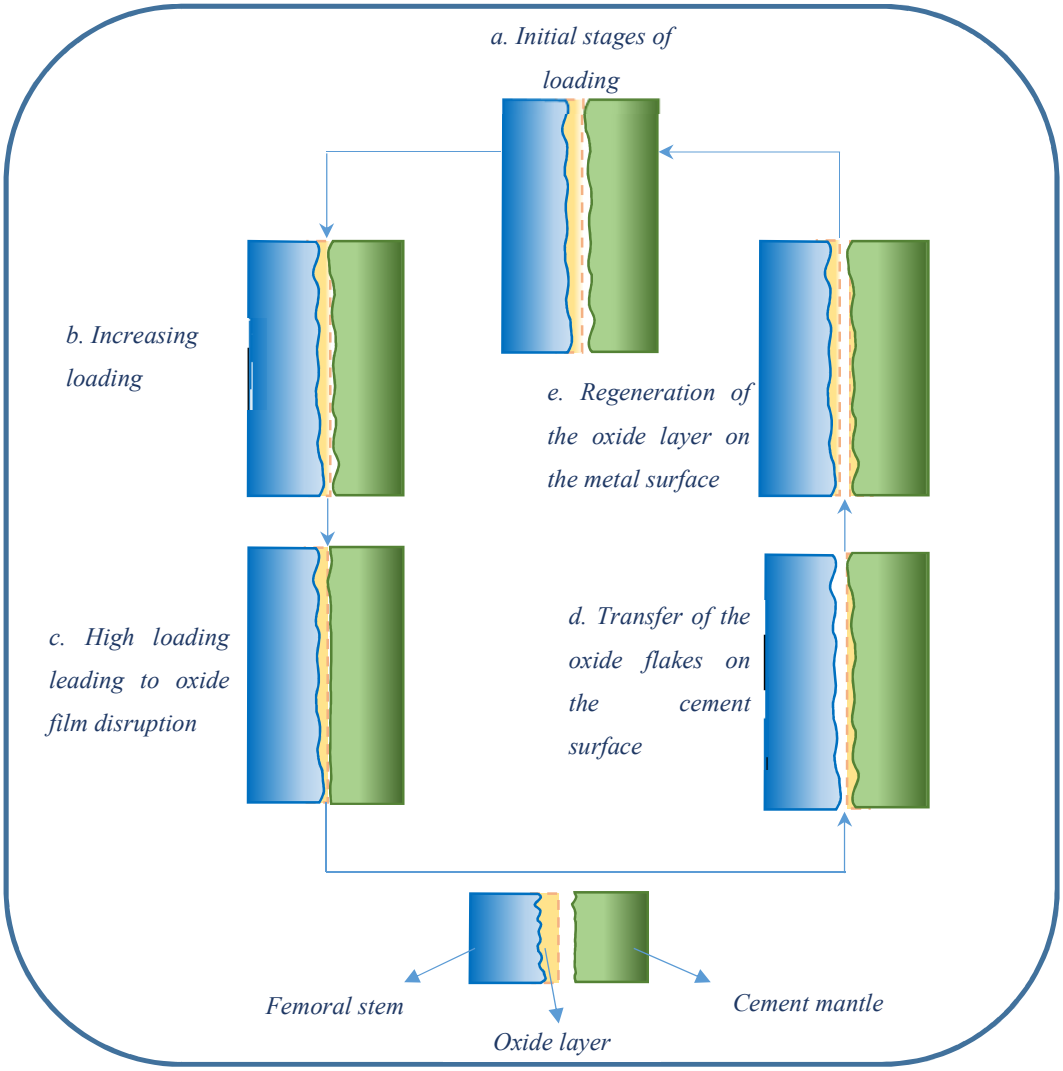

Figure 2.16 The steps involved in fretting corrosion at the stem-cement interface.

The fluid at the cement stem interface can facilitate the corrosion and transport of the wear debris in between the contact, potentially engaging in third body abrasion, or at the bone-cement interface, where they can initiate the release of cytokines and inflammatory markers, resulting in aseptic loosening[214]. The surface finish was found to affect the fluid flow at the cement-stem interface and polished components demonstrated better sealing with both well-fixed and debonded models[270]. The increased flow at the rough stems can result in debris being disseminated to the femoral bone, distal to the implant, through cement mantle defects, leading to particle or pressure induced osteolysis. It is believed that polished surfaces experience higher bonding forces with the cement layer which impedes the fluid ingress and flow across the interface[271]. The examination of the retrieved cement mantles showed highly damaged regions, covered with black, flaky corrosion products containing Cr

and traces of Co and Mo, as indicated by ICP-MS analysis[230]. The results supported the findings of Bryant et al.[233] and suggested that the flakes originated from the chromium oxide layer, the most thermodynamically stable compound among the Cr_2O_3, $Cr(OH)_3$ and CoO, which is reflected by the most negative Gibb's free energy ($\Delta G°$). This can justify the enrichment of Cr at the interface and the involvement in the repassivation of the worn out surfaces, while Co is rapidly released into solution. Similar results have been reported by Zhang et al. who identified dislodged material containing Cr and Fe at a ratio of 9:1, although the initial composition in the Exeter stems, used in these tests, was completely different (64.5% Fe and 17.5% Cr)[228,246]. The preferential localisation of Cr at the surface provides better corrosion resistance of the Exeter stems, which contain mainly Fe. The analysis of the corrosion products built up during an *in vitro* simulation of the effect of different cement formulations on the crevice corrosion of the 316L SS tapers, revealed it was rich in Cr, O and Cl, with traces of Fe and Mn[247].

Although it was initially believed that wear and corrosion at the stem was consistent with loose prostheses[272,273], others have reported damage and adverse reactions with apparently well-fixed components under plain radiographs or at the point of revision surgery[2,238,249]. The recognition of damaged areas in several cases was not possible by simple visual inspection and required the use of light microscopy (LM) to detect minor wear at the stem surface[249].

Wear and corrosion at the cement-stem interface is regarded as a complex, multivariable process, in which the cement formulation, femoral stem alloy, surface finish and geometry play an important role. The addition of radiopacifiers and antibiotics to the PMMA matrix[230,247], as well as the porosity of the cement mantle[12,246,265,266] have been proposed to have implications on the wear and corrosion of the stem. Different mechanisms were found to dominate the wear of the rough and smooth surfaces[249] and more material release was reported with CoCrMo alloy, when compared to Ti stems in similar conditions and femoral stem geometries[248]. Despite these findings, particularly high revision rates have been registered with certain Ti femoral components[240–242] and this implies that other factors, such as the presence of fluid at the interface[243] can affect the overall damage of the stem. With so many factors proposed to have implications on the wear and corrosion at the stem-cement interface, it can be expected that different wear mechanisms rule each situation and can result in the release of particles with variable morphologies and chemical composition. These properties, as well as the level of soluble ions within the body can further trigger different local and systemic body reactions.

Despite the numerous studies concerning the wear and corrosion processes at the cement stem interface, little is known about the nature of the particles released from this particular site. Except for the study of Bryant et al.[29] and Hothi et al.[214] which investigated the structural organisation of the corrosion deposits found on explanted CoCrMo stems, to our knowledge there is no other study reporting the nature of the particles originating at the stem-cement interface. Shanbhag et al.[274] reported Ti alloy particles isolated from the bone-implant interfacial membrane from modular and

monoblock cementless total hip replacements. The debris was believed to originate from the wear of Ti-alloy stem against the femoral bone, and was commonly found with an adherent layer of Ca-P rich material. However, this is a wear-dominant process resulting in metal particles with different morphology and properties than the wear and corrosion products released from the stem interface in cemented total hip replacements. More research is necessary to understand the morphological and chemical properties of the wear particles and corrosion products which might possess different reactivity and might have a different fate in the body.

2.3 Isolation and Characterisation of Metal Debris

2.3.1 Introduction

Characterisation of wear debris and corrosion products released from hip prostheses represents an important step in understanding the performance of different designs with various material combinations and fixation techniques. With the introduction of modularity and cemented femoral components, the number of sites susceptible to wear and corrosion has increased and not only the articulating bearings but also the taper junctions[2,4,31,49] and cement-stem interfaces[29,230,238,239] can release material. It has been suggested that CoCrMo debris originating from tapers can trigger more aggressive body reactions at lower wear rates compared to material released from CoCrMo bearings[6,7] and several studies have reported highly increased systemic Co with corroded tapers[2,4,160,190] or loose cement-stem interfaces[214,230]. These findings suggest that particles originating from different sites of hip prostheses can possess different characteristics, such as size, morphology, surface energy and chemical composition, further dictating their reactivity and fates within the body. Furthermore, the electrochemical environment at the various sites of wear and corrosion can differ, promoting the dissolution of certain elements and favouring the reactions with the surrounding biomolecules[29].

The comprehensive investigation of particulate debris requires characterisation techniques able to resolve individual particles and identify small variations in the chemical compositions of particles originating from different sites and released under different wear and corrosion processes. Not only the characterisation methods but also the sample preparation technique plays an important role in this process, as any biological contamination can impede the high-resolution imaging and can interfere with the chemical analysis. The majority of the particles released in the body require isolation from the biological fluids or tissue. Small particles have a high surface area to volume ratio[5], which makes them unstable and thus susceptible to engage in reactions with the biological environment[275]. The structural and chemical transformations can provide them with a more stable energy state and a better camouflage within the body, but at the same time it can promote agglomerations[275]. An ideal isolation protocol should recover as many particles as possible, preserve their initial composition and dispersion state, provide clean particles, free of biological/chemical contaminants, involve a reduced number of simple steps to avoid particle loss, and be repeatable under similar conditions. This is challenging as the particles are susceptible to chemical degradation, corrosion and dissolution[55,276], and most of the popular isolation protocols involve chemicals and harsh conditions such as high temperatures and boiling steps[20,98,111]. Even these treatments can sometimes fail in completely removing particles' biological makeup and can result in poor quality imaging and chemical analysis[23]. A compromise therefore has to be made between the risk of altering the original nature of the particles and the release of particles from the surrounding biological media, making them available for high-resolution investigation.

2.3.2 Metal Particle Isolation Protocols

The most popular techniques developed for the isolation of metal debris use either alkaline solutions or enzymes and in some cases a combination of both, to digest the organic matrix or serum in which these particulates are released. Many of the currently used protocols are over 20 years old and were changed and adjusted over the years, to fit the demands of the studies and different types of samples. Although less popular, and not used nowadays, there have been several acid approaches to isolate CoCrMo and Ti alloy particles generated *in vivo*[277,278]. In these protocols, tissue samples collected from patients after total hip and knee arthroplasty were digested with 70% nitric acid (HNO_3), washed and sonicated. Metal particles were collected either by centrifugation or filtration, electronically counted and sized (using a multisizer particle analyser), investigated with transmitted and polarised LM and SEM, and chemically identified by EDX analysis. Moreover, part of the filter used to collect the metal particles after digestion, was embedded in epoxy resin and characterised using TEM. However, due to both protocol and technical limitations (e.g. the high lower limit of detection of the particle size analyser was 0.58 μm), these studies reported mainly large metal particles, ranging from several hundreds of nm to several micrometres (0.63 μm the average mode diameter), but failed to identify nanometre sized particles which possess a higher mobility and thus, raise concerns of health implications[277].

One of the oldest alkaline protocols, which is still used in a modified form, was proposed by Shanbhag et al., to isolate wear particles from the bone-cement interfacial membrane, collected at revision time from patients with uncemented MoP total hip implants[274]. Tissue digestion was performed using 4M KOH (2 ml/g tissue) at 56°C for 48 h. The organic residue was collected by centrifugation (1000 x g, 1 h) and subjected to a second digestion using KOH in similar conditions. The collected pellets containing the particles were washed three times with deionised water (DIW) for 8 h, at 37°C and further digested with Pronase for 24 h at 37°C. Ultrasound techniques were used to disperse the particles, which were then washed three times with DIW. Metal and polyethylene particles were collected based on their density difference using a mixture of equal volumes of ethanol and hexane, spun until the polyethylene particles concentrated at the interface between the two solvents and the metal particles transferred into the ethanol phase. Both fractions were collected and subjected to a third step of alkaline digestion with KOH at 56°C. The isolated particles were characterised using SEM, EDX and FTIR and three different types of particulates were identified: polyethylene (mainly submicron), titanium based alloy and Ca-P rich bone fragments, with several anomalous particles, including SS and silicates fragments [274]. Ti flakes and wire-shaped fragments were believed to originate from the bulk Ti alloy stem and commercially pure Ti fibre-mesh pad (used to promote tissue ingrowth). The abrasive wear at the bone-implant interface can result in both metal and Ca-P rich particles, while SS and silicates can be contaminants from the surgical tools and sand-blasting process respectively[274].

Firkins et al. investigated the way the carbon content influences the wear behaviour of CoCr alloys used in THRs[279]. Their study was among the first to report data on the isolation and characterisation of metal debris released *in vitro* by MoM articulating surfaces. The particles were generated by a pin on plate test in 25% new-born calf serum (NCS) and were isolated using an alkaline digestion protocol to remove the proteins and lipids, and allow for particles to be collected free of contaminants. The single hydrolytic step used 12M KOH, at 60°C, for 48 h. Chloroform/methanol (2:1) and 50% acetone washes were used to remove the lipid and proteins residue, before collecting the particles on 0.1 μm polyester filters. In a latter study, the same research team isolated metal and ceramic particles from serum lubricant with the same protocol and characterised the resin embedded particles with TEM[279].

The main problem associated with the use of aggressive chemicals (such as alkaline solutions and acids) and harsh conditions (high temperatures) for the isolation of metal particles, is their reactivity and thus susceptibility to suffer morphological and chemical modifications. Campbell et al.[280] postulated the destructive effect of the use of alkaline treatments on metal particles as a result of the chemical digestion and the theory was further tested by other researchers working in this field[37,55,276]. This was the reason that led to the new techniques for the digestion of organic tissue and serum lubricants, involving less aggressive chemicals and hydrolytic mixtures.

One of the first enzymatic digestion protocols was proposed in 1998 by Doorn et al.[36] and constituted the basis of many other isolation techniques developed later by other investigators. In order to isolate metal particles from periprosthetic tissue collected from patients undergoing revision surgery, the authors used two different hydrolytic enzymes (papain and proteinase K) and several additives and solvents. Chloroform/methanol (1:1) was employed for tissue delipidation and preceded the specimen freezing step at -70°C, and lyophilisation. Two boiling steps were used to digest the proteins and the residues were removed by centrifugation at 14000 x g for 10 minutes. Three-(N-morpholino) propanesulfonic acid (MOPS) and acetone were used to wash the pellets prior to the first 24 h enzymatic digestion using papain at 55°C. Another boiling step prepared the sample for the second 24 h enzymatic treatment with proteinase K at 55°C. After the last boiling in sodium dodecyl sulphate (SDS), the particles were suspended in ethanol, sprayed on carbon coated copper grids and analysed by TEM[36].

Catelas et al.[55,276] investigated the effects of the digestion methods on the size, shape and composition of the metal wear particles released from CoCrMo bearings. The researchers compared an alkaline and an enzymatic protocol, which were adapted from some pre-existing digestion methods[36,274,279]. The particles, generated by dry abrasion in a reciprocating pin-on-disc test and by hip simulator trials in either DIW or 95% bovine serum lubricant, were concentrated by centrifugation at 16000 x g for 10 minutes and subjected to both alkaline and enzymatic treatments. The alkaline protocol was designed to assess the effects of different exposure times and alkali concentrations on particles characteristics and involved the use of 2N KOH, 12N KOH and 5N NaOH to which particles had

been exposed for either 2 or 48 h and then separated by centrifugation at 16000 x g for 10 min, and stored in 100% ethanol at 4°C prior to use.

Similarly, before applying the enzymatic treatment the particles were centrifuged at 16000 x g for 10 minutes and boiled in SDS. The first 24 h digestion step involved the use of papain, a proteolytic enzyme which requires an incubation temperature of 65°C, in either phosphate buffered saline-ethylenediamintetraacetic acid (PBS-EDTA) (protocol 1) or tris(hydroxymetyl)aminomethane-hydrochloric acid (Tris-HCl) (protocol 2) buffers. After this step, the particles were collected by centrifugation at 16000 x g for 10 minutes and resuspended in SDS and boiled for another 10 minutes. They were sonicated and subjected to the second 24 h digestion step with proteinase K in Tris-HCl, at 55°C. Like in the case of the alkaline treatment, the particles were isolated at 16000 x g and stored in 100% ethanol at 4°C prior to embedding in epoxy resin.

The TEM and EDX analysis were used to investigate the morphology and chemical composition of the particles isolated using either the alkaline or enzymatic protocols and to compare their characteristics with the control specimens (particles without treatment). This study[55,276] shows that both the enzymatic digestion (to a lesser extent) and the alkaline treatment affect the size and the shape of the metal particles. Moreover, these changes were directly proportional to the exposure time and alkali concentration, and the effects were more drastic with the use of 12N KOH for 48 h, especially in the case of the larger particles. The selection of the buffers used in enzymatic protocols has to be done carefully, as this study proved they also influence the particle characteristics.

It is worth mentioning that Catelas et al.[55,276] also demonstrated an initial protective effect of the proteins and lipids that surrounded particles in bovine serum lubricants. It has been proved that the changes in size and shape are minimal in the first 2 h of exposure to 2N KOH or during the enzymatic treatment. This might be explained by the fact that the reagents used for digestion do not get in contact with particle surface until the protective corona is completely removed. According to the investigators, the exposure time and alkaline concentration required for digestion depended on the protein concentration of the lubricant and must be adjusted accordingly.

The second part of the study of Catelas et el. [55,276] investigated the effects of the digestion protocols on particle chemical composition. The results of the ion level measurements, performed using flame atomic absorption spectroscopy (FAAS), show that both alkaline and enzymatic treatments affect the chemistry of the isolated debris. As it was also proven in the first part of the study, the extent of changes was proportional with the exposure time and alkalis concentration. Ion levels in solutions collected after alkaline digestion revealed a continuous release of Cr ions which increased with time and reagent concentration, and a release of Co ions which was more intense in the first hours of exposure (e.g. 2 h and 24 h). On the other hand, the changes induced by the enzymatic treatment led to Co ions release, especially in the first hours of incubation, but the extent was much lower compared to alkaline treatments. These findings were supported by EDX results, which indicate a decreased

Co and Cr peak intensities, with no Cr peak intensity after 48 h in particles treated with alkalis, and a slightly decreased Co peak intensity corresponding to particles isolated using enzymes. The study also demonstrated that the small metal particles are more susceptible to reagents attack, releasing more ions than the larger ones, thus emphasizing the need of ongoing research focused on artificial bearings and particles characterisation. Moreover, it has been proven that alkaline treatments affect chromium oxide particles, leading to their disappearance from the environment, the effect being dependent on time and reagent concentration. A shielding effect of the organic corona was demonstrated again when investigating the ion level in solutions treated with enzymes. Although the effect was considerably diminished by the organic matrix in 95% serum, the modifications could still be noticed, especially when alkaline reagents were involved[55,276].

The enzymatic isolation protocol proposed by Catelas et al.[55,276], proved to be the least damaging option among those reported in the literature and it was adopted by others and adjusted over the years to allow for the recovery of particles from both serum lubricants and periprosthetic tissue samples[20,28,111,281].

Encouraged by the more positive results (advantages) of the enzymatic protocols, others tried to improve the enzymatic protocol by Catelas et al.[55,276], by using new proteolytic mixtures. In 2007, Brown et al.[98] developed a new protocol for the isolation of metal particles from serum lubricants, involving the use of four types of enzymes (papain, proteinase K, yeast lytic enzyme and Zymolyase) coupled with high temperature treatments and boiling steps. The particles were recovered by filtration onto polycarbonate filters, coated with platinum/palladium (Pt/Pd) and characterised by EDX using field emission gun (FEG)-SEM.

Different enzymatic protocols were proposed by Kavanaugh et al.[282] to isolate metal wear particles from a knee SF sample. The complexity of this environment, compared to serum lubricants used in simulator trials, required the use of three different enzymes specialised in digesting proteins, lipids and glycosaminoglycans, such as hyaluronic acid. The sample was incubated with hyaluronidase (8 h), benzonase (8 h) and protease K (48 h) and the particles were recovered by centrifugation at 25 000 RPM on a silicon wafer pre-coated with an organic adhesive. The silicon wafer was sputter coated with gold and analysed using FEG-SEM. EDX analysis was employed to investigate the nature of the isolated particles, which were identified to be mostly titanium oxides with traces of V and Al, released from MoM wear of the titanium femoral component and tibial plate after wear-through of the polyethylene liner[282].

The same research group later proposed a method to isolate, collect and display metal particles generated by MoM hip implants in 90% serum lubricants[21]. The single digestion step involved the incubation of the concentrated sample (pelleted at 164000 x g, for 3 h at 25°C) with proteinase K for 24 h at 37°C. Particles were separated by gradient centrifugation (84000 x g, 4 h, at 37°C) through several layers of denaturants and collected on a silicon wafer coated with marine mussel glue, in a

metal-selective layer which serves as an anticontamination barrier against organic compounds. Particle morphology, size and shape were investigated using FEG-SEM and scanning transmission electron microscopy (STEM), while the chemical composition was revealed using EDX analysis[21]. Adaptations of this protocol were later used to isolate wear particles from periprosthetic tissue and synovial aspirates retrieved from around revised MoM (CoCrMo alloy) total hip replacements[24]. Briefly, tissue digestion process consisted of three days of incubation with increased amount of proteinase K, necessary to fragmentise the higher content of proteins. For the SF samples, in addition to proteinase K, aliquots of hyaluronidase and benzonase were used to digest hyaluronic acid and nucleic acids respectively. In both cases, the separation of metal particles from the organic residue was performed by density gradient centrifugation through successive layers of caesium salt solutions. The silicon wafers or TEM grids placed at the bottom of the centrifugation tubes were used for the direct collection and display of the particles during centrifugation. These were pre coated with a monolayer of marine mussel glue which aimed to stick the particles to the TEM/SEM support. The repeated washes required for the removal of the residual Cs salts can wash off the particles which need a better fixation. The salts can easily be confused with metal particles and only the chemical analysis can be used to distinguish between particles of interest and contaminants. Furthermore, the mussel glue, which is organic in nature, can alter the contrast and impede the high-resolution TEM or STEM imaging, particularly of the nanometre sized particles.

Another study aimed to assess and compare the efficiency of a newly proposed enzymatic protocol with adaptations of two enzymatic protocols, previously discussed in this section[36,55,276]. The novelty of the proposed protocol consists in a freeze drying to concentrate the particles in the serum lubricant by eliminating water. The resulting porous matrix was rehydrated and subjected to two identical protein digestion steps involving incubation with proteinase K for 24 h at 40°C. After several washes with different agents and detergents (such as SDS), the particles were collected by centrifugation at 165000 x g for 1 h and stored in DIW prior to TEM, EDX and graphite furnace atomic absorption spectrometry (GFAAS) investigations. This study emphasised the necessity of using high centrifugation speeds and a reduced number of steps, compared to the previously used protocols[36,55,276], which led to poor digestion of the organic material and promoted the formation of agglomerates. The efficiency of the enzymatic protocol proposed by Lu et al.[23] was assessed by GFAAS which measured the total amount of metal left in the supernatant after spinning. The analysis indicated a particle extraction efficiency of 46.1% compared to 3.2% and 0.6% for the adaptations of the protocols of Catelas et al.[55,276] and Doorn et al[36].

De Pasquale et al.[25] proposed to assess the correlation between the number and nature of particles released in vivo in synovial fluid and the systemic levels of Co and Cr ions. The isolation of debris from synovial aspirates was based on the alkaline digestion of the fluid displayed on polycarbonate filters (0.2 µm), using sodium hypochlorite (NaClO). At least three successive digestions were required before the filters could be gold sputtered and investigated with SEM and EDX. Despite the

fact that the purpose of the study was not the comprehensive characterisation of CoCrMo wear particles, but the assessment of how reliable the blood and serum ion levels are with respect to the actual wear in the joint cavity, the authors reported that the effect of the chemical treatment on particle composition and size was checked. The results were not shown and the study did not provide microscopy evidence of the investigated particles.

Simoes et al.[283] reported on the isolation of particles generated by *in vitro* milling of commercially available low and high carbon CoCrMo powders in bovine serum albumin. The protocol consisted of simple centrifugation at 8000 x g without the use of any digestion technique, which aimed at the separation of particles from the protein rich environment and the preservation of particles' bio-corona. Several techniques were used for particles size distribution (dynamic light scattering techniques (DLS), TEM), shape (TEM) and chemical analysis (TEM and EDX) while the high-resolution transmission electron microscopy (HRTEM) was employed for FCC and HCP phase identification and ICP-MS analysis aimed to verify the stability of the particles in the biological environment.

With so many isolation protocols and characterisation techniques published in the literature and tested on various sources, it is difficult to compare the results from one study to another and assess the reliability of *in vitro* joint simulators. To overcome these aspects, a standardised method for the isolation and characterisation of polymer and metal wear particles from both tissue samples and testing fluids was proposed (BS ISO 17853:2011). It is an adapted from the enzymatic protocol of Catelas et al.[55,276] which can be applied to serum lubricants used in joint simulators or on periprosthetic tissue and can be adjusted for SF/aspirates retrieved from patients at revision time. Particles separation can be performed by filtration or centrifugation with subsequent display on polycarbonate filter, commonly used for SEM analysis, or embedded in resin and thin sliced for TEM investigation. The standard also refers to the enzymatic protocols proposed by Billi et al.[21] and Kavanagh et al.[24] which separates and displays particles directly on polycarbonate wafers and advises on the use of EDX for chemical identification of the isolated metal particles.

2.3.3 Particle Morphology and Composition

This section summarises the literature reports on the isolation and characterisation of metal particle in general and CoCrMo debris in particular, focusing mainly on the size, shape and composition of the isolated debris. The findings of the more recent studies which used one of the isolation techniques described in the previous section are summarised in **Table 2.3** and are also detailed below. The comparison between the outcomes of different studies is often difficult to perform due to the various parameters used to evaluate the size and define the morphological descriptors of the investigated particles. The most widely used size parameters are d_{max} or length (L), d_{min} or breadth, fiber length (FL), fibre width (FW), width (W), perimeter (P) and area (A), which are further used to determine the morphological descriptors, such as equivalent circle diameter (ECD), aspect ratio (AR), elongation (E), roundness (R) and form factor (FF) (**Table 2.4**). Billi et al.[9] showed how particles with very different morphologies can have similar morphological descriptors and questioned their efficiency for particle characterisation. For a better evaluation of the particle morphology, several descriptors should be calculated based on the measured dimensions (ASTM F1877-05(2010)).

Table 2.3 Size and shape descriptors used for particles characterisation as reported by Billi et al. in agreement with ASTM F1877-05(2010).

Size and shape descriptors	**Formula**	**Observations**
ECD - equivalent circle diameter	$ECD = (4\frac{A}{\pi})^{\frac{1}{2}}$	The diameter of a circle with the same area as that of the particle
AR - aspect ratio	$AR = \frac{d_{max}}{d_{min}}$	The ratio between the longest straight line between 2 points on the outline (d_{max}) and the longest line perpendicular to it (d_{min})
E - elongation	$E = \frac{FL}{FW}$	It has the same significance as AR but it is normally used for elongated particle, where the major axis line does not stay within the particle boundaries
R - roundness	$R = (4A/\pi {d_{max}}^2)$	It varies from 0 to 1 (close to the circular shape) and reflects how much the particle shape resembles with a circle; A – the particle area
FF - form factor	$FF = (4\pi A/p^2)$	Similar to R but it is calculated based on the particle perimeter (p) and is more sensitive to particle's roughness

Firkins et al.[279] investigated particles generated by pin on plate tests in 25% bovine serum and isolated using an alkaline protocol. SEM characterisation revealed that the majority of the particles were round and oval CoCrMo particles (atomic absorption spectroscopy (AAS)), with a maximum diameter ranging between 50 and 90 nm. A later study conducted by the same researchers aimed to characterise wear particles generated by CoP, MoM and alumina CoC bearings in a hip joint simulator. Particles were investigated using SEM, after being isolated from the serum lubricants

using the same alkaline digestion, and by TEM analysis of thin sections of particles embedded in polymerised araldite resin. The study reported round to oval metal particles ranging between 9 and 66 nm, found both as individual entities and as agglomerates. They were an order of magnitude lower than polyethylene particle and larger than ceramic particle released from alumina CoC couples (size range of 2-27.5 nm)[279,284,285].

Doorn et al.[36] characterised particles released *in vivo* from MoM hip implants. Tissue sections and particles isolated from periprosthetic tissue using an enzymatic protocol were investigated by TEM and particle composition was determined by EDX analysis. In tissue sections, they appeared as single or clumped particles of Cr oxides (contained mainly Cr and O, but no Co) and CoCrMo alloy (higher Co peak than Cr). Particles varied from mainly round and oval to few spike-like shape particulates, ranging in size from 6 to 744 nm. Besides CoCrMo debris, particles containing Ti, Al and V were also identified. The size of Ti6Al4V particles ranged from 94 to 1179 nm, with very few larger than 400 nm and were mainly with spike like morphology. The CoCr particles isolated from tissue samples were similar in shape to those captured in cells and investigated in tissue sections. Their size ranged from 20 to 834 nm. The Ti6Al4V particles were also identified and were larger than those investigated in tissue, ranging from 39 to 938 nm. The study also reported that single particles were found more frequently in tissue sections and agglomerates were more abundant after isolation. Moreover, the isolated samples presented fewer small particle than tissue sections collected from the same patients. These findings emphasize the aggregation effect of the applied isolation protocol[36].

Table 2.4 The results of the most popular digestion techniques used for the isolation and characterisation of metal debris from biological fluids and tissues.

Reference	Source	Material	Digestion	Technique	Shape	Size	Composition
Lee, 1992[286]	Tissue (hip)	Ti, CoCrMo, SS	Commercial tissue solubiliser (Soluene, 350), 96 h, 65°C	LM (isolated and non-isolated) and TEM (tissue sections)	Round (CoCrMo and SS) and angular or shard-shaped (Ti particles)	Isolation method: 0.8 to 1.0 µm by 1.5 to 1.8 µm Non-isolation method: 0.3 to 0.4 µm by 0.6 t0 0.7 µm TEM: 0.05 to 0.5 µm	N/A
Margevicius, 1994[277]	Tissue (hip and knee)	Ti, CoCrMo, SS	Acid – HNO_3, 48 h, RT	LM, SEM and EDX, Particle size analyser with a limit of detection of 0.58 µm	N/A	Mean d_{max}: 0.63 µm	CoCr, Ti, and Fe-Cr containing particles
Shanbhag, 1994[274]	Tissue (hip)	CoCrMo and Ti alloy	Mixed alkaline – 4M KOH and enzymatic – pronase	SEM and EDX	Flakes and wire-shaped	Mean d_{max}: 10 to 400 µm 200-400 µm in size and 10-20 µm thick – Ti flakes from Ti alloy stem; 300-400 µm wire-form Ti particles from the Ti mesh pad;	Ti alloy and commercially pure Ti particles
Doorn, 1998[36]	Tissue (hip)	CoCrMo	Enzymatic – papain and proteinase K	TEM and EDX	Oval and round with irregular boundaries	6-834 nm	Co rich (crystalline zone) Cr and O reach (amorphous zone)
Firkins, 1999[285]	Serum lubricant – HS	CoCrMo	Alkaline – 12M KOH	SEM	Oval and round	Mean d_{max}: 25-36 nm	N/A
Tipper, 1999	Serum lubricant – pin on disc	CoCrMo	Alkaline – 12M KOH	SEM, TEM and AAS	Oval and round	Mean d_{max}: 50-90 nm	Cr, O and Co
Catelas, 2003[111]	Serum lubricant – HS	CoCrMo	Enzymatic – papain and proteinase K	TEM and EDX	Oval and round (majority) and needle-shaped	0-0.25 Mc 14-213 nm (round) 6-248 nm (oval) 23-253 nm (needle) 1.75-2 Mc 11-163 nm (round) 15-225 nm (oval) 20-225 nm (needle)	Cr and O rich with traces of C CoCrMo Type 1: Cr>Co, distinct C peak Type 2: Co>Cr, no C

Campbell, 2004[287]	Periprosthetic and fibrous tissue (hip)	CoCrMo (stem)	Enzymatic – papain and ptoteinase K	LM, backscattered electron imaging and EDX	Oval (40%), needle-shaped (40%) and round (20%)	18-472 nm Mean: 77 nm	CoCrMo (50%) Chromium oxide (50%)
Catelas, 2004[20]	Serum lubricant – HS and tissue (hip)	CoCrMo	Enzymatic – papain and proteinase K	TEM and EDX	Oval and round (majority) and needle-shaped	HS: as above Tissue (mean d_{max}): Short term implantation cohort: 39 nm Long term implantation cohort: 58 nm	HS: Cr and O rich (~ 86% mostly round and oval) CoCrMo particles (~14% mostly needle shaped) Tissue: Long term: Cr and O/CoCrMo
Brown, 2007[98]	Serum lubricant – HS normal and microseparation conditions	CoCrMo and alumina	Enzymatic – papain, proteinase K, yeast lytic enzyme and Zymolyase	SEM and EDX	Round and irregular	Normal conditions: MoM: 8-116 nm CoM: 8-139 nm Microseparation: MoM: 8-107 nm (1.5 Mc); 6-146 nm (4 Mc) CoM: 7-156 nm (1.5 Mc); 8-140 nm (4 Mc)	CoCrMo particles from all conditions and bearing couples
Pourzal, 2011[28]	Serum lubricant – HS and CoB	CoCrMo	Enzymatic – papain and proteinase K	EFTEM and EDX	HS: oval and round CoB: needle shape	HS: 15-80 nm (Type 1 and 2) 5-15 nm (Type 3) CoB: 100-500 nm	HS: Type 1: Cr, O and traces of Co (crystalline zone in Co rich area) Type 2: Cr and O rich Type 3: Cr_2O_3(smaller and more abundant) CoB: CoCrMo
Billi, 2012[21]	Serum lubricant – hip and spine simulator	CoCrMo and alumina	Enzymatic – proteinase K	FEG-SEM, STEM and EDX	Round and oval (CrOx) Irregular and rod shaped (Co rich particles)	From 12 nm to ~400 nm	MoM: CrOx (amorphous) Co rich particles (crystalline) CoM: Al, Cr and Co (Fe contaminant)

Goode, 2012[288]	Periprosthetic tissue	CoCrMo hip resurfacing	No diggestion	STXM, STEM/EELS and EDX	Mainly round particles and diffuse debris	Few nm to few µm, average size: 30 nm	Diffuse debris: mainly oxidised Cr (Cr^{3+}) with traces of oxidised Co (Co^{2+}) Dense particles: metallic Cr, Co and Mo core in an O rich and Co depleted shell
Lu, 2012[23]	Serum lubricant – hip simulator	CoCrMo	Enzymatic – proteinase K	TEM, EDX and GFAAS	Round, oval, rod-shape and flake shape	Small particles: 17 by 27 nm Large flakes: 100-800 nm	CoCrMo particles and chromium phosphate
Kavanaugh, 2013[24]	Tissue and synovial aspirate (hip)	CoCrMo	Enzymatic – proteinase K for tissue; hyaluronidase, benzonase and proteinase K for synovial aspirate	FEG-SEM and EDX	N/A	<100 nm to 10 µm	Cr rich particles with low levels of Mo, Co and Fe (contamination from surgical instruments); chromium phosphates
De Pasquale, 2014[25]	Synovial aspirate (hip)	CoCrMo	Alkaline (NaClO)	SEM and EDX	Oval and irregular	From <1 µm up to 5 µm	CoCrMo particles (similar to the alloy composition) and CoCr particles with altered Co/Cr ratio
Simoes, 2014[283]	BSA lubricant – milling of commercially available CoCrMo powders	Low and high C CoCrMo	No digestion	TEM, HRTEM, EDX, XRD, ICP-MS	Round	10-800 nm (majority between 10 and 200 nm)	Co rich particles (almost 100% Co), CoCrMo particles (with lower Co and/or higher Mo than that in the bulk alloy)
Loeschner, 2015[289]	Synovial aspirate	CoCrMo	Enzymatic – proteinase K	AF4-ICPMS, AEC-ICP-MS and spICP-MS	N/A	50-550 nm (subject to technique used)	CrCoMo, Cr_2O_3 and CoO particles

MMD: mean maximum diameter; MD: maximum dimension; APL: average particle length; CoB: cylinder on bar; HS: hip simulator; LM: light microscopy

Catelas et al.[55,276,287] reported mainly round (48% and 54% for 0-0.25 Mc and 1.75-2 Mc test period respectively) and oval (38% and 36% for 0-0.25 Mc and 1.75-2 Mc test period respectively) with few needle shaped particles (14% and 10% for 0-0.25 Mc and 1.75-2 Mc test period respectively). For the 0-0.25 Mc test period, particle size ranged between 14-213 nm for round particles, 6-248 nm for oval particles and 23-253 nm for needle shaped particles. For 1.75-2 Mc test period, round particles ranged between 11-163 nm, oval particles between 15-225 nm and needle shaped particles between 20-225 nm. The EDX spectra of debris released in 95% bovine serum, revealed two types of particles: particles containing Cr, C and O, but no Co, which were assumed to originate from the oxide layer and showed a distinct C peak and higher Cr peak compared to Co. These were called *Type I* particles by the authors, while *Type II* were CoCrMo particles with a smaller or inexistent Cr peak and a higher signal for Co over Cr[111].

Campbell et al.[26] investigated CoCrMo debris released from a McKee-Farrar MoM prostheses, isolated from periprosthetic tissue using the enzymatic protocol of Catelas et al.[55,276]. The implant had been well-functioning for almost 30 years without any complications or revisions. The post-mortem investigation of the retrieved joint revealed debonding and signs of fretting wear at the cement-stem interface, which in the absence of any signs of damage at the bearings, was assumed to be the main source of wear debris and corrosion products. The backscattered electron imaging and EDX analysis identified oval (40%), needle shaped (40%) and round (20%) CoCrMo particles (50%) and Cr oxides (50%), ranging in size from 18 to 472 nm (mean size 77 nm). The investigation of tissue biopsy from distant organs (liver, spleen, lymph nodes) failed to identify debris disseminated systemically (except for one CoCrMo particle), but confirmed the accumulation of metallic particles in the periprosthetic and fibrous tissue around the loose femoral stem.

Another study[20] aimed to compare the characteristics of the particles generated *in vivo* with those produced by hip simulator tests *in vitro*. The particles were isolated from either tissue samples (*in vivo*) or serum lubricants (*in vitro*) (95% bovine serum) using an enzymatic protocol, embedded in epoxy resin and characterised using TEM and EDX analysis. The particles released *in vitro* were mostly oval and round with a significant percent of needle shape (especially in the 0-0.25 Mc test period). Their size ranged between 14-213 nm, with the majority between 40-60 nm for 0-0.25 Mc (run-in wear period), and 11-225 nm, with the majority between 20-40 nm for 1.75-2 Mc (steady-state wear period). EDX analysis revealed mainly particles containing Cr and O (presumably Cr oxide particle), larger in size, and fewer CoCrMo particles with different Co/Cr ratios. Particles with higher Co peak compared to Cr, were needle shaped, or large round or oval particles, showing heterogeneous contrast. The majority of the particles released *in vivo* were between 20 and 50 nm, with few larger particles in the long-term group. The average length of the particles from the very short-term group (<15 months since implantation) was smaller than that of the longer-term group (>15 months since implantation) (39 nm and 58 nm respectively). The difference between the two groups was also observed when comparing the average length of round (34 nm for very short term

and 47 nm for the long-term group) and needle shaped particles (53 nm vs 99 nm for the long-term group). The relative proportion of round, oval and needle shaped particles between the long and the short-term cohorts was also different. The very short-term group had 43% round, 47% oval and 10% needle, while longer term group contained 47% round, 41% oval and 12% needle shaped particles. The EDX analysis revealed particles containing mostly Cr and O, with very few CoCrMo particles, especially in the long-term group of patients. This study demonstrated that particles retrieved from patients after 23 and 43 months since implantation, which was reported to be the run-in regime, are comparable in size, shape and composition with particles generated from hip simulator during the run-in wear period (0-0.25 Mc)[20].

A more recent study[28] proposed to characterise wear particles generated by MoM articulations in a reciprocating sliding wear tribometer (CoCrMo cylinder vs bar) and a hip simulator (CoCrMo head against CoCrMo cup). The particles were isolated from the testing lubricant (NCS, 30 g/l protein content) using the enzymatic protocol described by Catelas et al.[55,276] and were investigated by energy filtered transmission electron microscopy (EFTEM) and electron diffraction pattern analysis. The particles released from the tribometer showed a length of 300-800 nm and a width of 100-300 nm, consisting of CoCrMo bulk material, and were generated by a different wear mechanism than those released from the MoM implants from the hip simulator. The hip simulator test generated two main types of particles, called *Type I* and *Type II* respectively. *Type I* contained Cr, O and Co locally, while *Type II*, contained only Cr and O. Both types of particles were in the 30-80 nm size range. EFTEM mapping of the Type I particles revealed that Co appeared only locally, without forming a solid core. Moreover, smaller Cr oxide particles, named *Type III*, ranging between 5-15 nm, with a lattice structure of Cr_2O_3 were also identified, and the authors suggested they were flaked off the surface of the larger *Type II* particles. Bright field images showed defects in the lattice structure of these small Cr oxide particles, which can indicate that they had been subjected to high shear stresses[28].

Brown et al.[98] investigated particles by field emission gun (FEG)-SEM and EDX directly from the Pt/Pd coated polycarbonate filters involved in the separation of debris. The particles generated from the CoCrMo articulations under standard wear conditions were round and irregular shaped and ranged between 8 and 116 nm, with the majority between 30 and 39 nm (mean size 34.72 nm). Particles released under microseparation wear conditions had a similar morphology, ranging in size from 6 to 146 nm, with a mode distribution in the 20-29 nm range (mean size 35.62 nm after 1.5 Mc and 31.16 nm after 4 Mc). The EDX analysis revealed particles containing Co, Cr and Mo.

Particles generated from spine and hip simulator tests of MoM and MoC bearings in 90% bovine serum have been isolated with the enzymatic protocol proposed by Billi et al.[21] and investigated with FEG-SEM, STEM and EDX, revealing mostly round and oval amorphous Cr oxide particles with a d_{max} of ~ 0.1 μm, and fewer crystalline Co-rich particles, which were larger (d_{max} ~ 0.3 μm) irregular or rod shaped and had a smooth surface texture.

A comprehensive structural characterisation of the wear and corrosion debris released from CoCrMo hip resurfacings was performed by Goode et al.[288]. The study aimed to investigate particles from explanted periprosthetic tissue, using scanning transmission X-ray microscopy (STXM) coupled with X-ray absorption spectroscopy (XAS), and STEM coupled with electron energy loss spectrometry (EELS) and EDX. Both techniques provided clues on the speciation of the chemical elements in relation to their spatial distribution. STEM-EELS provided better energy resolution compared to STXM-XAS, while STEM-EDX allowed for the elemental mapping of Mo, which was not detected with the former technique. Diffuse and particulate debris organised in clusters of ~1 μm diameter or needle shaped regions were found in membrane-delimited organelles inside of the macrophages. A thick band of metal packed macrophages, distributed toward the surface of the cross-sectioned periprosthetic tissue, was identified following the histological analysis and electron-microscopy imaging. Visible cell alterations, including changes in the electron transparency of the mitochondria and in the structure of the nuclear membrane, were reported in several macrophages. The chemical speciation identified mainly diffuse Cr^{3+} with traces of Co^{2+}, and round or needle shaped electron dense structures composed of a Co, Cr and Mo metallic core, surrounded by an O rich and Co depleted shell. The later structures were found more rarely and, according to the authors, they represent partially corroded debris.

Lu et al.[23] isolated particles generated from a hip simulator in 25% bovine serum and characterised them using TEM and EDX analysis. Chemical composition revealed mainly particles containing Cr, P and O, which were thought to be Cr phosphate, and fewer particles consisting of Co, Cr, Mo, P and O as those previously reported by others. The small round, oval and rod-like shaped particles had an average length of 27 nm and average width of 17 nm, while fewer large asymmetric flake-like particulates were found to be in the 100-800 nm size range.

The particles isolated from synovial aspirates and characterised with SEM and EDX were either large CoCrMo particles (up to 5 μm), with a composition similar to that of the main alloy, or Cr rich debris with little or no Co, ranging in size from 1 to 5 μm. Depending on the number of wear particles identified in each hip aspirate, the samples were categorised as absent, physiological, mild and strong wear. The particles found in the mild and physiological wear groups were mainly oval and smaller than 1 μm, while particles found in the strong wear category were CoCrMo debris and particles with an altered (i.e. different than the Co/Cr ratio of the bulk alloy) and irregular shape[25].

Simoes et al.[283] demonstrated that low carbon CoCrMo alloy generated more nanoparticles than the high-carbon alloy. This might reside in the improved ductility induced by the carbon content in the latter alloy tested. The size of the particle varied from 10 to 600 nm for the low C alloy and from 10 to 800 nm for the high C material, with the majority between 10 and 200 nm, as confirmed by both DLS and TEM measurements. X-ray diffraction (XRD) and high-resolution (HR)-TEM successfully demonstrated the stress induced FCC-HCP transformation, previously proposed by others[148], showing mainly FCC phase in the coarse particles and HCP phase in finer particles, smaller than 200

nm. Interestingly, the authors reported 10 nm particulates containing almost 100% Co and CoCrMo particles with 10-20% Mo, which exceeds the proportion of Mo in the main alloy. This is not in agreement with others who suggested that small particles are mainly Cr oxides, while large particles can contain Co in concentrations below that in the main alloy and only traces of Mo[20,21,28]. The ICP-MS results also demonstrated the dissolution of Mo and Co by the BSA solution, which could explain the reduction of Co in some of the particles, compared to the bulk alloy, but it cannot justify the enrichment of Mo in some of the milled fragments. This study has several limitations, including the use of commercially available CoCrMo particles and the *in vitro* milling in BSA solution, which might not correctly simulate the *in vivo* electrochemical environment. The conditions in which the initial powders were generated and further milled to provide comparable particles sizes to debris originating from the articulating bearings, might be responsible for the relatively high concentrations of Co and Mo reported in this study[283,290].

Another study[291] reported on the characterisation of particle released from CoCrMo prosthesis in SF. The sample was initially fixed in glutaraldehyde, then dehydrated and embedded in resin. Thin microtome sections were displayed on formvar coated copper grids, C coated to minimise charging and investigated with TEM, EDX and EELS. The study reported debris which ranged in size from 5 to 50 nm, which is in agreement with others[20,28,36,98]. In terms of composition, crystalline particle similar to the bulk alloy (Cr and Co rich, with evidence of Mo), amorphous Cr and Mo rich particle and smaller Cr and O rich structures were identified using EDX. TEM micrographs did not show individual nanoparticles but clusters of ~100 nm which appeared to be made of smaller entities difficult to distinguish. The EELS analysis identified mainly Cr^{3+} species with evidence of Cr^{4+} in the small, amorphous particles rich in Cr and O. The authors suggested that these particles originated from the passivating Cr oxide layer, formed at the surface of the CoCrMo bearings[283].

2.3.4 Summary

Despite the significant amount of work in this field, there is still a lack of consensus regarding the size, morphology and chemistry of debris released from CoCrMo bearing surfaces. Most of the previous isolation protocols aimed to release debris from hip or knee bearings, released into SF[24,292,293], serum lubricants[23,28,55,98,111,276,279,284] or periprosthetic tissue[20,36,274,277]. To our knowledge, nobody has ever before tried to clean and isolate particulate debris originating from other wear sites of the hip replacements, such as the tapers or cement-stem interfaces, although the principles of cleaning should be the same.

The analysis of particles suspended in either natural or simulated body fluids require their separation from the supernatant[24,25,55,98,111,276,279,284,287,292], while in the case of periprosthetic tissue, the particles can be directly analysed in thin histological slices (70-100 nm) with TEM or LM[26,100,294,295] or can be extracted using tissue digestion and isolation methods[20,36].

Previous studies have suggested that some of the biomolecules commonly found in biological and simulated lubricants (i.e. lipids, proteins, hyaluronic acid etc.[296,297]) can interact with the particles, forming an organic corona which impedes the direct contact between the particle and the environment[9,23]. This can result in particle being entrapped into an organic layer, potentially forming agglomerates which are difficult to separate and investigate individually. As a consequence, most of the researchers have designed their work based on three main steps, as shown in **Figure 2.17**.

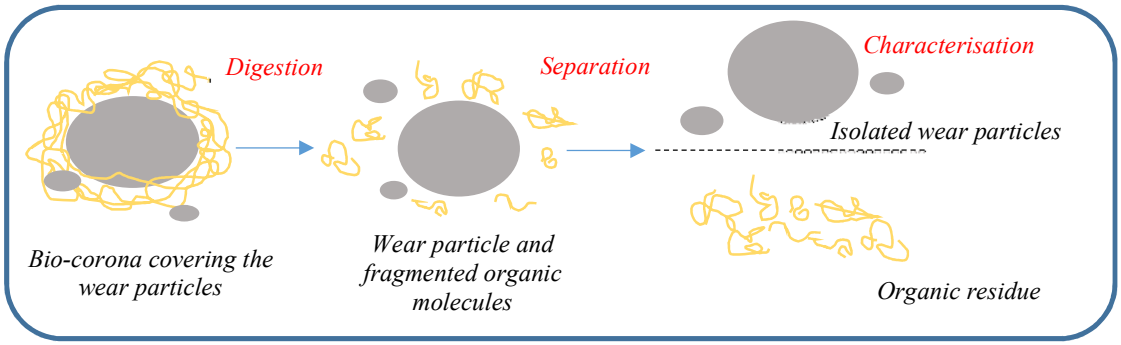

Figure 2.17 Particle isolation protocol involving digestion of the organic material cover.

Regardless of the particle material and surrounding environment, the first step proposed in most of the previous studies[23,24,28,36] involves digestion of the organic compounds to release the particle. Once the fragmentation of the large biomolecules is accomplished, the particle can be separated from the organic residue and the resulting particle, which are desired to be free of contaminants, can be investigated using appropriate techniques. The main steps of the cleaning treatments are summarised below:

A. Tissue and Serum Digestion

This step aims to release the particles from the biological environment in which they have been generated and which can entrap some of the smallest particle[9]. The most popular digestion protocols proposed for the isolation of metal debris involve the use of chemicals and/or enzymatic treatments[21,24,36,55,276,279]. Ceramic and polyethylene particles are less susceptible to dissolution and have been isolated using either acidic[298,299], alkaline[98,292] or enzymatic treatments. The most commonly used alkali for tissue and serum digestion are sodium and potassium hydroxide (NaOH and KOH)[55,276,279,300], while nitric and hydrochloric acids (HNO_3 and HCl) are often involved in acidic lyses[277,298]. Enzymatic protocols use enzymes such as Papain and Proteinase K[21,24,28,98,276] to assist the fragmentation of the large proteins which form the bio-corona. Nine et al. suggested that an efficient digestion step should consist of tissue and sample delipidation, proteins fragmentation and precipitation, followed by separation, usually accomplished by centrifugation[27]. Prior to centrifugation, the particles must be dispersed by ultrasound, which disintegrates the cluster and separates the particles.

B. Separation Methods

Most of the popular isolation protocols employ multiple digestion steps and either centrifugation or filtration for the particle recovery[21,55,98,276]. Separation of particles by centrifugal sedimentation is based on the difference of density between the particle and the biological media in which they are suspended. The denser the particle, the easier the migration to the bottom of the tube during centrifugation, separating them from the supernatant, resulting in highly concentrated particles suspensions[27]. Similarly, particle separation by filtration is based on the retention of all particles larger than the size of the pores while the supernatant passes through the filter and is discarded. Studies have shown that the selection of appropriate centrifugation speed and filter membranes represents one of the most important decisions, as these criteria can directly influence the morphology and size distribution of the isolated particles, and thus the quality of the results[21,23,301]. Based on a theoretical simulation, Lu et al. proved the effect of the centrifugal force and duration on the efficiency of particle isolation[23]. According to their study, 60 minutes of centrifugation at 165000 x g, can recover up to 62.3% and 100% of the total amount of the 5 nm and 10 nm particles respectively. By reducing the centrifugal force at 16000 x g, after the same period (60 min) only 4.8% and 20.9% of the same size ranges were isolated, which means the particle size distribution (PSD) was shifted towards the higher sizes, as most of the small particles were still in suspension[23]. However, most of the previous studies used centrifugation speeds below 50 000 x g for the isolation of particulate debris, and may have lost some of the small particle.

When particle separation is performed by filtration, the size of the pores is extremely important, as the small particle can pass through the filter and do not count for the PSD. Scott et al. performed a study in which polyethylene particles generated in bovine serum lubricant were isolated using an acidic digestion protocol and separated by filtration through either a 0.2 µm or 0.05 µm pore size membranes[301]. The size distribution in the first case (0.2 µm pore size) was shifted towards higher values, since only the larger particle with a mean diameter of 0.23 µm and a median value of 0.19 µm were separated. The median size of the retained particles is below the size of the pores, which might imply that some of the small particles were lost during filtration and passed with the supernatant. When a smaller pore size membrane was used, the mean diameter of the retained particles was 0.19 µm and the median size was 0.18 µm. Moreover, it has been suggested that the distribution of the pores size within the membrane can induce particle agglomeration by a funnel effect, concentrating the particulates around the pores[9]. This would result in an unrealistic size distribution which does not reflect the characteristics of all the particle in the sample. An increased number of centrifugation steps, can also lead to particle loss as they can stick to the wall of the centrifugation tubes, which means that with every separation step the number of particle available for quantification and analysis decreases. Furthermore, the risk of contamination with particle from the laboratory atmosphere also raises with the transfer of the particle from a vial to another, which affects their characterisation[9,23].

C. Particle Characterisation Techniques

Wear particle characterisation usually combines various imaging techniques, such as LM[40], SEM[98], TEM [28,97,281] and atomic force microscopy (AFM) [302,303], with methods that provide information about the particle chemistry, such as EDX[39,276], EELS[288], synchrotron x-ray analysis[14,100], electron microprobe analysis (EMPA)[40], infrared spectroscopy (IR/FTIR), X-ray photoelectron spectroscopy (XPS)[97], x-ray diffraction (XRD)[39] and Raman spectroscopy[40]. Each imaging technique has a specific theoretical resolving power which indicates the size range appropriate for investigation. **Figure 2.18** illustrates the resolution of the imaging methods used in previous studies to investigate wear debris, with examples of biological structures falling into each size range.

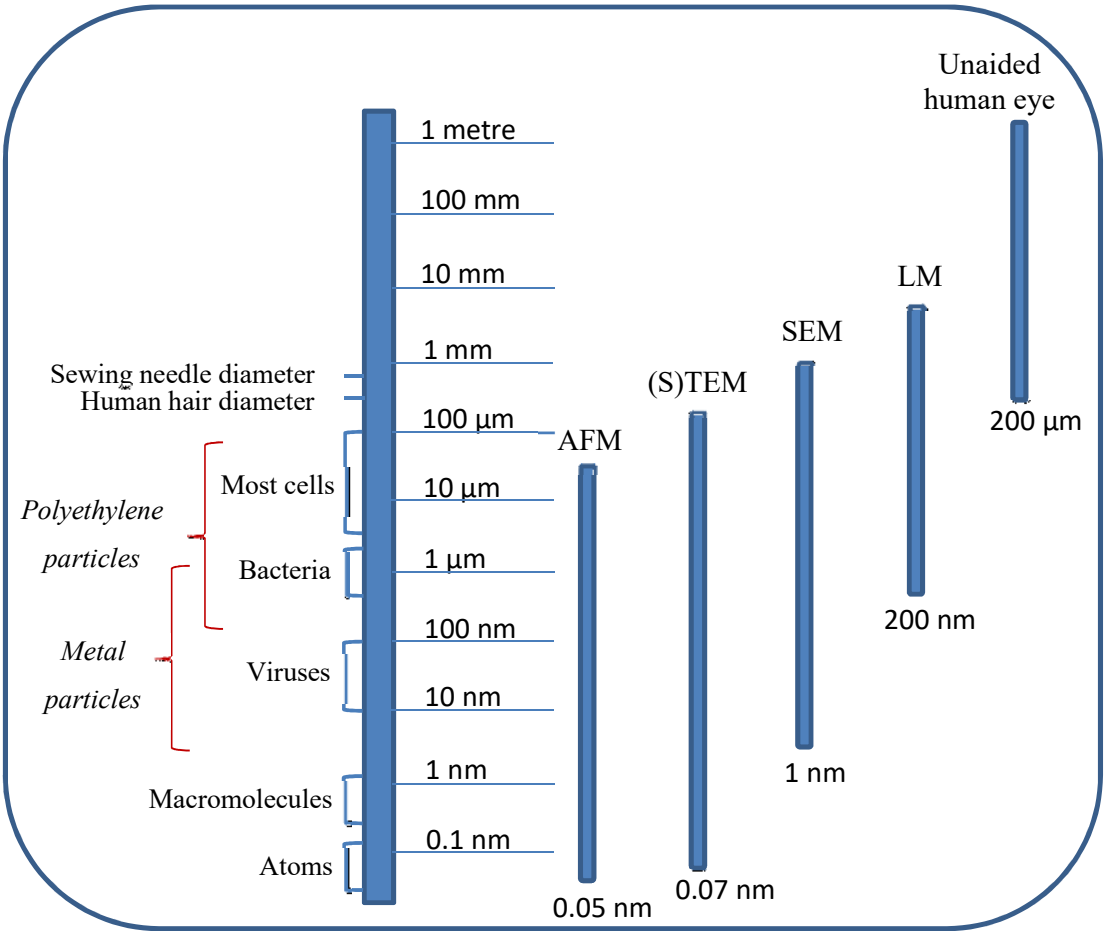

Figure 2.18 Resolution of commonly used microscopic techniques, in relation with the size of polyethylene and metal wear particles released from hip bearings.

LM has been used to identify mainly polyethylene particles, which are larger in size and easier to depict. However, the technique has been successfully used to image metal and ceramic particles embedded in periprosthetic tissue retrieved from patients, although Ingham et al. suggested an overestimation of the particle size reported in the past with the use of optical microscopy due to its

limited resolution[304]. The size range of metal particle found on retrieved tissue and investigated with LM was 0.1-400 μm, while other studies reported metal debris between 10 and 400 nm, with the majority between 15 and 25 nm. Lee et al.[286] investigated the size of CoCrMo wear particles using both LM and TEM. The size range determined with the use of the LM was in the micrometre range, while with the TEM the particle ranged from 0.05 to 0.5 μm, with the majority below 0.1 μm[286]. The authors suggested that the reduced tissue slice thickness required for TEM analysis, limited the number of micrometre sized particle which were very likely expulsed during the slice cutting process and provided a lower size distribution[286]. The most commonly used microscopy techniques with metallic debris are TEM/STEM and SEM which have the highest resolutions among the available methods[27] (**Figure 2.18**). Although TEM has a better resolution than the SEM, the two imaging techniques are based on different principles and provide different information. TEM generates a projection of the particle encountered in the beam path, thus two or more overlapped particle can be projected as a single, larger particle. The orientation can also induce errors that lead to incorrect size and shape estimations. SEM is a valuable tool for investigating particle topography and researchers have often combined the two techniques to gain data on both the crystallinity and particle surface. These methods are usually coupled with EDX to provide insight on the chemical composition of the metal debris, while IR and Raman have been successfully employed for polyethylene particle characterisation[27].

None of the previous isolation protocols has ever been applied to the wear and corrosion flakes released from the metallic secondary interfaces in total hip replacements. The investigation of the flakes and the characterisation of the individual nanoparticles, released with a cleaning treatment, can provide useful information about the processes and transformations of debris in the body.

More research is needed to understand the nature of the wear and corrosion products released from the bearing surfaces, taper junctions and cement-stem interfaces, and fill the gaps in the knowledge of the particle physicochemical characteristics, which are linked to debris reactivity. The limitations identified in the previous studies, such as the low resolution of the characterisation techniques, the loss of the small particle due to the use of low centrifugation speeds, the alteration of their morphology and chemistry, can be overcome by using efficient cleaning treatments, which have minimal effects on the particle characteristics, and state-of-the art techniques for the isolation and characterisation of debris. The imaging techniques must have the resolution required to image individual nanoparticles, to correctly measure their size, and must be used in association with sensitive analytical techniques able to reveals their chemical nature. Thus, it is avoided the over or under estimation of the particles size and the species that make up the wear and corrosion flakes are more accurately identified. Finally, it is important to investigate debris which can be correlated to a certain wear site, to understand the characteristics of the particle in relation to their origin. This has not been properly addressed by previous studies, in which debris from the periprosthetic tissue or released in the synovial fluid may have originated from any of the metallic interfaces (i.e. bearing

surfaces, taper junctions or cement-stem interfaces). All these demonstrate the need of further research to provide a better understanding of the wear and corrosion products released from hip replacements and advance the current knowledge in the field.

Chapter 3 Materials and Methods

3.1 Introduction

The comprehensive characterisation of the wear and corrosion flakes in this study used state-of-the-art techniques, which revealed the structure and composition of the hip-related debris from the micro scale down to the nano level. A simple outline of the sample preparation and characterisation steps, and the outcomes expected from the use of each technique are shown in **Figure 3.1**. The detailed presentation of the techniques, the parameters used to characterise the as-retrieved flakes or the particulate debris, and the methods used to provide clean nanoparticles are described later in this chapter. Some of the analytical techniques, such as ICP-MS, are destructive by their nature and the exclusion of the samples with minimal amounts of debris was necessary. Other techniques, such as SEM, required loading the wear and corrosion flakes on carbon coated double tape stubs, from which debris could be retrieved and further used in the characterisation process. The recovery of the flakes from the SEM stubs, however, was avoided where possible, with other pieces of the wear and corrosion flakes from the same retrieval and wear site used. STEM characterisation coupled with EDX and EELS, as well as the STXM and X-ray near edge absorption structure (XANES) analysis are time consuming and very expensive techniques, which restricted the number of samples and grids investigated (8 hours of beamtime on the high-resolution STEM cost ~£1700). Other techniques, such as SEM and LM were only used for a small number of samples because the results provided were enough to prove a pre-defined hypothesis (i.e. non-homogeneous nature of the as-retrieved corrosion flakes). For the samples which yielded small amounts of debris, the retrieved wear and corrosion products were only used in particular steps during the characterisation process, whereas for others the collected debris was sufficient to be used in more steps of the investigation. The types of techniques used for the characterisation of debris from each retrieval are shown in **Table 3.1**. The sections below provide the technical details of the investigations performed in the study and allow for future experiments to be repeated under the same experimental conditions.

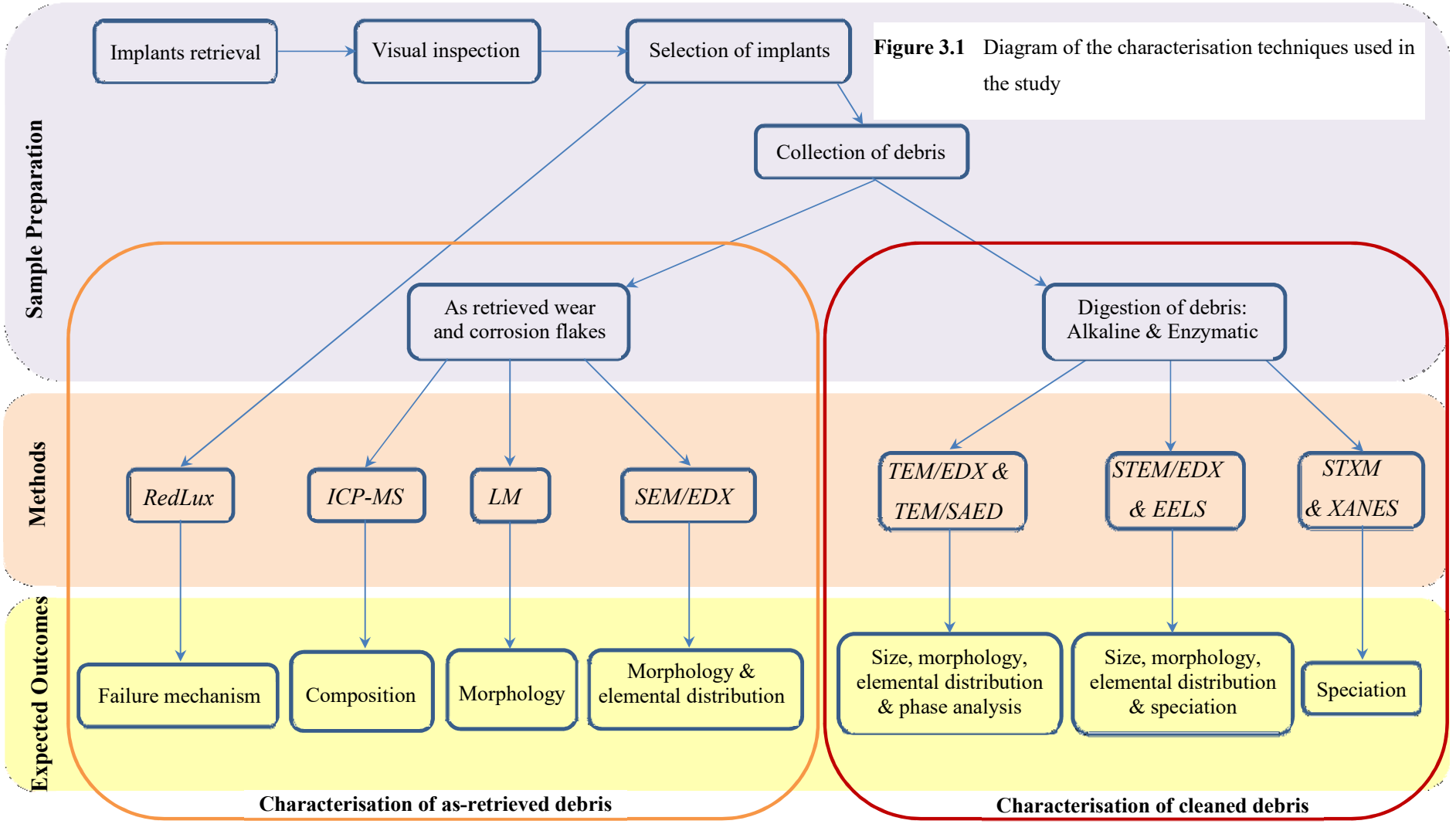

Figure 3.1 Diagram of the characterisation techniques used in the study

Table 3.1 The matrix of samples and techniques used in the study, showing the types of analysis used for the investigation of debris from each retrieval.

Sample	Origin of debris	RedLux*	ICP-MS	SEM/EDX	LM	Alkaline Digestion	Enzymatic Digestion	TEM/ EDX**	STEM/ EDX	TEM/ SAED	STEM/ EELS	STXM/ XANES
1	Taper	✓	✓	✓	✓	✓	✓	✓	✓	✓	✓	-
	Stem		✓	-	-	-	✓	✓	✓	✓	✓	-
2	Taper	✓	✓	✓	-	✓	✓	✓	✓	-	-	✓
	Stem		✓	-	-	-	✓	✓	✓	-	-	✓
3	Taper	✓	✓	✓	-	✓	-	✓	✓	-	-	-
4	Taper	✓	✓	-	-	✓	-	✓	✓	-	-	-
5	Taper	-	✓	-	-	✓	-	✓	✓	-	-	-
6	Taper	✓	-	-	-	-	✓	✓	✓	-	-	-
7	Taper	✓	-	-	-	-	✓	✓	✓	✓	✓	✓
8	Taper	✓	✓	-	-	-	✓	✓	✓	✓	✓	✓
9	Stem	✓	✓	✓	✓	✓	✓	✓	✓	-	-	-
10	Stem	✓	✓	✓	-	✓	✓	✓	✓	-	-	-
11	Stem	✓	✓	✓	-	✓	-	✓	✓	-	-	-
12	Stem	✓	-	-	-	✓	-	✓	✓	-	-	-

*RedLux analysis of the female taper/bore of the head;

**TEM/EDX was used to check the quality of the TEM grids and the degree of sample digestion; not all the results were included in the comparative studies;

3.2 Retrievals and Collection of Debris

The wear and corrosion products investigated in this study were collected from hip retrieved implants, from around the taper junctions and/or cement-stem interface. The revision surgery had occurred following the patient reported pain and the diagnosis of abnormally high Co and Cr levels in the body fluids (i.e. blood, plasma or synovial aspirate). The circulatory level of metals was not available for all the retrieved implants, but representative values of the Co, Cr and Mo yields in blood and/or synovial aspirate samples from donors in this study were reported by Crainic et al[37]. The analysis of the systemic metals and their implications to the patients were beyond the remit of this study, which is why the values were not included in this or other chapters of the thesis. The patients provided written consent and agreed for the retrieved implants to be investigated to understand the failure modes and the amounts of material loss. The study received approval from the National Research Ethics Service Committee, South Central-Southampton A (REC reference: 11/SC/0091).

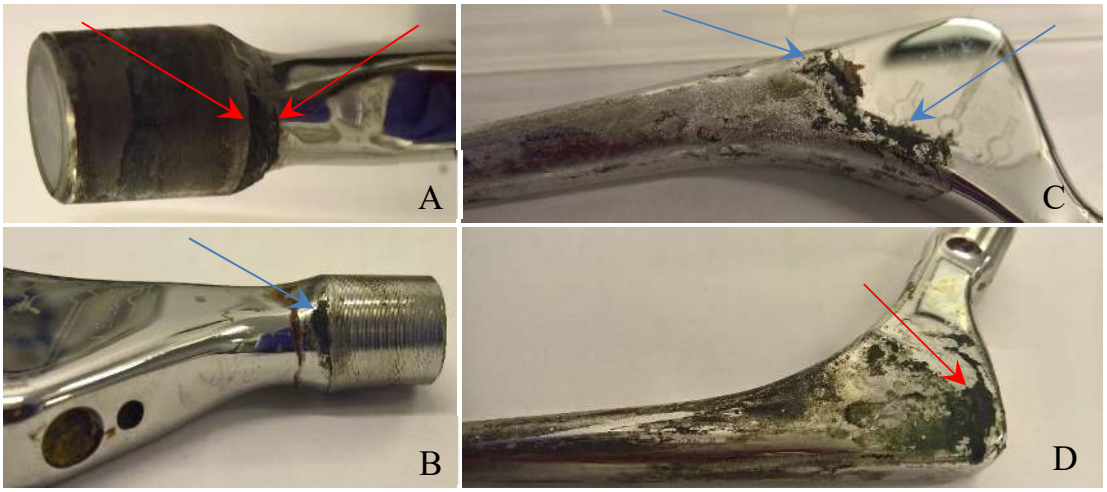

Figure 3.2 Deposits of wear debris and corrosion products around the tapers (A and B) and in the proximal region of the cemented stems (C and D).

The selection of the implants was based on the visual inspection of the retrievals, which provided an empirical evaluation of the level of mechanical damage and extent of corrosion at the secondary metallic interfaces (taper-trunnion junction and/or cement-stem interface). Twelve retrievals which had visible deposits of wear and corrosion products at the base of the trunnion, inside the bore of the head and/or at the cement-stem interface were selected to be investigated in the study. **Figure 3.2** shows representative wear and corrosion deposits located at the base of the trunnion (**A, B**) and in the proximal region of the cement-stem interface (**C, D**). In most of the cases, the corrosion deposits were localised in the proximal region of the cemented stems while the amounts of debris in the distal area were usually minimal.

Table 3.2 Implant make and size of the femoral head and stem.

Implant	Head	Head size and offset (mm)	Stem make	Taper size (mm)
1	Adept	46+0	CPT	12/14
2	BHR	50+4	CPT	12/14
3	Adept	42+3.5	CPT	12/14
4	BHR	42+0	CPT	12/14
5	BHR	46-4	Synergy (+CoCrMo sleeve)	12/14
6	Adept	54+0	Alloclassic	12/14
7	M2a	38+0	Bi-metric uncemented	Type 1
8	M2a	38+3	Bi-metric uncemented	Type 1
9	BHR	42+4	CPT	12/14
10	Adept	46+0	CPT	12/14
11	BHR	42+0	CPT	12/14
12	Adept	46+3.5	CPT	12/14

The corrosion at the tapers mainly resulted in deposits of black and flaky debris around the base of the trunnions, with little debris observed inside the bore of the head. The make and size of the femoral heads and stems in the selected retrievals are shown in **Table 3.2**. Three different designs of the heads (Adept, BHR and M2a) all made of as-cast CoCrMo alloy were matched either with cemented CoCrMo alloy stems (CPT – forged CoCrMo) or Ti stems (Synergy – forged Ti6Al4V, Alloclassic – forged Ti6Al7Nb and Bi-metric uncemented – forged Ti6Al4V). One retrieval consisted of a CoCrMo head fitted on a Ti alloy stem using a CoCrMo sleeve (retrieval no 5), and based on the visual inspection, the wear and corrosion products originated from the sleeve-male taper interface.

After revision surgery, the retrievals were sterilised and stored for over 48 h in 10% buffered formalin to ensure sterilisation, before being removed, dried and stored dried until further investigation. The lose wear and corrosion flakes from around the base of the trunnion, bore of the head or from the cement-stem interface were collected with plastic tweezers and pipette tips, and were stored in clean plastic Eppendorf tubes, away from light and heat. During the process of debris recovery, the use of metallic tools which could have contributed to the release of metal from the investigated interfaces was completely avoided. No other special conditions were granted to the collected wear and corrosion products, prior to analysis or cleaning treatment.

3.3 RedLux Analysis

The loss of material from the bearing surfaces and female side of the taper (i.e. bore of the head) was investigated with a RedLux Artificial Hip Joint Profiler (RedLux, Southampton, UK). The instrument[2,305] has the ability to perform ultra-precision three-dimensional (3D) form metrology, with a spatial resolution of 20 nm. The RedLux imaging of the female tapers was performed based on replica casting made using Microset 101RF (Microset Products, Ltd, Nuneaton, UK), capable to reproduce fine details to a resolution down to 0.1 μm. The outcomes of the RedLux analysis helped identify the taper failure mechanisms and allowed the selection of the joints for the comparative study (toggling vs non-toggling taper-head couples). The extent of material loss from the bearing surfaces and the shape and localisation of the wear patches did not represent the main purpose of the study but provided information about the wear mechanisms at the bearing surfaces (i.e. normal wearing vs edge wearing), which can influence the distribution of the load and the wear of the taper junction. All retrievals except for one (implant 5) were investigated with RedLux to determine the regions of material loss and the modes of wear and corrosion.

3.4 ICP-MS Analysis

ICP-MS was used to investigate the presence and proportion of metallic species in the wear and corrosion flakes retrieved from around the taper junctions and/or cement-stem interface of 9 retrievals out of 12 (see Table 3.1). The technique has been previously used by Shearwood et al.[230] to analyse black deposits of debris observed on explanted fragments of cement mantle. Nine metals were analysed, including Co, Cr and Mo (the main elements of the CoCrMo alloy), Al, Ti, V, Mn, Ni and Zr. These elements may originate from the wear of implant components or surgical tools made of Ti alloy (Ti6Al4V) or from the bone cement radio-pacifier (ZrO_2). After retrieval, the corrosion flakes were weighed in Teflon digestion vessels and subject to a sequential overnight digestion in Aqua Regia at 130°C, followed by HNO_3/H_2O_2 at 130°C. The dissolved samples were evaporated to dryness and redissolved in 3% HNO_3 and spiked with 1 ppb of In and Rh, as internal standards. Mass spectrometry was performed using a high-resolution inductively coupled plasma mass spectrometry (HR-ICP-MS) Thermo Fisher Scientific Element XR (Bremen, Germany). Data was acquired using medium resolution via a perfluoroalkoxy alkanes (PFA) nebuliser and cyclonic spray chamber. After each sample analysis, a wash solution containing 3% HNO_3 was run until background levels were achieved. The raw data were blank and internally corrected and then calibrated against synthetic standards (Inorganic Ventures, Virginia, USA).

3.5 Digestion Techniques

Some fragments of the wear and corrosion flakes retrieved from around the tapers or from the cement-stem interface were subject to digestion or cleaning treatments, which aimed to break down the clusters of particles and dissolve the bio-corona. Various digestion methods have been previously used to clean particulate debris released from the hip bearing surfaces in synovial fluid or periprosthetic tissue, but digestion of flakes from around explanted tapers or cemented stem has never been reported before. The alkaline and enzymatic methods used in this study are explained below and in Crainic et al. (2017)[37].

Enzymatic Digestion

The protocol was adapted from those of Doorn et al.[36] and Catelas et al. [55,276], and consisted of a 24 hr incubation of the flakes (~0.8 mg) with 0.25 mg lyophilised Papain (Sigma Aldrich, UK) in 2 ml 50 mM Tris-HCl, at 65°C, under continuous stirring at 180 rpm (Stuart, SSM1). After the first incubation, the pellets (metal debris) were recovered by centrifugation at 50 000 x g (Optima MAX-XP, Beckman Coulter, TLA-55 fixed angle rotor) and were subject to a second incubation with 0.8 mg Proteinase K (Sigma Aldrich. UK) in 2 ml of 50 mM Tris-HCl, for 24 hrs, at 55°C. Before each incubation, the debris was washed with 2 ml 2.5% SDS (Sigma Aldrich, UK) at room temperature and subject to ultrasound for 15 mins. In order to preserve the native characteristics of the metal particles, the boiling steps for 10 mins in the original protocols were avoided. The particles were finally recovered by centrifugation at 50 000 x g, washed twice with 2 ml DIW and stored in 100-200 µl DIW at -20°C, prior to further analysis. The steps of the enzymatic digestion are schematically represented in a diagram in **Figure 3.3**.

Alkaline Digestion

The chemical treatment was also adapted from the protocol of Catelas et al. [55,276], developed for the isolation of metal particles released from bearing surfaces in bovine serum or periprosthetic tissue. The main steps are schematically shown in a diagram in **Figure 3.4**. The solid debris (0.5-1 mg flakes) was submerged in 1 ml 12N KOH, mechanically fragmented with a plastic pipette tip and subject to 15 mins of ultrasound. The suspensions were incubated at 37°C under continuous stirring (180-200 rpm), for 48 hrs. During this time, the samples were subject to 15 mins of ultrasound every 8-10 hrs, to assist and enhance the digestion process. After 48 hrs, the suspensions were centrifuged at 50 000 x g. The pellets were recovered and washed twice with 1 ml DIW and submerged in 100-200 µl DIW (depending on the amount of debris recovered from the treatment). The particle suspensions were stored at -20°C, until further investigation.

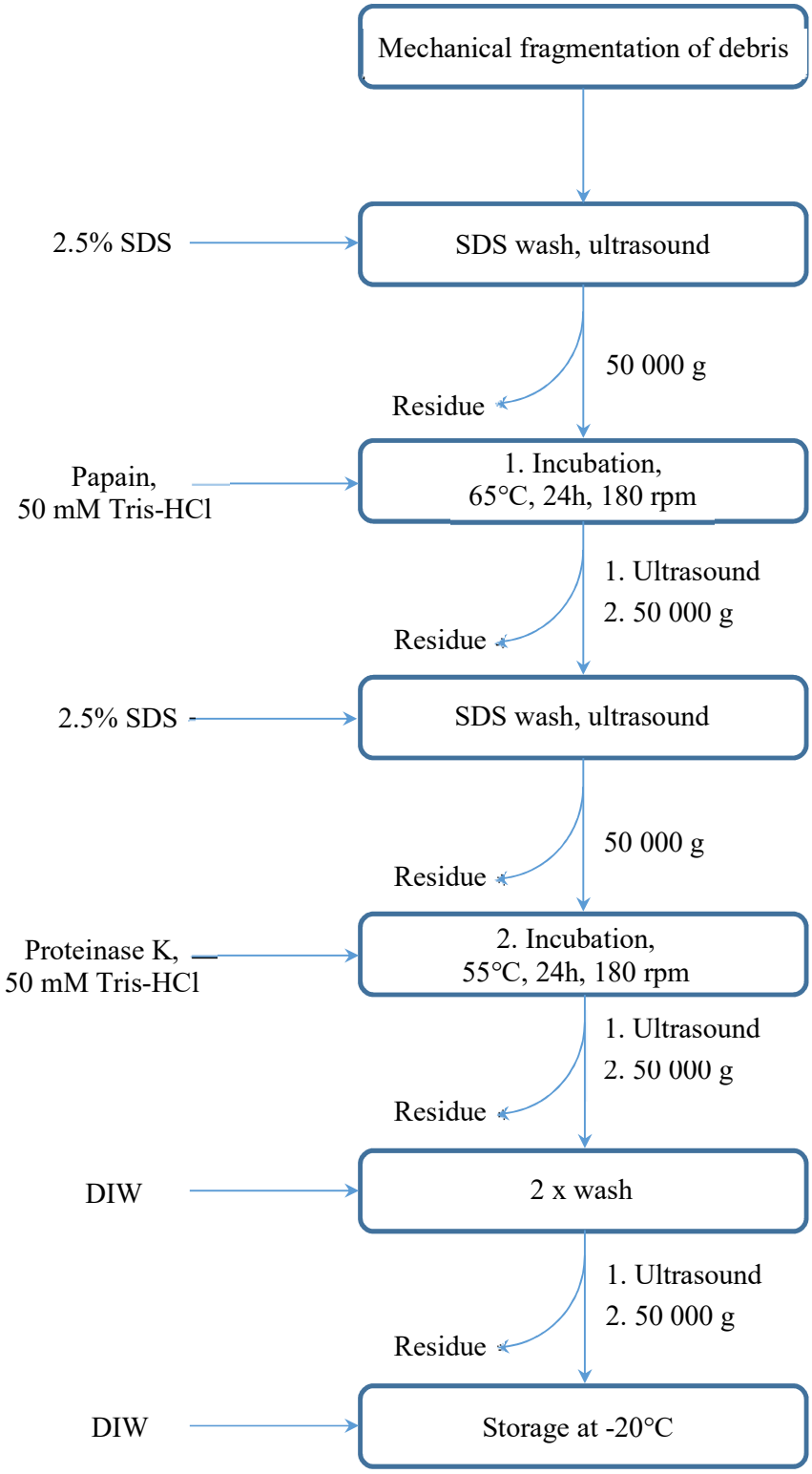

Figure 3.3 The steps of the enzymatic digestion.

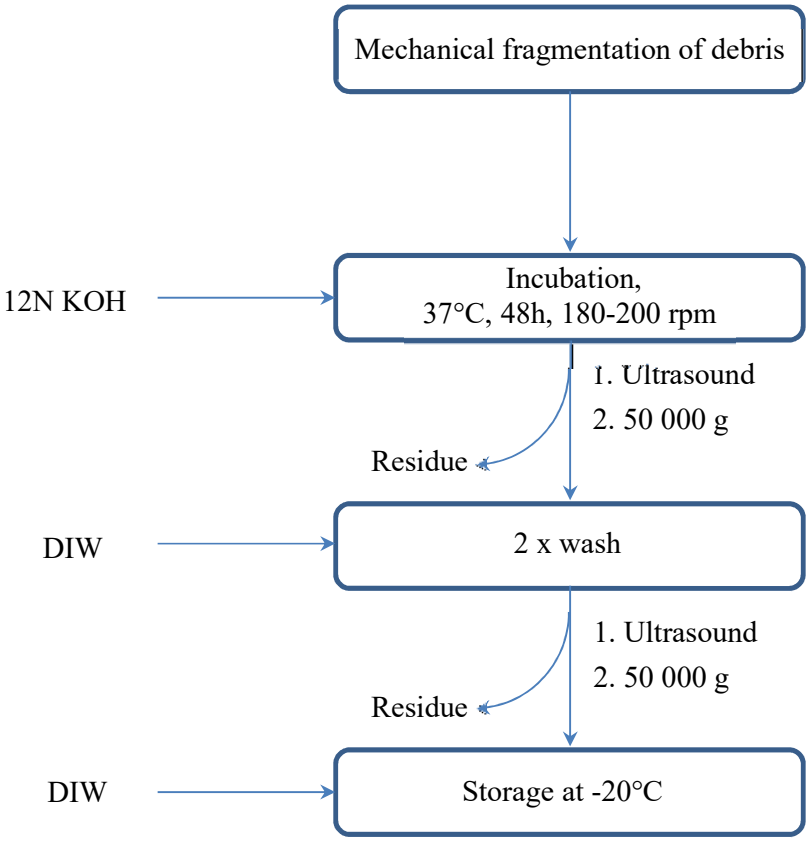

Figure 3.4 The steps of the alkaline digestion.

3.6 Electron Microscopy

SEM and EDX

The as-retrieved flakes were studied for morphology, microstructure and elemental distribution with a FEI Quanta 200 SEM, fitted with EDX and operated at 20 kV. The fragments of the flakes were loaded on the SEM stubs using carbon conductive adhesive tape. The micrographs were recorded at different magnifications to show the size and structural features, such as the roughness or smoothness of the flakes. The chemistry of the debris was checked with EDX analysis, operated in spectral mode at a working distance of 10 mm, which identified the elements present in the samples and confirmed the metallic or non-metallic nature of the flakes. The metal rich flakes were further investigated in mapping mode which collected the individual elemental maps. Two or more maps were overlapped and checked for the preferential elemental distribution across the surface of the flakes, using the EDAX software. Additionally, corrosion flakes from two retrievals (implant 1 and 9) were imaged using an Olympus SZX9 photomicroscope, for correlation with the SEM/EDX maps.

TEM and STEM imaging

The high-resolution characterisation of the digested debris was performed with a Cs probe-corrected JEOL ARM200F (cold-FEG) TEM/STEM operated at 200 kV and equipped with a 100 mm^2 Centurion EDX detector (Thermo-Fisher Scientific Inc., Madison, Wisconsin, USA) EELS. The microscope was operated in STEM mode and was used to record images only after the spherical aberrations were corrected and the Ronchigram (i.e. the projection image of a specimen found in the diffraction plane) was suitable for atomic resolution imaging. The calibration and adjustment of the electron beam was performed using a standard gold sample (i.e. gold nanoparticles ~5-10 nm, uniformly spread on a carbon coated copper grid).

Prior to investigation, the particle suspensions (100-200 µl) were thawed and subjected to 15 mins of ultrasound to break down the aggregates and homogenise the suspensions. To avoid particle oxidation, the grids were prepared shortly before the STEM analysis and were stored in a dry and cool place. Small volumes (3 µl) of the particle suspensions were loaded on carbon coated copper grids and blotted with lint free paper, to remove excess water. Prior to detailed investigation with STEM, the grids were checked with TEM (FEI Tecnai T12) to ensure a uniform particle loading and the number of suspension aliquots (3 µl each) used to load each grid was adjusted accordingly. At least 75 particles from 15 to 20 micrographs were imaged per sample and cleaning treatment in order to acquire enough data for the statistical analysis. Most of the STEM images were high-resolution micrographs of individual nanoparticles or small clusters of debris. Each sample included at least two low-resolution micrographs of large particle clusters, comprising 20-30 nanoparticles each. The Fast Fourier transform (FFT) images of the high-resolution micrographs were processed with Gatan Microscopy Suite (GMS3) and the measured d-spacing was correlated with the d-spacing of the

pristine Cr_2O_3 phase from the XRD database: PDF 00-006-0504 (PDF-2, 2012). The d-spacing was measured by drawing a perpendicular line between 10 parallel atomic planes on the particle micrograph, using GMS3. The line profile was generated by the software and indicated the distance between the 10 successive atomic planes which was then divided by 10 to obtain the distance between two successive planes, or d-spacing. **Figure 3.5** shows the GMS3 software interface and details the procedure used to measure the particle d-spacing.

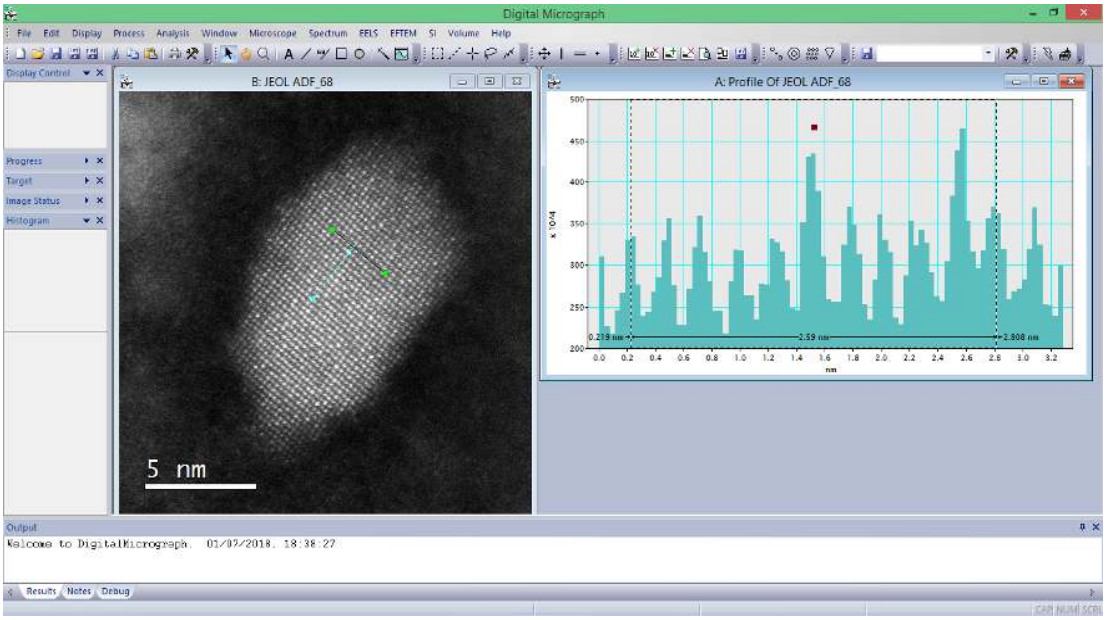

Figure 3.5 The interface of the GMS3 software showing the steps for the d-spacing measurement.

STEM and EDX

The composition of taper and stem debris was determined from the STEM and EDX analysis of individual nanoparticles and clusters, with the Cs probe-corrected JEOL ARM200F (cold-FEG) TEM/STEM operated at 200 kV. The EDX maps were processed using the NSS software (Thermo-Fisher Scientific Inc., Madison, Wisconsin USA) to reveal the metal rich regions. The average proportions of Cr, Co, Mo and other elements in individual particles and clusters were calculated using the Quant Results function in NSS. After the spectrum is generated and the individual peaks are identified either manually or automatically, the elements of interest can be selected to include in the quantification analysis. In the particular case shown in the screenshot in **Figure 3.6**, the elements selected for the Quant Results function are O, Cr, Co and Mo. The screenshot shows their extracted maps and exemplifies how the compositions and errors are calculated and reported. The comparison between the treatments and between debris from different wear sites was made based on the average compositions of all the particles from each sample and cleaning treatment. The composition study included 30 to 50 particles for the sample cleaned with the alkaline treatment (30 particles from taper 1, 50 particles from taper 2 and 34 particles from stem 9) and 16 to 60 particles for the samples

cleaned with the enzymatic treatment (16 particles from taper 1, 60 particles from taper 2 and 32 particles from stem 9).

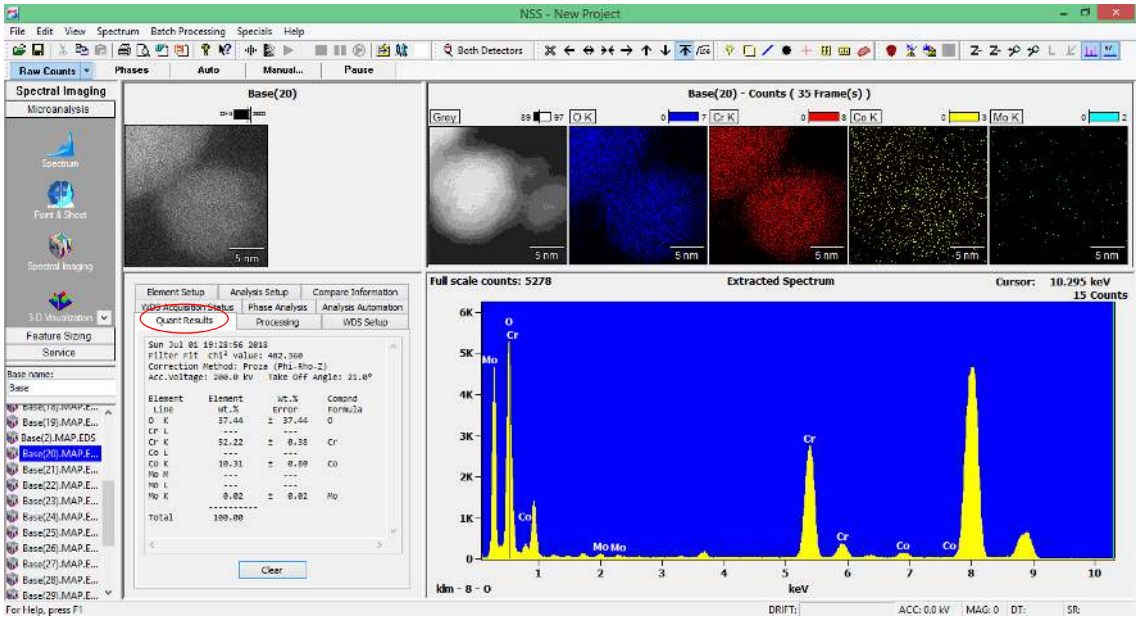

Figure 3.6 The interface of the NSS software showing how the elemental composition is generated using the Quant Results function.

STEM and EELS

EELS data was acquired with the Cs probe-corrected JEOL ARM200F (cold-FEG) TEM/STEM operated at 200 kV in STEM mode, by using an energy dispersion of 0.1 eV/channel and collection and convergence semi-angles of 40 and 30 mrad respectively, following the method described by De Castro et al[306]. Prior to undertaking the quantitative elemental analyses using GMS3, the EELS data was corrected for energy drift using the low-loss energy spectrum acquired on the same region of the corresponding core-loss energy spectrum. The high-loss energy spectrum was extracted from the corresponding EELS image, using the Picker Tool in GMS3. The EELS quantification function was further used for the automatic identification of the spectral peaks (peak ID), background removal and quantification. The software then generates a report of the quantification analysis, similar to that shown in **Figure 3.7** below.

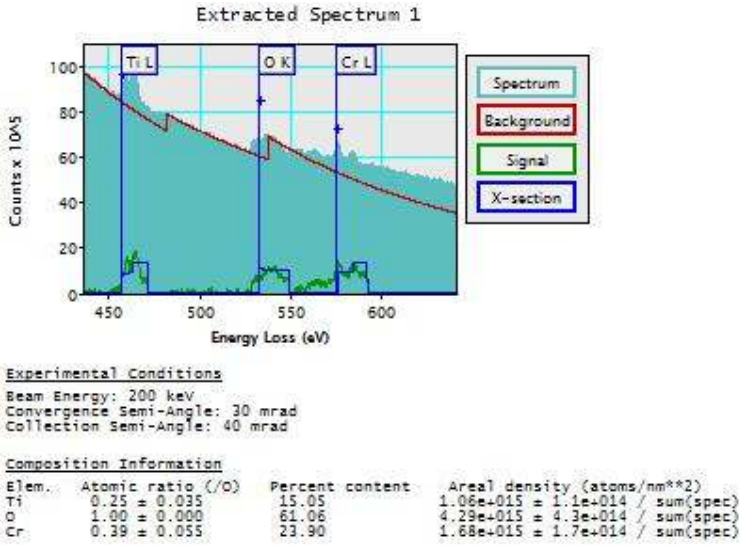

Figure 3.7 The quantification report provided by GMS3 after using the EELS quantification function. It shows the background removal function (red), the extracted signal (green), experimental conditions and the composition information.

TEM and SAED

Selected area electron diffraction (SAED) patterns of the samples and Cr_2O_3 standard (Fisher Scientific) were acquired with a JEOL JEM-2100 operated at 200 kV. The STEM micrographs and SAED data were processed using GMS3, as shown in **Figure 3.8**. The SAED patterns were opened with GMS3 and the distance between two opposite points on the diffraction circles was measured using the Cal Line tool (red circle). For each diffraction circle the diameter was measured at three different positions and the three measurements were averaged. The d-spacing of the planes responsible for generating the circles was calculated by dividing the average distance (i.e. 8.32 1/nm in **Figure 3.8**) by 2. This value (i.e. 4.16 1/nm) was then inverted to obtain the d-spacing in nm

(1/4.16=0.240 nm) which was further compared to the d-spacing of the possible phases (i.e. Cr_2O_3, TiO_2, CoO) using the XRD database (2017 International Centre for Diffraction Data). These phases were selected and prioritised based on the complementary information received from the TEM and EDX analysis and the stability of the various oxides of the major elements (such as Cr, Ti and Co).

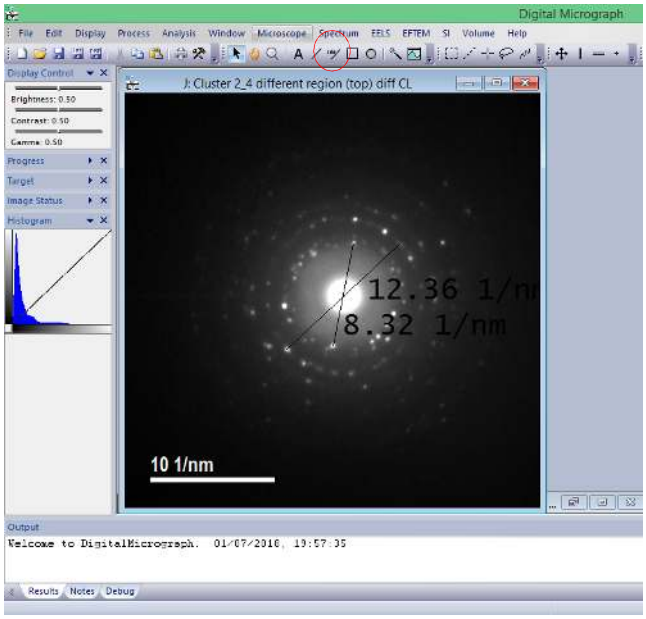

Figure 3.8 d-spacing calculation using GMS3.

3.7 STXM Analysis

The speciation analysis was performed using the STXM at beamline I08 at Diamond Light Source Ltd. (Harwell, Science and Innovation campus, UK). This beamline uses soft X-ray radiation in the 250-4200 eV photon energy range and can achieve a lateral resolution of ~20 nm, depending on the imaging mode. The samples were loaded on carbon coated TEM grids from aqueous solutions and were blotted to dry using lint-free paper. Prior to STXM and XANES analysis, the grids were checked using TEM (FEI Tecnai T12) and light microscopy, to ensure a uniform spread of the particles. Supplementary safety precautions were taken when handling the CrO_3 (Cr^{6+}) standard, which is a highly toxic and carcinogenic substance. The Cr XANES spectra were recorded over five energy regions, from 572 to 598 eV, covering the characteristic Cr $L_{2,3}$-edges, at an energy step of 1 eV for the first (572-576 eV) and last energy ranges (593-598 eV), and a step of 0.2 eV for the middle interval (576-593 eV). For Co speciation, the energy range covered the 770-805 eV interval and the steps varied across the sub regions and aimed to identify the finest spectral details of the characteristic peaks. The tails of the Co spectra (i.e. 770-777.7 and 803.5-805 eV) and the region between the peaks (786.5-794 eV) were recorded using an energy step of 0.5 eV, while for the peak regions (i.e. 778.1-786 and 795.1-803 eV) an energy step of 0.1 eV was used. The Ti XANES spectra were acquired

from 450 to 480 eV. The first (450-457 eV) and the last (469.5-480 eV) energy ranges were recorded at an energy step of 0.5 eV, and the peaks region (457.1-469 eV) was acquired using a higher energy resolution of 0.1 eV. The characteristic XANES spectra of the Co and Cr standards were compared to the spectra of the standard Cr_2O_3 (Cr^{3+}), $CrPO_4$ (Cr^{3+}), CrO_3 (Cr^{6+}), CoO (Co^{2+}), $Co(OH)_2$ (Co^{2+}) and $Co_3(PO_4)_2$ (Co^{2+}) samples (Fischer Scientific), which were also used for the spectral match using linear combination fitting in Athena 0.9.25. The spectra of the Ti rich nanoparticles were matched using TiO and TiO_2 spectra, reported in the literature.

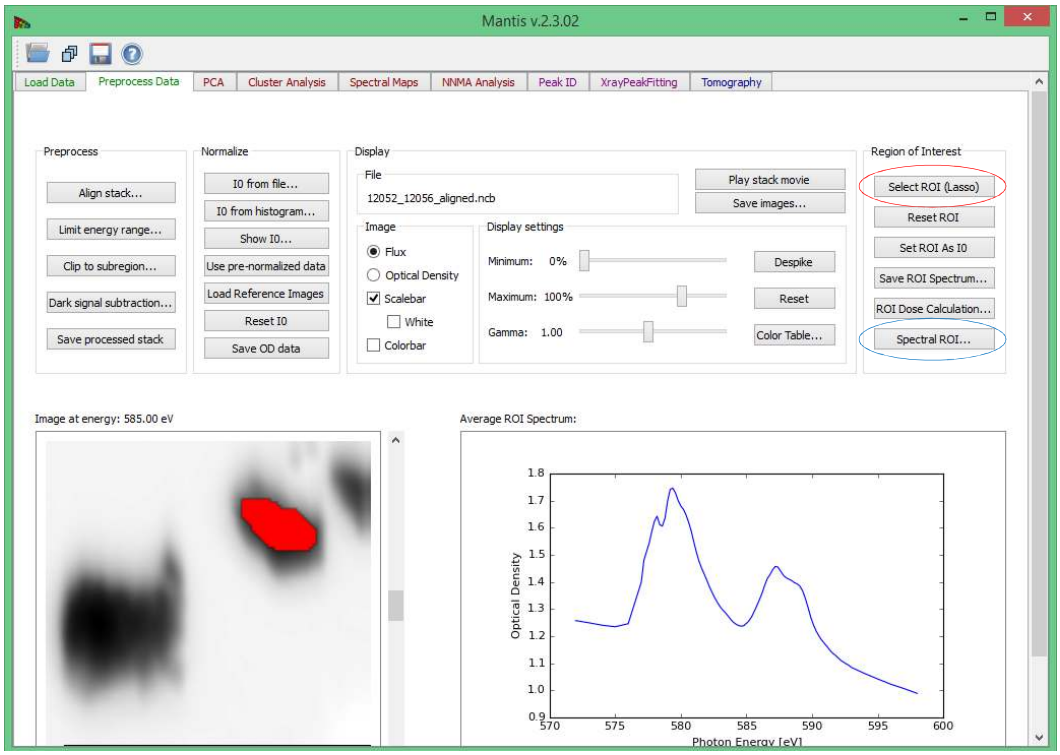

Figure 3.9 Mantis v2.3.03 interface and the main functions used to extract the XANES spectra.

The XANES spectra were aligned and processed using Mantis v2.3.02. Where more than one particle was measured, the spectra of each individual particle was extracted by selecting a region of interest (ROI) (red circle in **Figure 3.9**). After confirming that all the particles have the same spectral features, which means they are identical species, other functions, such as PCA or Cluster Analysis were used to process the whole cluster. **Figure 3.9** shows a screenshot of Mantis v2.3.02 in which a region of interest was selected (marked by the red spot) and the corresponding XANES spectra was displayed. Other functions are localised on the top bar of the software and can be used to distinguish between regions with different spectral properties (e.g. for coated samples or aggregates). The Spectral ROI function (blue circle) can be used to check the spectrum in different regions of the particle/cluster. The spectra generated by either of these functions can be exported and processed using Origin Lab or Microsoft Office Excel. In this study, Origin Lab was used to process and integrate the peaks after adjusting the baseline. The software was also used to remove the energy

points responsible for spectral features corresponding to measurement glitches (such as spikes which were outside the absorption peaks). The processed spectra were then fitted with the spectra of the standard materials, where available, using Athena Ltd. Software, or were compared to the published spectral data (for TiO_2). The species were identified based on the positions and features of the absorption peaks and the relative intensity of the main peaks.

3.8 Statistical Analysis

Particle size distribution (PSD) and morphological characterisation was performed according to BS ISO 17853/2011. Gatan Microscopy Suite (GMS3) software was used to measure the maximum dimension (d_{max} or length) and the maximum orthogonal dimension (d_{min} or width), defined as the longest straight line between two opposite points on the particle outline and the longest orthogonal line respectively (**Figure 3.10**). The maximum diameter (d_{max}) was used to define the PSD, while d_{max}/d_{min} ratio value, hereafter referred to as the aspect ratio (AR), was used for the morphological characterisation. The particles were classified as round for $1 \leq AR < 1.5$, oval for $1.5 \leq AR < 2.5$ and needle shaped for $AR \geq 2.5$. **Figure 3.10** shows examples of round, oval and needle-like particles and shows how d_{max} and d_{min} are determined.

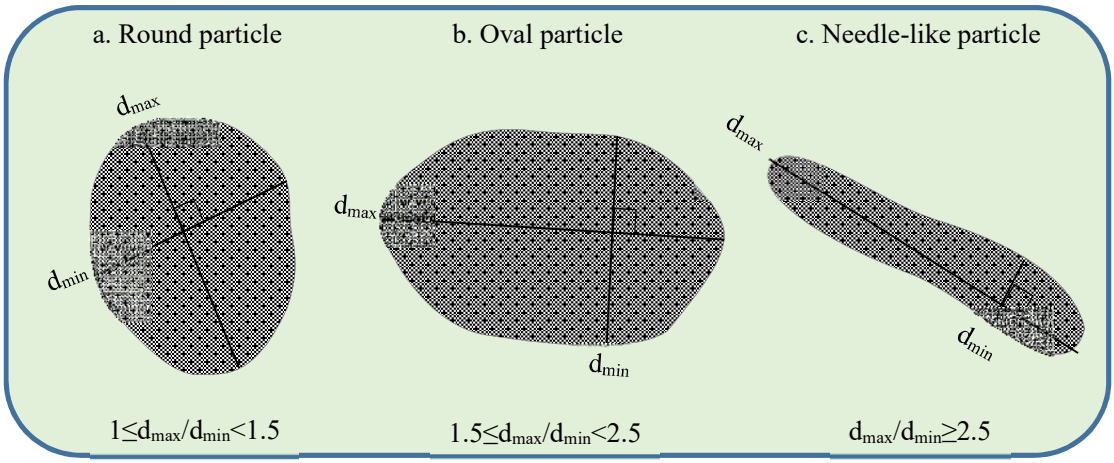

Figure 3.10 Schematic representation of round, oval and needle-shaped particles, showing the relation between d_{min} and d_{max}, and how their ratio dictates the morphological category.

The statistical significance of the data set (comparison of the mean sizes) was verified using the null-hypothesis two-sample t-test in Origin Lab, at a level of confidence of 0.05. None of the size distributions were normally distributed, but the compared data sets had similar asymmetry which allowed the statistical comparison using t-test. The selection of the appropriate t-test was based on the results of the f-test for each compared data sets (equal or non-equal variance assumed). The repeatability of the PSD was checked by performing three consecutive measurements for one of the three samples. The results of the three independent measurements were not statistically different ($p > 0.3$).

Chapter 4 Results

4.1 Investigation of As-Retrieved Wear and Corrosion Flakes

4.1.1 Composition of Debris – ICP-MS Analysis

The elemental compositions of debris released from tapers and/or cement-stem interface are reported in **Table 4.1**. The limited amount of debris originating from the taper junctions and/or cemented stems of retrievals 7, 8 and 12 prevented analysis and hence ICP-MS data was not available for all 12 samples. On the other hand, retrieval 1 showed visible signs of wear and corrosion damage with deposits of debris around the base of the trunnion, inside the bore of the head and at the cement-stem interface. From some retrievals more than one flakes from the wear sites were available for investigation.

Table 4.1 Composition of as-retrieved debris from tapers and cement-stem interfaces.

Implant	Wear site	%Cr	%Co	%Mo	%Ti	%Metal
1	Taper	5.9	7.8	6.1	-	20.0
	Bore	2.2	0.5	0.5	-	3.3
	Stem	14.5	2.3	2.0	-	19.1
2	Taper	29.2	5.6	3.1	-	38.0
	Stem	10.1	2.3	1.5	-	14.3
3	Taper	12.4	10.6	1.4	-	24.9
4	Taper (flake 1)	7.2	3.7	1.0	-	12.0
	Taper (flake 2)	0.3	23.5	-	-	24.1
5	Taper	8.9	0.2	9.9	1.6	20.7
6	Taper	8.4	3.7	1.3	0.2	13.7
7	Taper	Data not available				
8	Taper	Data not available				
9	Stem	20.5	3.2	2.9	-	27.0
10	Stem	15.9	3.6	0.8	-	20.5
11	Stem	6.8	1.6	0.2	-	8.7
12	Stem	Data not available				

The ICP-MS analysis of the wear and corrosion flakes listed in **Table 4.1** revealed the major elements that make up the CoCrMo alloy. In none of the investigated flakes the proportions of Cr, Co and Mo matched the composition of the bulk alloy (~65% Co, 29% Cr and 6% Mo). In most of the cases, Co

was the second most abundant element in the retrieved flakes, after Cr. Debris from taper 1 contained similar proportions of Cr, Co and Mo, of which Co was the most abundant (7.8%). From implant 4, two different types of wear and corrosion products were available for the ICP-MS analysis. Flake 1 was characterised by a black and flaky appearance, and contained less metals (12%) than flake 2 (24.1%), with Cr being the most abundant (7.2%). The second flake (Flake 2) comprised mainly Co (23.5%), with minimal amounts of Cr (0.3%), and resembled a precipitate with a light-pink colouration. Other samples (flakes from taper 1 and taper 3) consisted of mixed black and light-pink fragments which could not be separated for distinct analyses. The ICP-MS characterisation of debris from around the base of the trunnion and debris from inside the bore of the head of implant 1 revealed different amounts of metals and proportions of Cr, Co and Mo.

The ICP-MS analysis also identified Ti in the flakes released from the mixed material taper junctions, such as taper 5 and 6, which consisted of CoCrMo heads matched with Ti stems. The amount of Ti (1.6% and 0.2% respectively), however, was small compared to the amount of debris released from the opposite CoCrMo interface.

The proportions of all metals in the investigated samples were less than 40% mass and varied from 3.3% to 38.0% (w/w). The rest of the flakes' mass was represented by organic material which originated from the body. The average metal content for taper and stem debris was 19.6% and 17.9% respectively, and the results were not statistically different (p>0. 5).

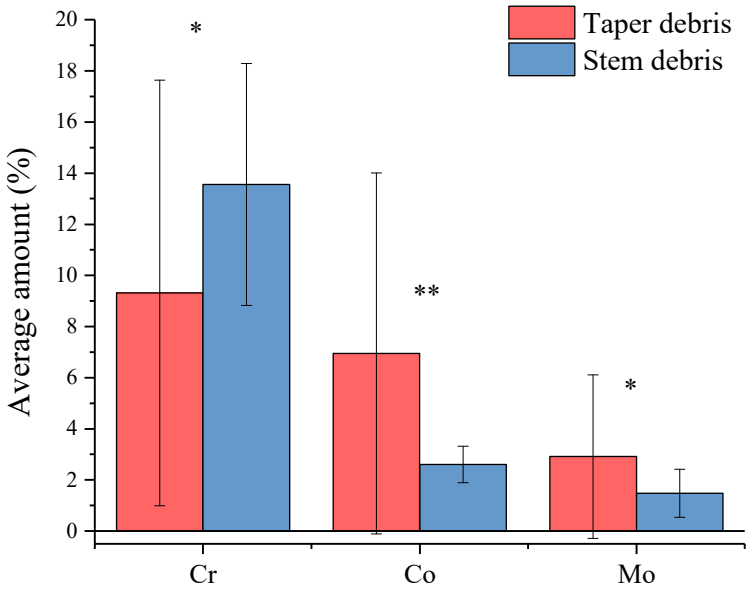

Figure 4.1 The comparison between the composition of debris from tapers (red) and cement-stem interface (blue), which were not statistically different (*p>0.3; **p>0.2).

The comparison between the proportions of Co, Cr and Mo from tapers and stems debris is shown in **Figure 4.1** and reveals more Cr and less Co or Mo in the flakes collected from the stems than in the flakes retrieved from around the tapers. The statistical analysis, however, showed no significant differences between the amounts of Co, Cr and Mo in debris from tapers and cement-stem interfaces ($p>0.3$ for Cr, $p>0.2$ for Co and $p>0.3$ for Mo).

Summary

The ICP-MS analysis demonstrated the organo-metallic nature of the wear and corrosion flakes released *in vivo* from the tapers and cement-stem interface. Regardless of the origin of debris, the most abundant elements were Cr, Co and Mo, and traces of Ti released from the mixed material taper junctions. The analyses, however, did not find statistically significant differences between the compositions and total amounts of metal in debris from tapers and cement-stem interface.

4.1.2 Distribution of Elements across the Surface of the Flakes

Fragments of the wear and corrosion flakes released from two tapers (taper 1 and taper 2) and one cement-stem interface (stem 10) were characterised by SEM and EDX analysis. The investigation revealed the presence of Co, Cr and Mo, mixed with non-metallic species, such as C, P and Ca, which supported the results of the ICP-MS analysis, confirming once again the organo-metallic nature of the wear and corrosion flakes. The SEM and EDX mapping also provided visual information about the distribution of the elements across the surface of the flakes.

The EDX maps of the main elements found in a fragment of the flake retrieved from taper 1 are shown in **Figure 4.2**. The distributions of Co, Cr and Mo do not overlap, indicating that the metal debris does not originate from the bulk CoCrMo substrate. There is, however, a good match between the Cr and Mo distributions which are mainly localised towards the right and left extremities of the flake and correspond to a metallic like region on the associated photomicrograph, shown in **Figure 4.3 b**. Cobalt (Co) is mainly distributed centrally on the flake's surface and overlaps with the P map. The Co and P rich regions match the pink patches in **Figure 4.3 b** and are similar in appearance to the Co rich pink flakes investigated by ICP-MS analysis. The presence of P and Co ions in the same proximity suggests the existence of $Co_3(PO_4)_2$ in debris released from the secondary interfaces in hip replacements. The EDX mapping also identified a Ca rich region, which partially matches the P distribution and corresponds to a white patch on the flake's photomicrograph in **Figure 4.3 b**. The white coloration suggests the presence of $Ca_3(PO_4)_2$, which could have formed by precipitation at the taper interface. The presence of all these species in the composition of the wear and corrosion flake once again emphasises their organo-metallic nature.

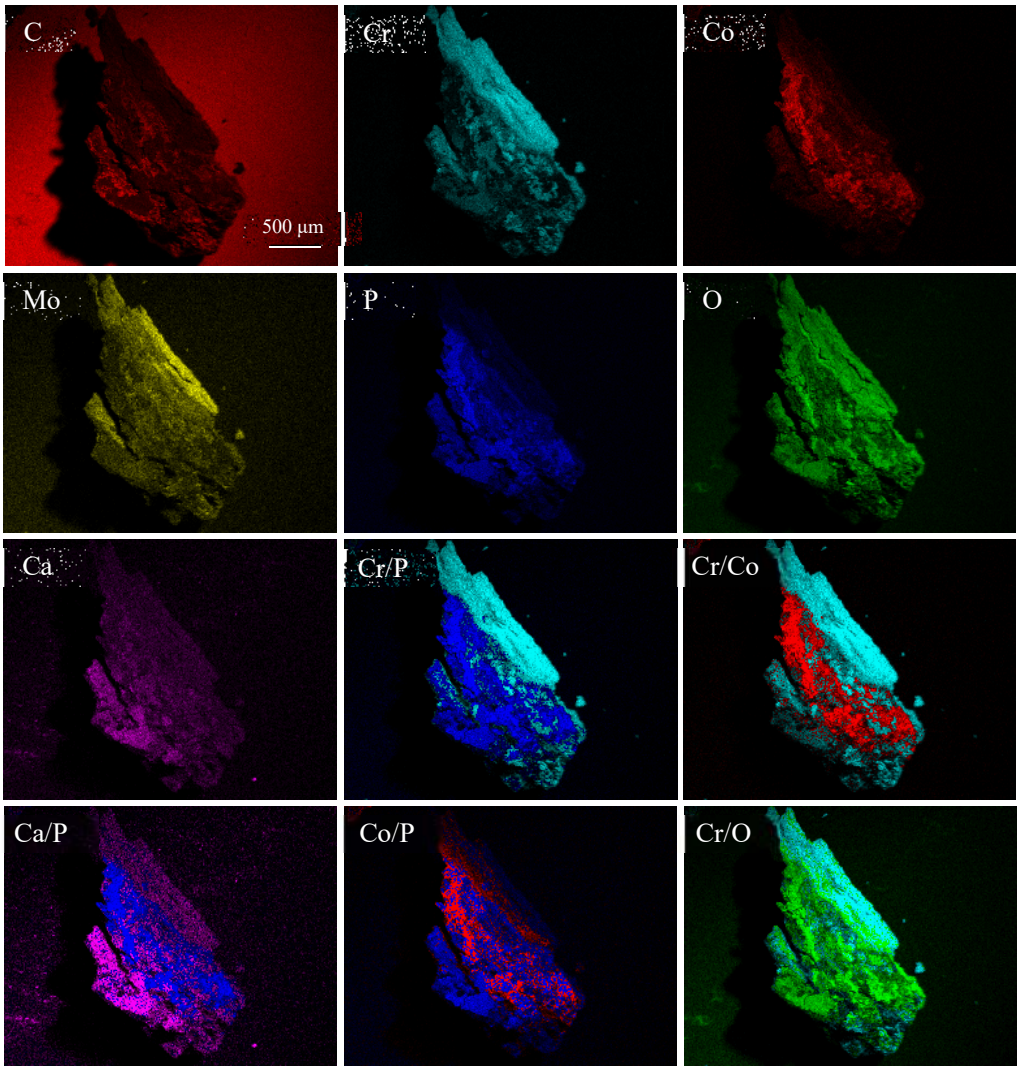

Figure 4.2 The SEM/EDX maps of a fragment of wear and corrosion debris from taper 1, which show the preferential distributions of elements across the flake's surface. The Co map overlaps the P map, whereas Cr and Mo are co-localised in the O rich region of the top right side of the flake. Ca partially overlaps the O and P maps in the left side of the micrograph.

The SEM and EDX characterisation of another fragment of flake from taper 1 and two fragments of flakes from taper 2, showed similar elemental distributions (see Appendix A). In general, a preferential distribution of the elements was observed, which resulted in unmatched Cr and Co maps, and P spread across the entire flakes, with more prominent distributions in the Co rich regions.

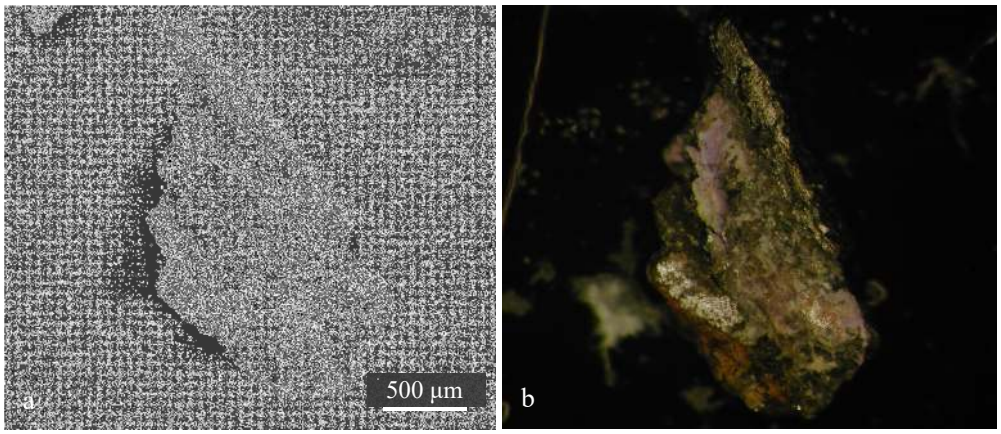

Figure 4.3 The SEM image (a) and the corresponding photomicrograph (b) of the wear and corrosion flake retrieved from taper 1. The pink region on the photomicrograph corresponds to the Co and P rich regions on the SEM and EDX maps in Figure 4.2. Similarly, the metallic regions on the top right side of the photomicrograph represents the Cr, Mo and O rich regions on the EDX maps. The white patch on the left side of the flake matched the distribution of Ca, which was co-localised with P and O.

Compositional variability between samples, such as flakes from different retrievals or different flakes from the same wear site, was observed in this study. In **Figure 4.4**, the SEM and EDX mapping of a fragment of debris released from stem 10 revealed intense C, P and O distributions, and weak and localised Cr and Co patches. In this flake, the organic phase was dominant over the metallic component, represented by the Cr, Co and Mo distributions. The Cr signal originated from the left margin of the flake and the randomly distributed Co did not match the Cr localization. The Mo map matched the Cr rich region, and Ca showed a weak map with small areas corresponding to some of the P rich patches.

Another fragment of debris from stem 10 is shown in **Figure 4.5** and comprises more Cr, Mo, P and Ca, distributed across the entire flake, and small patches of Co intense maps. The metallic species represented the major part of the organo-metallic composite and were dominate by Cr. Like the other fragment of debris from stem 10, shown in **Figure 4.4**, the Co rich patches matched the P rich areas. Also, the P distribution partially overlapped the Cr map and suggested the possibility that $CrPO_4$ was among the species comprising the flake. The maps in **Figure 4.4** and **4.5** emphasised the compositional variability of the wear and corrosion products and demonstrated that different results can be obtained from the analysis of different flakes/fragments from the same origin.

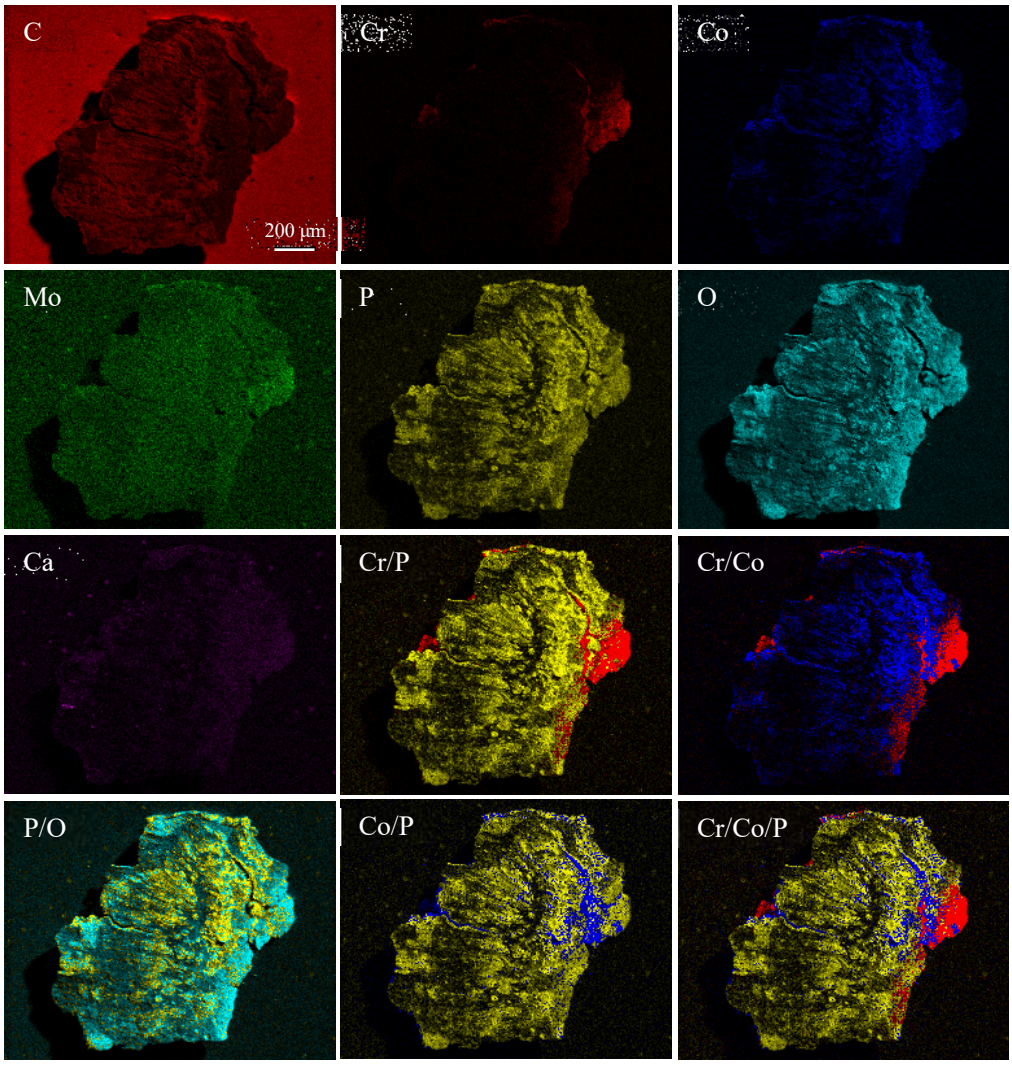

Figure 4.4 The SEM and EDX maps of a fragment of the wear and corrosion flake retrieved from stem 10, showing the preferential distributions of the elements across the flake's surface. In this case, Cr is localised on the right side of the flake, partially overlapping the O and P maps, while Co distribution matches the P and O rich regions. Both Co and Cr maps, however, are weak compared to the P and P maps. Small regions of Ca rich regions can be observed on the left side of the flake, partially matching the P map.

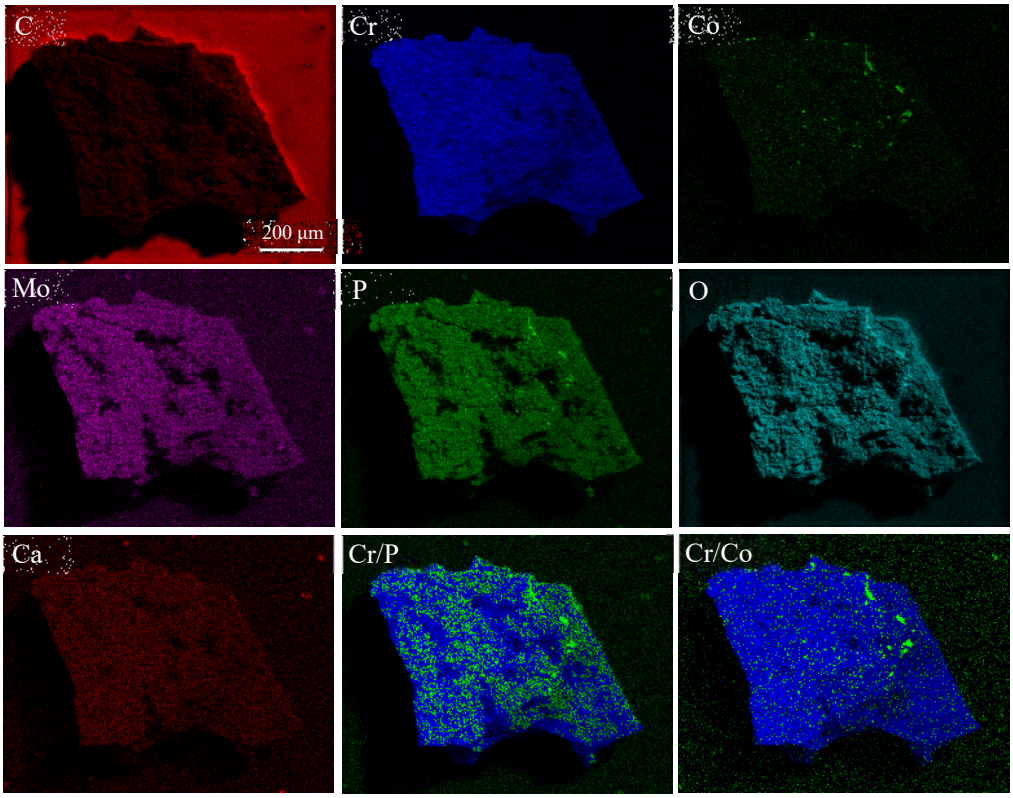

Figure 4.5 The SEM and EDX maps of another fragment of the wear and corrosion flake retrieved from stem 10, which shows intense Cr, Mo, P and O maps, and weak and highly localised Co distribution, represented by the bright green spots on the corresponding EDX map.

Summary

The SEM and EDX investigation demonstrated the organo-metallic nature of the wear and corrosion flakes, in addition to the results from the ICP-MS analysis. The elemental distributions suggested the formation of different species, resulting from the wear and corrosion processes, which were mixed at the interface. The elemental maps indicated the presence of a Cr, Mo, O and P rich phase, potentially in the form of oxides or phosphates, a Co and P pink precipitate, likely in the form of $Co_3(PO_4)_2$ and a white Ca and P rich precipitate, resembling $Ca_3(PO_4)_2$. The investigation, however, provided information about the distribution of elements at the surface of the flakes, which could be different from the composition below the surface.

4.2 The in-depth Characterisation of Taper Debris

4.2.1 Alkaline treatment

The wear and corrosion debris released from five mixed and matched material taper junctions (tapers 1-5 in **Table 4.1**, section 4.1.1.) were subjected to an alkaline treatment, which aimed to fragment the organo-metallic composites, to reveal the structural details and the building blocks that comprise the large flakes. The STEM and EDX investigation of the partially digested flakes revealed clusters of Cr and O rich nanoparticles and traces of Co, Mo and Ca. The morphology and elemental distributions of a partially digested fragment of debris released from taper 1 are shown in **Figure 4.6**. The strong Cr and O maps suggested that Cr and O were the most abundant species, while Mo, Co and Ca were only present as trace elements. The resolution at which the images were obtained made the exact localisation of the elements inside or outside the particles difficult to assess.

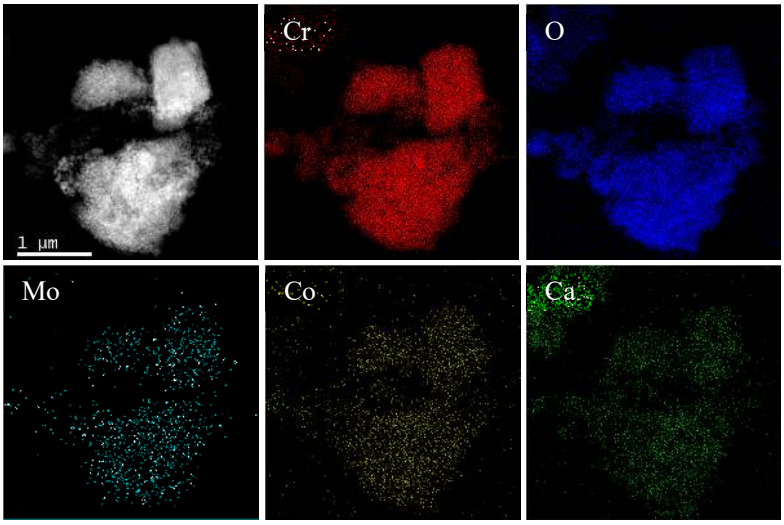

Figure 4.6 The high-angle annular dark field (HAADF)-STEM micrograph and EDX maps of a partially digested flake released from taper 1, showing the distribution of Cr, Co, O, Mo and Ca.

At higher magnification, the STEM and EDX investigation of the cluster of debris shown in **Figure 4.6**, revealed more structural details and provided a better understanding of the elemental distributions. The STEM micrograph and corresponding EDX maps are shown in **Figure 4.7** and reveal the presence of Cr, Co, Mo, O and P, distributed across the aggregate's surface. The Cr, Mo and O maps matched the bright areas in the STEM image, which corresponded to the nanoparticles. In contrast, Co and P are localised in the surrounding organo-metallic matrix, outside the particles, and suggests that Co was present in an ionic form (either bound to biomolecules or precipitated as phosphate) rather than in a solid metallic state. The corresponding map, however, showed that part of Cr was also present in the less dense surrounding matrix, potentially in a dissolved ionic form.

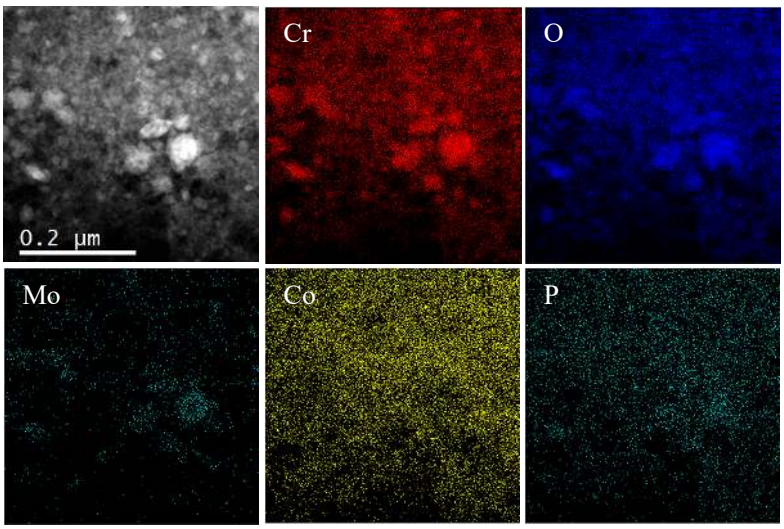

Figure 4.7 The high-resolution HAADF-STEM micrograph and EDX maps of the partially digested flake in Figure 4.6, showing Cr and O rich particles, surrounded by an organo-metallic phase with traces of Co and P.

A closer look to the clusters that comprised the partially digested flakes provided evidence of the organic matrix which holds the particles together. The STEM image and EDX maps, shown in **Figure 4.8**, revealed Cr and O rich nanoparticles surrounded by a Ca rich bio-corona, and traces of Co localised outside the particles. The results showed that Co was not part of the particulate debris and was distributed in the surrounding phase, probably in a dissolved/ionic form.

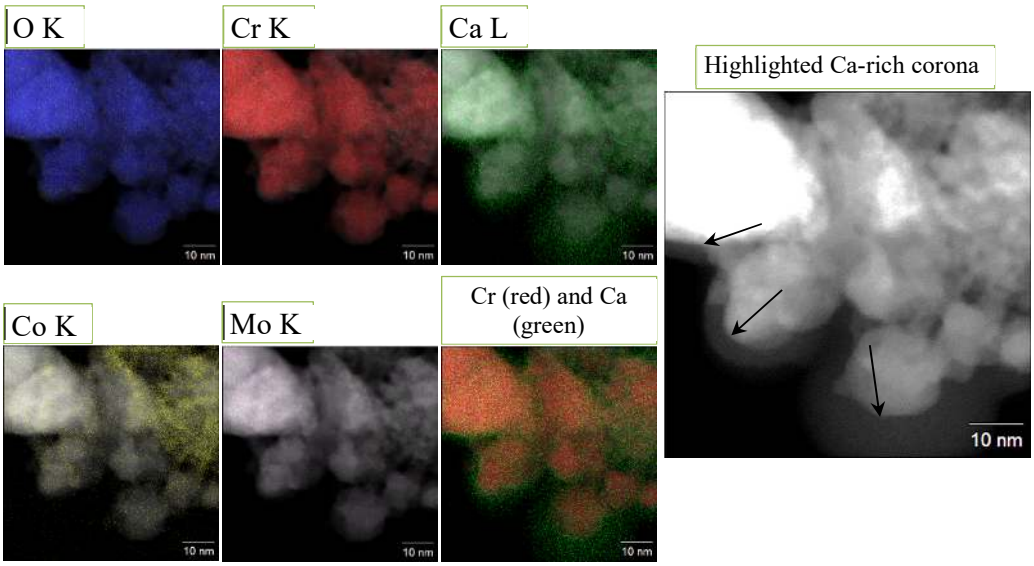

Figure 4.8 The high-resolution HAADF-STEM micrograph and EDX maps showing the presence of a Ca-rich bio corona around the Cr and O rich nanoparticles. Co is localised outside the particles, potentially in a dissolved/ionic form.

To enable a detailed characterisation of the metal nanoparticles that comprised the aggregates and the micron-sized wear and corrosion flakes, the fragments were subjected to a complete digestion, which provided clean particulate debris, released from the surrounding matrix. The high-resolution micrographs, shown in **Figure 4.9**, revealed clusters and individual crystalline nanoparticles (see the Fast Fourier Transform patters shown as insets in **Figure 4.9**), which originated from the CoCrMo tapers from retrievals 1, 2 and 3. The low-resolution images (left column) showed clusters of nanoparticles which, in some cases, were only partially released from the surrounding matrix. The treatment, however, provided numerous clean and well-separated nanoparticles, which revealed the structural, morphological and compositional details of the smallest building blocks that made up the wear and corrosion flakes from the CoCrMo taper interface.

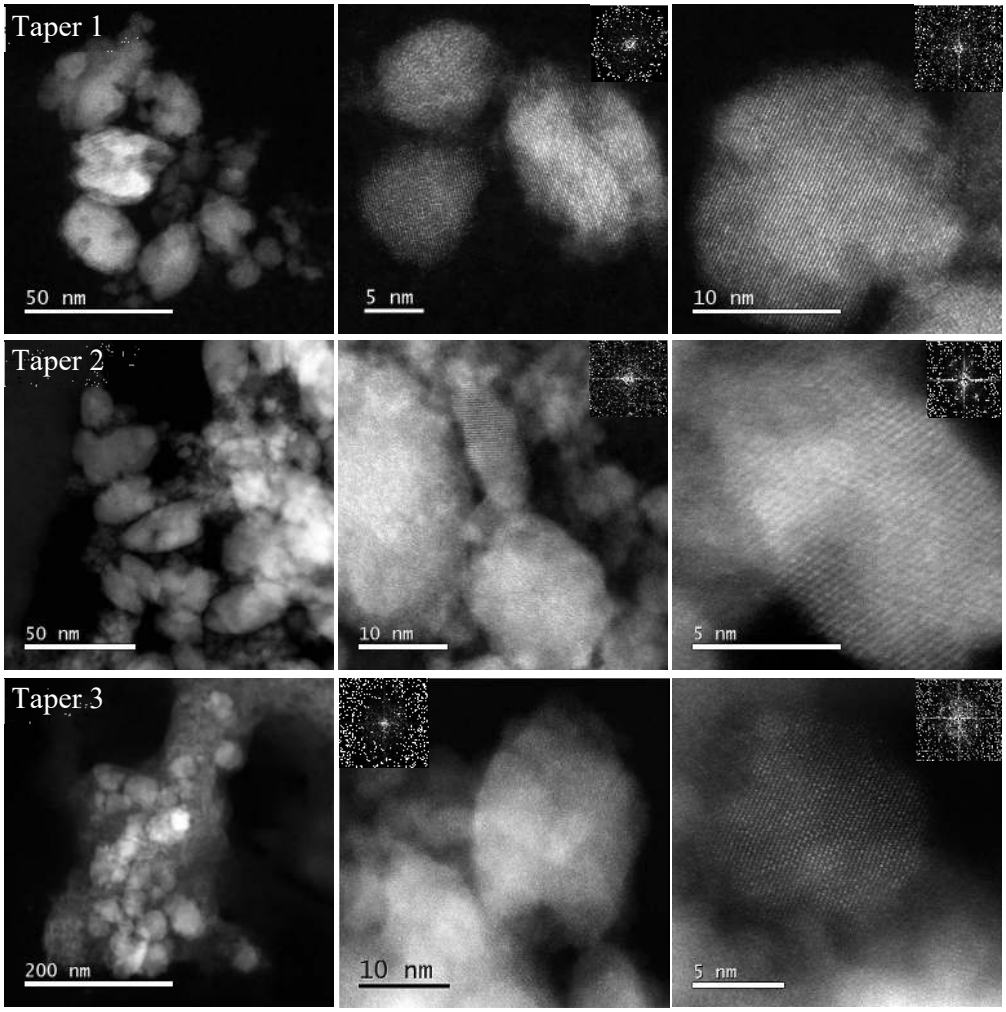

Figure 4.9 The HAADF-STEM micrographs of representative nanoparticles released *in vivo* from taper 1, 2 and 3 and cleaned with the alkaline treatment. The treatment revealed clusters of crystalline nanoparticles completely or partially removed from the surrounding bio-corona.

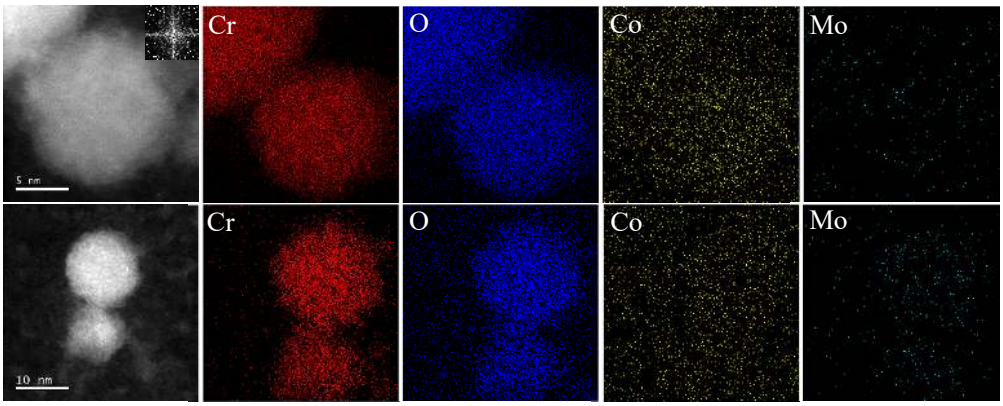

Figure 4.10 The HAADF-STEM micrograph and EDX maps of representative particles released from taper 1 and cleaned with the alkaline treatment. The composition analysis revealed 81.2% Cr (±0.6), 18.8% Co (±1.4) and 0.4% Mo (±0.4) for the particle in the top micrograph.

The EDX characterisation of the cleaned debris revealed Cr and O rich nanoparticles, with traces of Co and Mo. The elemental maps and composition analyses of two representative clusters of cleaned debris released from taper 1 are shown in **Figure 4.10**. The quantification analyses were performed after the exclusion of O, which although present in the sample, was associated with high measurement errors (37.44% (±37.44)). The nanoparticle shown in the top row is crystalline and contained more Cr (81.2% (±0.6) vs 73.12% (±1.2)) and less Co (18.8% (±1.4) vs 25.9 (±3.8)) than the amorphous particles in the bottom micrograph. Cr remains, however, the dominant element regardless of the structure of the nano-sized debris and the results suggested that the nanoparticles are Cr oxides, with traces of Co and Mo.

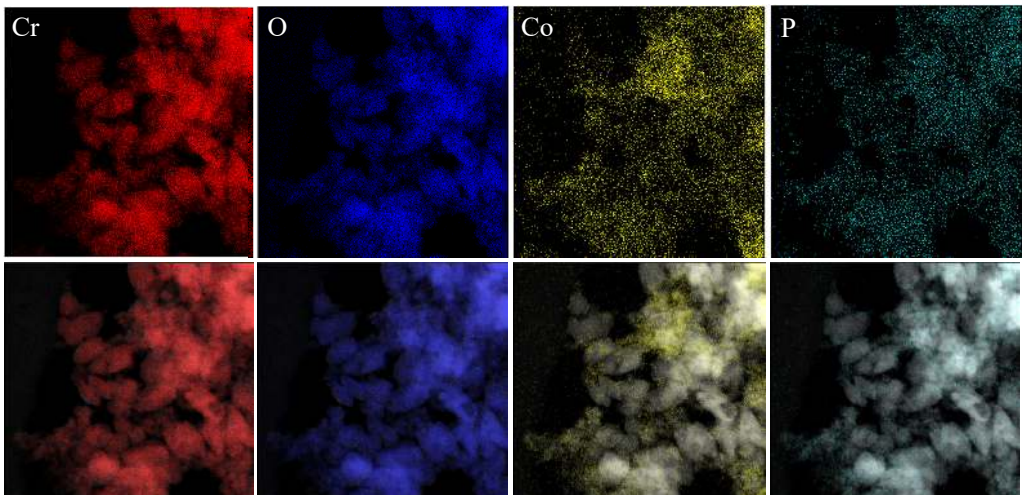

Figure 4.11 The HAADF-STEM micrograph and EDX maps of a cluster of particles released from taper 2 and cleaned with the alkaline treatment. The EDX maps show the particles are made of Cr and O, while Co and P are co-localised in the surrounding organic matrix.

The EDX maps of one cluster released from taper 2 are shown in **Figure 4.11**. The Cr and O maps matched with the nanoparticles, whereas Co and P showed a preferential distribution in regions outside the particles, which corresponded to a less electron dense phase. In this cluster, Mo provided a weak and random map and therefore was not included in the figure.

All the results from the STEM and EDX investigation showed reliable evidence that the metal debris released from taper junctions was Cr oxide, while Co was mainly localised in the proximity of the particles and together with P and Ca, were parts of the bio-corona. The amounts of Mo in these samples were low and it was mainly distributed within the particles' boundaries, as a trace element.

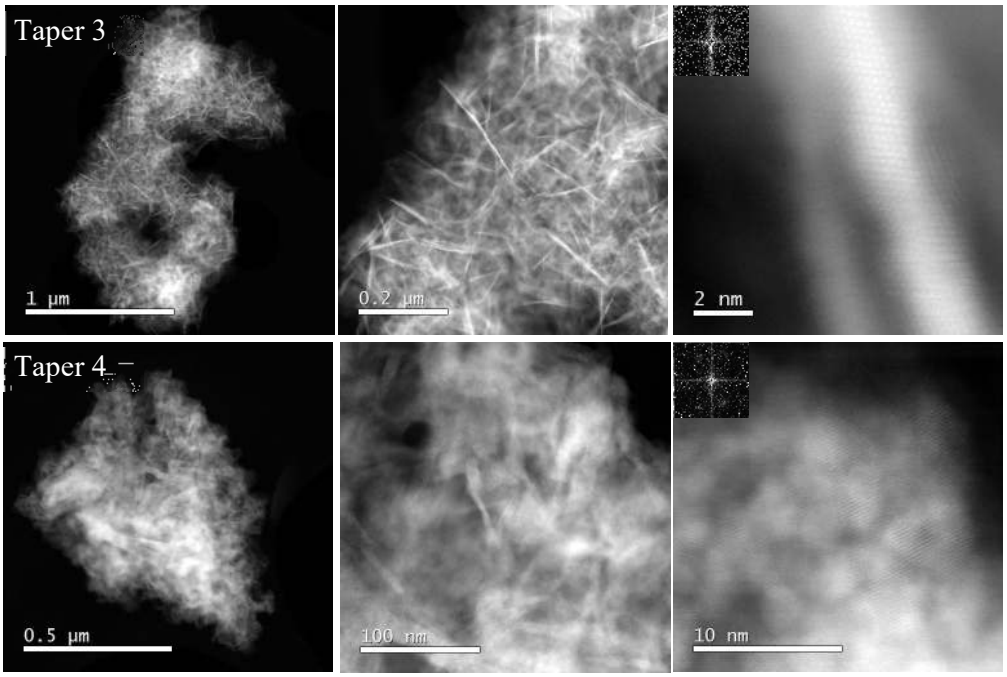

Figure 4.12 The HAADF-STEM micrographs of needle-shaped debris released from taper 3 and taper 4. The FFT patterns suggest these particles are crystalline structures.

Besides the round Cr rich particles, the digestion of debris from taper 3 revealed large aggregates of needle-like structures, which are shown in **Figure 4.12**. Similar debris resulted after the alkaline digestion of the wear and corrosion flakes released from taper 4, also shown in **Figure 4.12**. In this sample, however, the round and oval nanoparticles, reported with debris from tapers 1-4 could not be found. The high-resolution micrographs of the needle like debris and the corresponding FFT patterns in **Figure 4.12** (see insets) suggested that these structures were crystalline. The morphology and size of the crystalline needle-shaped debris from taper 3 were different from those of the debris which comprised the wear and corrosion products from taper 4, although some needle like structures were also present in the latter sample. The STEM and EDX characterisation revealed the composition of the needle-shaped debris, which contained mainly Co (49.2% (±0.2)) and elements of biological origin, such as Mg, Ca and P (26.6% (±0.4), 14.2% (±0.1) and 3.0% (±0.2) respectively). The composition analysis and the Co and Cr maps are shown in **Figure 4.13**. The Co distribution is well

matched to the needle-shaped debris, whereas Cr (4.0% (±0.07)) was only present in a region which did not have a corresponding morphology in the STEM micrograph. The round shape of the Cr rich map indicated the presence of an individual particle or a cluster of nano-sized debris entrapped in the Co rich net of needle-like structures.

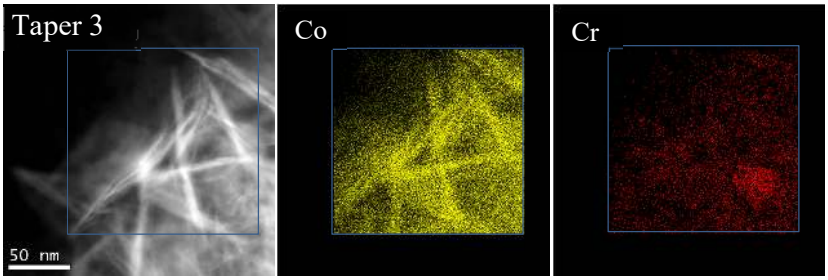

Figure 4.13 The HAADF-STEM micrograph and EDX maps of a cluster of Co rich needle-like debris from taper 3. The composition analysis showed 49.2% Co (±0.2), 4.0% Cr (±0.07), 26.6% Mg (±0.4), 14.2% Ca (±0.1) and 3.0% P (±0.2).

The presence of both Cr rich nanoparticles and Co needle-like structures in debris released from taper 3 was confirmed by the STEM micrographs and EDX maps in **Figure 4.14**. The low-resolution image showed an aggregate of round Cr and O rich particles, surrounded by a cluster of Co and K rich needles at the bottom, and a less electron dense diffuse mass at the top and left side of the micrograph.

Potassium (K) originates from the alkaline treatment (12N KOH) and it is distributed in the same regions where Co is localised, suggesting that these structures have an organic component which makes them susceptible to the chemical attack. The EDX analysis of the Cr rich region confirmed the presence of all the main elements of the CoCrMo alloy, of which Cr was the most abundant (61.9% (±0.9)). In contrast, the composition of the needle-shaped debris showed predominantly Co (87.9% (±1.9)), with less Cr (12.1% (±0.6)) and none of Mo. The quantification results of both the Cr rich region (1) and Co rich needle like debris (2) are shown in **Table 4.2**.

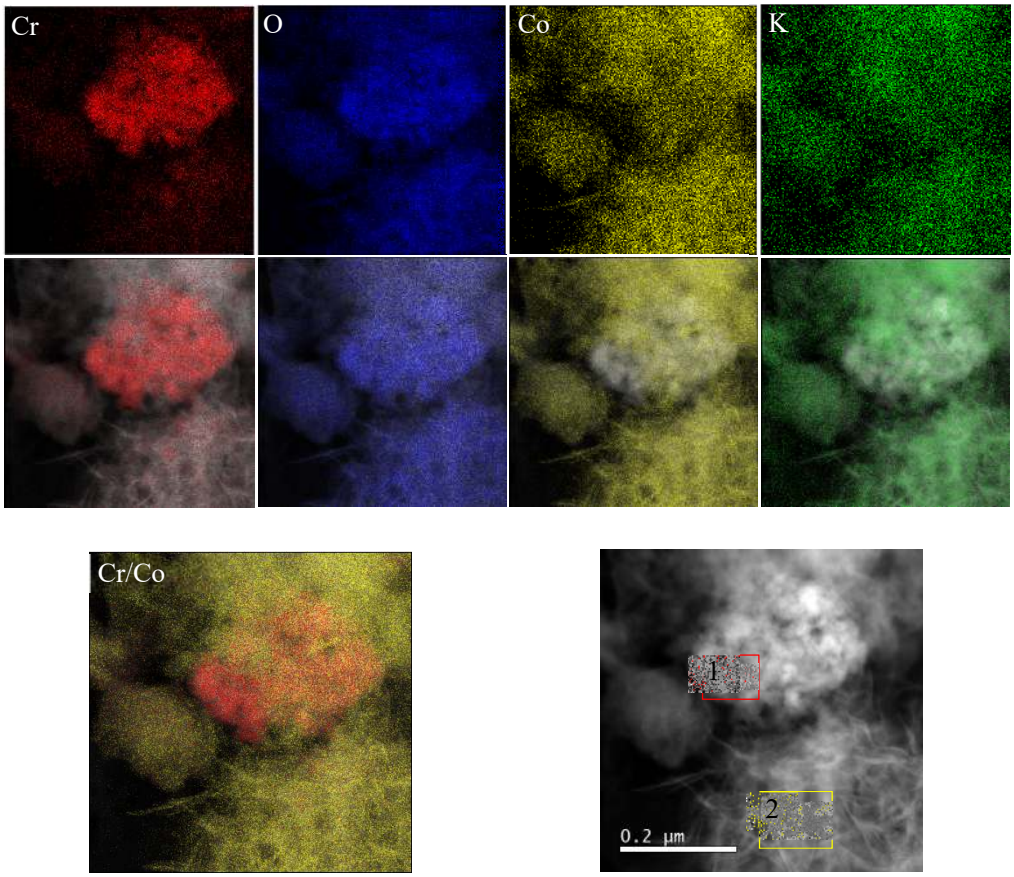

Figure 4.14 The HAADF-STEM micrograph and EDX maps of a cluster of Cr rich nanoparticles and Co rich needle-like debris from taper 3.

Table 4.2 The results of the quantitative EDX analysis, showing the composition of the regions 1 and 2 in Figure 4.14, rich in Cr and Co respectively.

EDX region 1		
Element	Element Wt. %	Wt. % error
Cr	61.9	0.9
Co	37.9	2.0
Mo	0.2	0.2

EDX region 2		
Element	Element Wt. %	Wt. % error
Cr	12.1	0.6
Co	87.9	1.9
Mo	0.0	0.0

The spatial separation of the Co and Cr rich debris and the differences in their morphologies was further emphasised by the STEM micrograph in **Figure 4.15**. The variations of the Cr and Co concentrations across the needle-like and round nano-sized debris respectively was illustrated by the EDX line profiles in **Figure 4.15** and confirmed the Co enrichment of the needle-like net (94.7% Co (±1.1) and 5.3% Cr (±0.3)), while Cr was the major element in the cluster of nanoparticles (81.32% Cr (±4.8) and 18.44% Co (±11.83)). The investigation showed that Mo was only present as a trace element in both types of debris. This suggested that Mo can exist in a metallic or ionic form in the wear and corrosion flakes, but it might be washed away by the cleaning procedure.

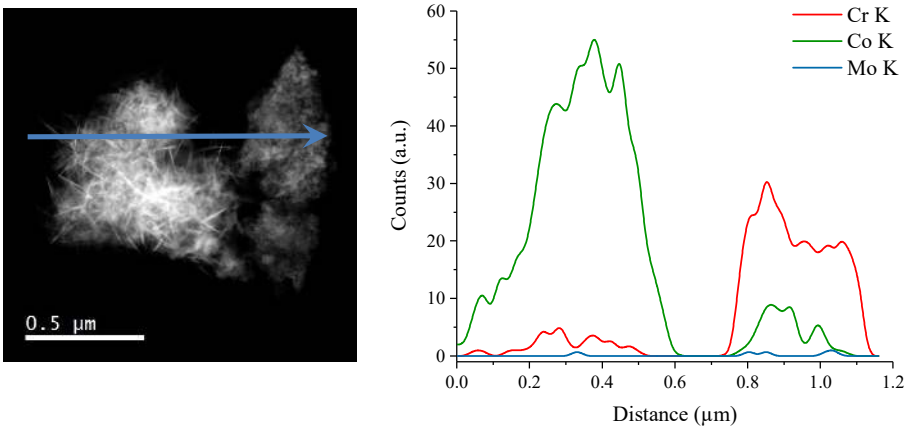

Figure 4.15 The HAADF-STEM micrograph and EDX line profile of Co and Cr rich debris released from taper 3. These suggest the needle structures are made of Co and the round nanoparticles in the right cluster consist mainly of Cr.

The STEM and EDX characterisation of debris released from the mixed CoCrMo/Ti taper junction (taper 5) and cleaned with the alkaline treatment, revealed both Cr and Ti debris, with traces of Co and Mo. The morphology of the isolated debris and the corresponding EDX maps are shown in **Figure 4.16**. The low-resolution micrograph revealed a micron-sized flake-like debris which did not consist of smaller building blocks, such as individual nanoparticles.

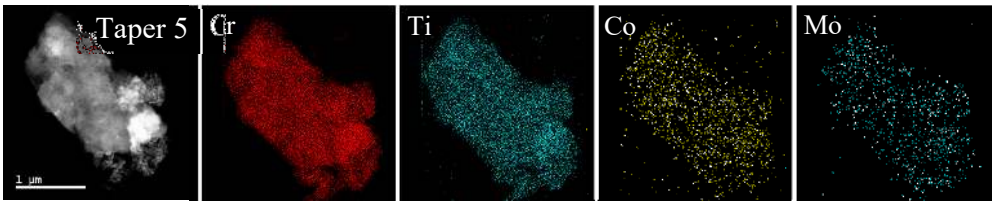

Figure 4.16 The HAADF-STEM micrograph and EDX maps of a mixed Cr and Ti debris from taper 5. The Cr and Ti distributions were co-localised and the composition analysis revealed 81.5% Cr (±0.4), 13.3% Ti (±0.1), 5.1% Co (±0.4) and 0.1% Mo (±0.05).

The major component of the debris was Cr (81.5% (±0.4)), followed by Ti (13.3% (±0.1)), and they were uniformly distributed across the entire surface of the flake. Similarly, Co and Mo did not show preferential distributions and their weak maps matched the boundaries of the Cr and Ti rich debris.

At high-resolution, the mixed debris seemed to be made of smaller entities embedded in a diffuse phase, which made it difficult to assess the size and morphology of the individual building blocks. The micrographs of two fragments of Cr and Ti rich debris and the corresponding EDX line profiles are shown in **Figure 4.17**. In both cases Cr showed more counts than Ti, which is in agreement with the results of the EDX quantification of the flake in **Figure 4.16**. The morphology of the mixed Cr and Ti debris suggested that some small particles corresponding to the bright regions in **Figure 4.17** may comprise the flakes, but the predominant phase is the diffuse phase, which was visible in both micrographs in **Figure 4.17**.

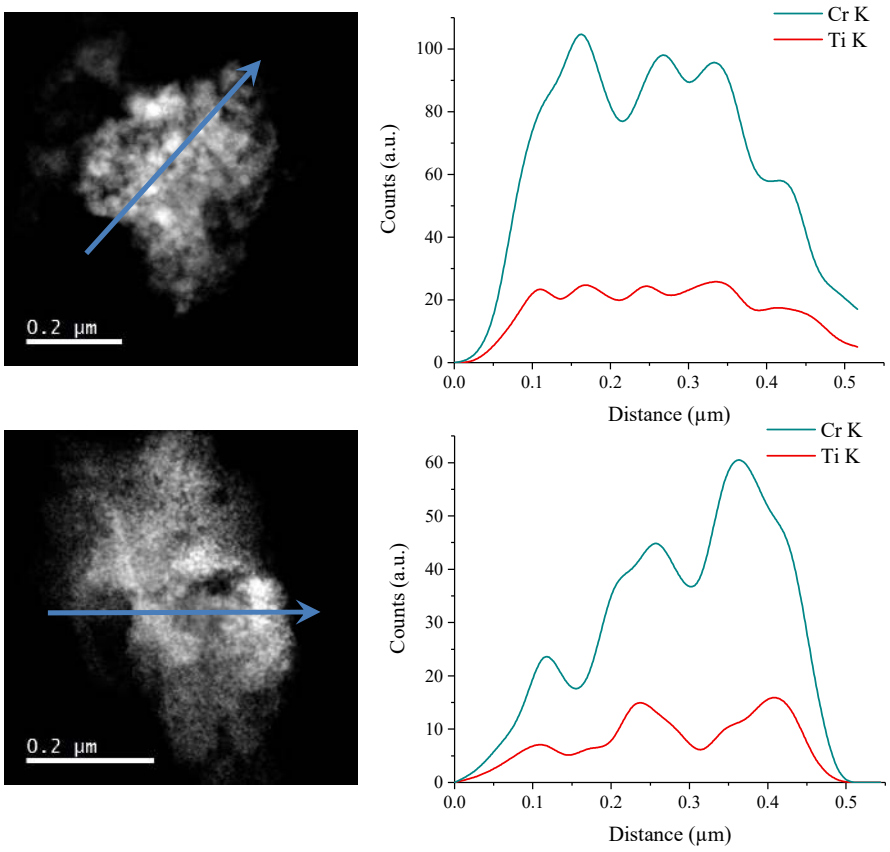

Figure 4.17 The HAADF-STEM micrograph and EDX line profiles of Cr and Ti rich debris released from taper 5, which show that both elements co-exist in the clusters.

Particle size distribution and morphology

The morphology and size distribution of the particles released *in vivo* from the CoCrMo tapers and cleaned with the alkaline treatment, included only the particulate debris which was well separated from the organic matrix. To allow the accurate measurement of the particle length (d_{max}) and width (d_{min}) the particles boundaries needed to be easily distinguished from the surrounding bio-corona. A total of 260 particles from taper 1, 2 and 3 were assessed, with the needle-shaped debris from taper 3 and 4 and the diffuse fragments reported with taper 5 excluded. The size distribution of the particles from all tapers (i.e. taper 1, 2 and 3) are shown in **Figure 4.18** and ranged from 3 nm to 77 nm. The average particle size was 20.8 nm and the median size was 16.8 nm. The details about the number of particles from each taper, the individual size ranges, mean and median particle sizes are shown in **Table 4.3**.

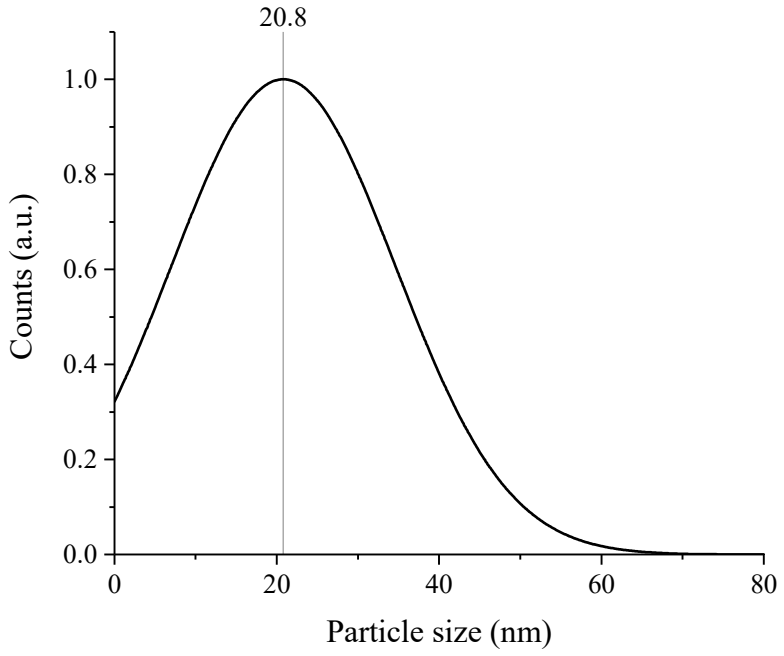

Figure 4.18 The size distribution of the particulate debris released from taper 1, 2 and 3, cleaned with the alkaline treatment.

Table 4.4 shows the percentage of round, oval and needle-shaped particles found in each sample and the distribution of the particle morphology for all taper debris. The majority of the particles released from the tapers were round or oval, with few needle-shaped (i.e. elongated) structures.

Table 4.3 The number of particles characterised for each taper sample and the corresponding size ranges and mean and median d_{max}.

Sample	No of particles	Size range	Mean d_{max}	Median d_{max}
Taper 1	100	3-60 nm	15.9 nm (±11.0)	11.8 nm
Taper 2	110	3-65 nm	20.3 nm (±13.3)	16.8 nm
Taper 3	50	7-77 nm	31.9 nm (±13.9)	30.7 nm
All tapers	260	3-77 nm	20.8 nm (±13.8)	16.8 nm

Table 4.4 The morphology of the particles released from taper 1, 2 and 3 released from the organic matrix using the alkaline treatment.

Sample	Round %	Oval %	Needle shaped %
Taper 1	69	29	2
Taper 2	57	41	2
Taper 3	68	30	2
All tapers	64	34	2

Summary

The alkaline digestion of the wear and corrosion flakes retrieved from around five taper junctions (both mixed and matched material tapers) revealed three types of debris. The most predominant type was the Cr and O rich nanoparticles, released from taper 1, 2 and 3. The mean size of the particulate debris released from the CoCrMo taper interface and cleaned with KOH was 20.8 nm, and 50% of the particles in the study were smaller than 16.8 nm. The second type of debris was the Co rich needle-like structures which were present in 2 samples out of 5. The results of the EDX characterisation showed that besides Co, these structures also contained elements of biological origin which indicated that Co existed in a dissolved ionic form, rather than in a solid metallic state. The third type of debris was released from a mixed CoCrMo/Ti taper interface and consisted of a diffuse mass of Cr and Ti debris. The investigation did not show any crystalline structures, although some of the characterised flakes contained bright, round or oval structures that could be attributed to the presence of nanoparticles embedded in the diffuse phase.

4.2.2 Enzymatic treatment

The enzymatic digestion of the wear and corrosion flakes from taper junctions was used as an alternative to the alkaline treatment, due to concerns regarding the possible deleterious effects of the alkaline reagents on the particles. The enzymatic treatment was applied to fragments of wear and corrosion flakes released from both matched CoCrMo and mixed CoCrMo/Ti alloy taper junctions and aimed to reveal the types of wear and corrosion products that made up the flakes.

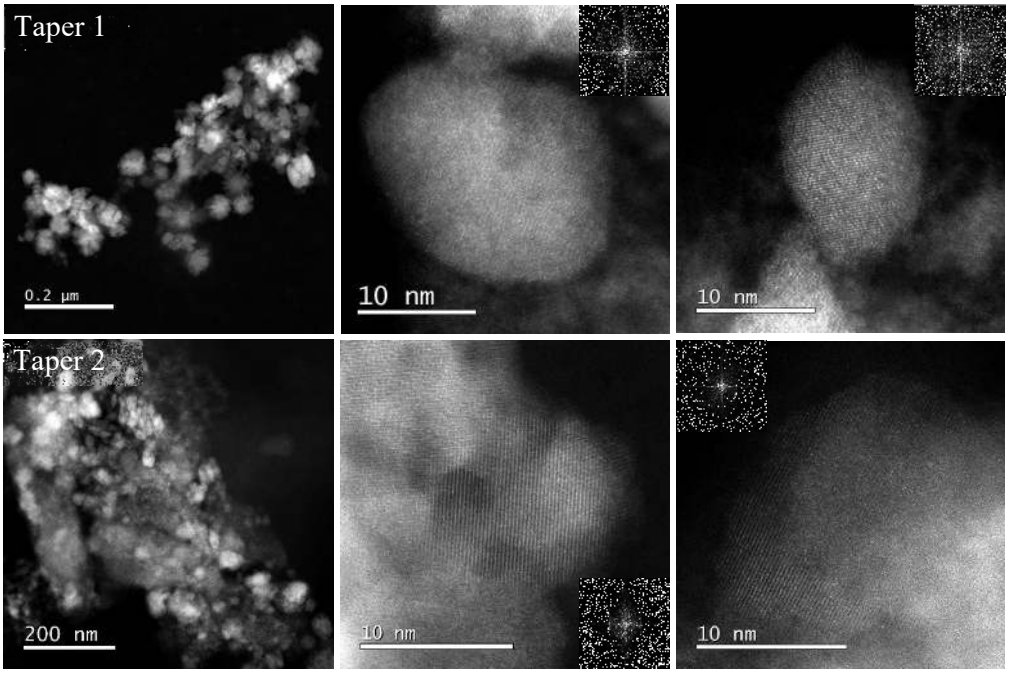

Figure 4.19 The HAADF-STEM micrographs of clusters and individual nanoparticles released from taper 1 and taper 2 and cleaned with the enzymatic treatment. The FFT patterns are produced by the crystalline particles, which were completely removed from the surrounding bio-corona.

The enzymatic cleaning of debris from taper 1 and taper 2 revealed clusters of round and oval crystalline nanoparticles, as well as partially digested flakes that comprised particles embedded in a diffuse matrix. The STEM micrographs of the representative debris released from the CoCrMo tapers and cleaned with the enzymatic protocol are shown in **Figure 4.19**. The particles from both tapers were crystalline (see FFT insets in **Figure 4.19**) and surrounded by the bio-corona, which was represented in the micrographs by a less electron dense phase around the individual particles and aggregates.

The STEM images and EDX maps of two representative clusters of debris are shown in **Figure 4.20**. The Cr and O distributions matched the bright regions of the micrographs, which corresponded to the nanoparticles, and Co and Mo have weak maps, randomly distributed across the flake's area. The results suggested that these particles are Cr oxides with traces of Co and Mo.

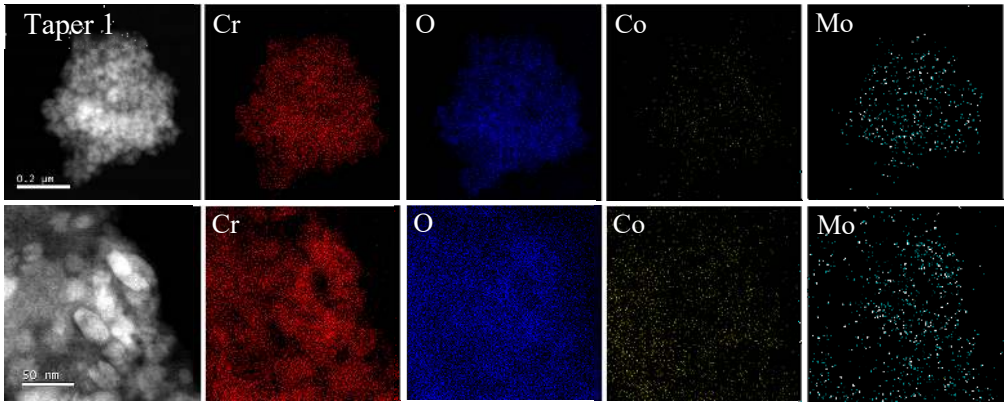

Figure 4.21 The HAADF-STEM micrograph and EDX maps of clusters of debris from taper 1 and 2, cleaned with the enzymatic treatment. The EDX maps showed the particles were made of Cr and O, with little or no Co and Mo.

The STEM and EDX investigation of debris released from taper 6 and cleaned with the enzymatic treatment revealed fragments of P, Cr and O rich debris, with small amounts of Co and Mo. The micrograph of one of the flakes and the corresponding EDX maps are shown in **Figure 4.21**. All the elements present in the sample were uniformly distributed across the surface of the debris, without any preferential localisation of the species.

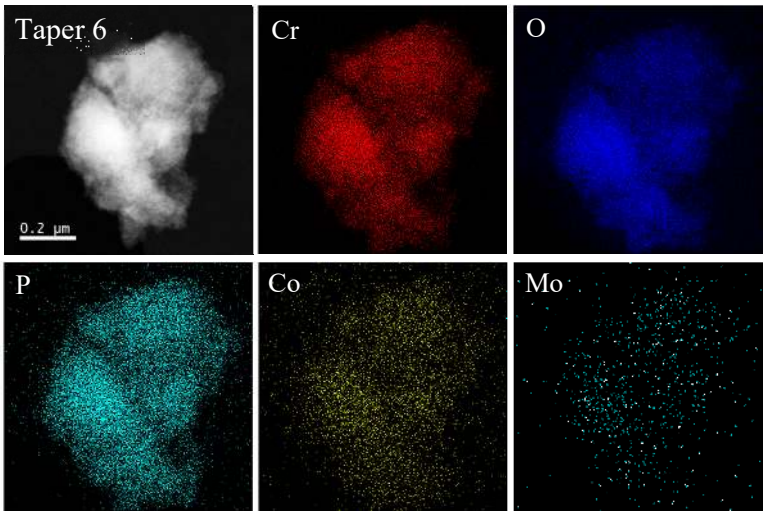

Figure 4.20 The HAADF-STEM micrograph and EDX maps of a fragment of debris released from taper 6 and cleaned with the enzymatic treatment. Th EDX maps showed co-localisation of Cr, O and P, and traces of P and Mo.

The results of the EDX quantification, shown in **Table 4.5**, and the EDX line profiles, shown in **Figure 4.22**, revealed that the amount of P (14.9% (±0.1)) was more than the amount of Cr (7.1% (±0.02)), Co (0.4% (±0.01)) and Mo (0.02% (±0.0)). The EDX analysis was performed over a long acquisition time which provided a high number of counts for all elements, including O, and resulted

in small measurement errors. As such, the quantification analysis based on the counts of all metallic and non-metallic species, showed mainly O, P and Cr, with traces of Co and Mo. The morphology of the flake did not show the presence of any smaller entities that comprised the debris and resembled a fragment of a heterogeneous mass detached from a larger flake, such as a precipitate of $CrPO_4$.

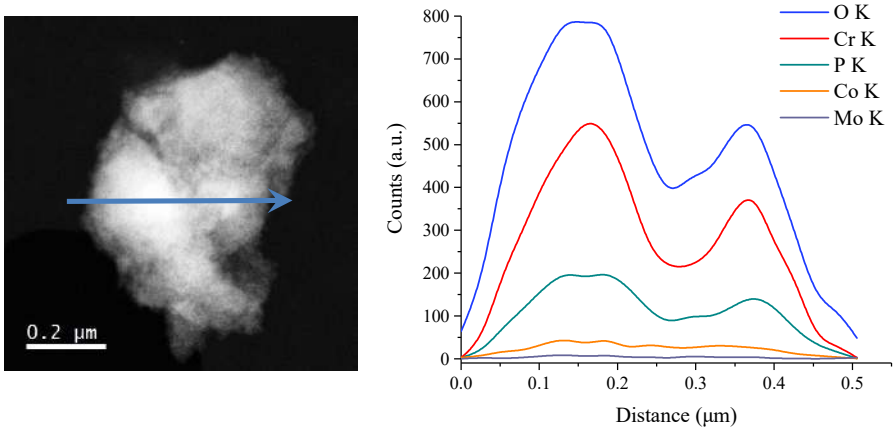

Figure 4.22 The HAADF-STEM micrograph and EDX line profile of debris released from taper 6, showing the distribution of the constituent elements across the flake.

Table 4.5 The results of the quantitative EDX analysis of debris from taper 6, shown in Figure 4.21 and 4.22.

EDX – Taper 6		
Element	Element Wt. %	Wt. % error
O	77.6	0.9
P	14.9	0.1
Cr	7.1	0.02
Co	0.4	0.01
Mo	0.02	0.0

The composition analysis (% ratio Cr:O:P=0.5:5.2:1), however, did not match that of $CrPO_4$, which contains 35.4% Cr, 43.54% O and 21.1% P (% ratio Cr:O:P=1.7:2.06:1). Despite the small measurement errors of the O quantification, which provided reliable results, the amount of O determined from the EDX analysis can originate from other sources. It is thus not excluded the presence of Cr phosphates in the piece of flake released from taper 6 and shown in **Figure 4.21**, although the % composition from the EDX analysis did not match the theoretical % composition of $CrPO_4$.

The enzymatic digestion and STEM characterisation of debris from two mixed CoCrMo/Ti alloy tapers revealed clusters of nano-sized debris and corrosion products. The size, morphology and

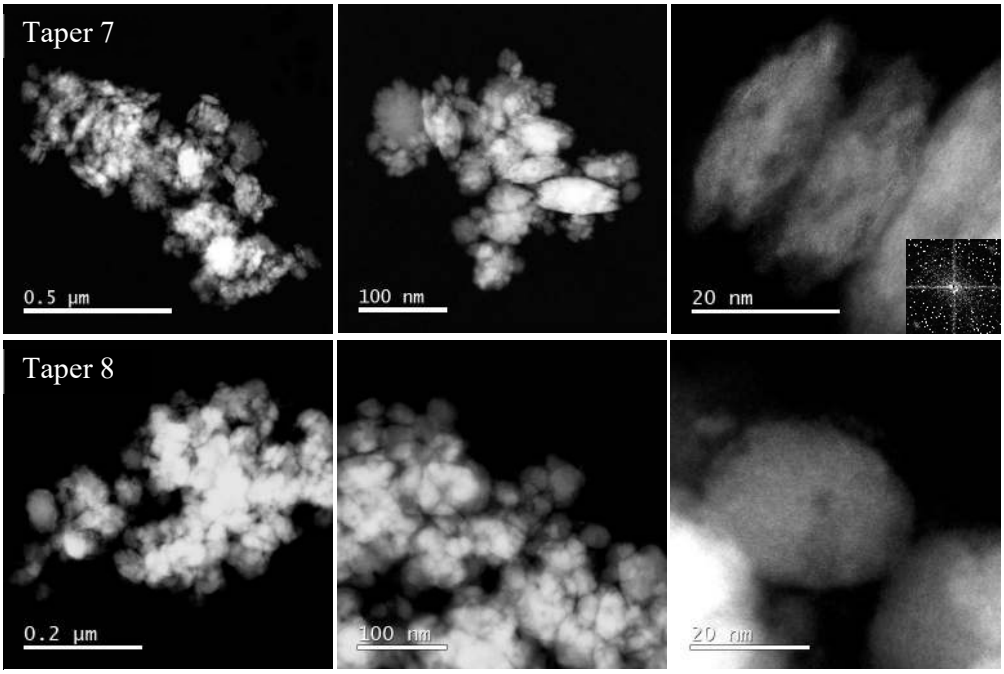

Figure 4.23 The HAADF-STEM micrographs of clusters and individual nanoparticles released from the mixed CoCrMo/Ti alloy tapers (taper 7 and 8) and cleaned with the enzymatic treatment.

aggregation state of the representative nanoparticles released from taper 7 and 8 can be seen in **Figure 4.23**. The micrographs showed clean particles and aggregates, which despite being removed from the surrounding biological matrix, showed little evidence of crystallinity, characterised by weak FFT diffraction patterns (see insets in **Figure 4.23**).

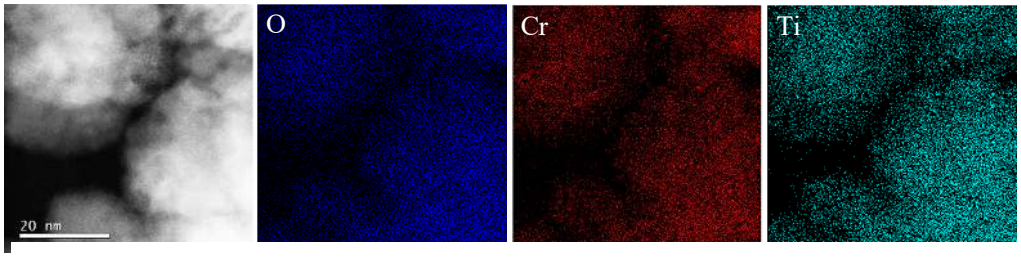

Figure 4.24 The HAADF-STEM micrograph and EDX maps of a cluster of nanoparticles released from taper 7 and cleaned with the enzymatic treatment. The EDX maps show the co-localisation of Cr, Ti and O across the particles.

The STEM and EDX characterisation of the nanoparticle clusters identified mainly Cr, Ti and O, uniformly distributed across the surface of the debris. The micrograph and EDX maps of a cluster of particles from taper 7 are shown in **Figure 4.24**. Besides Cr, Ti and O, the samples also contained P, Co and Mo, which showed weak maps and therefore were not included in **Figure 4.24**. After the exclusion of O, which according to the EDX quantification represented 97% of the sample, the analysis found mainly Cr (54.1% (±0.4)) and Ti (33.9% (±0.2)), with traces of P, Co and Mo. The results of the quantification and the measurement errors for each element are shown in **Table 4.6**.

Table 4.6 The results of the quantitative EDX analysis of debris from taper 7, shown in Figure 4.24.

EDX – Taper 7		
Element	Element Wt. %	Wt. % error
P	9.9	0.6
Ti	33.9	0.2
Cr	54.1	0.4
Co	1.6	0.3
Mo	0.5	0.1

To better understand the nature of debris and the distributions of the main elements (i.e. Cr and Ti) in the particles, a second cluster of debris was subjected to EDX mapping and quantification analysis. The distributions of O, Cr and Ti, and the corresponding overlapped maps are shown in **Figure 4.25**.

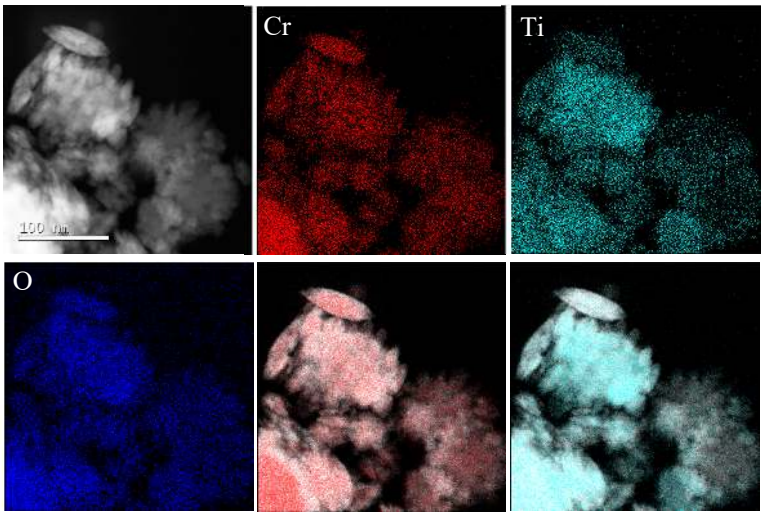

Figure 4.25 The HAADF-STEM micrograph and EDX maps of a cluster of Cr and Ti rich nanoparticles released from taper 7 and cleaned with the enzymatic treatment.

Although Cr and Ti were distributed across the same regions, their concentrations varied from one cluster to another. This variation was best illustrated by the EDX line profile analysis, which showed the concentration of elements across a Cr and a Ti rich region respectively. The line profile and composition of the Cr rich particle at the top of the cluster is shown in **Figure 4.26** and **Table 4.7**. Of all the elements identified, Cr was the most abundant (77.9% (±0.6)), followed by Ti and P. The EDX line profile and the composition of the Ti rich debris is shown in **Figure 4.27** and **Table 4.8** respectively. Although Cr was still the major element (54.6% (±0.7)), the amount of Ti (38.0% (±0.4)) was higher compared to its proportion in the Cr rich debris in **Figure 4.26**. Also, the amount of P increased in the Ti rich region, while Co and Mo were constant between the two areas. The morphology and composition analyses suggested that the particles are Cr and Ti oxides embedded in

an organic matrix with various proportions of dissolved ions, including Cr, Ti, Co and Mo. In certain regions, the Cr and Ti oxides formed clusters which were responsible for the mixed Cr and Ti maps. The proportions of these elements are therefore dictated by the ratio of the various Cr and Ti oxides in those particular regions.

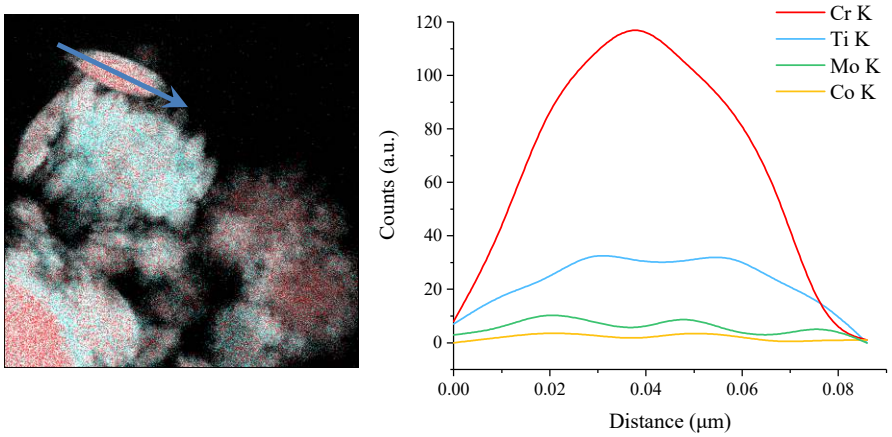

Figure 4.26 The HAADF-STEM micrograph overlapped with the Cr (red) and Ti (blue) maps and EDX line profile of the Cr rich particle from across the arrow. The EDX line profile showed Cr was the predominant element of the particle, followed by Ti, Mo and Co.

Table 4.7 The results of the quantitative EDX analysis of the Cr rich particle shown in Figure 4.26 (marked by the arrow).

EDX Quantification		
Element	Element Wt. %	Wt. % error
P	4.6	0.5
Ti	15.8	0.2
Cr	77.9	0.6
Co	1.2	0.3
Mo	0.5	0.2

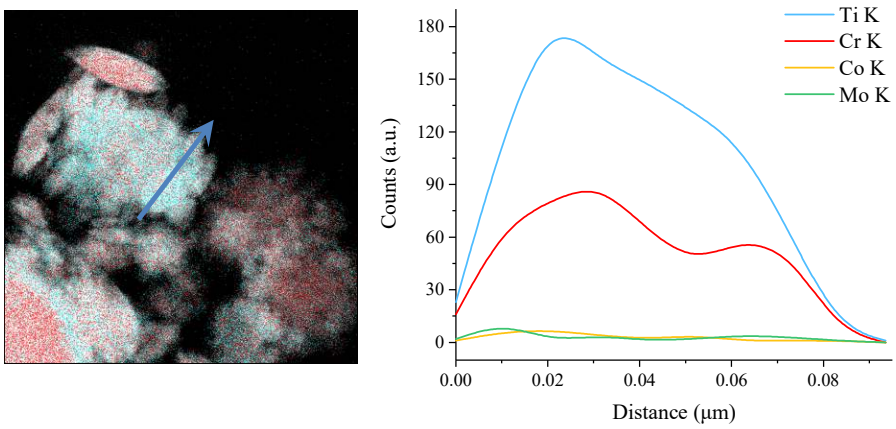

Figure 4.27 The HAADF-STEM micrograph overlapped with the Cr (red) and Ti (blue) maps and EDX line profile of the Ti enriched particle from across the arrow. The Ti, which was the predominant element of the particle, was followed by Cr, Co and Mo.

Table 4.8 The results of the quantitative EDX analysis of the Ti rich particle shown in Figure 4.27 (marked by the arrow).

EDX Quantification		
Element	Element Wt. %	Wt. % error
P	6.1	0.9
Ti	38.0	0.4
Cr	54.6	0.7
Co	1.1	0.2
Mo	0.2	0.1

Particle size distribution and morphology

The size distribution and morphological characterisation included 448 particles originating from taper 1 and 2 (matched CoCrMo alloy) and taper 7 and 8 (mixed CoCrMo/Ti alloy), released from the surrounding bio-corona with the enzymatic treatment. The normalised size distribution is shown in **Figure 4.28** and ranged between 4 and 149 nm. The mean size of all the particles was 33.1 nm, with a median size of 28.9 nm. The number of particles from each sample, their individual size ranges, mean and median d_{max} are shown in **Table 4.9**.

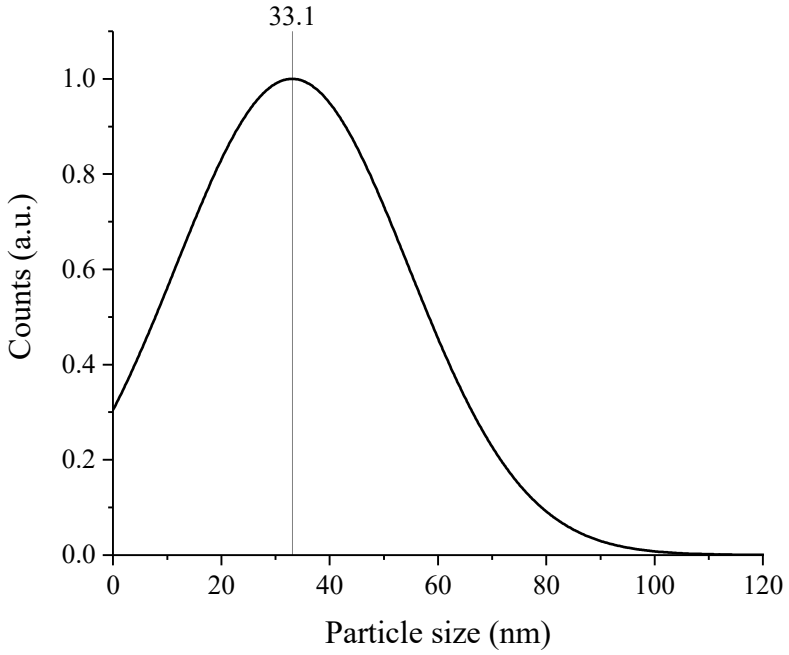

Figure 4.28 The size distribution of the particulate debris released from taper 1, 2, 7 and 8, cleaned with the enzymatic treatment.

Table 4.9 The number of particles characterised for each taper sample and the corresponding size ranges and mean and median d_{max}.

Sample	No of particles	Size range	Mean d_{max}	Median d_{max}
Taper 1	75	4-64 nm	23.5 nm (±14.0)	20.3 nm
Taper 2	107	6-67 nm	24.4 nm (±12.6)	22.1 nm
Taper 7	128	4-149 nm	38.2 nm (±27.7)	30.2 nm
Taper 8	138	6-130 nm	40.2 nm (±19.4)	31.9 nm
All tapers	448	4-149 nm	33.1 nm (±21.4)	28.9 nm

The proportions of round, oval and needle-shaped particles released from all tapers and cleaned with the enzymatic treatment are shown in **Table 4.10**. Most of the particles were round and oval, with few needle-shaped structures. Some flower-like, dendritic particles like those shown in **Figure 4.29** were found after the digestion of debris from taper 2. The method used here to classify the morphology of the particles, however, would have characterised them as round or oval category, depending on their AR values.

Table 4.10 The morphology of the particles originating from all tapers and released from the organic matrix using the enzymatic treatment.

Sample	Round %	Oval %	Needle shaped %
Taper 1	48	49	3
Taper 2	40	53	7
Taper 7	41	44	15
Taper 8	74	25	1
All tapers	52	41	7

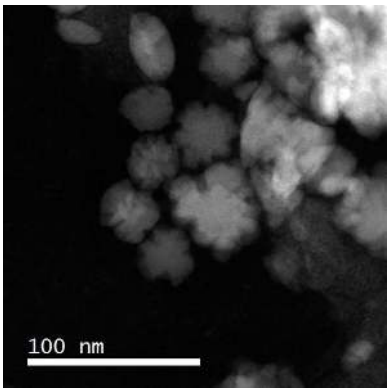

Figure 4.29 The HAADF-STEM micrographs of dendritic (flower-like) particles released from taper 1 and cleaned with the enzymatic treatment.

Summary

The STEM and EDX characterisation of debris released from five tapers and cleaned with the enzymatic treatment revealed three types of wear and corrosion products. Debris from taper 1 and 2 contained mainly round and oval Cr and O rich nanoparticles, with a mean size of 33.1 nm. Debris from taper 6 comprised mainly a diffuse phase rich in Cr and P, probably resulting from a corrosion process, rather than from mechanical wear. The two mixed CoCrMo/Ti alloy tapers generated Cr and Ti rich debris, with traces of P, Co and Mo. The EDX mapping and quantitative analysis suggested the particles were Cr and Ti oxides, embedded in an organic matrix and dissolved metals.

4.3 The in-depth Characterisation of Stem Debris

4.3.1 Alkaline treatment

The alkaline digestion of the wear and corrosion debris released from the cement-stem interface of 4 retrievals (i.e. stem 9-12) revealed clusters of clean nanoparticles, some of which are shown in **Figure 4.30**. The high-resolution characterisation and the corresponding FFT diffraction patterns (see insets in **Figure 4.30**) demonstrated the crystalline nature of the individual particles, which resembled the particulate debris released from the CoCrMo taper junctions, cleaned with the alkaline and enzymatic treatments. The EDX mapping identified mainly Cr and O, with minimal amounts of Co and Mo, and indicated that these particles were also Cr oxides. The elemental maps and the results of the quantitative EDX analyses for two particles and clusters released from stem 9 and stem 10 are shown in **Figure 3.31**. After the exclusion of O, Cr was the major element in the particles from both cement-stem interfaces (78.8% (±0.3) and 85.8% (±0.6)), followed by Co and Mo, whose proportions varied between the samples.

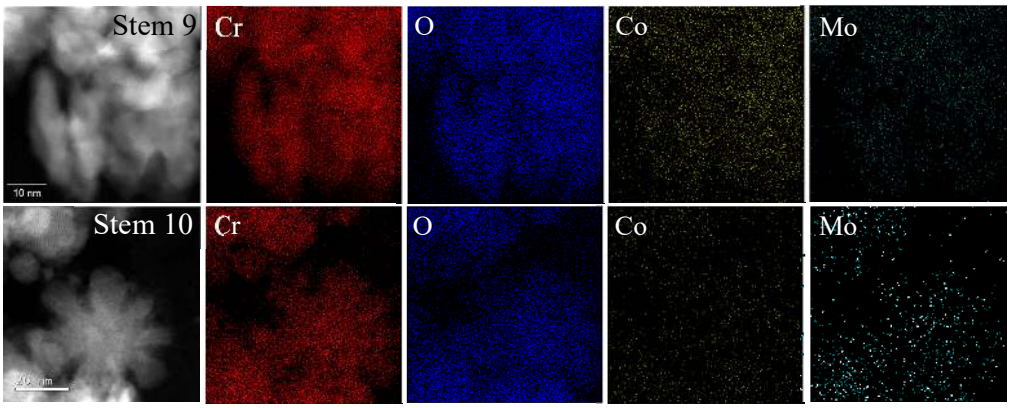

Figure 4.30 The HAADF-STEM micrograph and EDX maps of debris released from stem 9 and 10. The composition analyses showed 78.8% Cr (±0.3), 20.5% Co (±0.7) and 0.7% Mo (±0.1) for the particles from stem 9, and 85.8% Cr (±0.6), 12.6% Co (±1.3) and 1.6% Mo (±0.3) for debris from stem 10.

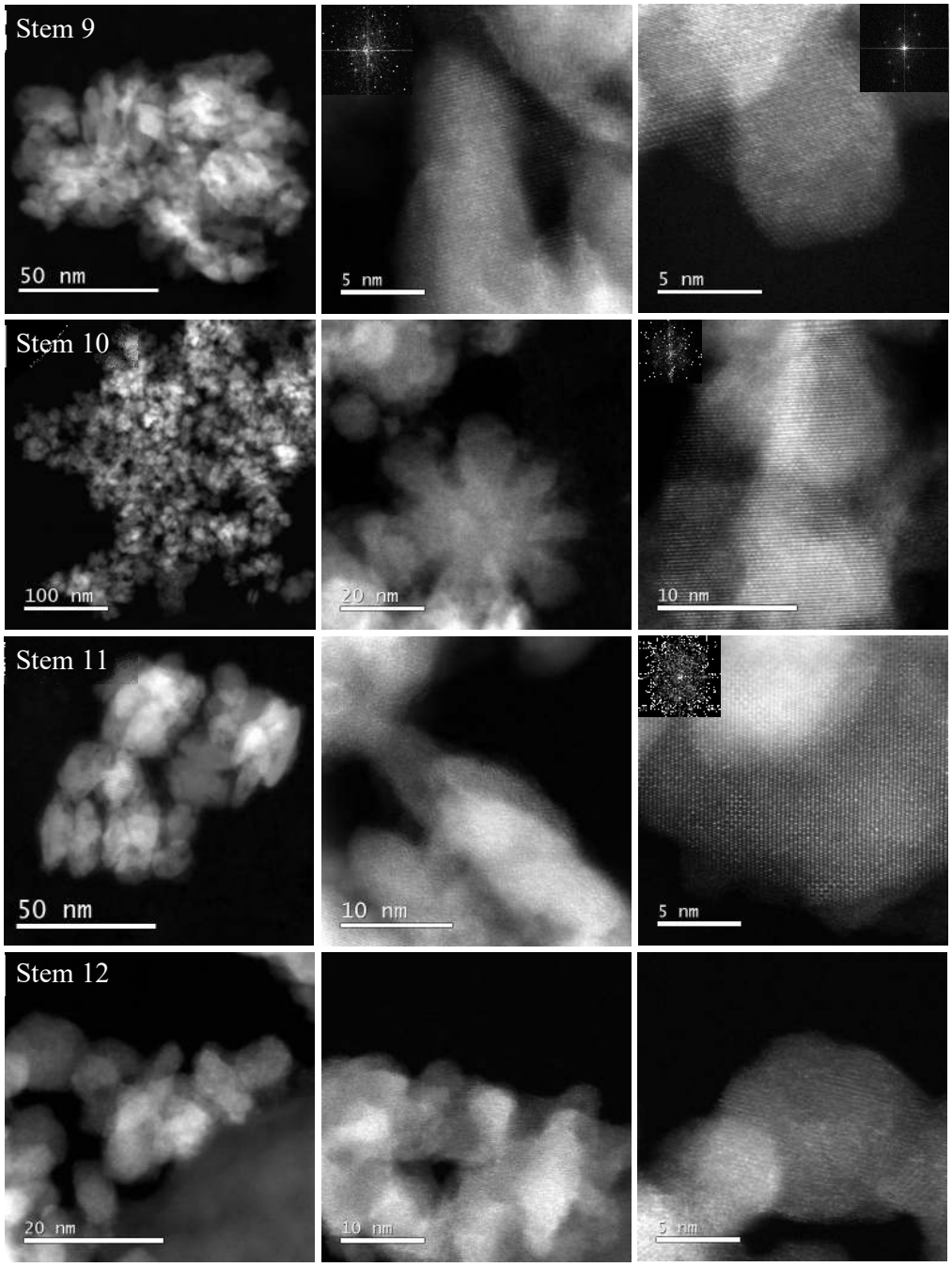

Figure 4.31 The HAADF-STEM micrographs and corresponding FTT patterns of clusters and individual nanoparticles released from the cement-stem interface of implants 9, 10, 11 and 12 and cleaned with the alkaline treatment. The FFT patterns demonstrate the particles were crystalline and completely released from the surrounding matrix.

Besides the O and Cr rich nanoparticles, the alkaline digestion also revealed a diffuse phase, which consisted of clustered nanoparticles embedded in a needle-like net. The micrographs and the EDX quantitative analyses of the particles and net-like regions of debris from stem 11 are shown in **Figure 4.32** and **Figure 4.33** respectively. Both regions were characterised by high amounts of Mg (14.8% (±1.2) and 20.4% (±1.9)) and Ca (12.9% (±0.7) and 16.9% (±0.8)), elements which originated from the body, and K (16.8% (±0.6) and 20.1% (±0.6)) which was used in the cleaning procedure. The presence of metal debris was confirmed by the Cr and Co contents, which varied between the regions. The Cr concentration was higher in the nanoparticle region (50.3% (±0.8)) than in the net-like diffuse phase (36.8% (±0.8)) and in both samples Cr was the most abundant element. Co was also present in both regions, but their amounts were reduced compared to Mg, Ca or P. The presence of these elements indicated an incomplete digestion of the wear and corrosion flakes. In these fragments of partially digested wear and corrosion products, the solid debris, in the form of Cr rich nanoparticles, was embedded in a matrix of biomolecules bound to the Cr and Co ions. The high concentration of K in these flakes showed once again the susceptibility of the biological material to the chemical attack, using alkaline solutions.

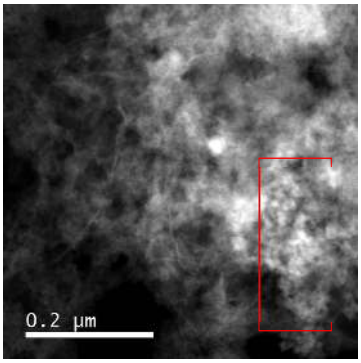

EDX Region 1		
Element	Element Wt. %	Wt. % error
Mg	14.8	1.2
P	0.3	0.3
K	16.8	0.6
Ca	12.9	0.7
Cr	50.3	0.8
Co	4.9	0.6
Mo	0.04	0.04

Figure 4.32 The HAADF-STEM micrograph of debris from stem 11 and the results of the EDX quantitative analysis of a cluster of nanoparticles embedded in a diffuse matrix.

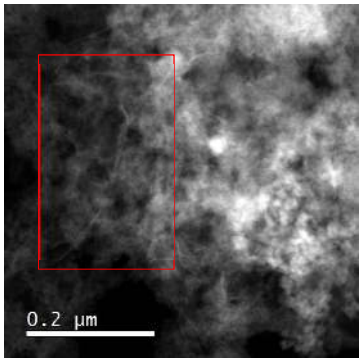

EDX Region 2		
Element	Element Wt. %	Wt. % error
Mg	20.4	1.9
P	0.00	0.0
K	20.1	0.7
Ca	16.9	0.8
Cr	36.8	0.8
Co	5.9	0.6
Mo	0.00	0.00

Figure 4.33 The HAADF-STEM micrograph of debris from stem 11 and the results of the EDX quantitative analysis of the net-like phase.

Particle size distribution and morphology

The normalised size distribution of the Cr and O rich debris released from stems 9, 10, 11 and 12 are shown in **Figure 4.34** and included 155 particles, ranging from 5 to 37 nm. The number of particles released from each cement-stem interface and characterised with STEM, the size ranges and the mean and median sizes are shown in **Table 4.11**. The mean size of all the particles was 16.4 nm, with a median d_{max} of 15.1 nm.

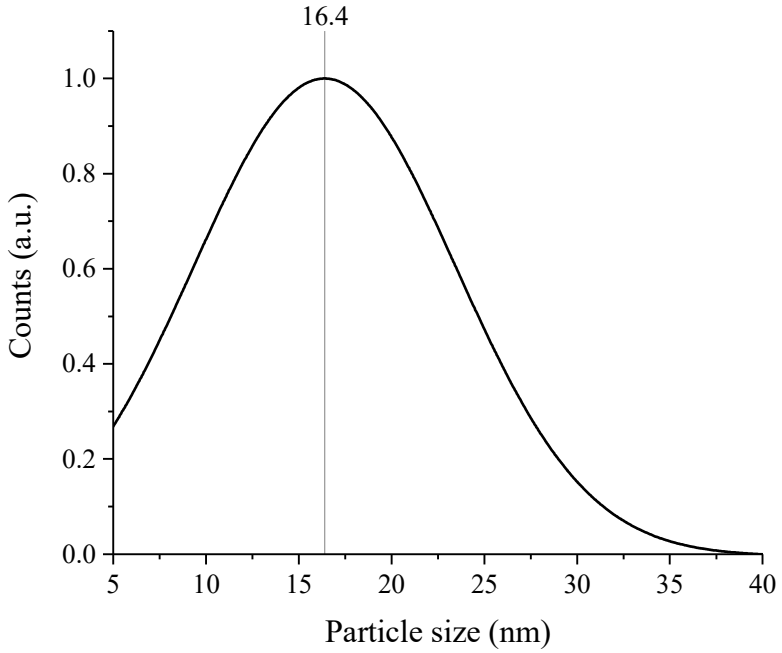

Figure 4.34 The size distribution of the particles released from stem 9, 10, 11 and 12, cleaned with the alkaline treatment.

Table 4.11 The number of particles characterised for each stem sample and the corresponding size ranges and mean and median d_{max}.

Sample	No of particles	Size range	Mean d_{max}	Median d_{max}
Stem 9	83	6-37 nm	17.1 nm (±7.1)	15.9 nm
Stem 10	33	6-34 nm	15.7 nm (±6.9)	14.3 nm
Stem 11	22	9-31 nm	19.9 nm (±5.7)	19.8 nm
Stem 12	17	5-18 nm	9.6 nm (±3.6)	8.8 nm
All stems	155	5-37 nm	16.4 nm (±7.1)	15.1 nm

Most of the particles released from the cement-stem interface of the CoCrMo femoral components were round or oval, with few needle-shaped particles. The proportions of round, oval and needle-shaped particles from each stem sample and all cement-stem interfaces cleaned with the alkaline treatment are shown in **Table 4.12**. Dendritic, flower-like particles, like the one shown in **Figure 4.31** - stem 10, were also found.

Table 4.12 The morphology of the particles originating from all stems and released from the organic matrix using the alkaline treatment.

Sample	Round %	Oval %	Needle shaped %
Stem 9	52	37	11
Stem 10	85	12	3
Stem 11	36	64	0
Stem 12	59	35	1
All stems	58	35	7

Summary

The alkaline digestion of the wear and corrosion flakes released from the cement-stem interface revealed mainly Cr and O rich nanoparticles, completely removed from the surrounding matrix or partially embedded in the diffuse phase. The STEM and EDX characterisation suggested that the building blocks of the debris released from CoCrMo stems are Cr oxides with traces or Co and Mo.

4.3.2 Enzymatic treatment

The enzymatic treatment was used to clean debris from four CoCrMo stems, corresponding to the retrievals 1, 2, 9 and 10. Some representative STEM micrographs of the particles and clusters released from the cement-stem interface and cleaned with the enzymatic treatment are shown in **Figure 4.35**. The digestion protocol resulted in partially cleaned flakes, which comprised clusters of nanoparticles embedded in the organic matrix (aggregates from stem 1 and 9 in **Figure 4.35**). The presence of bio-corona was visible around debris from stem 10, in which crystalline particles of 5-10 nm were surrounded by a diffuse and less electron dense phase. The FFT insets of the high-resolution micrographs in **Figure 4.35** demonstrated the crystallinity of the particulate debris released from the stems. In some of the samples, however, the crystalline structures were not completely isolated/detached from the aggregates and were characterised at the edges of the clusters.

The STEM and EDX investigation found Cr and O rich structures with small amounts of Co and Mo. The high-resolution micrographs of representative particles originating from stem 1 and their corresponding elemental maps are shown in **Figure 4.36**. The distribution of the elements suggested that the particles were Cr oxides, with traces of Co and Mo. The digestion process also revealed some crystalline needle-like structures, which are shown in **Figure 4.37** and appear to be still embedded in the surrounding diffuse matrix. The quantitative analysis of the needle-like debris is shown in **Table 4.13** and contains mainly P, Cr and Co, as well as Ca and Mg. These structures resembled the Co rich needle-like debris revealed after the alkaline digestion of the wear and corrosion flakes from the taper interface. There was however a difference, with high concentrations of P (35.2% (±1.5)) and Cr (31.4% (±1.2)) in debris from the stems and cleaned with the enzymatic protocol. The EDX quantitative analysis of the needle-shaped structures revealed after the alkaline digestion of the taper debris identified mainly Co (49.2% (±0.2)) and minimal amounts of P (3.0% (±0.2)) (section 4.2. A, **Figure 4.13**). The results demonstrated needle-like structures within both the taper and stem debris, which are either Co and Cr phosphates, or metal ions entrapped in the organic matrix. The lack of P in the taper debris after the alkaline treatment may be caused by the chemical dissolution of the phosphates after the incubation with KOH, which is then removed from around the clean oxide particles. The milder effects of the enzymatic treatment may have resulted in higher P content in the debris cleaned with this treatment.

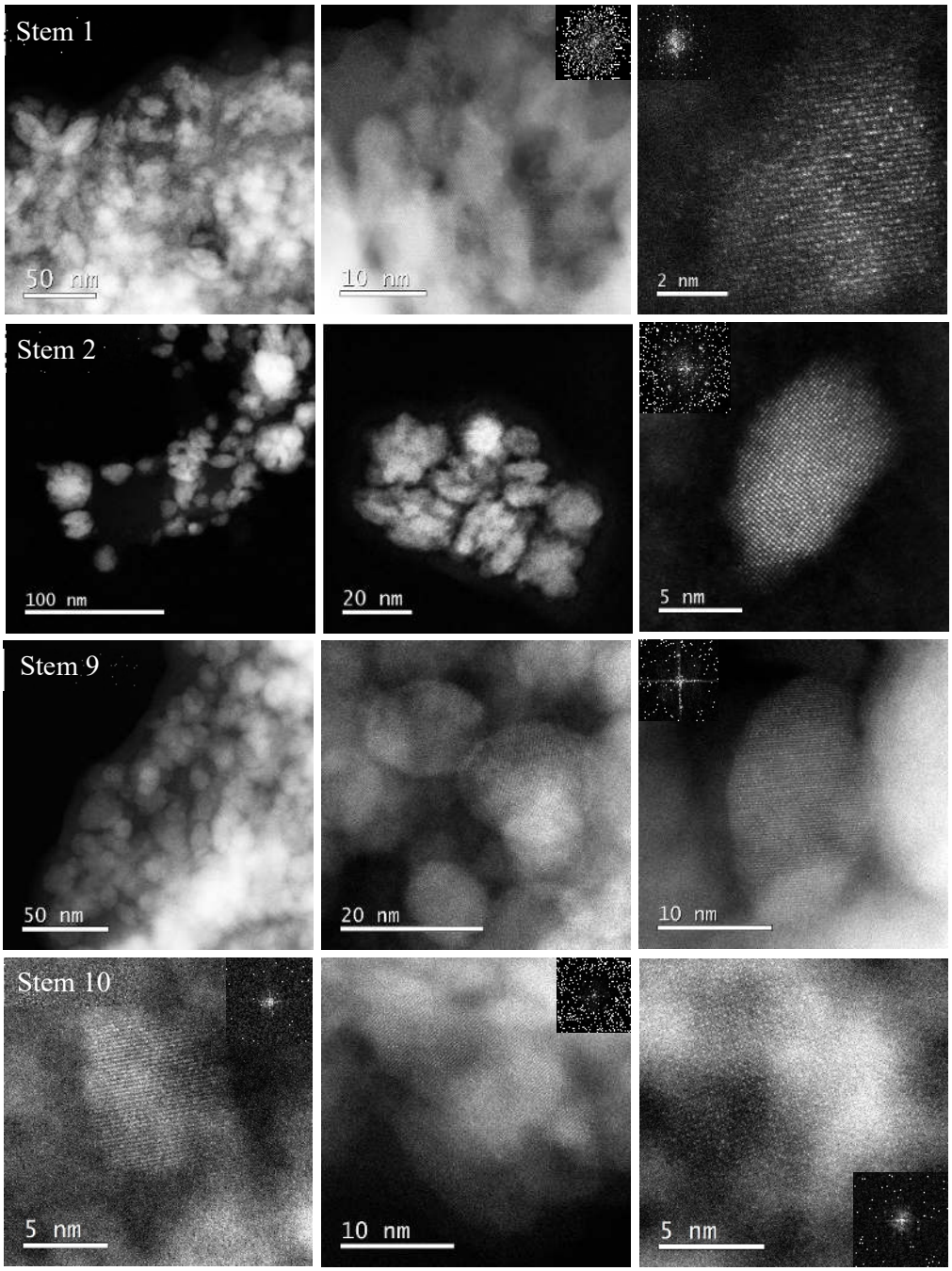

Figure 4.35 The HAADF-STEM micrographs and corresponding FTT patterns of clusters and individual nanoparticles released from the cement-stem interface of implants 1, 2, 9 and 10 and cleaned with the enzymatic treatment. The micrographs show both clusters of partially cleaned debris and crystalline particles completely removed from the organo-metallic phase.

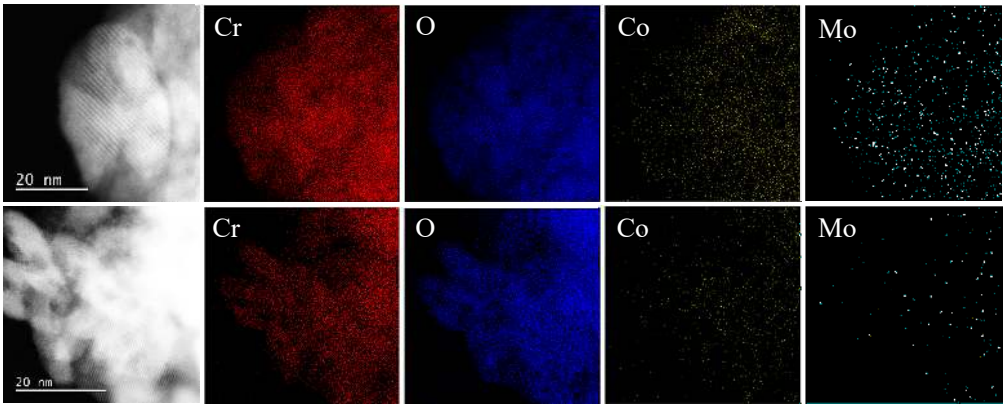

Figure 4.37 The HAADF-STEM micrograph and EDX maps of debris from stem 1, cleaned with the enzymatic treatment. The EDX maps show the particles consist of Cr and O, with little Co and Mo.

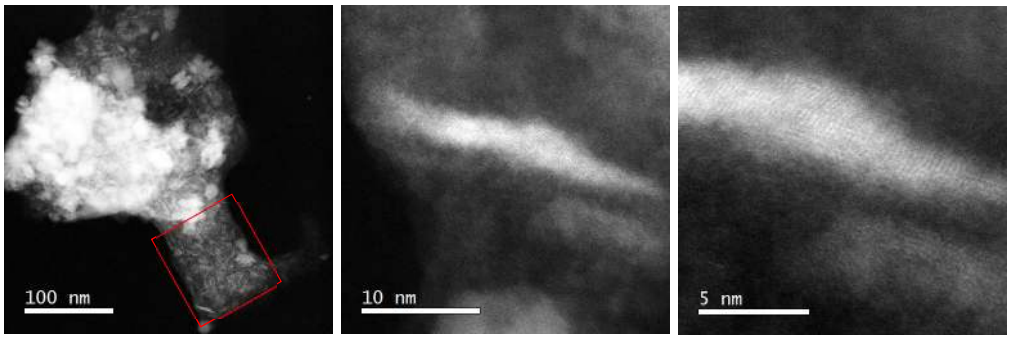

Figure 4.36 The HAADF-STEM micrographs of the needle-like structures originating from stem 2 and revealed after the enzymatic digestion of the wear and corrosion flakes.

Table 4.13 The results of the quantitative EDX analysis of the needle-like structures shown in Figure 4.37.

EDX Quantification		
Element	Element Wt. %	Wt. % error
Mg	8.2	2.4
P	35.2	1.5
Ca	9.8	1.1
Cr	31.4	1.2
Co	15.5	1.3
Mo	0.0	0.0

Particle size distribution and morphology

The size distribution and morphological characterisation of debris released *in vivo* from the cement-stem interfaces and cleaned with the enzymatic treatment, included 290 particles from the four samples. The normalised size distribution is shown in **Figure 4.38** and ranges from 4 to 49 nm, with a mean size of 16.4 nm and a median size of 14.9 nm. The number of particles released from each taper interface, the corresponding size ranges and the mean and median sizes are summarised in **Table 4.14**.

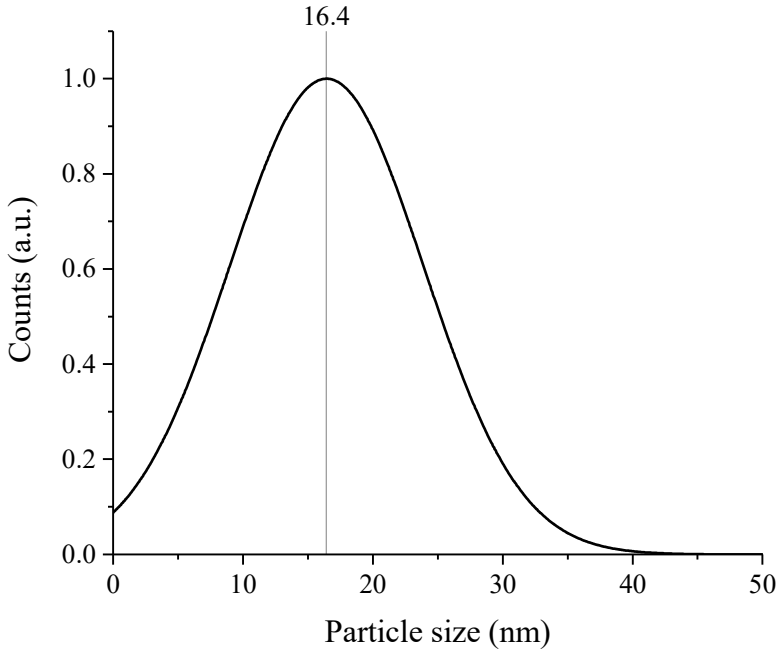

Figure 4.38 The size distribution of the particles released from stem 1, 2, 9 and 10, cleaned with the enzymatic treatment.

Table 4.14 The number of particles characterised for each stem sample and the corresponding size ranges and mean and median d_{max}.

Sample	No of particles	Size range	Mean d_{max}	Median d_{max}
Stem 1	85	4-49 nm	16.8 nm (±8.7)	15.5 nm
Stem 2	115	6-37 nm	16.0 nm (±7.4)	14.2 nm
Stem 9	82	7-32 nm	16.9 nm (±6.1)	15.2 nm
Stem 10	8	6-23 nm	13.7 nm (±6.5)	13.0 nm
All stems	290	4-49 nm	16.4 nm (±7.5)	14.9 nm

The proportions of round, oval and needle-shaped particles originating from the cement-stem interface and cleaned with the enzymatic treatment are shown in **Table 4.15**. Most of the particles were round and oval, with only few needle-shaped (elongated) debris.

Table 4.15 The morphology of the particles originating from all stems and released from the organic matrix using the enzymatic treatment.

Sample	Round %	Oval %	Needle shaped %
Stem 1	54	41	5
Stem 2	72	27	1
Stem 9	68	32	0
Stem 10	75	25	0
All stems	66	32	2

Summary

The results of the enzymatic digestion support the findings of the alkaline treatment and suggest that the Cr and O rich nanoparticles are the major type of debris released *in vivo* from the CoCrMo stems. The Cr/Co and P rich needle-like debris indicated that other species such as Cr and Co phosphates may also be generated at this particular interface.

4.4 Speciation Analysis

4.4.1 Introduction

The complex nature of the taper and stem debris can make speciation analysis difficult and a single technique might not always provide the best results. Here, we proposed to identify the oxidation state of Cr, Co and Ti, and the chemistry of debris using STEM/EELS, TEM/SAED and STXM/XANES. The main objective of the study was to elucidate the nature of the Cr rich nanoparticles, Ti nanoparticles and the oxidation state of Co in the partially digested flakes released from both mixed and matched tapers and/or the cement-stem interface.

4.4.2 The speciation of Cr debris released from Taper 1 and Stem 1 and cleaned with the enzymatic treatment – STEM/EELS and TEM/SAED analysis

Analytical characterisation of the Cr rich nanoparticles using EELS was performed on three clusters of debris from stem 1 and one cluster of debris from taper 1. The corresponding EELS spectra are shown in **Figure 4.39**, and are plotted together with the EELS spectrum from a cluster of commercially available Cr_2O_3, acquired under identical experimental conditions. The O K and Cr $L_{2,3}$ core-loss edges at 532 and 577 eV respectively are shown in **Figure 4.39** and matched well for the samples and commercially available Cr_2O_3.

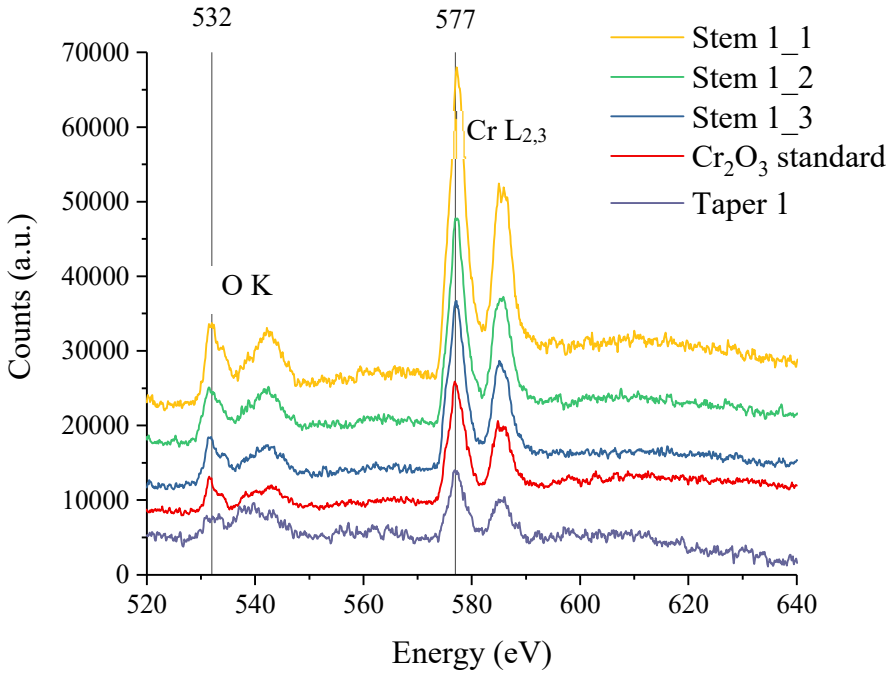

Figure 4.39 The EELS spectra of a standard Cr_2O_3 sample and debris from taper 1 and stem 1, showing the O K and Cr $L_{2,3}$ peaks at 532 and 577 eV respectively.

A small shift to a higher energy value (from 575 to 577 eV) was observed for the Cr core-loss peak in all samples, including the standard Cr_2O_3, and has been previously reported for other transition metals and their oxides, as a result of the increase of the metal oxidation state[307].

The results of the quantitative EELS analyses are shown in **Table 4.16**. All the samples and clusters, including the commercially available Cr_2O_3, showed a variation from the theoretical 0.66 ratio, characteristic to the pristine Cr_2O_3. The quantification analysis of one cluster of debris from stem 1 yielded a Cr/O ratio of 0.63, while the mean ratio of all stem clusters was 0.74. This value and the ratio obtained for taper debris (0.73) are equal or similar to the ratio reported experimentally for Cr_2O_3 in a previous study (0.74) and confirms the presence of this species in taper and stem debris[306].

Table 4.16 The Cr/O ratio and composition of Cr_2O_3 standard material and debris released from taper 1 and stem 1, as provided by the quantitative EELS analysis.

Sample	O (at.%)	Cr (at.%)	Cr/O
Cr_2O_3	50.3±1.1	49.7±1.1	0.99
Stem 1_1	56.5±1	43.5±1	0.77
Stem 1_2	61.2±2	38.8±2	0.63
Stem 1_3	54.9±0.4	45.1±0.4	0.82
Taper 1	58.6±1.5	41.2±1.5	0.71

Alternative methods, TEM and SAED, were further used to confirm the chemical form of the Cr and O rich nanoparticles originating from the taper and cement-stem interface of retrieval 1. The investigation was performed on three clusters of debris from the CoCrMo taper and three clusters of debris from the cement-stem interface, which were previously investigated with TEM and EDX, to confirm the presence of Cr and O. The indexed SAED patterns matched the d-spacing of the various hkl planes of Cr_2O_3 and provided a further evidence of the speciation, in addition to the results of the STEM and EELS investigation. A representative SAED pattern of a cluster of nanoparticles from taper 1 and the corresponding EDX spectrum are shown in **Figure 4.40**. **Table 4.17** contains the measured d-spacing, the matching theoretical d-spacing and the corresponding hkl plane of Cr_2O_3. The variations from the standard d-spacing, corresponding to the pristine Cr_2O_3 samples from the XRD database, can be justified by the presence of other elements, such as Mo and traces of Co, or by the errors associated with the d-spacing measurement. A representative cluster of debris from stem 1 and the corresponding EDX spectra and the indexed SAED pattern are shown in **Figure 4.41**. The values for the measured and standard d-spacing and corresponding hkl planes are provided in **Table 4.18**. The speciation results from both techniques provided sufficient evidence that the Cr and O rich nanoparticles released from taper and stem 1 are Cr_2O_3.

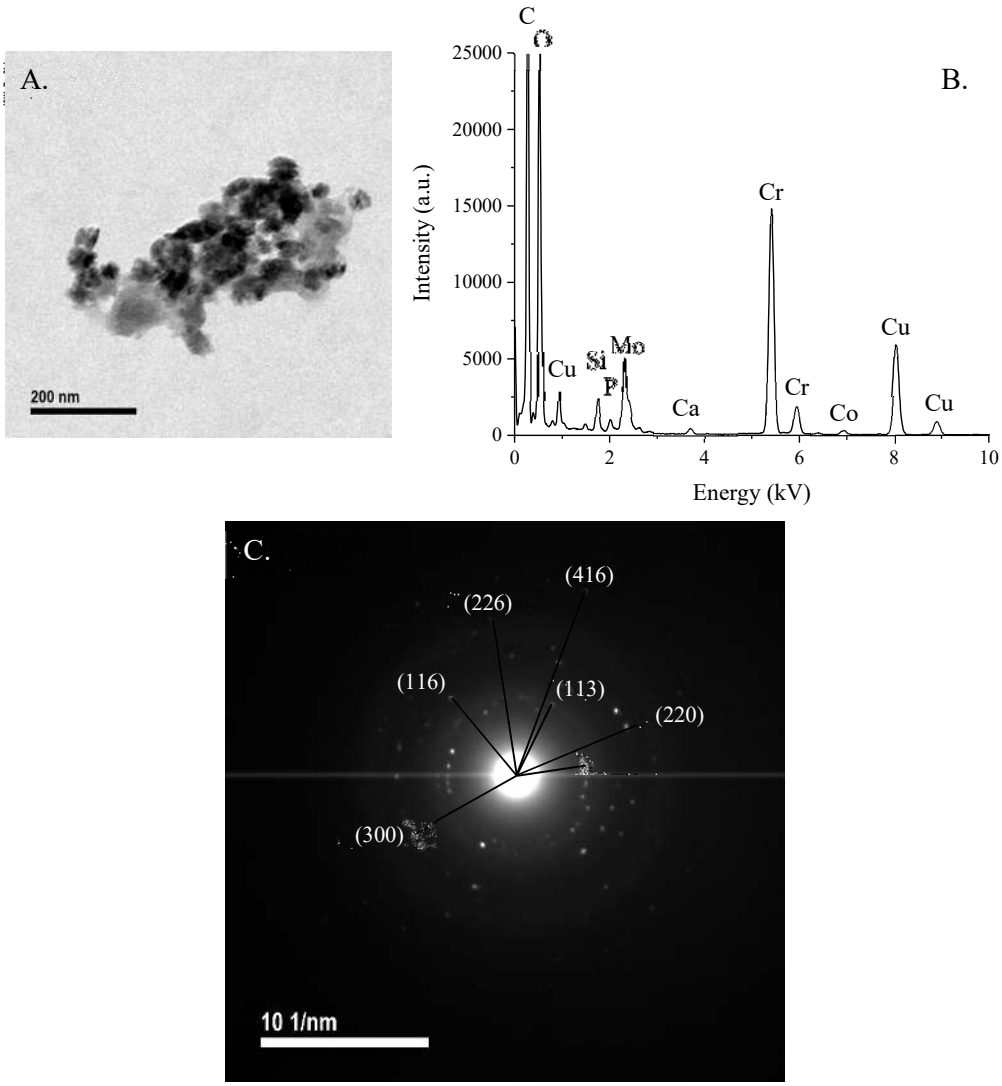

Figure 4.40 The TEM/SAED investigation of debris from taper 1: A. The TEM micrograph of a representative cluster; B. The EDX spectrum of the cluster of particles shown in A; C. The indexed SAED pattern of the cluster shown in A.

Table 4.17 The measured d-spacing of debris from taper 1 and the matched standard d-spacing and hkl planes of the pristine Cr_2O_3.

Measured d [nm]	Standard d [nm]	hkl
0.2481	0.2479	110
0.1669	0.1672	116
0.2176	0.2175	113
0.1421	0.1431	300
0.1241	0.1239	220
0.1083	0.1087	226
0.0863	0.0866	416

Table 4.18 The measured d-spacing of debris from stem 1 and the matched standard d-spacing and hkl planes of the pristine Cr_2O_3.

Measured d [nm]	Standard d [nm]	hkl
0.2478	0.2479	110
0.1661	0.1672	116
0.1436	0.1431	300
0.1061	0.1060	40-2

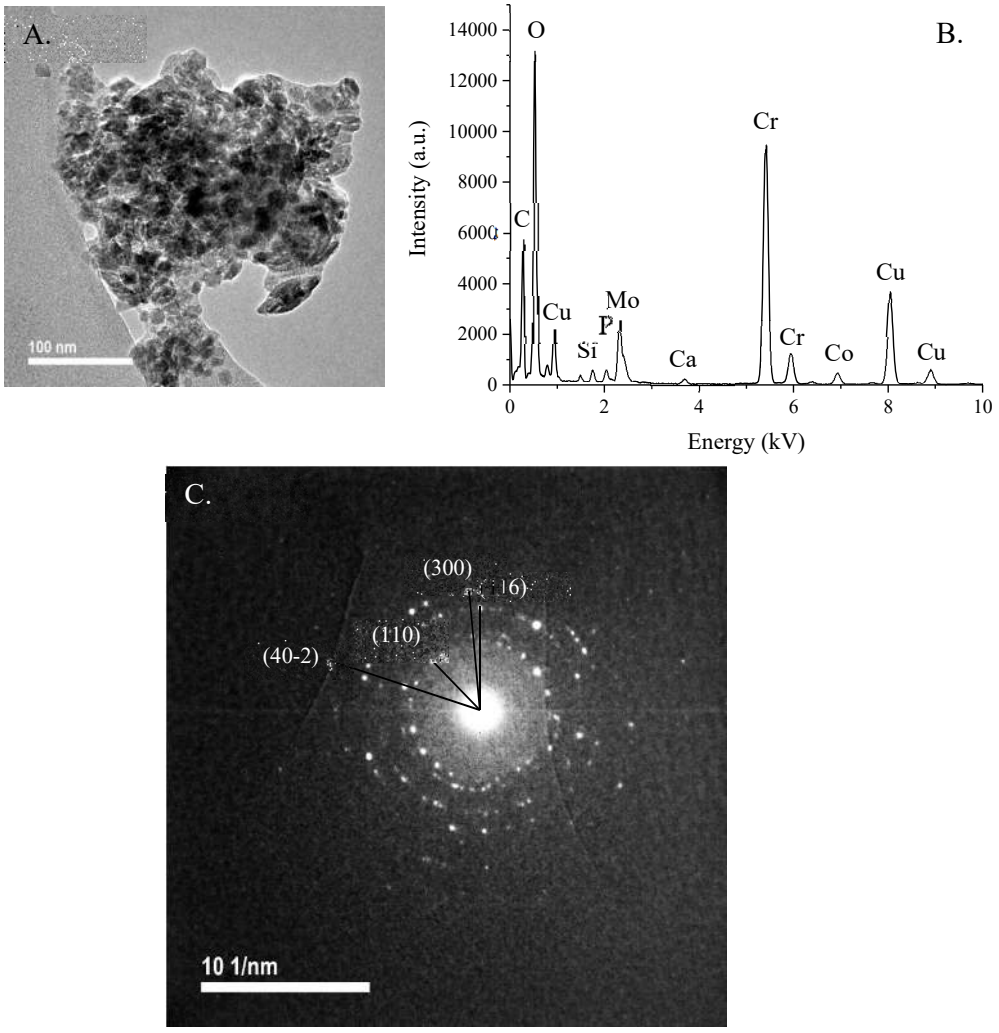

Figure 4.41 The TEM/SAED investigation of debris from stem 1: A. The TEM micrograph of a representative cluster; B. The EDX spectrum of the cluster of particles shown in A; C. The indexed SAED pattern of the cluster shown in A.

4.4.3 The speciation of Cr and Co debris released from Taper 2 and Stem 2 and cleaned with the enzymatic treatment – STXM and XANES analysis

The Cr XANES spectra of some representative clusters of nanoparticles from taper and stem 2, and the commercially available Cr_2O_3 and $CrPO_4$, serving as standard materials, are shown in **Figure 4.42**. The investigation was performed on three different clusters from taper 2 and three clusters from the stem debris. The Cr species released from the CoCrMo interfaces were identified based on the similarities and differences between the Cr $L_{2,3}$ edges of the samples and standard materials (i.e. Cr oxide and phosphate).

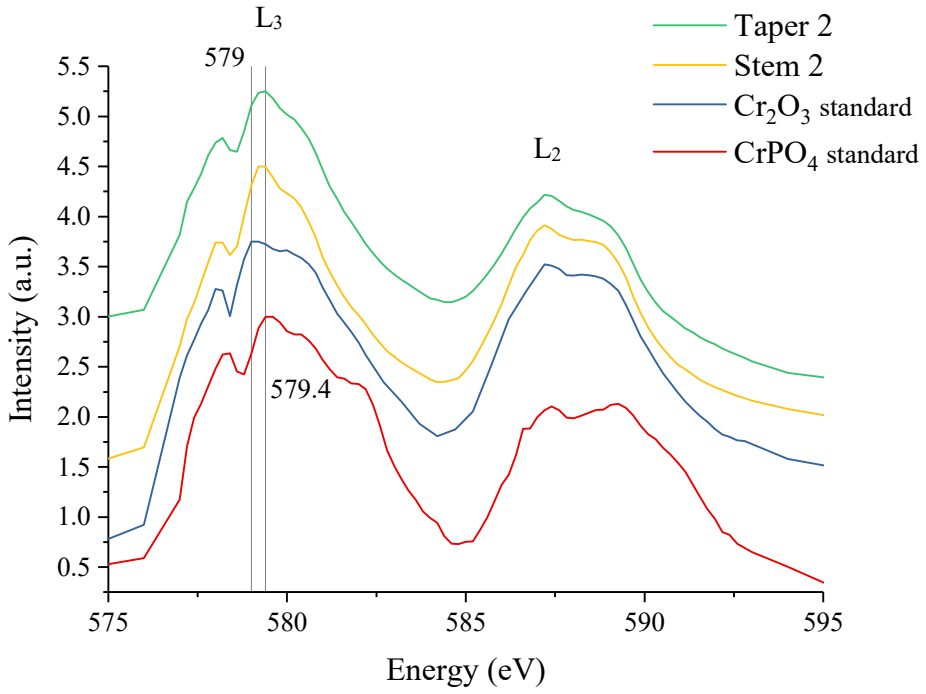

Figure 4.42 The representative Cr $L_{2,3}$ XANES spectra of debris from taper 2, stem 2 and standard Cr_2O_3 and $CrPO_4$ material.

The linear combination fitting yielded a good match between the spectra of the particles and the spectrum of the commercially available Cr_2O_3 sample (standard material). Despite the similarities, the Cr $L_{2,3}$ edges of the $CrPO_4$ showed particular spectral features, such as the shoulder at 582.2 eV, which was missing from the XANES spectra of the implant debris. The edge peaks of the samples (579.2 eV), however, appeared at higher energies compared to the edge peak of the standard Cr_2O_3 (579 eV) and at lower energies compared to the edge peak of the standard $CrPO_4$ (579.4 eV). The shift of the edge peaks could be justified by the presence of both Cr oxide and phosphate species in the partially digested flakes.

In theory, the spatial resolution of the I08 beamline (Diamond Source Ltd. Harwell, Science and Innovation campus, UK) is ~20 nm, but this can be difficult to achieve experimentally. The clusters analysed with this technique, were therefore larger than the clusters of Cr_2O_3 investigated with STEM and EDX, which were completely released from the organic matrix and contained mainly Cr and O. It is possible therefore, that the large clusters (d_{max}~1-5 μm) characterised with STXM and XANES contained Cr_2O_3 nanoparticles embedded in a matrix of organic material and $CrPO_4$. However, the STEM and EDX analysis of the cleaned nanoparticles originating from the taper and stem 2 did not show any P. The combined results of the STEM/EDX and STXM/XANES analysis, therefore, confirm that the Cr and O rich nanoparticles are Cr_2O_3.

The average Co XANES spectrum of a cluster of debris released from taper 2 (**Figure 4.43**) and the spectra of the standard $Co(OH)_2$, $Co_3(PO_4)_2$ and CoO are shown in **Figure 4.44**. The spectra given by the distinct Co rich regions of the cluster were weak and noisy, and could not be used for individual spectral matching. The analysis of the mean spectrum of the taper debris revealed that Co L_3 edge appeared at 781.5 eV and matched the L_3 edge photon energy of the Co^{2+} standard materials. The spectral features of the L_3 peak (781-784 eV) and the presence of a pre-peak at 780 eV, demonstrated the taper debris is $Co(OH)_2$. It is possible however that a blend of various proportions of Co oxide, hydroxide and phosphate are present in the individual flakes, but because of their low concentrations, suggested by the weak individual particle signals, the spectral features were difficult to identify. Also, the point analysis demonstrated that Co species were only present in certain flakes of the clusters and were completely lacking in others.

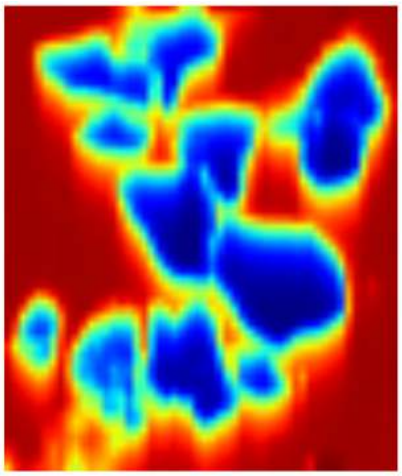

Figure 4.43 The STXM micrograph used to determine the Co speciation in debris from taper 2 (resolution: 26x31μm).

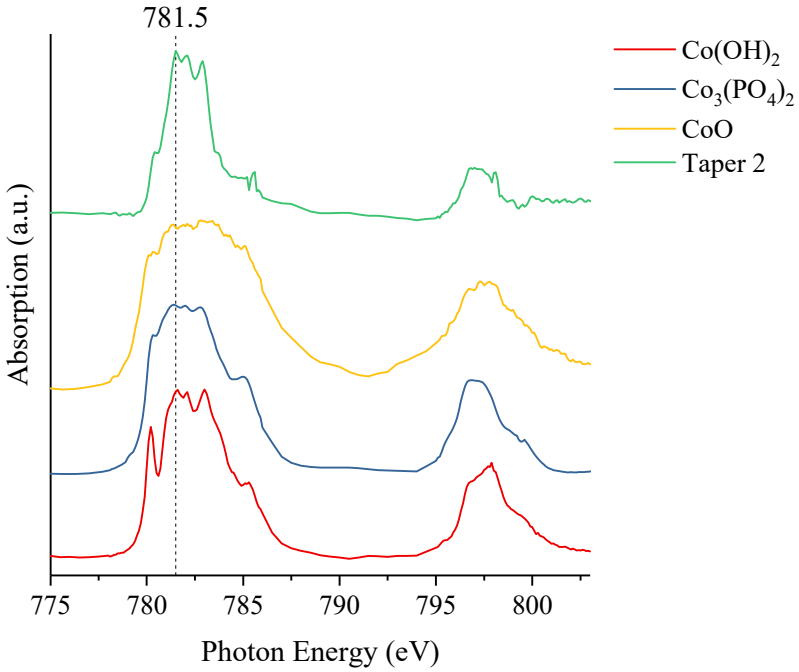

Figure 4.44 The Co $L_{2,3}$ XANES spectra of a cluster of debris from taper 2 and $Co(OH)_2$, $Co_3(PO_4)_2$ and CoO standard materials.

4.4.4 The speciation of debris released from the mixed CoCrMo/Ti alloy tapers (7 and 8) and cleaned with the enzymatic treatment – STXM/XANES, STEM/EELS and TEM/SAED analysis

The STEM and EDX characterisation of the debris released from the mixed CoCrMo/Ti alloy tapers and cleaned with the enzymatic treatment revealed both Ti and Cr rich debris, co-localised or preferentially distributed across the flakes. In order to identify the species released from the mixed material taper interface, several techniques, such as STXM/XANES, STEM/EELS and TEM/SAED were used.

The STXM/XANES analysis investigated the speciation of Cr in debris released from taper 7 and 8, by comparing the spectral features of the representative clusters with the characteristic features of Cr_2O_3 and $CrPO_4$ standard materials. The analysis included one cluster from each taper and the corresponding average spectra are shown in **Figure 4.45**, together with the representative spectra of the standard materials. For both samples, the Cr L_3 edge peak was localised at ~579.2 eV, between the edge peaks of Cr in the Cr_2O_3 (at 579 eV) and $CrPO_4$ respectively (at 579.4 eV).

The shift of the sample's edge peak from the energy level characteristic to Cr_2O_3 standard material to the edge peak of the $CrPO_4$ standard material suggested that both species existed in the debris released from the mixed material tapers. The results of the spectral analysis was also supported by

the linear fitting, which demonstrated a better match with the Cr_2O_3 than with the $CrPO_4$ standard. The weight proportions indicated that ~70% of the Cr rich debris was Cr_2O_3 with the remaining ~30% corresponding to the $CrPO_4$ phase. The set up used in the study, however, was not able to map the Cr_2O_3 and $CrPO_4$ regions to provide a visual localisation of the species across the clusters of debris.

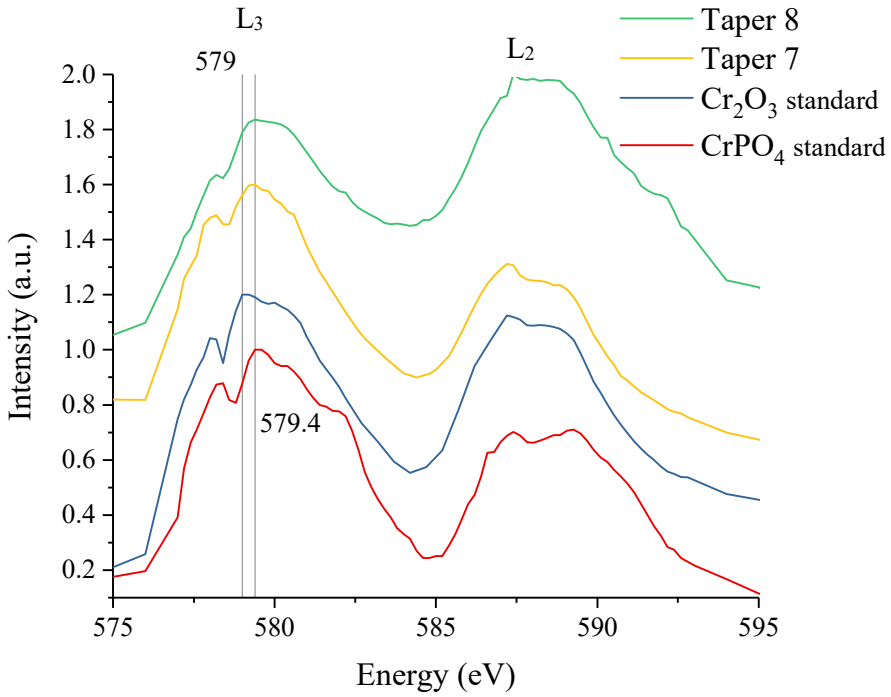

Figure 4.45 The representative Cr $L_{2,3}$ XANES spectra of debris from taper 7, taper 8 and standard Cr_2O_3 and $CrPO_4$ material.

The Co XANES spectra of a cluster of debris released from taper 7 and the spectrum of the Co^{2+} standard materials are shown in **Figure 4.46**. The spectra of the taper debris represent the average absorption signal of the individual particles in the cluster. The concentrations of the Co species in the mixed material taper debris were minimal and localised, and the individual spectra of the distinct fragments, identified with the point analysis, were weak and difficult to interpret. The L_3 edge of the average spectra matched the L_3 edges of the Co^{2+} standard materials (781.5 eV), but the spectra features did not resemble any of the standards. The rough features of the L_3 peak (781-784 eV) are similar to those of the $Co(OH)_2$, but the pre-peak edge at 780 eV was not present. The unclear results are potentially the consequence of the low amounts of Co and the possibility that more Co species comprise the wear and corrosion flakes, which result in an average XANES spectra that doesn't match any of the standard materials.

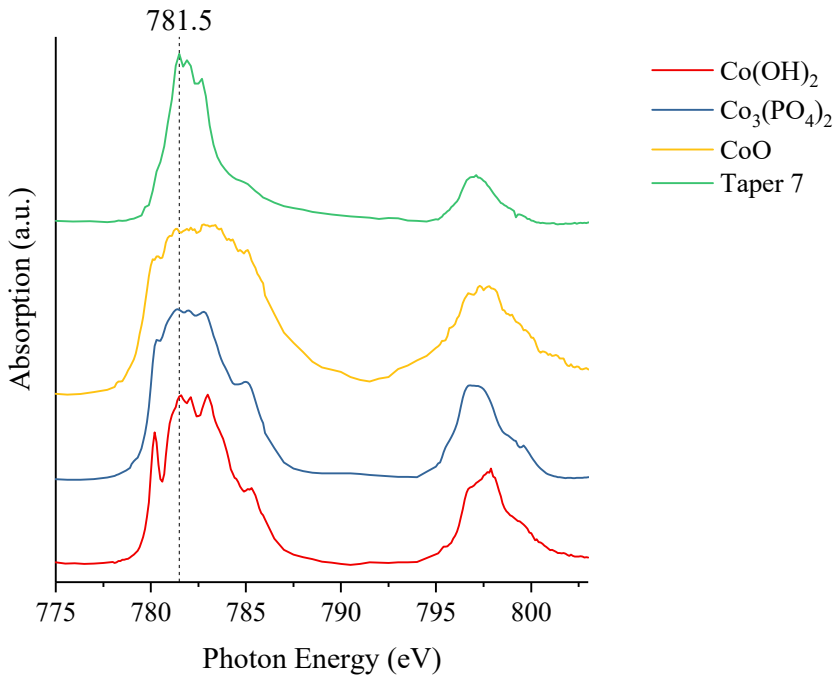

Figure 4.46 The representative Co $L_{2,3}$ XANES spectra of debris from taper 7 and $Co(OH)_2$, $Co_3(PO_4)_2$ and CoO standard materials.

The XANES analysis of one cluster of Ti debris released from each mixed material taper junction (taper 7 and 8) demonstrated the presence of TiO_2. The features of the average spectrum shown in **Figure 4.47** were compared to the XANES spectrum of the TiO_2 standard materials reported in the literature[308]. The $L_{2,3}$ edges of both samples matched the energies of the TiO_2 rutile phase. The spectral features, however, differed from that of the pristine TiO_2. The shape variation of the second peak of the L_3 edge could be explained either by the particular experimental conditions used in this study (such as the energy steps) or by the presence of other metallic species, such as Cr and/or Co. Nevertheless, the XANES analysis demonstrated the speciation of Ti in debris from mixed material taper junctions, and identified mainly Ti^{4+}, as TiO_2.

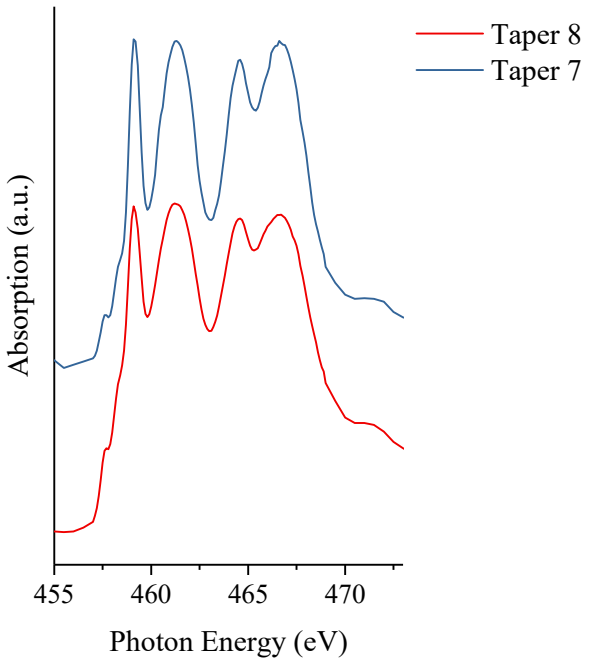

Figure 4.47 The representative Ti $L_{2,3}$ XANES spectra of debris from taper 7 and taper 8.

Three clusters of debris from each taper 7 and 8, were investigated with STEM and EELS analysis. The investigation revealed Ti, Cr and O, whose representative K (for O) and $L_{2,3}$ edges (for Cr and Ti) are shown in **Figure 4.48**. The Cr L_3 edge for all the clusters occurred at 576 eV, close to the theoretical edge peak energy characteristic for Cr (575 eV). The Ti L_3 core loss peak was also shifted to higher energy values (from 462 to ~464 eV), but the sharp spectral features confirmed the presence of Ti species. The O K line was visible at ~532 eV, indicating the existence of oxidised Cr and Ti phases.

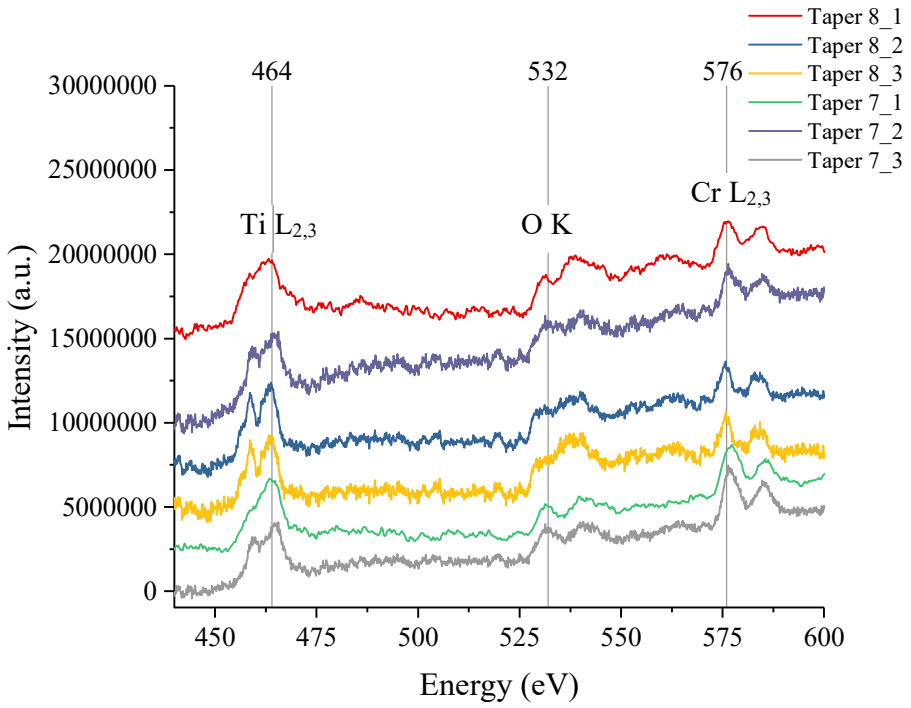

Figure 4.48 The EELS spectra of mixed Cr and Ti debris from taper 7 and 8, showing the Ti $L_{2,3}$, O K and Cr $L_{2,3}$ peaks at 464, 532 and 576 eV respectively.

In addition to STEM and EDX analysis, the distribution of Cr, Ti and O across the particles aggregates was also investigated with STEM and EELS mapping. **Figure 4.49 A** shows the localisation of Cr, Ti and O in a representative cluster of debris released from taper 7 and characterised with STEM and EELS analysis (EELS spectra Taper 7_1 in **Figure 4.48**). Although both metals were widely spread across the surface of the particles, the preferential distribution of Cr and Ti was observed on the top region of the cluster in **Figure 4.49 B**. Cr was mainly localised on the round and oval structures, which resemble the particles, while Ti partially overlaps the Cr rich debris, without following the particle shape. The high-resolution image of the debris marked '2' in **Figure 4.49 B** is shown in **Figure 4.49 C** and corresponds to a crystalline Cr rich nanoparticle. The measured lattice spacing (0.266 nm) was characteristic of the (104) plane of the Cr_2O_3 phase and provided the speciation of the Cr rich debris[309].

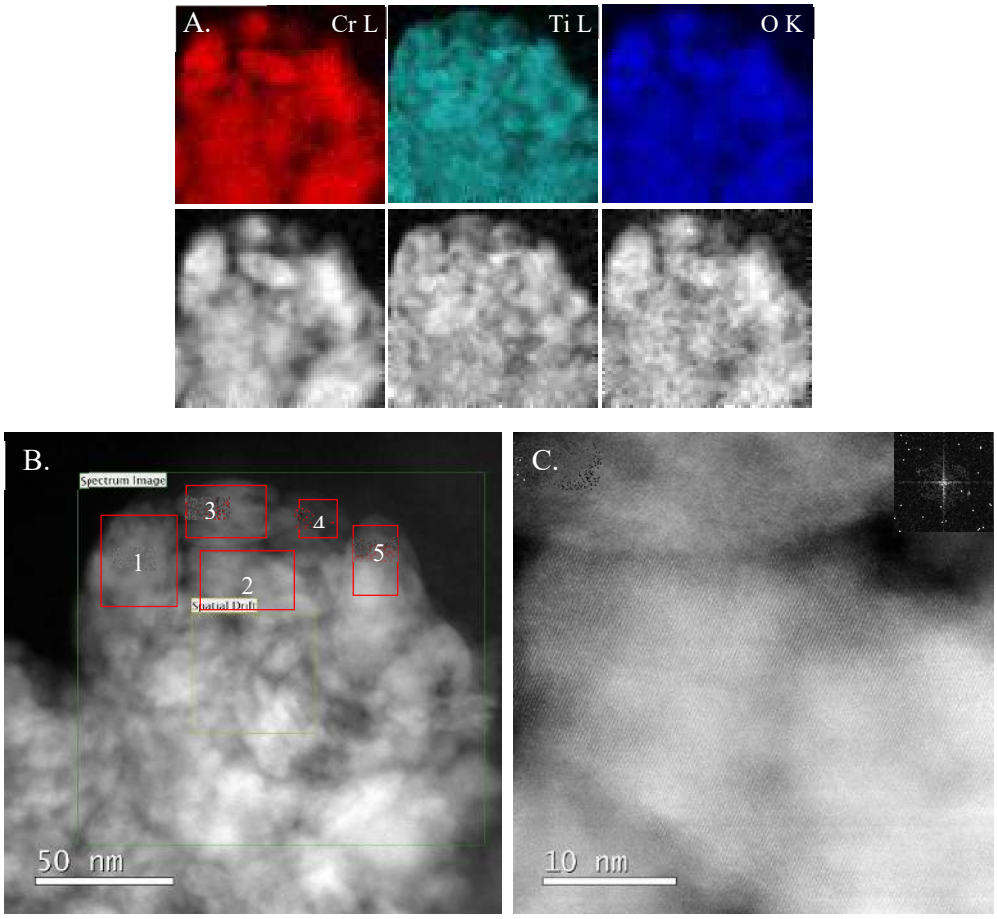

Figure 4.49 The HAADF-STEM and EELS analysis of debris released from taper 7; A. the STEM/EELS maps showing the distribution of Cr, Ti and O; B. the STEM micrograph of the cluster investigated with EELS; C. the high-resolution image of the particle marked with 2.

The quantitative analysis provided the composition of debris in the regions marked 1-5 in **Figure 4.49 B**. The atomic ratio (Cr/O or Ti/O, represented in tables as X/O) and the atomic percentage (at. %) for the whole cluster and regions 1-5 are shown in **Table 4.19**. In most of the regions, the quantitative results showed an atomic ratio and atomic % matching Cr_2TiO_5. This mixed Cr and Ti oxide has an atomic ratio of 0.20:0.40:1/Ti:Cr:O and an atomic percentage of 25% Cr, 62.5% O and 12.5% Ti. This phase, however, requires high pressures and temperatures to form and is therefore unlikely to be generated in the body, at the taper interface. The results may also suggest the presence of an equimolar mixture of Cr_2O_3 and TiO_2 which has the same atomic ratio and atomic percentage as the Cr_2TiO_5.

Table 4.19 The atomic ratio (X/O, where X is Ti, O or Cr) and atomic % of the cluster and marked regions in Figure 4.49 B.

Cluster	Atomic ratio (X/O)	At %
Ti	0.23 (±0.04)	13.94
O	1.00 (±0.00)	60.01
Cr	0.43 (±0.06)	26.05

Reg 1	Atomic ratio (X/O)	At %
Ti	0.21 (±0.03)	12.29
O	1.00 (±0.00)	59.36
Cr	0.48 (±0.06)	28.35

Reg 2	Atomic ratio (X/O)	At %
Ti	0.23 (±0.03)	13.09
O	1.00 (±0.00)	55.79
Cr	0.56 (±0.08)	31.12

Reg 3	Atomic ratio (X/O)	At %
Ti	0.20 (±0.03)	12.63
O	1.00 (±0.00)	62.26
Cr	0.40 (±0.06)	25.12

Reg 4	Atomic ratio (X/O)	At %
Ti	0.24 (±0.03)	14.95
O	1.00 (±0.00)	61.14
Cr	0.39 (±0.05)	23.91

Reg 5	Atomic ratio (X/O)	At %
Ti	0.20 (±0.03)	12.40
O	1.00 (±0.00)	60.51
Cr	0.45 (±0.06)	27.09

Similar results were obtained from the STEM and EELS mapping of another cluster of particles originating from taper 7, whose corresponding EELS spectra is shown in **Figure 4.48**, labelled Taper 7_3. The elemental maps are shown in **Figure 4.50 A** and demonstrate the co-localisation of Cr, Ti and O. The high-resolution image of the Cr rich crystalline nanoparticle marked '1' in **Figure 4.50 B** is shown in **Figure 4.50 C** and allowed the measurement of the lattice spacing. The value (0.267 nm) corresponds to the (104) plane of the Cr_2O_3 and confirms the release of this particular phase at the mixed material taper interface. The overlapping Cr and Ti maps suggest that the Cr rich nanoparticles and Ti debris are independent phases which are stacked on top of each other, forming the debris agglomerate.

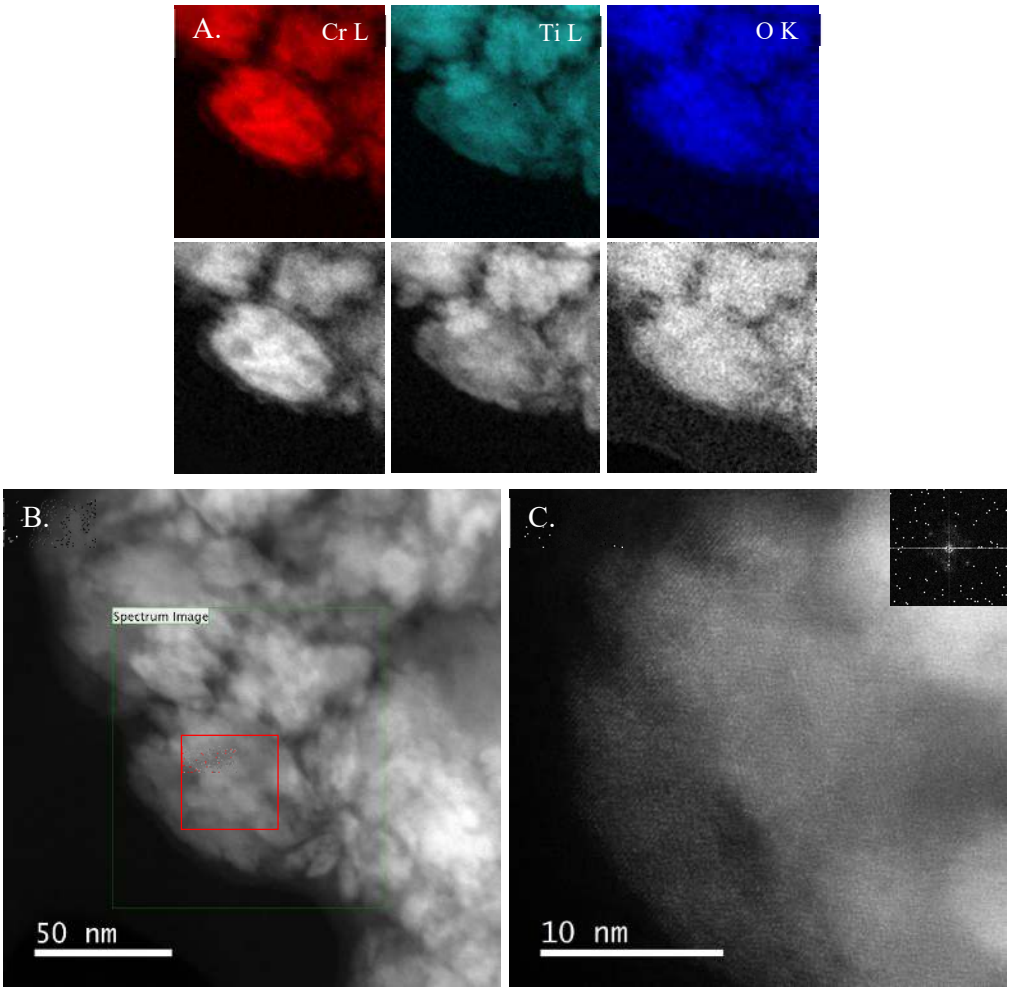

Figure 4.50 The HAADF-STEM and EELS analysis of debris released from taper 7; A. the STEM/EELS maps showing the distribution of Cr, Ti and O; B. the STEM micrograph of the cluster investigated with EELS; C. the high-resolution image of the particle marked with 1.

The quantitative analysis of the whole cluster shown in **Figure 4.50 B** and the Cr rich crystalline nanoparticles marked '1' and represented in **Figure 4.50 C**, also confirmed the presence of mixed Cr_2O_3 and TiO_2. The results are shown in **Table 4.20** and correspond to an equimolar mixture of Cr_2O_3 and TiO_2, or the mixed Cr and Ti oxide (i.e. Cr_2TiO_5).

The STEM and EELS mapping and quantitative and qualitative analysis of more clusters of debris released from the mixed CoCrMo/Ti taper junctions (i.e. taper 7 and 8) are available in Appendix B and C.

Table 4.20 The atomic ratio (X/O, where X is Ti, O or Cr) and atomic % of the cluster and marked regions in Figure 4.50

Cluster	Atomic ratio (X/O)	At %
Ti	0.28 (±0.04)	16.63
O	1.00 (±0.00)	58.61
Cr	0.42 (±0.06)	24.76

Reg 1	Atomic ratio (X/O)	At %
Ti	0.23 (±0.04)	13.88
O	1.00 (±0.00)	60.24
Cr	0.43 (±0.06)	25.88

The methods used so far in this study to understand the speciation of the Cr and Ti rich debris (i.e. STXM/XANES and STEM/EELS) provided reliable evidence of the presence of Cr_2O_3 and TiO_2. The quantitative EELS results showed that equal amounts of Cr and Ti oxides were released from the mixed material taper interface. To confirm the presence of TiO_2 in addition to Cr_2O_3, TEM and SAED analysis were used. The investigation included one cluster of debris released from taper 7 and three clusters of debris released from taper 8. **Figure 4.51 A** and **B** show the TEM micrograph of a cluster of particles released from taper 8, and the corresponding SAED pattern.

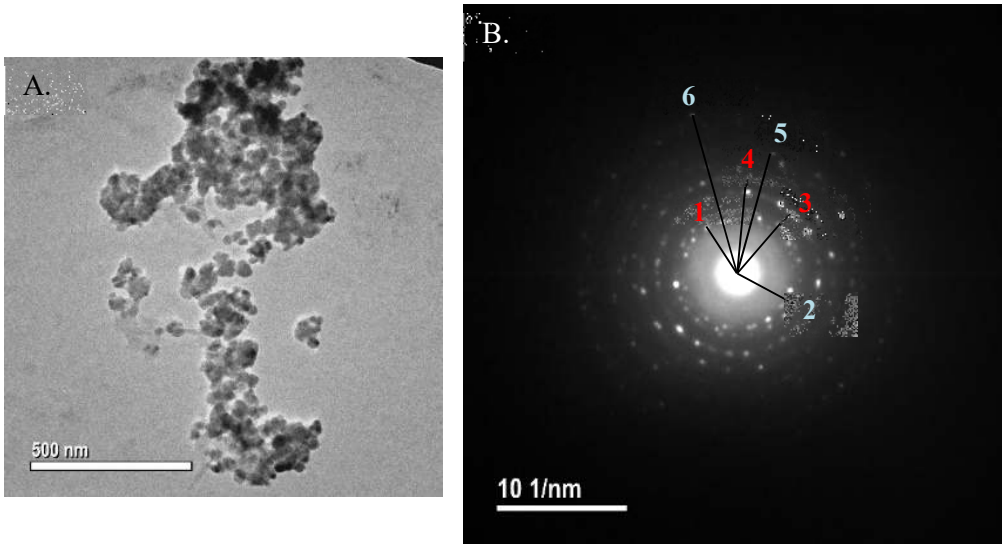

Figure 4.51 The TEM/SAED investigation of debris from taper 8: A. The TEM micrograph of a representative cluster; B. The indexed SAED pattern of the cluster shown in A.

The measured d-spacing and the lattice spacing of the possible oxides (standard Cr_2O_3, TiO_2 and Cr_2TiO_5) and the associated hkl planes are shown in **Table 4.21**. Some of the measured lattice spacing matched the d-spacing of more different planes of the distinct phases (i.e. Cr_2O_3, TiO_2 or Cr_2TiO_5 pristine materials). Others, however, corresponded to either TiO_2 or Cr_2O_3 and thus demonstrated their release from the mixed material taper junctions. For all the investigated clusters, the results suggested the presence of a mixture of Cr_2O_3 and TiO_2, but their proportion remained unknown.

Table 4.21 The measure d-spacing of debris from taper 8 and the matched standard d-spacing and hkl planes of the pristine Cr_2TiO_5, Cr_2O_3 and TiO_2.

	Measured d [nm]	**Standard d [nm]**					
		Cr_2TiO_5	hkl	Cr_2O_3	hkl	TiO_2	hkl
1	0.234	0.233	-211	-	-	0.234	220
2	0.207	0.210	-311	0.205	202		
3	0.161	0.163	400	-	-	0.161	113
4	0.135	-	-	-	-	0.136	400
5	0.103	-	-	0.104	21 10	-	-
6	0.081	-	-	0.083	330	-	-

4.5 Comparative Studies

4.5.1 The effects of the alkaline and enzymatic treatments on the particle characteristics

The study assessed the efficiency of the alkaline and enzymatic treatments, with respect to:

i) The ability to breakdown the organic matrix (biomolecules and salts) and provide clean particles for the detailed structural characterisation;

ii) Their effects on the particle morphology and size distribution;

iii) Their effects on the particle composition;

The investigation included debris from three CoCrMo secondary interfaces (taper 1, taper 2 and stem 9), which were subjected to the alkaline and enzymatic cleaning and were characterised using state-of-the-art imaging techniques. The ability of the treatments to release particles from the organic matrix was assessed by comparing the STEM micrographs of cleaned debris with micrographs of as-retrieved debris (i.e. uncleaned) from the same wear site. The micrographs corresponding to the as-retrieved debris from taper 1 are shown in **Figure 4.52** column A and revealed the level of native contamination. The low and high-resolution micrographs showed clusters of nanoparticles embedded in a less electron dense phase, compared to the metal particles, which represented most of the sample's area. The micrographs of the particles cleaned with the enzymatic and alkaline treatments are shown in **Figure 4.52** column B and C respectively. Both treatments resulted in large aggregates surrounded by less organic matrix and more particles exposed for analyses. The high-resolution micrographs of the particles cleaned with the alkaline and enzymatic treatments revealed the lattice fringes of the crystalline structures, which served as a method to identify the Cr oxide phase (Cr_2O_3). Despite the efficiency of the cleaning procedures which resulted in clean debris, traces of biological contamination were still visible after both treatments.

The comparison between debris released from taper 1, cleaned with the alkaline and enzymatic treatments did not reveal differences between the levels of contamination. However, the comparison of debris released from taper 2 and stem 9 and cleaned with the alkaline and enzymatic treatment suggested that cleaner particles resulted from the alkaline digestion. Representative micrographs of debris cleaned with each of the treatments are shown in Chapter 4.2. for taper 1 and 2, and in Chapter 4.3 for stem 9. The comparison, however, did not provide any quantitative or statistical results to support the conclusions drawn from the visual assessment of the level of contamination, which indicated that the alkaline treatment was more efficient in breaking down the organic matrix to release clean particulate debris.

A. As-retrieved debris. B. Enzymatic cleaning. C. Alkaline cleaning.

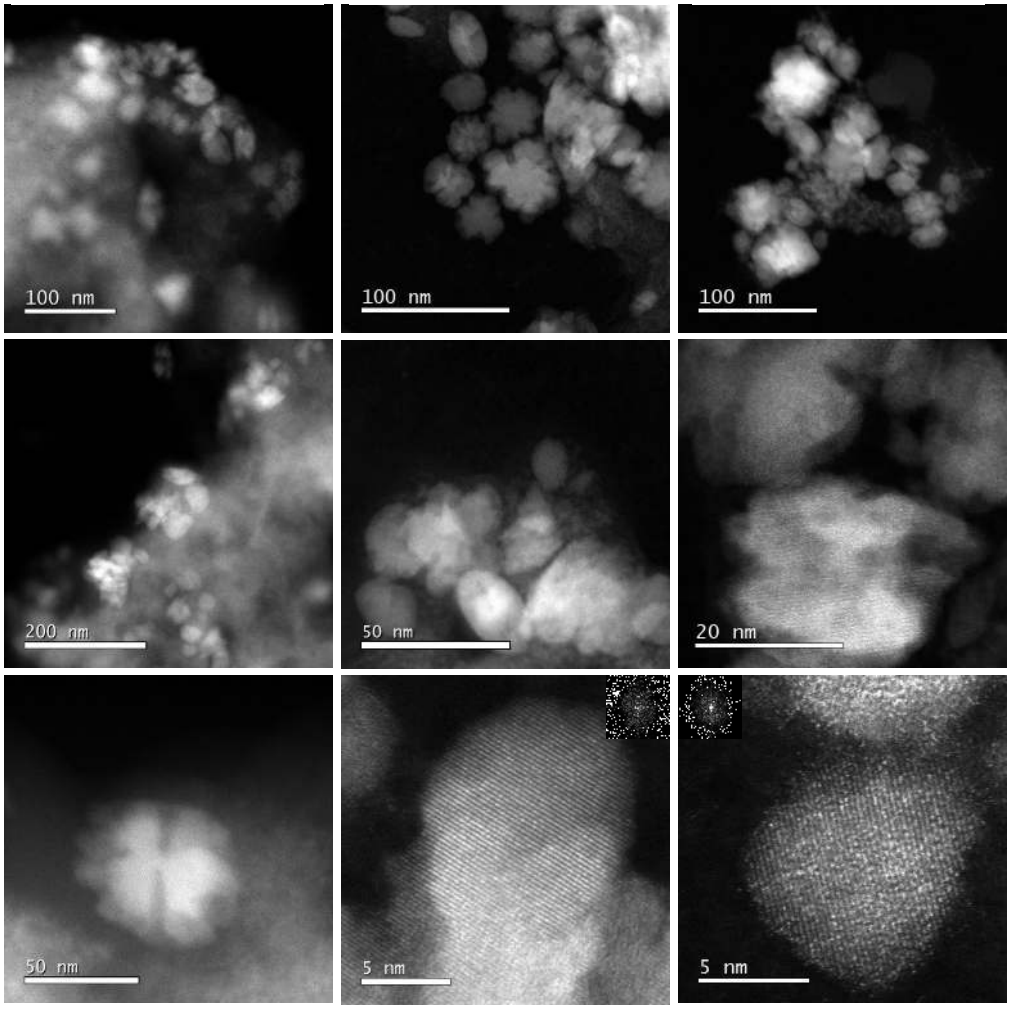

Figure 4.52 The HAADF-STEM micrographs as-retrieved debris from taper 1 (Column A), cleaned with the enzymatic (Column B) and alkaline treatment respectively (Column C), showing the level of biological contamination before and after the treatments.

The effect of the treatments on the particle morphology and size distribution was assessed based on the investigation of at least 75 particles from each sample and digestion treatment. The number of particles characterised, the size ranges and the mean and median d_{max} for each sample and treatment are shown in **Table 4.22**. **Figure 4.53** shows the size distributions of the particles released from taper 1, taper 2 and stem 9, cleaned with both treatments.

Table 4.22 The number of particles characterised for each sample and the corresponding size ranges and mean and median d_{max} after the alkaline and enzymatic treatment.

Sample	Treatment	No particles	Size range	Mean d_{max}	Median d_{max}
Taper 1	Enzymatic	75	4-64 nm	23.5 nm (±14.0)	20 nm
	Alkaline	100	3-60 nm	15.9 nm (±11.8)	12 nm
Taper 2	Enzymatic	107	5-67 nm	24.4 nm (±12.6)	22 nm
	Alkaline	110	3-65 nm	20.3 nm (±13.3)	17 nm
Stem 1	Enzymatic	82	7-32 nm	16.9 nm (±6.1)	15 nm
	Alkaline	83	6-37 nm	17.1 nm (±7.1)	16 nm

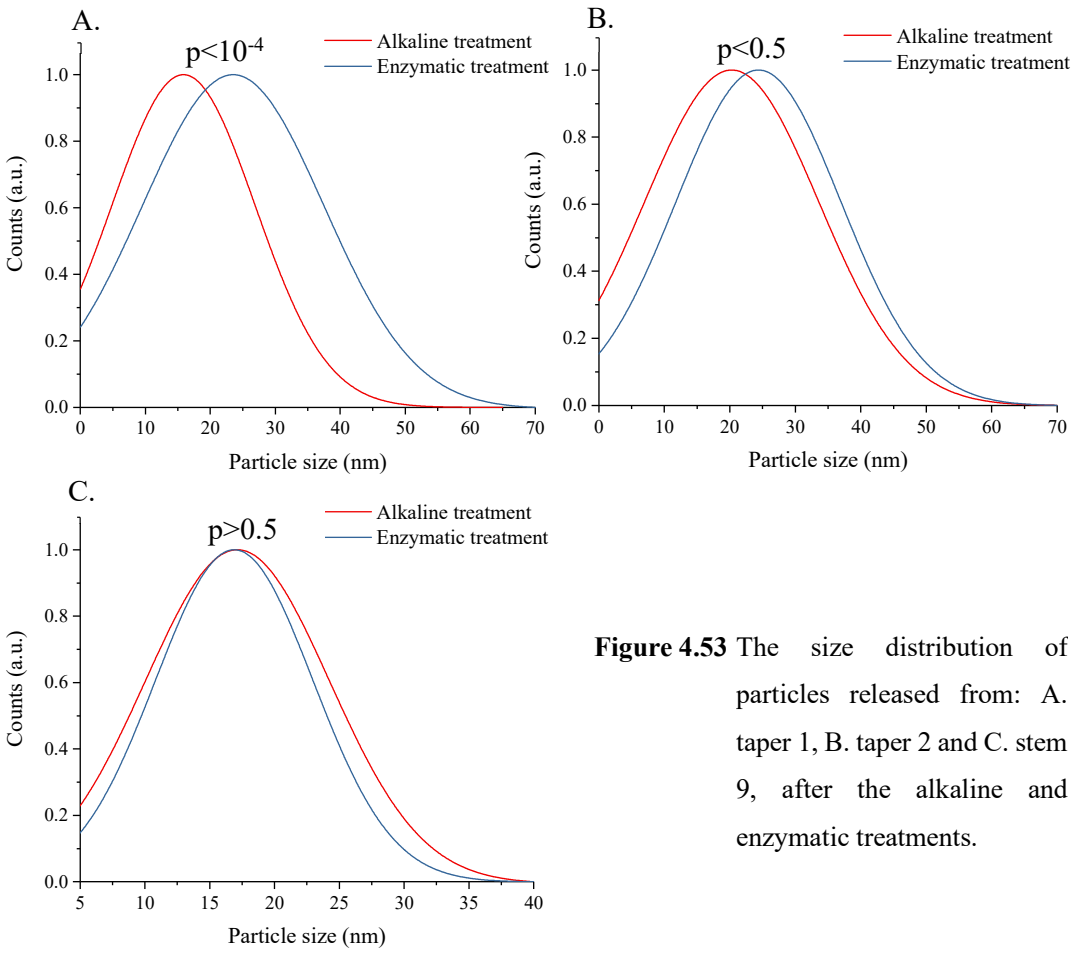

Figure 4.53 The size distribution of particles released from: A. taper 1, B. taper 2 and C. stem 9, after the alkaline and enzymatic treatments.

The particles released from the same wear site (i.e. taper 1, taper 2 or stem 9) and cleaned using the alkaline or enzymatic digestion, had similar size ranges, regardless of the treatment used. However, for each taper sample, the average particle sizes were smaller after the alkaline treatment (15.9 nm (±11.0) vs 23.5 nm (±14.0) for taper 1; 20.3 nm (±13.3) vs 24.4 nm (±12.6) for taper 2) and the differences between the mean sizes after the two treatments were statistically significant ($p<0.0002$ for taper 1 and $p<0.03$ for taper 2). In contrast, the particles released from the stem interface had a smaller average size after the enzymatic treatment (16.9 nm (±6.1) vs 17.1 nm (±7.1)), but the difference between the two distributions was not statistically significant ($p>0.5$).

The morphological characteristics of the particles, assessed from the AR values, are shown in **Table 4.23**. With both treatments, the particles released from the stem interface are mainly round or oval, with few needle-shaped debris.

Table 4.23 The morphology of the particles originating from taper 1, taper 2 and stem 9, cleaned with the alkaline and enzymatic treatments.

Sample	**Treatment**	**Round**	**Oval**	**Needle shaped**
Taper 1	Enzymatic	48%	49%	3%
	Alkaline	69%	29%	2%
Taper 2	Enzymatic	39%	53%	8%
	Alkaline	61%	39%	0%
Stem 1	Enzymatic	62%	32%	0%
	Alkaline	52%	37%	11%

The average proportions of Cr, Co and Mo in the particles cleaned with the enzymatic and alkaline treatments are shown in **Figure 4.54**. After the alkaline treatment, the particles released from tapers (**Figure 4.54 A** and **B**) experienced a significant decrease in the Cr content, concomitant with an increase of the Co proportion, compared to the particles cleaned with the enzymatic treatment ($p<0.0003$ for taper 1 and $p<0.02$ for taper 2). For taper 1, the proportions of Cr and Co in particles cleaned with the enzymatic treatment were 88.0% (±3.5) and 10.5% (±4.0) respectively, and those in debris cleaned with the alkaline treatment were 79.7% (±3.6) and 19.4% (±3.6) respectively. For

taper 2 the concentrations of Cr and Co after the enzymatic treatment were 91.3% (±5.4) and 7.9% (±5.7) respectively, and 73.4% (±3.3) Cr and 25.6% (±3.3) Co after the alkaline treatment.

The particles released from the cement-stem interface (**Figure 4.54 C**) contained more Cr in the particles cleaned with the alkaline treatment (78.4% (±0.9)) than in the particles treated with the enzymatic protocol (76.7% (±1.2)). The difference was statistically significant, but p=0.04 was close to the level of confidence (i.e. 0.05).

In contrast, the P content in the taper and stem samples was lower after the alkaline treatment (Figure 3 D) (6.9% (±3.6) vs 23.2% (±6.9), $p<10^{-5}$ for taper 1; 9.8% (±1.0) vs 20.3% (±6.8), $p>0.05$ for taper 2; 2.5% (±1.1) vs 21.1% (±1.7), $p<10^{-5}$ for stem). The proportion of P, therefore, suggested that the alkaline treatment was more efficient in breaking down and dissolving the organic matrix, compared to the enzymatic treatment. The number of particles used to determine the composition of debris with EDX analysis, varied from 16 to 60 for the samples cleaned with the enzymatic treatment and from 30 to 50 for the samples cleaned with the alkaline protocol.

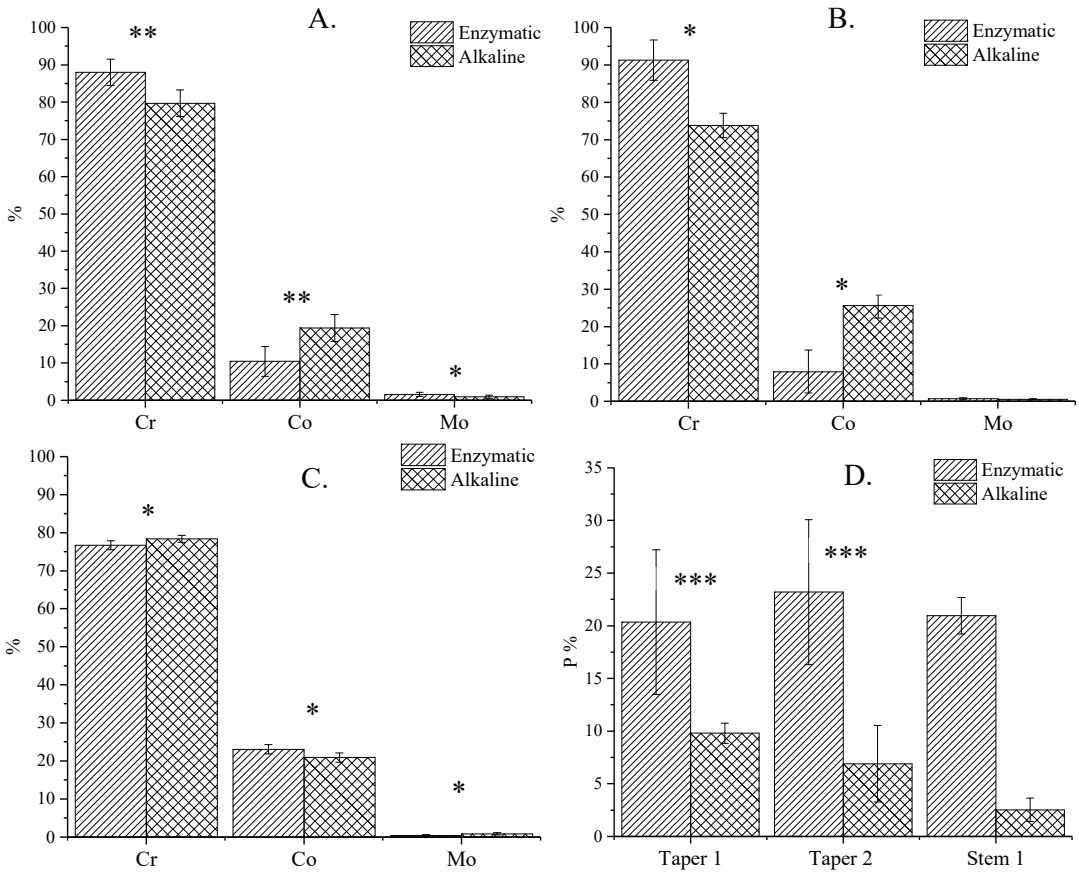

Figure 4.54 The variation of Cr, Co and Mo proportions with treatments, for A. taper 1, B. taper 2 and C. stem 9. The variation of P (decrease) after the alkaline treatment in comparison to the enzymatic digestion is shown in D. ($p<0.05$*; $p<0.001$**; $p<10^{-5}$***)

4.5.2 Comparison between imaging techniques: TEM vs STEM

The TEM investigation was used as a complementary imaging technique which aimed to select the grids and sample to be investigated with the HR-STEM. The technique revealed all types of debris shown in the previous sections using HR-STEM after the alkaline and enzymatic cleaning. Representative micrographs of the Cr oxide nanoparticle or Co rich needle-like debris are shown in **Figure 4.56**. The EDX maps in **Figure 4.55** revealed the metallic elements that comprised the partially digested flakes or the Cr rich clusters of nanoparticles. However, due to the limited spatial resolution, the structural details of the individual debris could not be determined by TEM imaging.

The investigation using TEM identified mainly clusters of debris, which in some cases, allowed for the measurement of the particle size. In some situations, particularly when the clusters were dense and thick, the particle boundaries could not be easily distinguished and the measurement of the particle size was difficult, and potentially associated with errors. This study proposed to assess the differences between the particle size distributions of the taper and stem debris, determined using a TEM representative for the old generation of the electron microscopes, and a HR-STEM, which allowed a more detailed and accurate characterisation of the particles.

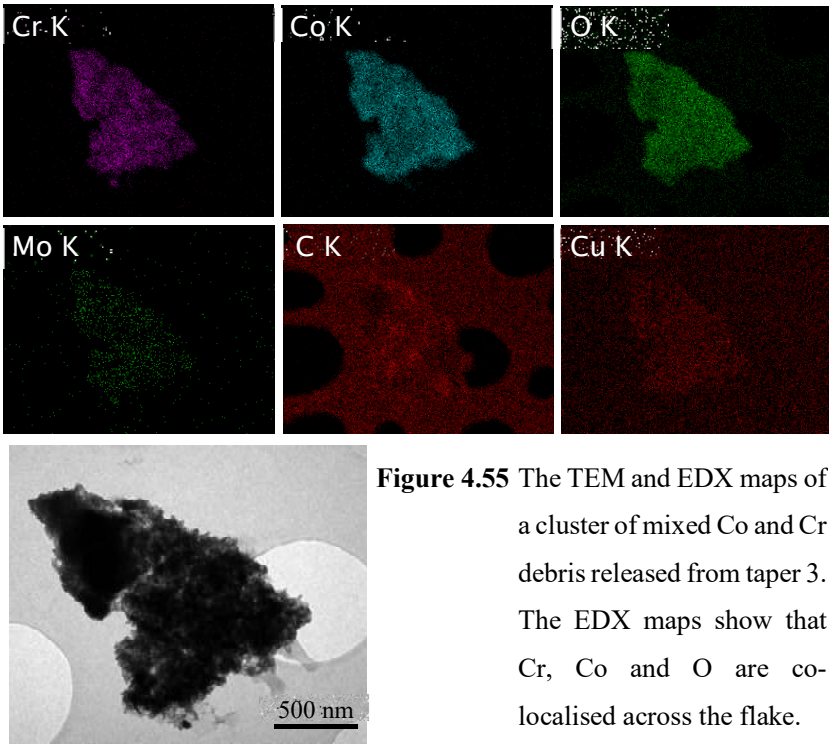

Figure 4.55 The TEM and EDX maps of a cluster of mixed Co and Cr debris released from taper 3. The EDX maps show that Cr, Co and O are co-localised across the flake.

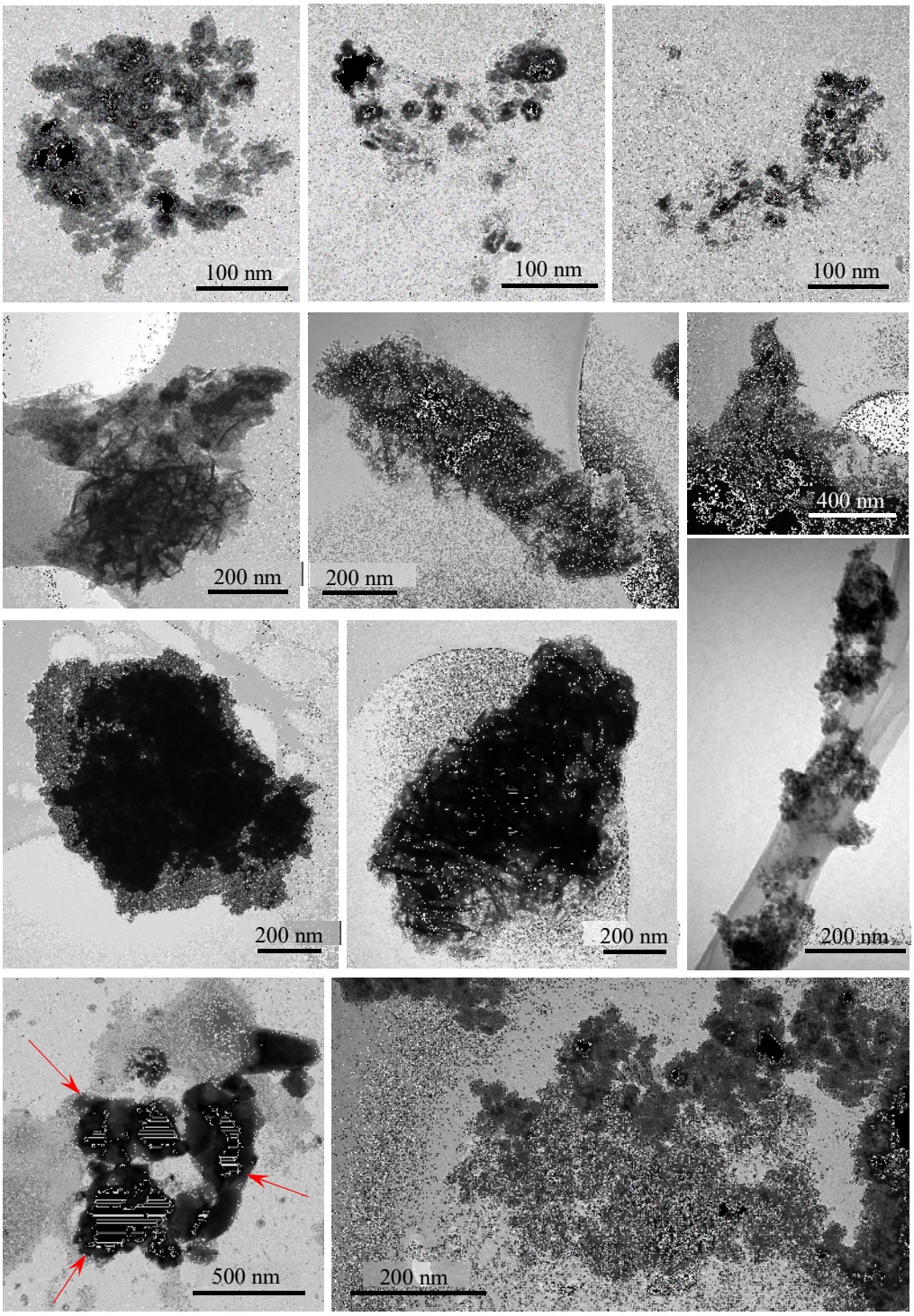

Figure 4.56 The TEM micrographs of round clusters of Cr rich nanoparticles, needle-like Co rich structures and Ca agglomerates (see arrow) released from taper and cement-stem interface and cleaned with the alkaline or enzymatic treatment.

The particles size distributions of debris from 2 tapers (taper 1 and 2) and 3 stems (stem 9, 10 and 11), cleaned with the alkaline or enzymatic treatments and characterised by both TEM and HR-STEM are shown in **Figure 4.57**. The number of the particles investigated and the corresponding size ranges and mean and median d_{max} are shown in **Table 4.24**. For all the samples, the size ranges after the TEM characterisation were shifted to higher sizes than those revealed after the STEM investigation. Both the smallest and the largest particles of the size rages that resulted after the TEM characterisation were larger than those revealed by STEM. Also, the mean and median sizes were smallest for all the samples characterised by STEM, although only for three samples the differences were statistically significant ($p<0.002$ for taper 1 – alkaline, $p<10^{-5}$ for stem 9, and $p<10^{-4}$ for stem 10).

Table 4.24 The number of particles characterised for each sample using TEM and STEM, and the corresponding size ranges and mean and median d_{max} after the alkaline or enzymatic treatment.

Sample	**EM**	**No of particles**	**Size range**	**Mean d_{max}**	**Median d_{max}**
Taper 1 (enzymatic)	TEM	75	7-64 nm	26.4 nm (±11.4)	27.3 nm
	STEM	75	4-64 nm	23.5 nm (±14.0)	20.3 nm
Taper 1 (alkaline)	TEM	67	5-98 nm	22.6 nm (±14.7)	22.1 nm
	STEM	100	3-60 nm	15.9 nm (±11.0)	11.8 nm
Taper 2 (alkaline)	TEM	25	4-66 nm	22.3 nm (±14.9)	18.1 nm
	STEM	110	3-65 nm	20.3 nm (±13.3)	16.8 nm
Stem 9 (alkaline)	TEM	28	12-43 nm	25.8 nm (±9.4)	22.6 nm
	STEM	83	6-37 nm	17.2 nm (±7.1)	15.9 nm
Stem 10 (alkaline)	TEM	38	10.6-40 nm	22.5 nm (±8.1)	21.5 nm
	STEM	33	6.2-34 nm	15.7 nm (±6.9)	6.2 nm
Stem 11 (alkaline)	TEM	50	10-39 nm	22.8 nm (±6.8)	22.2 nm
	STEM	22	9-31 nm	19.9 nm (±5.7)	19.8 nm

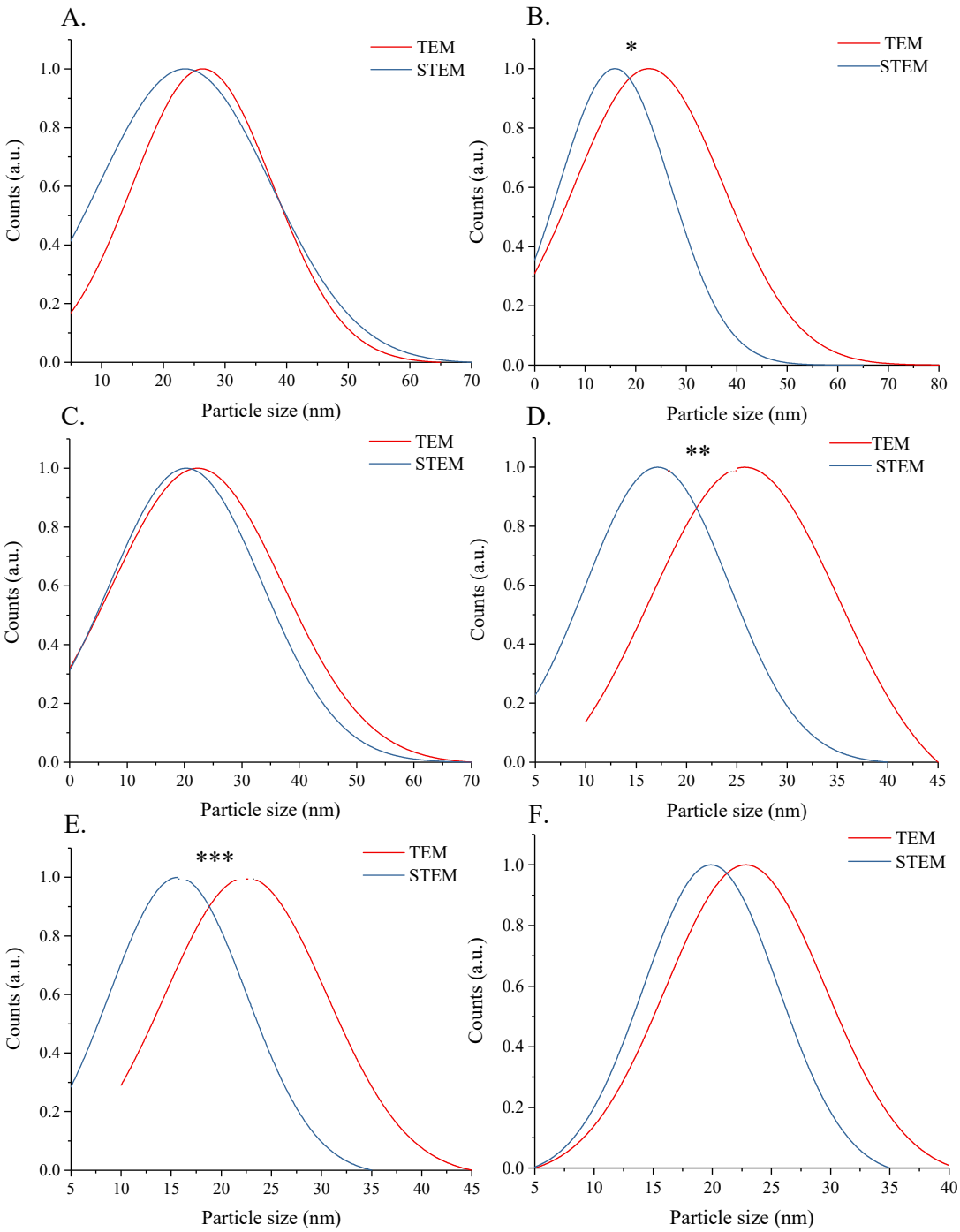

Figure 4.57 The size distribution of particles released from A: taper 1 (enzymatic), B: taper 1 (alkaline), C: taper 2 (alkaline), D: stem 9 (alkaline), E: stem 10 (alkaline) and F: stem 11 (alkaline), investigated with TEM (red) and STEM (blue). *$p<10^{-2}$; **$p<10^{-5}$; ***$p<10^{-4}$

The distributions of the particles in the three main morphology categories are shown in **Table 4.25**. The particles released from all the samples were mainly round and oval, but their proportions depended on the imaging technique. For taper 1 (alkaline), stem 10 and stem 11, the particle morphology classifications were in agreement after the TEM and STEM characterisation. For the other three samples, however, the proportions of the round, oval and needle-shaped particles differed with the electron microscopy technique. The differences, however, may not be necessarily attributed to the use of different techniques. The characteristics of the particles may differ from one fragment to another, although they originated from the same wear site and retrieval.

Table 4.25 The morphology of the particles characterised for each sample using TEM and STEM.

Sample	**EM**	**Round %**	**Oval %**	**Needle shaped %**
Taper 1 (enzymatic)	TEM	71	28	1
	STEM	48	49	3
Taper 1 (alkaline)	TEM	55	33	12
	STEM	69	29	2
Taper 2 (alkaline)	TEM	36	56	8
	STEM	61	39	0
Stem 9 (alkaline)	TEM	29	50	21
	STEM	75	25	0
Stem 10 (alkaline)	TEM	87	13	0
	STEM	85	12	3
Stem 11 (alkaline)	TEM	26	60	14
	STEM	36	64	0

Here, the comparative study suggested that the particles size distributions may be different when using TEM and STEM. However, statistical significance ($p<0.05$) was only found between half of the investigated samples. The size ranges were different for all the samples, with the TEM characterisation revealing larger particles as a consequence of the limited spatial resolution.

4.5.3 Comparison between debris released from the CoCrMo tapers and cement-stem interface of the same retrieval

The main objectives of this section were:

i) To assess the differences between the morphology and size distribution of taper and stem debris;

ii) To compare the composition and speciation of debris in relation to the origin;

The investigation included debris released from the taper and cement-stem interface of retrievals 1 and 2 (i.e. taper and stem 1, taper and stem 2). The particles were subjected to cleaning using the enzymatic treatment and were characterised with STEM/EDX, STEM/EELS and TEM/SAED to determine the morphology, size distribution, composition and phase analysis.

At least 75 particles from each wear site were characterised to investigate the morphology and size distribution of the representative particulate debris. **Table 4.26** shows the number of particles, the corresponding size ranges and the mean and median d_{max} of the particles in relation to their origin.

Table 4.26 The number of particles characterised for each sample and wear site, and the corresponding size ranges and mean and median d_{max} after the enzymatic treatment.

Sample	**No of particles**	**Size range**	**Mean d_{max}**	**Median d_{max}**
Taper 1	75	4-64 nm	24 nm (±14.0)	20 nm
Stem 1	85	4-49 nm	17 nm (±8.7)	16 nm
Taper 2	107	6-67 nm	24 nm (±12.6)	22 nm
Stem 2	115	6-37 nm	16 nm (±7.4)	14 nm
All tapers	182	4-67 nm	24 nm (±13.2)	21 nm
All stems	200	4-49 nm	16 nm (±7.9)	15 nm

The size distributions of the particles released from each taper-stem couple (i.e. taper and cement-stem interface of the same implant retrieval) are shown in **Figure 4.58 A** and **B**. The particles originating from the CoCrMo tapers have significantly wider size distributions and larger mean (24 nm (±14.0 nm) vs 17 nm (±8.7 nm) for taper-stem 1 and 24 nm (±12.6 nm) vs 16 nm (±7.4 nm) for taper-stem 2) and median d_{max} than the particles released from the corresponding stem interfaces ($p<0.001$ and $p<10^{-8}$ for taper-stem 1 and taper-stem 2 respectively). The comparison between the size of the particles from taper 1 and taper 2, and stem 1 and stem 2 respectively, showed no significant differences ($p=0.7$ for tapers and $p=0.5$ for stems). Comparison between the size

distributions of the particles from tapers and stems (**Figure 4.58 C**) showed significant differences between the taper and stem debris ($p<10^{-10}$). The particles from all tapers and stems were in the nanometre size range, with none larger than 70 nm.

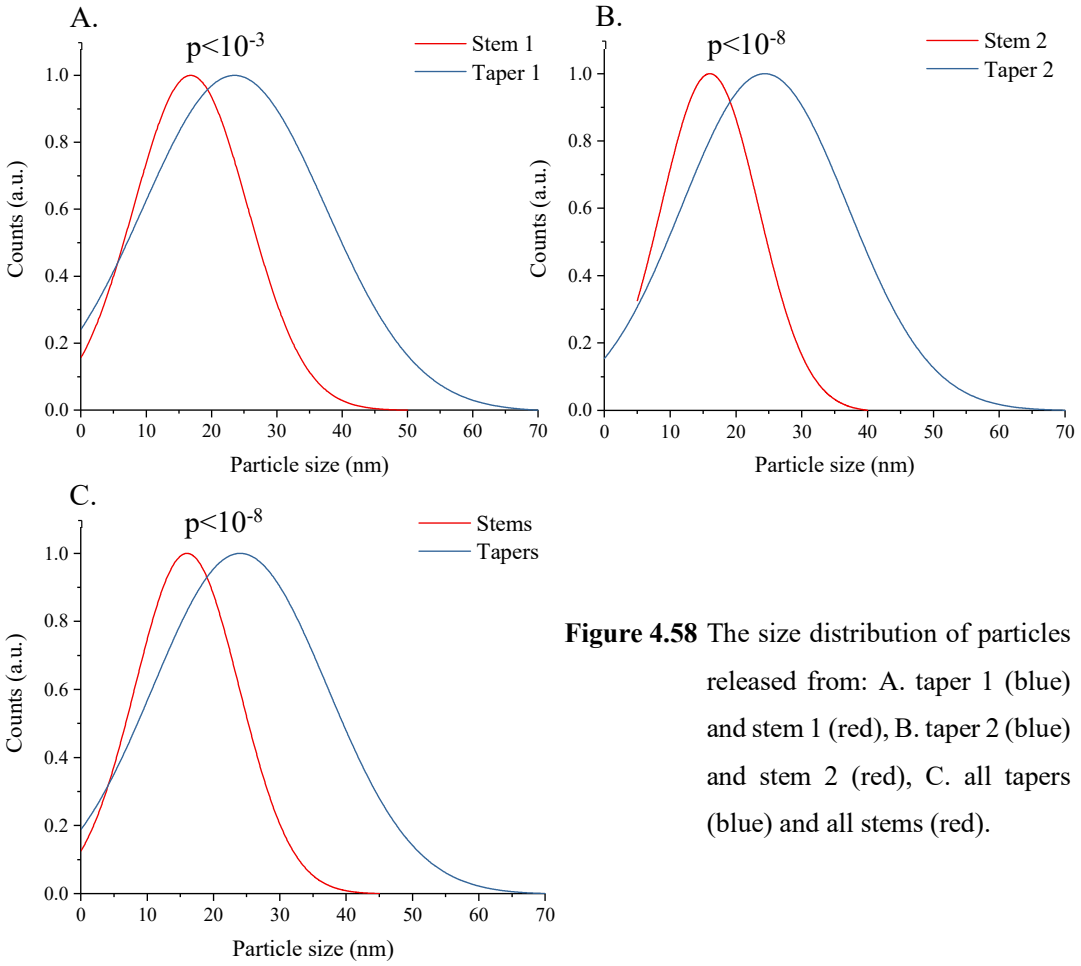

Figure 4.58 The size distribution of particles released from: A. taper 1 (blue) and stem 1 (red), B. taper 2 (blue) and stem 2 (red), C. all tapers (blue) and all stems (red).

The results of the morphology comparison are summarised in **Table 4.27** and show that more oval particles were released from the tapers, compared to the particles released from the cement-stem interface, which were mainly round.

The mean sizes of the round, oval and needle-shaped particles released from each taper and cement-stem interface are shown in **Table 4.28**. The round particles were the smallest and the particle sizes increased for the oval and needle-shaped debris. The statistical analysis, however, only showed significant differences between the sizes of the round and needle ($p<0.05$), and oval and needle-shaped particles ($p<0.05$) originating from stem 1, and between the round and needle-shaped particles released from taper 2 ($p<10^{-5}$). The percentage of needle-shaped particles varied from 1 to 8% for all the samples, while the round and oval debris was more abundant (see **Table 4.27**) and the statistical differences could be a consequence of the small number of particles in the needle-shaped category.

Table 4.27 The results of the morphology analysis, showing the percentage of round, oval and needle-shaped particles released from each taper and stem sample.

Sample	**Round %**	**Oval %**	**Needle shaped %**
Taper 1	48	49	3
Stem 1	54	41	5
Taper 2	39	53	8
Stem 2	72	27	1

Table 4.28 The mean sizes of the round, oval and needle-shaped particles released from tapers and associated stems.

Sample	**Mean d_{max}**		
	Round	*Oval*	*Needle-shaped*
Taper 1	21 nm	25 nm	37 nm
Stem 1*	15 nm	19 nm	23 nm
Taper 2**	21 nm	26 nm	32 nm
Stem 2	15 nm	18 nm	25 nm

The average elemental composition of the round and oval particles released from tapers and stems are shown in **Table 4.29**. The results were obtained from the STEM/EDX quantitative analysis of 5 to 11 particles from each wear site and morphology type, and did not include needle-shaped particles, which were more difficult to find to gain enough data for the statistical analysis. The comparison between the composition of the round and oval particles from the same source (i.e. round vs oval particles from tapers and round vs oval particles from stems) showed no significant differences ($p>0.1$ for both tapers and stems). Similarly, the comparison between the composition of the particles with the same morphology but with different origin (i.e. round particles from tapers vs round particles from stems and oval particles from tapers vs oval particles from stems) showed no significant differences between the mean Cr, Co and Mo amounts ($p>0.5$ for round particles and $p>0.1$ for oval particles).

Table 4.29 The average composition of round and oval particles released from tapers and stems, resulted from the STEM and EDX quantitative analysis.

Sample	**Morphology**	**Composition**		
		Cr%	Co%	Mo%
Tapers	Round	82	17	1
	Oval	85	13	2
Stems	Round	84	15	1
	Oval	81	18	1

The speciation analysis, discussed in the previous sections (4.4.), identified mainly Cr_2O_3 debris released from both wear sites.

4.5.4 Comparison between the morphology and size distributions of debris released from all tapers and all stems (alkaline and enzymatic treatments)

The comparison between the size of the particles released from the tapers and cement-stem interfaces included 442 particles from three CoCrMo tapers (taper 1, 2 and 3) and 445 particles from six CoCrMo stems (stem 1, 2, 9, 10, 11 and 12). The classification of the particles with respect to the origin and cleaning procedure, the corresponding size ranges and the mean and median d_{max} for each category of debris are shown in **Table 4.30**. The comparison between the size of the particles released from tapers and stems and cleaned with the same treatment (i.e. alkaline or enzymatic), revealed that significantly larger particles originated from the taper interface, regardless of the treatment used ($p<10^{-4}$ for the alkaline treatment; $p<10^{-11}$ for the enzymatic treatment). Similarly, the comparison between the size distributions of all the particles released from the CoCrMo tapers and all the particles originating from the cement-stem interface (cleaned with either of the treatments) supported the fact that smaller particles were released from the cemented stems ($p<10^{-14}$). The comparisons between the particle size distributions for each category are shown in **Figure 4.59**.

Table 4.30 The number of particles used to determine the size distribution of debris released from tapers and cement-stem interface, classified according to the treatment used for particle cleaning. Tapers cleaned with the alkaline procedure: taper 1, 2 and 3; stems cleaned with the alkaline treatment: stem 9, 10, 11 and 12; tapers cleaned with the enzymatic procedure: taper 1 and 2; stems cleaned with the enzymatic protocol: stem 1, 2, 9 and 10.

Sample	**No of particles**	**Size range**	**Mean d_{max}**	**Median d_{max}**
Tapers (alkaline)	260	3-77 nm	20.8 nm (±13.8)	16.8 nm
Stems (alkaline)	155	5-37 nm	16.4 nm (±7.1)	15.1 nm
Tapers (enzymatic)	182	4-67 nm	24.0 nm (±13.2)	21.4 nm
Stems (enzymatic)	290	4-49 nm	16.4 nm (±7.4)	14.9 nm
Tapers (all)	442	3-77 nm	22.1 nm (±13.6)	18.6 nm
Stems (all)	445	4-49 nm	16.4 nm (±7.3)	14.9 nm

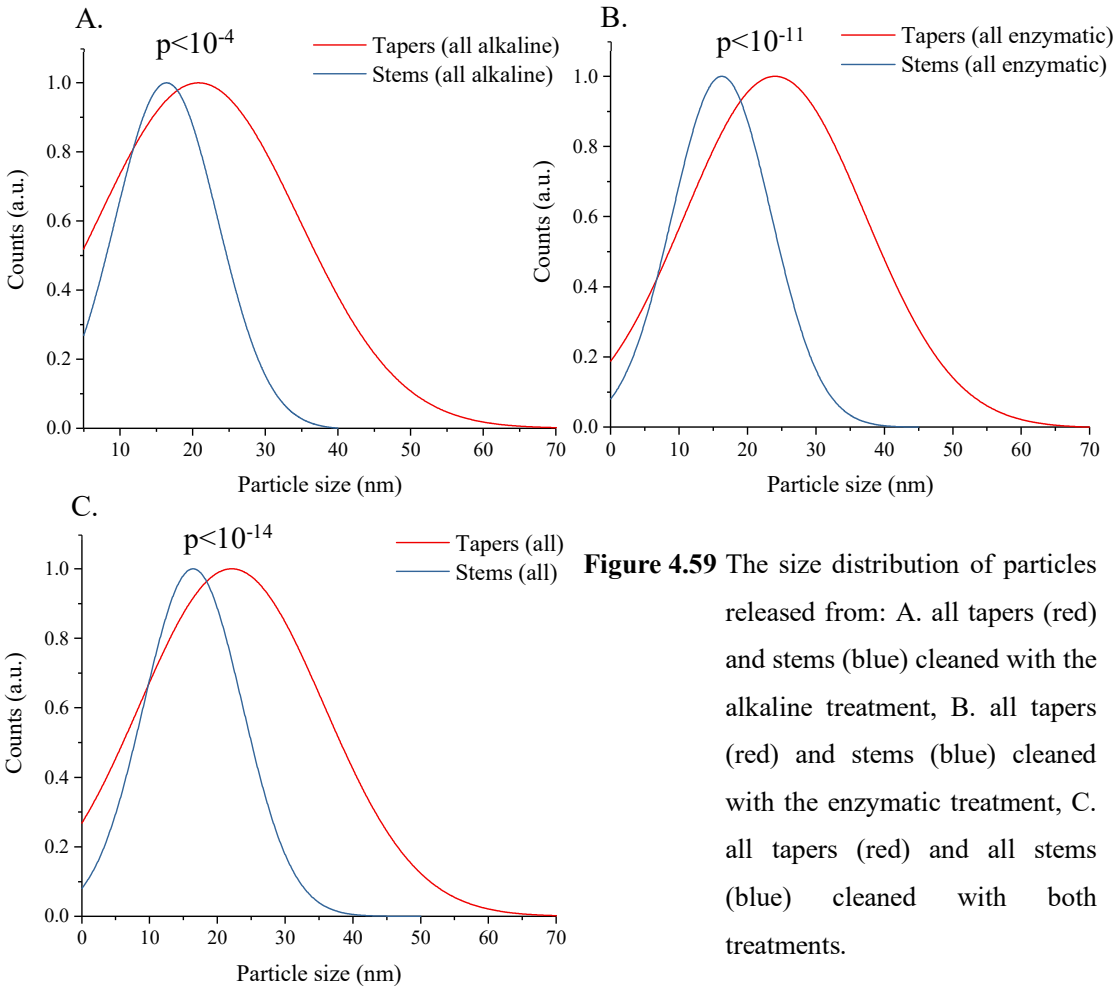

Figure 4.59 The size distribution of particles released from: A. all tapers (red) and stems (blue) cleaned with the alkaline treatment, B. all tapers (red) and stems (blue) cleaned with the enzymatic treatment, C. all tapers (red) and all stems (blue) cleaned with both treatments.

The taper debris cleaned with the enzymatic treatment comprised a higher percentage of oval particles than the stem debris cleaned with the same treatment (52% vs 31%). The results of the morphology study are shown in **Table 4.31** and indicate that both taper and stem debris (alkaline and enzymatic treatments) contain mainly round and oval particles, with few needle-shaped structures.

Table 4.31 The results of the morphology analysis, showing the percentage of round, oval and needle-shaped particles released from each taper and stem category.

Sample	**Round %**	**Oval %**	**Needle shaped %**
Tapers (alkaline)	66	33	1
Stems (alkaline)	56	35	7
Tapers (enzymatic)	43	52	5
Stems (enzymatic)	68	31	1
Tapers (all)	56	41	3
Stems (all)	65	32	3

4.5.5 Comparison between debris from toggling and non-toggling tapers

The RedLux Imaging was used to identify the wear mechanisms underlying the release of debris from the CoCrMo taper interfaces and helped select the retrievals suitable for the comparative study. According to the RedLux investigation, taper 1 and taper 2 were subjected to different wear mechanisms and were further used for comparison. The retrieved wear and corrosion flakes were cleaned using the enzymatic and alkaline treatments and the isolated debris was characterised to determine the particle size and morphology. The main objectives of study were to:

i) Correlate the characteristics of the particles in relation to the dominant wear mechanism;

ii) Compare the characteristics of debris released from CoCrMo tapers by different wear processes;

Figure 4.60 represents the height maps for retrievals 1 and 2 and shows the deviation of the tapers from their initial geometry, as a result of wear and corrosion. The original surface is preserved for 2-3 mm at the proximal and distal end of the tapers, appearing in green for taper 1, and yellow for taper 2, while the regions affected by material loss are in blue, purple or black.

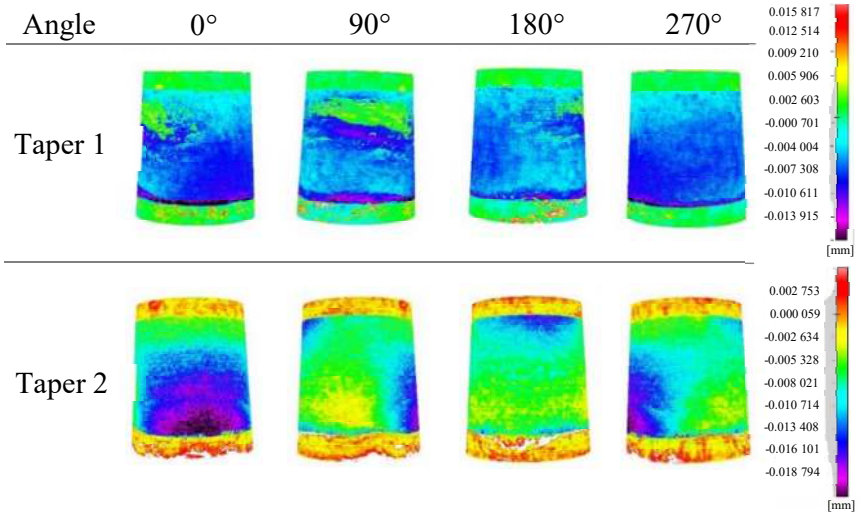

Figure 4.60 RedLux images showing the loss of material from the female side of the taper junctions 1 and 2 (bore of the head).

In the case of taper 1 (non-toggling taper), the damage is uniformly distributed around the circumference and along the length of the taper-trunnion overlap, with a ring of material loss around the distal open end of the taper-trunnion overlap, likely due to a corrosion-dominated process. The total volumetric loss from the female taper of implant 1 was 3.291 mm^3, with a maximum depth of the wear scar of 25.75 µm.

The damage profile for taper 2 demonstrates that a toggling motion occurred between the taper and the trunnion, characterised by the deepest points of loss being at the distal end of the 0° and the proximal end of the 180° images in **Figure 4.60**. The most affected region was the distal region of the taper-trunnion contact with a maximum depth of 19.9 µm and a total volumetric material loss of 3.479 mm^3.

Table 4.32 The number of particles characterised for the toggling and non-toggling tapers, and the corresponding size ranges and mean and median d_{max} after the enzymatic and alkaline treatments.

Sample	**No of particles**	**Size range**	**Mean d_{max}**	**Median d_{max}**
		Enzymatic treatment		
Taper 1 (non-toggling)	75	4-64 nm	23.5 nm (±14.0)	20.3 nm
Taper 2 (toggling)	107	6-67 nm	24.4 nm (±12.6)	22.1 nm
		Alkaline treatment		
Taper 1 (non-toggling)	100	3-60 nm	15.9 nm (±11.0)	11.8 nm
Taper 2 (toggling)	110	3-65 nm	20.3 nm (±13.3)	16.8 nm

The STEM micrographs of the cleaned particles released from taper 1 and taper 2 can be found in section 4.2. A and B. At least 75 particles from each wear site were characterised to investigate the morphology and size distribution of the representative particulate debris. **Table 4.32** shows the number of particles, the corresponding size ranges and the mean and median d_{max} of the isolated debris, in relation to their origin and cleaning treatment.

The size distributions of the particles released from the toggling and non-toggling CoCrMo taper junctions are shown in **Figure 4.61 A** and **B**. Debris from both tapers and cleaned with the enzymatic treatment have similar size ranges, and are not statistically different ($p>0.5$) (**Figure 4.61 A**). These results, however, are not supported by the statistical analysis of the size distributions of debris from taper 1 and 2 and cleaned with the alkaline treatment (**Figure 4.61 B**), which revealed significantly smaller particles from the non-toggling taper ($p<0.01$).

The morphology classification of the cleaned debris, in relation to the wear mechanism and cleaning procedure is shown in **Table 4.33**. The comparison between the particles released from the toggling and non-toggling tapers and cleaned using the same protocols, showed similar results. The morphology of the particles appears to be more dependent on the cleaning procedure than on the wear mechanisms responsible for their release.

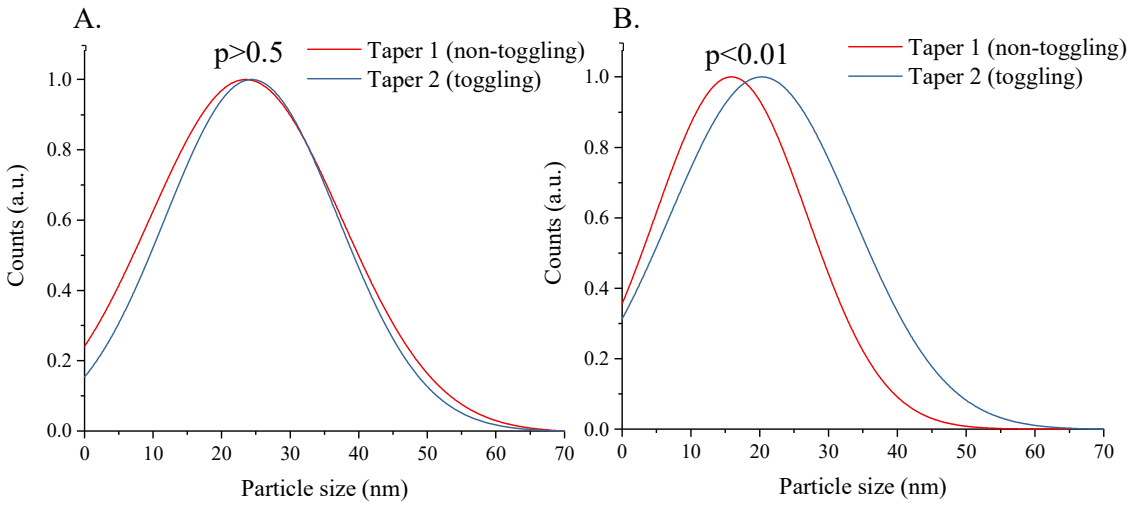

Figure 4.61 The size distribution of particles released from a toggling (blue) and non-toggling (red) CoCrMo taper junction, cleaned with: A. the enzymatic treatment and B. the alkaline treatment.

Table 4.33 The comparison between the morphology of the particles released from a toggling and non-toggling taper junction and cleaned with the alkaline or enzymatic treatment.

Sample	**Round %**	**Oval %**	**Needle shaped %**
Enzymatic treatment			
Taper 1 (non-toggling)	48	49	3
Taper 2 (toggling)	40	53	7
Alkaline treatment			
Taper 1 (non-toggling)	69	29	2
Taper 2 (toggling)	57	41	2

The speciation analysis (section 4.4.) did not find any difference between the Cr rich phases (i.e. Cr_2O_3) released from the toggling and non-toggling tapers (taper 1 and taper 2).

4.5.6 Comparison between debris from mixed (CoCrMo/Ti alloy) and matched (CoCrMo/CoCrMo) material taper junctions

The comparison between the wear and corrosion products released from the mixed and matched material taper junctions included debris from two retrievals from each taper category (i.e. taper 1 and taper 2 for the matched material tapers and taper 7 and 8 for the mixed material group), cleaned with the enzymatic treatment. Representative STEM micrographs of the particles originating at these particular interfaces are shown in section 4.2. B. The study proposed to:

i) Assess the differences between the size and morphology of debris from mixed and matched material tapers;

ii) Identify the main Cr and Co species released from the mixed and matched material tapers;

The particle morphology and size distribution resulted from the STEM characterisation of at least 182 particles from each taper group. The number of particles included in the study and the corresponding size ranges and mean and median d_{max} are shown in **Table 4.34**. The associated particle size distributions are shown in **Figure 4.62**. The particles released from the matched material taper junctions had a narrower size distribution and smaller mean and median d_{max} in comparison to debris released from the mixed taper junctions. The statistical analysis revealed significant differences between the size distributions of the particles originating from the mixed and matched material taper interfaces ($p<10^{-14}$).

Table 4.34 The number of particles included in the mixed and matched taper categories and the corresponding size ranges and mean and median d_{max}.

Sample	**No of particles**	**Size range**	**Mean d_{max}**	**Median d_{max}**
Matched (CoCrMo)	182	4-67 nm	24.0 nm (±13.2)	21.4 nm
Mixed (CoCrMo/Ti)	266	4-149 nm	39.2 nm (±23.7)	34.4 nm

The morphology of the particles from each taper category is shown in **Table 4.35**. The matched material taper junctions released mainly oval and round particles, with few needle-shaped structures.

The speciation analysis using STEM/EELS, STXM/XANES and TEM/EDX was detailed in section 4.4. and found mainly Cr^{3+} as Cr_2O_3 and Co^{2+} potentially in the form of $Co(OH)_2$, in debris from both taper groups. The investigation revealed that the same Cr species are released regardless of the taper material combination, but larger nanoparticles originate from the mixed CoCrMo/Ti alloy taper junctions than the particles released from the matched CoCrMo taper junctions.

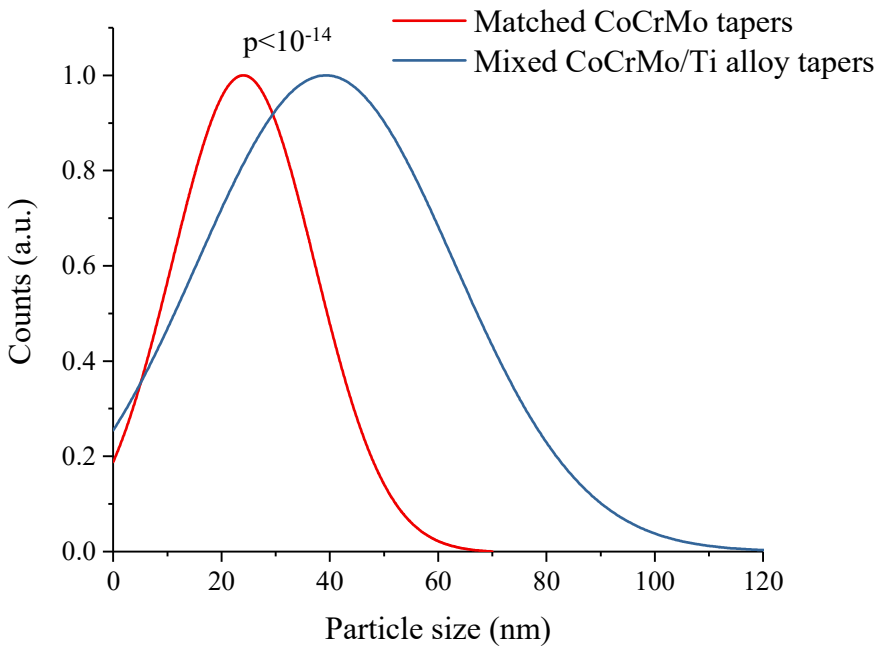

Figure 4.62 The comparison between the size distributions of debris released from the mixed and matched material taper junctions, cleaned with the enzymatic treatment.

Table 4.35 The comparison between the morphology of the particles released from mixed and matched material tapers and cleaned with the enzymatic treatment.

Sample	**Round %**	**Oval %**	**Needle shaped %**
Matched (CoCrMo)	43	52	5
Mixed (CoCrMo/Ti)	58	34	8

Chapter 5 Discussion

5.1 Introduction

The chapter addresses how the results of the present study relate to the findings of the previous research and outlines the contribution of the project to the progress of the field. The number of studies reporting on debris released from the bearing surfaces exceeds that of studies which characterise debris from the secondary interfaces in total hip replacements. Even less journal papers succeeded to reveal the fine structural details and composition of the particles that comprise the wear and corrosion flakes from around retrievals, regardless of the source/interface of material loss. This makes the comparison between studies difficult and provides room for discussions, which are mainly caused by the lack of standardised particle characterisation methods. Apart from emphasising the relevance of the findings and how they fill in the gaps of the previous research, the chapter also brings up the limitations of the actual study and advises on how these could be addressed in the future work.

5.2 The Structure and Composition of the Wear and Corrosion Flakes

Previous retrieval studies reported black and flaky wear and corrosion products around the modular tapers or at the cement-stem interface in total hip replacements[2–4,26,29,31,32,41,49,169,174,177,180,190,214,220,230,238,239,246,310–313]. The presence of debris was associated in most cases with signs of mechanical damage or tribocorrosion of the retrieved components[2–4,26,29,31,32,41,49,169,174,177,180,190,214,220,230,238,239,246,310–313]. The previous characterisation of these products using SEM and EDX revealed various metals originating from the adjacent metallic interface[26,32,214,230,313,314]. The origin of debris and the underlying mechanisms responsible for their release are not fully understood yet, although some of the existing theories are well sustained by experimental findings[29,224,230,246,265,315].

Here, the results of the ICP-MS analysis and SEM/EDX mapping revealed the organo-metallic nature of the wear and corrosion flakes. These comprised metal debris and corrosion products mechanically mixed with salts and organic material, and support the mechanisms proposed by Bryant et al.[29] and Zeng et al.[224] to explain the material loss from tapers and cement-stem interface. The composition of the flakes and the proportion of the various elements in the investigated fragments was initially confirmed by ICP-MS analysis, which according to our knowledge, has only been used once before to characterise wear and corrosion products from secondary interfaces in total hip replacements[230]. The previous study revealed black deposits of Co and Cr debris on the cement mantle and demonstrated the transfer of material from the stem, as a result of tribocorrosion. The ICP-MS results were in agreement with the findings of the present study and reported more Cr than Co in the wear

and corrosion products collected from the retrieved fragments of the cement mantle. The method provided the rapid analysis of numerous samples and allowed the simultaneous quantification of various metals, by the use of pre-defined concentrations of metal standard aliquots. The analyses revealed that only a small proportion of the flakes' weight corresponded to metals, suggesting that non-metallic species might also be part of the flake's composition. The flakes comprised mainly Cr, Co and Mo, and the proportions of these elements varied with the sample, although there was no relation with the site of material loss. The SEM/EDX characterisation of fragments of flakes provided the visual distribution of the metallic and non-metallic elements across the surface of the investigated debris. The distribution maps confirmed the presence of Ca, P and C, which likely originate from the biological fluids bathing the metallic interfaces in the joint cavity. One such fluid is the synovial fluid which has a composition similar to that of the blood plasma and is rich in proteins, such as albumin, hyaluronic acid and surface active lipids, believed to play an important role in the lubrication of the artificial joints[296,297,316]. The presence of non-metallic species in the wear and corrosion flakes, can be therefore easily justified. The most important clue that supports the presence of the organo-metallic composites at the tapers and cement-stem interface is the preferential distribution of the various metallic and non-metallic elements in different fragments of debris released from the same wear site. The different morphologies and compositions of the pink and black flakes suggested the release of different chemical species from the wear sites, which are mechanically mixed at the interface, resulting in flakes with heterogeneous compositions. Both ICP-MS and EDX/SEM analysis suggested that the flakes are not homogenous and result from a mechanical mixing process of metal debris, corrosion products, salts and biomolecules from the body. This process resulted in unevenly distributed metallic and non-metallic species inside the bore of the head or around the base of the trunnion, which coincided to metal rich or metal depleted fragments of flakes, which were reported with both ICP-MS and SEM/EDX characterisation.

The investigation of the bore surface of the CoCrMo heads, performed by Zeng et al.[224], found a carbonaceous layer believed to result from the absorption of proteins and biomolecules from the synovial fluid. The underneath layer consisted of packed Cr_2O_3 and a nanocrystalline layer deep under the surface. At the head-stem contact region, however, the investigation revealed a mixture of Cr, C and O, which suggested the formation of a mechanically mixed layer. This description matches the findings of the present study, which resulted from the ICP-MS and SEM/EDX characterisation of the CoCrMo taper flakes and revealed mechanically mixed metal debris and non-metallic species. A similar mechanism was proposed by Bryant et al.[29] to explain the release of debris at the cement-stem interface, and by Wimmer et al.[129,130] to explain the wear of the MoM bearing surfaces.

Despite the previous studies[29,224,230] which investigated the sub structure of the taper and stem surfaces to reveal the origin of debris, little is known about the morphology and composition of the wear and corrosion products released from these interfaces. To our knowledge, the present study is the first to digest and clean the wear and corrosion flakes, to reveal the smallest building blocks that

make up the taper and stem debris. The use of complementary imaging and analytical techniques contributed to a better understanding of the structure of the wear and corrosion flakes and revealed the fine structural details of the particulate debris. The presence of nano-sized Cr_2O_3 particles embedded in an organic matrix of Ca, C and P mixed with traces of corrosion products, such as $Co_3(PO_4)_2$, support the mechanism proposed by Zeng et al.[224], Bryant et al.[29] and Wimmer et al.[130] to explain the formation of debris at the metallic interfaces. The Cr_2O_3 layer reported by Zeng et al.[224] at the head-taper interface and by Bryant et al.[29] at the cement-stem interface is very likely the origin of the Cr rich nanoparticles found in the present study by the HR-STEM characterisation. The formation of Co and P rich precipitate at the surface of the taper flakes can be a consequence of the corrosion processes occurring at the crevice. Here, the harsh conditions, characterised by the low pH and reduced O concentrations, as well as the presence of corrosive anionic species, such as Cl^-, are believed to favour the leach of the highly soluble Co and Mo ions[2,161,180]. The joint cavity is rich in phosphate ions, which can originate from the hydroxyapatite layers at the back of the acetabular components. Hydroxyapatite is also involved in the formation of bone[317] and it is therefore expected to be around the joints. The presence of ions (i.e. Cr^{3+}, Co^{2+} and PO_4^{3-}) in the same proximity can favour the formation of Cr and Co phosphate[32,94], and the present study provided evidence of a Co and P rich precipitate, with a pink coloration characteristic of $Co_3(PO_4)_2$.

The release of $CrPO_4$ from the taper interface has been previously reported by Urban et al.[41], Huber et al.[174] and Di Laura et al.[100] In these previous studies, $CrPO_4$ was found as the main species or mixed with oxides in periprosthetic tissue collected from the joint area of patients undertaking revision surgery. The uptake of the particles by cells can take place through different routes, depending on the type of cells and particle size and aggregation state[5,48,56,108]. The small particles (nano sized) can pass the cellular membrane through a simple diffusion process or by the anionic channel route and can therefore be internalised by both phagocytic and non-phagocytic cells[38,108]. The large debris (large particles or aggregates), however, can only be internalised by phagocytic cells which uptake micron sized debris by phagocytosis. The phagocytosed particles are subjected to a lysosomal environment, characterised by a low pH (~4), which aims to digest debris[38,318]. It is therefore possible that the particles internalised through this route and exposed to the harsh lysosomal content, can suffer alterations from the original native conditions. This can result in different size, morphology and composition of debris after the cell internalisation. It is therefore possible that the $CrPO_4$ species, reported in some of the previous studies as the main taper wear and corrosion product, is the result of the transformations suffered by Cr rich debris inside the lysosomes[94].

In the present study some of the fragments of the as-retrieved taper debris consisted of Cr and P rich patches, which could be in fact $CrPO_4$. The alkaline treatment could have dissolved the phosphate species around the Cr oxide nanoparticles, which were discarded through the particle isolation process and were therefore not characterised with the high-resolution techniques. After the enzymatic treatment, however, debris from taper 6 was still rich in Cr, O and P. Although the quantitative EDX

analysis of the Cr and P rich debris did not provide a composition which matched that of the pristine $CrPO_4$ (i.e. 35.4% Cr, 43.5% O and 21.1% P), it is likely that $CrPO_4$ was the main species released at this particular taper interface. The enzymatic treatment is milder than the alkaline one[55,276] and is mostly efficient at breaking down the biomolecules (mainly proteins) present in the flakes. The salts, such as Cr and Co phosphates, are more susceptible to dissolution when using the alkaline treatment. The presence of the needle-like structures after the alkaline cleaning of the stem and taper debris suggested the implication of the treatment in the formation of these products. The composition of the needle-like debris from the stem interface was rich in Cr, K, Mg and Ca, whereas the needle structures in taper debris comprised mainly Co. It is likely that initially these phases were $CrPO_4$ and $Co_3(PO_4)_3$ respectively, which resulted in the Cr and Co rich needles after the alkaline cleaning.

The quantitative EDX analysis of the Co rich needle debris from around the CoCrMo tapers revealed small amounts of P in comparison to Co, and excluded the presence of $Co_3(PO_4)_2$ after the alkaline treatment. The formation of the needle like morphologies, however, is characteristic for $Co(OH)_2$, which could have formed from the chemical reaction of the Co^{2+} ions or $Co_3(PO_4)_2$ with KOH, during the alkaline cleaning[319,320]. In fact, the K map matches well the Co distribution on top of the needle-like debris and supports the cleaning mechanism by which KOH attacks the Co rich species, resulting in the needle like structures revealed by the STEM investigation.

Although the study did not include the SEM/EDX characterisation of the flakes released from the mixed material taper junctions, nor the distributions of the elements across the various parts of the flakes, it can be assumed that the same mechanism is involved in their formation. The STEM and EDX investigation of the Ti and Cr rich debris cleaned with the enzymatic treatment showed crystalline nanoparticles and a diffuse phase which comprised both Ti and Cr species. This phase may correspond to a non-metallic matrix which entrapped dissolved ions resulting from the corrosion of the Cr and Ti rich nanoparticles. The proportion of the organic matrix in the mixed Cr and Ti debris (taper 7 and 8), however, was less than that in debris from the similar material taper debris (taper 1 and 2). The study suggested that the Cr and Ti oxide nanoparticles released from the wear of dissimilar material taper junctions are mechanically mixed with biomolecules from the body fluids, resulting in black and flaky debris like the flakes originating from the matched material taper junctions.

Despite some similarities discussed above, the flakes formation mechanisms at the tapers and cement-stem interfaces might have their own particularities. The crevice formation and the continuous ingress of fluid at the taper interface can favour debris' migration and accumulation at the base of the trunnion. The flakes incorporate Cr oxide particles, released by mechanical wear at the taper-trunnion interface, and ions and corrosion products which can result from the crevice corrosion. These species can interact with the bio-molecules and surface-active compounds found in the proximity of the joint, building up the organo-metallic flakes. The pathway by which the wear and corrosion products travel to the periprosthetic tissue and macrophages was not in the scope of

the study. One hypothesis, however, could be the gradually released of the flake's fragments to the synovial fluid, which facilitates debris transportations to the surrounding tissue. Depending of their size, the released fragments can be either captured by the macrophages (larger flakes) or can travel systemically, spreading to distant sites (smaller debris). Cobalt is believed to be the culprit for the systemic reactions to hip-related metal debris, but the form in which it is spread to the body's organs it is still not well understood. The results of the present study suggest that Co exists in an ionic form ($Co_3(PO_4)_2$), rather than in a solid metallic form, which could favour the released of Co in the body's fluids, in concentrations close or above the toxicological thresholds. This hypothesis could also justify the severe ALTRs to taper debris, despite the smaller volumetric wear rates compared to the bearing surfaces.

At the cement-stem interface, the material is released by tribocorrosion. At this interface, due to the position of the crevice opening (i.e. upwards), the particles cannot easily escape the crevice to accumulate in the periprosthetic tissue. The particles, therefore, can be entrapped at the cement-stem interface longer and can be subjected to multiple loading cycles which could favour debris transfer to the cement mantle or particles resizing. The present study showed that the particles released from the cement-stem interface are smaller than those released from the matched CoCrMo tapers. Also, the electrochemical conditions at the cement stem-interface may be different than the conditions at the taper crevice and may not favour the Co dissolution from the CoCrMo alloy and the subsequent formation of Co compounds, such as $Co_3(PO_4)_2$. This hypothesis is supported by this study's results, which reported Co and P, potentially in the form of $Co_3(PO_4)_2$, in taper debris, but not in the wear and corrosion products released from the cement-stem interface. Further research is needed to properly understand and elucidate the mechanisms by which the wear and corrosion flakes are formed at each secondary interface in total hip replacements and understand how they are transported to the tissue and distant sites.

5.3 The Speciation of Nano-Sized Debris

The speciation analysis represents an important aspect of the comprehensive study of the wear and corrosion debris released *in vivo* from the mixed and matched material taper junctions and cement-stem interfaces. The physicochemical characteristics of the particulate debris, determined by the high-resolution STEM, and the oxidation state and phase analysis of the Cr, Co and Ti products, identified here using STEM/EELS, STXM/XANES and TEM/SAED, are believed to dictate the fate of the particles within the body[106,110,321–325]. The permeability of cellular membrane and susceptibility of the ions to bind to proteins and nucleic acids, altering their functions, are highly dependent on the particle size, morphology and oxidation state of the metal ions[38,48,94]. The methods used in the study to assess the speciation of debris from around six retrievals (2 CoCrMo tapers, 2 CoCrMo/Ti tapers and 2 CoCoMo stems) provided complementary information which helped elucidate the dominant Cr, Co and Ti species. Although equally important, the oxidation state of Mo species has not been determined in the present study and will therefore not be discussed in this section.

STEM and EELS analysis is a popular and reliable method widely used to determine the oxidation state of metal species[288,306]. The results, however, can be difficult to interpret and the quality of the acquired data depends on the level of sample purity. Despite the use of the cleaning procedures, not all of the particles investigated in this study were fully released from the organic matrix. In some cases, therefore, the signal to background ratio was low and the peak integration was not easily to perform. The speciation analysis using EELS provided an indication of the Cr and Ti oxidation state, which was further confirmed by the other methods. In all of the CoCrMo samples, Cr^{3+} was the main species released from both the tapers and cement-stem interface. The EDX characterisation of the clean particles originating from the same wear sites, showed mainly Cr and O, with little amounts of P or other elements which comprise the CoCrMo alloy. The lack of P, the good match between the Cr and O EDX maps and the results of the EELS analysis, showing Cr^{3+}, suggest that Cr_2O_3 is the main species released from the CoCrMo secondary interfaces in total hip replacements, although little amounts of $CrPO_4$ may also be present. These results were also supported by the quantitative STEM/EELS analysis which provided a Cr/O atomic ratio close to that of the pristine Cr_2O_3[306], and by STXM and XANES analysis, which also indicated Cr^{3+}. The limitation of the STXM/XANES analysis using the I08 beamline at Diamond Ltd., is the low spatial resolution compared to the alternative methods, such as STEM/EELS analysis. The particles investigated in this study with STXM and XANES, were part of large clusters (micron sized) and were probably not fully digested, containing several mixed species. In some of the samples, the fitting process did not match 100% the spectrum of the pristine Cr_2O_3 and partially matched that of $CrPO_4$. The presence of both the oxide and phosphate species in the large clusters suggest that Cr exists in both states, but the clean particles investigated with STEM/EDX and EELS are Cr_2O_3.

The TEM and SAED phase analysis was in agreement with the findings of the STEM/EELS and STXM/XANES investigation, and revealed the presence of Cr_2O_3. The analysis using TEM and SAED is also associated with difficulties and require prior knowledge of the species that might generate the diffraction pattern. For a polycrystalline material, such as the samples used in the present study, the speciation analysis is based on the measurement of the crystal planes d-spacing from the corresponding diffraction rings. The measured d-spacing is correlated with the d-spacing of the species likely to be present in the investigated sample (in the present case, Cr_2O_3). The measurement of d-spacing is usually associated with errors which together with the small differences between the d-spacing values of the possible species can make the phase identification difficult. It is clear therefore that each of the speciation techniques used in this study can be limited in certain ways, and in order to obtain reliable results, the use of complementary techniques can represent an optimum solution.

The speciation of nanoparticles released from the mixed material tapers (CoCrMo/Ti alloy) revealed both Cr_2O_3 and $CrPO_4$, as well as TiO_2. The presence of these species at the taper interface has been previously reported by others[14,39,100], and this is expected considering the composition of the wearing surfaces.

Besides Cr and Ti species, the XANES analysis of debris released from the mixed and matched material taper junctions also revealed Co^{2+} species in the form of hydroxide, oxide and/or phosphate. In the previous studies, the analysis of CoCrMo and CoCrMo/Ti taper debris entrapped in periprosthetic tissue or in biopsies from distant organs revealed Cr_2O_3, $CrPO_4$ and CoCr debris[14,39,100]. In these studies, Di Laura et al.[100] and Swiatkowska et al.[14] reported TiO_2 (rutile form), metallic Cr (Cr^0), and Cr^{3+} in the form of oxide. The speciation of Co revealed mainly Co^{2+} and metallic Co (Co^0), in the form of CoCr debris[14,100]. In a different study, Xia et al.[39] reported the elemental distribution of Co, Cr and Ti within debris released from bearing surfaces and taper junctions and the XRD analysis of the crystalline Cr rich particles revealed mainly Cr_2O_3. The results of the present study are therefore in agreement with these previous studies and provide additional information about the structure and morphology of the individual Cr_2O_3 and TiO_2 nanoparticles which have never been revealed before.

Of the possible oxidation states of Cr, Cr^{3+} is the most stable form and it is spontaneously generated at the surface of the CoCrMo alloys[157]. The presence of this superficial oxide layer provides the metallic components a good corrosion resistance, which recommends the CoCrMo alloy for implantation purposes[10,158,326]. The wear of the CoCrMo alloy, however, results in the release of Cr_2O_3 flakes from the superficial layer, which then exposes the underneath CoCrMo bulk alloy[326]. Under proper electrochemical conditions, the oxide layer can be regenerated, impeding the dissolution of the more soluble Co[327] and Mo[290] ions and restoring the corrosion resistance[180,326]. The oxidation of Ti and Ti based alloys also results in the formation of a protective layer of TiO_2[10,328], which can be subject to wear and the release of TiO_2 debris[180]. At the interface of the mixed material

taper junctions, the galvanic current between the dissimilar interfaces can result in galvanic corrosion[166,180], which accelerates the degradation process and the release of ions from both surfaces. It is believed however, that the CoCrMo alloy is more affected by the corrosion process[186], which results in the release of ions from its composition.

The study also provided evidence of the presence of $Co_3(PO_4)_2$ in the as-retrieved flakes, and Co^{2+} species, either as $Co(OH)_2$ or CoO in the partially digested debris. The results of the high-resolution characterisation, showed mainly Cr oxide nanoparticles with minimal amounts of Co, localised in the surrounding matrix. The alkaline treatment may have resulted in the formation of $Co(OH)_2$, characterised by the needle like morphology observed under STEM investigation. Cobalt (Co) is more soluble and is therefore leached from the particles more rapidly[158,318,327], while Cr remains in an oxide solid state (nanoparticles). The release of Co ions can occur from the exposed CoCrMo alloy, before the passivation, or from the CoCrMo particles released in conditions of severe wear. The dissolution of Co and Cr, and the morphological changes of the CoCrMo particles was recently shown to occur over a potential limit of ~0.7 V[327]. In the present study the speciation analyses did not reveal the presence of CoCrMo particles, however, it is not excluded that CoCrMo debris is released from the tapers and cement-stem interfaces. The particles may leave the joint space, traveling systemically[14,40,41], or can be entrapped in the periprosthetic tissue[39,288,327], where they are taken up by the macrophages which attempt to digest them. The means by which the resulting Co ions are released from the cells, reaching the circulatory and excretion systems is not fully understood yet. However, the high levels of Co found in the blood and urine samples of the patients implanted with failing CoCrMo hip prostheses could explain the pathway of the Co ions in the body and why Co is rarely present in debris from the CoCrMo retrievals[2,4,169].

The toxicity of the CoCrMo debris and the associated inflammatory reactions are suggested to be related to the release of Co ions in the body[34,48,103]. The present study provided reliable evidence of the presence of $Co_3(PO_4)_2$ around the revised taper junctions, although based on the Co speciation analysis it was difficult to assess the exact form of Co^{2+} species. One of the previous studies reported $Co_3(PO_4)_2$ in periprosthetic tissue from around failing hip bearings, which could have resulted from the intracellular corrosion of the CoCr debris[288]. To our knowledge, the cellular effects of this particular species have not been assessed in any of the previous *in vitro* studies, but could be responsible for the increase *in vivo* reactivity of the CoCrMo debris. This hypothesis is even more plausible since the *in vitro* studies assessing the toxicity of the Cr_2O_3 nanoparticles and $CrPO_4$ debris did not reveal abnormal changes in the cellular structure and cell viability[329–331].

5.4 The Effects of the Digestion Treatments

The alkaline and enzymatic methods used in this study to digest the wear and corrosion flakes[37] were adapted from the protocols used in the previous studies to clean metal debris released from the bearing surfaces[21,36,55,276]. These protocols were initially proposed for the isolation of particulate debris released in the synovial fluid, serum lubricants, or periprosthetic tissue and biopsies. To our knowledge, none of the previous studies which reported on the wear and corrosion flakes from around revised hip components have used methods to release and investigate the particulate debris. The need of a cleaning procedure is justified by the results of the present study, which confirmed the presence of particle bio corona, salts and precipitates in the wear and corrosion flakes.

The alkaline treatment was associated with concerns regarding the potential dissolution of the particulate debris, which would have resulted in smaller particles with altered morphology and composition[55,276]. Chronologically, the enzymatic treatment was released later than the alkaline treatment and in some of the previous studies it was used combined with the chemical treatment[274]. Other studies used it as a milder alternative to the alkaline cleaning and aimed to overcome the shortcomings of the chemical procedure[28,98]. Catelas et al. compared the effects of the alkaline and enzymatic treatments on the particle characteristics and reported that both treatments led to the particles size, morphology and composition alteration[55,276]. The changes, however, were more prominent after the use of the alkaline treatment and increased with the concentration of the alkaline solution. The study of Catelas et al. used commercially available particles of known size, morphology and composition and debris from *in vitro* simulations, stored in water or serum lubricants[55,276]. Their investigation revealed that the particles stored in bovine serum, were less affected by the alkaline and enzymatic treatments than those stored in water. The proteins and surface active compounds in the serum lubricants are believed to bind to the particle's surface, creating a particle bio corona which acts as a shield against the cleaning reagents (enzymes and alkaline solutions)[296,316]. The enzymes and alkaline solutions used in these treatments need to digest and remove the bio corona, before they reach to the particle surface and initiate the dissolution process.

The present study proposed to assess the effects of the alkaline and enzymatic treatments on the physicochemical characteristics of the particles released from the CoCrMo tapers and cement-stem interfaces, using high-resolution imaging techniques. The heterogeneous nature of the corrosion flakes was expected to protect the particulate debris against dissolution or corrosion, by the mechanism proposed by Catelas et al. in their study[55,276]. The STEM characterisation of the digested flakes revealed the presence of an organic matrix around the metal particles, which was still present after both treatments, although it was more prominent after the enzymatic cleaning. The particles cleaned with the alkaline treatment still had traces of the bio corona and suggested that an incomplete digestion may have minimised the chances of particle alterations from the chemical reagents.

In this study, however, the comparison between the PSDs revealed that the particles released from tapers and cleaned with the alkaline treatment were significantly smaller than those cleaned with the enzymatic method. In contrast, the particles released from the cement-stem interface were larger after the alkaline treatment than after the enzymatic cleaning, although the difference was not statistically significant.

The compositions of the particles also seemed to vary with the treatment used for the particle cleaning. The investigation revealed significant differences between the proportions of Cr, Co and Mo in debris released with the alkaline or enzymatic protocols. The analysis of taper debris showed lower Cr and higher Co concentrations in the particles treated with the alkaline solution, compared to debris cleaned with the enzymatic treatment. The alkaline protocol also dissolved more of the amorphous organic phase from around the metal particles, represented by the proportion of P after the treatment, and yielded cleaner debris, whose boundaries were well-delimitated and provided more accurate size measurements. The STEM micrographs showed that the particles cleaned with the enzymatic treatment were not fully released from the surrounding matrix, and were thus more difficult to measure. The high-resolution STEM only revealed the clean particles localised at the edge of the partially digested flakes, while the particles embedded in the amorphous phase could not be imaged or measured and therefore had no contribution to the PSD.

The STEM and EDX characterisation in this study revealed that the nanoparticles released *in vivo* from the CoCrMo tapers and cement-stem interfaces are largely composed of Cr, with traces of Co and Mo. The amount of O present in the samples cannot be accurately quantified by the EDX technique, hence the composition of debris was estimated from the normalised proportions of Cr, Co and Mo after the exclusion of O. The analysis showed mainly Cr in all of the investigated particles, but the percentage of Cr, Co and Mo for the taper debris varies with the treatment. Because Co and Mo are only present as trace elements, the normalisation process applied to the small amounts of Co and Mo has larger associated uncertainties and may have resulted in a significant difference in the composition of debris cleaned with the alkaline or enzymatic protocols. In addition, there were also significant differences between the composition of the particles originating from the same wear site (and patient) and cleaned with the same treatment, suggesting the variability of the particle compositions. This could be responsible for the different particle compositions observed after the alkaline and enzymatic treatments.

The measured composition of debris can also be influenced by the amorphous biological matrix or precipitates covering the particles, which were more prominent after the enzymatic treatment. The proteins and surface active compounds in the body show an affinity to metal ions[289], forming organo-metallic structures, believed to facilitate the absorption of the biomolecules at the surface of the implant[94,297]. Hence, the organic matrix around the metal particles likely contains dissolved Cr, Co and Mo ions which were detected by EDX analysis and contributed to the different composition totals.

The proportion of P in the debris was used to evaluate the efficiency of the digestion treatments in removing the phosphates from around the oxide particles. The dissolution of phosphates during the cleaning treatments outlined here, allows the physicochemical characteristics of the metal particles to be more fully evaluated. Thus, the reduction of the P content after the alkaline treatment indicates this method is more efficient at digesting the phosphates and leads to cleaner particles, which is in agreement to the STEM results for all three samples.

To our knowledge this is the first study to provide a direct comparison of the chemical and enzymatic techniques to release metal particles from the flakes from around CoCrMo tapers and cement-stem interfaces. The advantages and disadvantages of both cleaning treatments are summarised in **Table 5.1** and could be used to decide which method is most suitable, depending on each study's objectives. The alkaline treatment provided a more efficient dissolution of the amorphous matrix, releasing cleaner particles appropriate for the high-resolution characterisation and more accurate morphological analyses of the particles. The method, however, is not recommended if the aim of a study is to understand the bio-corona formation, composition and its role in the onset of ALTRs. The enzymatic treatment might be more suitable in this particular case, because it is milder and can preserve the bio-corona, when it is needed for characterisation. Depending on the purpose of the study, either of the treatments may be used to reveal the nano-scale debris forming the large flakes generated at tapers or cement-stem interfaces. Detailed structural characterisation of the nano-sized debris does, however, require clean particles, completely released from the organic matrix, which was best achieved in this study by the use of the alkaline treatment.

A limitation of the comparative study is the small number of samples investigated (i.e. 2 taper and 1 stem debris). However, this is understandable considering the amount of work necessary to fully characterise nanoparticles, and the costs for using state-of-the-art imaging techniques, such as the HR-STEM.

Table 5.1 Advantages and disadvantages of the alkaline and enzymatic treatment.

	Alkaline Treatment	**Enzymatic Treatment**
Advantages	• Requires less sample mass; • Consists of few incubation and centrifugation steps which minimise particle loss and/or contamination; • More efficient in removing particle bio-corona and precipitates; • Results in cleaner particles, suitable for high-resolution characterisation; • Reveals the smaller particles (smaller than 10-5 nm) and results in more accurate particle size measurements; • Cleaner particles facilitate structure, composition and speciation analysis, providing more accurate results.	• Milder treatment which was shown to minimise particle alterations (i.e. morphology and composition); • Preserves particle bio-corona and precipitates which are part of the flakes and could be investigated to understand their role in the onset of adverse local reactions to hip-related debris; • Efficient in cleaning individual particles, detached from the large wear and corrosion flakes, which can be investigated with high resolution characterisation techniques.
Disadvantages	• Concerns regarding potential particle dissolution and morphology, structure and composition alteration; • Removes higher proportion of particle bio-corona and precipitates, which makes their characterisation - when required - impossible;	• Requires more sample mass; • The cleaning treatment consists of more incubations, centrifugation and cleaning steps which can results in particle loss and risk of sample contamination; • Partial dissolution of particle bio-corona and precipitates which means less efficient particle cleaning, preventing particle size measurement and composition analysis; • Partially cleaned particles cannot be characterised with high resolution techniques, such as HR-STEM and EELS.

5.5. The Characteristics of Debris in Relation to the Origin

5.4.1 Debris from CoCrMo tapers vs CoCrMo stems

The low-resolution characterisation techniques used in the previous studies to characterise metal debris released from tapers and stems, provided general information about the morphology and composition of the micron-sized wear and corrosion flakes, observed around the retrieved implants[41,94,214]. The ICP-MS technique used in this study and in one of the previous works[230], gave information about the metals (type and amount) in these organo-metallic composites, but failed as a method to compare the characteristics of the particulate debris released from both wear sites and cannot therefore explain the initiated ALTRs. To understand the factors that are involved in the particle toxicity, the metal debris has to be released from the surrounding biological matrix, using either of the methods proposed in this study, and needs to be characterised to assess the particles' physicochemical properties in relation to the origin of debris. The source of material loss (i.e. the junction or interface, material combinations) and the particular electrochemical conditions at the sites of wear and corrosion (i.e. crevice)[327] can imprint the particles with specific physical and chemical characteristics which may then reflect in the nature and severity of ALTRs. It is therefore imperative to understand what type of debris is released from the various wear sites and further asses how they affect the function and viability of the cells and organs, where evidence of hip related debris is usually found[14,39,40,100].

The detailed investigation of the digested flakes and the comparison between the isolated nanoparticles in the present study, revealed some differences between the physicochemical characteristics of debris released from CoCrMo tapers and cement-stem interfaces. To eliminate interpatient variabilities, such as local pH, host responses and immunological particularities that could affect the biochemical conditions at the joint cavity and the physicochemical characteristics of the released debris, the taper and stem flakes used in this study originated from the same retrieval (or patient). The comparison between all the tapers and stems debris was performed based on the cleaning procedure (taper vs stem debris cleaned with the alkaline treatment, or taper vs stem debris cleaned with the enzymatic treatment) and thus eliminated the differences potentially induced by the use of different treatments. Although both CoCrMo interfaces produced particles in the nanometre size range, most of them smaller than 20 nm, the metal particles originating from the stems were significantly smaller than those released from the corresponding tapers. The same trend was observed after the comparison of debris from all tapers and stems, regardless of the cleaning procedure. The proportion of round, oval and needle-shaped particles also varied with the origin, but the size of the particle in relation to morphology did not show significant differences for the major morphology groups (round and oval).

These differences may be caused by the particular conditions at the taper and cement-stem interfaces. The cemented stems release material by micromotion between the hard ZrO_2 clusters (radio pacifier), localised at the surface of the cement mantle, and the proximal region of the CoCrMo stem[230]. This results in the release of Cr_2O_3 flakes from the surface of the CoCrMo stems, which are then entrapped at the cement-stem interface and are subjected to repeated loading conditions. The cyclic steps proposed by Bryant et al.[29] to describe the fretting corrosion at the cement-stem interface could result in a resizing of the oxide debris, and the generation of small Cr_2O_3 nanoparticles, detached from the large oxide flakes. A similar resizing mechanism was proposed by Pourzal et al. to explain the types of debris released from the CoCrMo bearing surfaces, which included large chromium oxide flakes and small Cr_2O_3 particles believed to flake off the surface of the large debris[28]. Most of the taper-trunnion debris investigated in the present study was found at the base of trunnion, outside the contacting area. This suggests that the particles released from tapers might be eventually flushed out from the crevice space, forming organo-metallic deposits around the male taper. Thus, the Cr_2O_3 flakes and particles might be subject to a limited number of loading steps before leaving the contact area which results in significantly larger particles from tapers than those released from the corresponding cemented stems.

The size of the particles to which an organism is exposed, dictates how the hosts deal with the foreign body and the responses they trigger[35]. An important implication of the small particles found in this study from both tapers and stems is related to the particle mobility and their ability to leave the joint space and travel systemically[35,39,41]. The synovial fluid in the joint cavity is regenerated by blood plasma, which brings in nutrients and clears up the released debris (metal particles, bone and hydroxyapatite fragments etc.). The excess of fluid is recirculated and filtered at the lymphatic nodes, which captures the macrophages engulfed with metal and free debris[332]. Debris from hip replacements, found in the lymphatic nodes, suggests this route as a plausible pathway for the particle dissemination particularly when the wear is excessive and the debris is too much to be retained in the lymphatic nodes[14]. This results in particles being released by the circulatory system and then spread to sites distant from the hip joint. The journey can stop at the kidneys, from where both the solid and soluble debris (ions) are excreted. This route, however, is likely to disseminate and remove from the body the small particles which are not retained in the periprosthetic tissue or lymphatic nodes.

At equal volumes of debris, the small particles show an increased specific area compared to the large particles, which makes them more susceptible to dissolution[35]. This results in the release of Cr and Co ions both locally and at distant sites. Co^{2+} is listed among the carcinogenic compounds and is believed to be the culprit for the ALTRs and systemic manifestations induced by hip related debris[34,103]. Cr^{3+} is the most thermodynamically stable form of Cr, but other species such as Cr^{2+} or Cr^{6+} can result from the *in vivo* redox processes. Among these species, Cr^{6+} has a well-documented cytotoxicity and genotoxicity[333] but its presence in the body, following hip replacements, has only

been reported once and may have resulted from the oxidation of the reduced Cr species after the prolonged exposure to the X-ray beamline, used for analysis[14]. Cr^{6+} is an unstable form of Cr, and tends to be rapidly reduced to the more stable Cr^{3+} phase, which means it is unlikely to exist in the body under normal conditions. The rapid dissemination of the small particles through the circulatory system, means that both Co and Cr ions can be released at distant organs, exerting their harmful and toxic effects far from the joint space. Heart failure has been associated with metal debris originating from hip replacements and spread systemically[54,89,334,335]. Other effects, including the loss of sight and hearing, were also linked to abnormally high levels of systemic Cr and Co ions from the wearing hip devices[34]. These, however, are extreme and isolated cases, in which pre-existing medical conditions were amplified by the released ions and particulate debris. Some of these adverse reactions are fortunately reversible, and the symptoms improve after the ions clear up from the body and the source of metal is removed.

In this study, the composition and phase analyses using EELS, SAED and XANES identified only Cr_2O_3 (Cr^{3+}) nanoparticles and Co^{2+} species from both CoCrMo tapers and cement-stem interfaces. The composition and chemistry (phase) did not differ with the origin, nor with the particle morphology. The release of the same species from both the wear sites means that it is may not be the speciation which provides the increased *in vivo* reactivity of the CoCrMo tapers debris, but the size and morphology of the particles, which was found in this study to vary with the origin.

The small size of the Cr_2O_3 particles released from both CoCrMo tapers and cement-stem interfaces are able to initiate the ALTRs reported with the failing hip devices. The smaller particles released from the stems, however, may be more easily removed from the body through systemic dissemination, eventually reaching the kidneys and leaving the body. This hypothesis needs to be validated by *in vitro* studies assessing the toxicity and potential to disseminate systemically of the Cr_2O_3 nanoparticles within the size ranges and morphologies reported here. Resolution of these issues may lead to a better understanding of the pathways involved in the initiation of ALTRs and solutions could be found to minimise their incidence.

5.4.2 Debris from CoCrMo tapers vs CoCrMo/Ti alloy tapers

The present study investigated the characteristics of taper debris from similar and dissimilar taper junctions and revealed morphological differences, linked with the interface material combination. The matched material CoCrMo taper junctions released significantly smaller particles compared to the mixed CoCrMo/Ti taper interfaces. The differences, however, might be due to the release of both Cr_2O_3 and TiO_2 particles from the dissimilar material tapers, whereas the matched CoCrMo taper junctions produced mainly Cr_2O_3 nanoparticles. The size distribution of the particles released from the mixed material taper junctions overlap the size distribution of debris from the matched CoCrMo tapers. This suggests that the Cr_2O_3 particles, which originate from both taper types, are smaller than

the TiO_2 nanoparticles, which are present only in the mixed material taper debris and widens the particle size range of this debris category (up to 120 nm). The size of Ti debris released from the stems and acetabular cups was reported in one of the previous studies[336]. The particle size ranged between 0.12 and 6.46 μm, with more than 50% being smaller than 0.4 μm. The size distribution, however, included both ZrO_2 particles released from the cement-mantle and Ti debris from the metallic components of the hip replacements (acetabular cup and cement-stem interface), and may not be representative for the debris released from the Ti interfaces. Also, the resolution limits of the technique used in the study to determine the size of the particles internalised in periprosthetic tissue (i.e. light microscopy) may have dictated the lower end of the size range (i.e. 0.12 μm). It is therefore possible that particles smaller than 0.12 μm were present in the periprosthetic tissue but could not be imaged and did not contribute to the reported size distribution. Another study used SEM and EDX to characterise *in vivo* released Ti debris from uncemented Ti alloy stems and revealed flakes 200-400 μm long and 10-20 μm thick[274]. A more recent study, however, reviewed the characteristics of Ti debris released from orthopaedic implants and concluded that the majority of the TiO_2 particles are smaller than 1000 nm[337]. Despite some obvious limitations of these previous studies, they suggest that larger particles are released from the Ti alloy interfaces than are released from the CoCrMo alloy and support the findings of the present research.

To our knowledge, a direct comparison between debris from similar and dissimilar material tapers has never been performed before, although the comparison between the material released from the MoM bearing surfaces (CoCrMo hip resurfacings) and that released from the additional taper interfaces in total hip replacements (CoCrMo sleeve on Ti stems or CoCrMo dual modular neck on Ti stems) has been recently reported[39]. The study, however, investigated debris from periprosthetic tissue and did not use any method to isolate the particles for a direct and reliable size comparison. The study revealed that larger particles are released from the dissimilar taper junctions in comparison to those released from the CoCrMo hip resurfacings. Most of the particles from the taper interfaces ranged between 10 and 100 nm, with few larger particles in the double neck taper group. The composition analysis also revealed differences between taper and bearings debris. While some of the particles originating from the CoCrMo/Ti interfaces comprised mainly Cr in the form of Cr_2O_3, others contained both Cr and Ti, but the phase was not identified. The results of the particle size, morphology and composition analyses were also correlated with the histological findings, which revealed evidence of more severe adverse reactions in periprosthetic tissue from around the modular taper junctions. The authors of the study concluded that the severity of the adverse reactions may have been triggered by the highest particle composition complexity of the Cr and Ti rich debris, which were also associated with the shortest time of implantation among the three investigated groups (28 months for non-MoM THA with CoCrMo dual modular neck and Ti stems, vs 48 and 60 months for the MoM HRA and MoM THA (CoCrMo sleeve on Ti stem) group respectively). For the resurfacings hip prostheses group and non-MoM total hip replacements, the origin of metal debris is well-known and can be attributed to a single source (i.e. the CoCrMo bearing surfaces or the CoCrMo

dual modular neck/Ti stem interface for the non-MoM THR). On the contrary, for the MoM THR group, metal debris can be released from the bearing surfaces and from the interface of the CoCrMo sleeve and Ti stem. In this case, the characteristics of debris cannot be attributed to a certain origin and the results cannot be compared to the outcomes of the present study.

Here, the speciation analysis of the Cr rich debris released from both the similar and dissimilar material taper junctions revealed Cr_2O_3, which is in agreement with the study of Xia et al.[39] and Munir et al.[338] which also reported Cr_2O_3 released from the mixed material taper junctions. In addition, the investigation of debris from the ceramic-on-ceramic (CoC) hip replacements with modularity at the CoCrMo/Ti alloy tapered interface (stem-sleeve), reported by Munir et al., revealed $Fe_2Ti_3O_9$, Co_3O_4 and CrO from the non-metallic implant group. In their study, Munir et al.[338] performed the speciation analysis of taper debris entrapped in periprosthetic tissue using XRD, and the identification of multiple species was attributed to the different stages of the *in vivo* oxidation. The ABG stem in the CoC implant group consisted of Ti-Mn-Zr-Fe alloy which explains the presence of the mixed Ti and Fe oxide.

The STXM and XANES investigation in the present study suggested that part of the Cr rich debris in the partially digested flakes from the mixed material taper junctions is $CrPO_4$. The Cr rich crystalline particles investigated with STEM and EDX, however, did not comprise P and were Cr_2O_3, as confirmed by the complementary analysis techniques used in this study. The TEM/SAED characterisation and STEM/EELS analysis of the mixed material taper debris provided information about the Ti species released at these particular interfaces. Both techniques suggested that besides Cr_2O_3 nanoparticles, TiO_2 particles were generated from mechanically assisted crevice corrosion at the mixed CoCrMo/Ti tapers. The findings are in agreement with the study of Swiatkowska et al. which identified by synchrotron analyses (μ-XRF and μ-XAS) TiO_2 (rutile phase) debris in periprosthetic tissue from around dissimilar material taper junctions[14]. The speciation of Co revealed the same species released from both similar and dissimilar material taper junctions.

5.4.3 Debris from toggling vs non-toggling tapers

The correlation of the physicochemical characteristics of the taper debris with the wear mechanism responsible for their release (toggling vs non-toggling CoCrMo tapers), did not reveal significant differences when the particles were cleaned using the enzymatic treatment. The particle size was smaller for the particles released from the non-toggling CoCrMo taper than that of the particles originating from the toggling taper, but the difference was not statistically significant. The release of debris from the toggling head was dominated by the mechanical wear, which resulted from the toggling motion. In contrast, the release of debris from the non-toggling CoCrMo taper was controlled by a corrosion dominated process, which resulted in the formation of a Co and P rich phase, believed to be $Co_3(PO_4)_2$, and found in the as-retrieved flake. The electrochemical conditions

at the toggling and non-toggling taper junction can be different, resulting in particles of different sizes and morphologies. The fragment of debris released from the toggling taper and investigated with SEM and EDX mapping did not show any evidence of corrosion products. Also, the composition analysis of another fragments of debris from the toggling taper using ICP-MS, showed mainly Cr, with less amounts of Co and Mo. In contrast, the composition of one piece of debris from the non-toggling taper revealed more Co and Mo, than Cr. Co and Mo are more soluble than Cr, and a corrosive environment may have resulted in their leach from the CoCrMo particles. The closed environment at the crevice, did not allow the release of ions systemically which accumulated around the edge of the flake. These products are brittle and can therefore easily break, resulting in small fragments of different compositions. The cleaning procedure of other fragments, however, revealed mainly Cr_2O_3 nanoparticles from both tapers, and the particles had similar sizes and morphology. The presence of cobalt phosphate, removed in the study by the cleaning treatments, may provide debris from the non-toggling CoCrMo tapers with different *in vivo* reactivity and an increased potential to trigger more severe adverse body reactions.

5.5 How the Taper and Stem Debris relates to Debris from the Bearing Surfaces

The vast majority of the previous studies reported the physicochemical characteristics of metal debris released *in vivo*[20,24,36,274,277,286,291] and *in vitro*[20,21,23,28,98,279] from the MoM bearing surfaces in hip replacements. The *in vitro* studies used anatomical hip simulators or pin on disk tribometers to generate debris from the bearing surfaces and assess the wear performances of the metals and alloys used for the design of the hip implants. Other *in vivo* studies used hip aspirates and periprosthetic tissue to understand the nature of debris released in patients from the failing hip prostheses. In most of these cases, however, the origin of the investigated debris was not known. In the particular case of MoM total hip replacements, the wear particles and corrosion products can originate from the bearing surfaces, taper junctions or the cement-stem interface. This can make it difficult to understand the particularities of debris, in relation to the sites of wear and wear mechanism.

In the present study the wear and corrosion flakes were collected from around the taper junctions and cement-stem interfaces of revised components, forensically investigated to understand the failure modes. The origin of debris is therefore well-known (tapers and cement-stem interface) and the characteristics of the investigated particles are representative for debris released from these particular interfaces. The particles revealed in the present study and characterised with state-of-the-art investigation techniques were in the nanometre size range. Despite the different origins, the size distributions of the taper and stem debris are in agreement with the size distributions of particles from the MoM bearing surfaces, reported in the previous studies[20,23,28,36,98,285]. In most of these studies the size distributions were wider than those reported in the present study. A reason for that might be the limitations of the techniques used to determine the size of the particles, which in most cases found large clusters of debris, rather than individual nanoparticles. This hypothesis was verified in the present study and the comparison suggested that the particle size ranges reported after the TEM characterisation are generally larger than those reported after the use of the high-resolution techniques, such as the HR-STEM. The statistical analysis, however, revealed that only for half of the samples the differences between the sizes of debris characterised with TEM and STEM respectively were statistically significant. Others reported debris from the bearings in the size ranges found in the present study (<100 nm), but failed to provide evidence of particles smaller than 10-15 nm[20,28,111,276,281]. One of the previous studies compared the characteristics of debris released from the CoCrMo bearings under normal and microseparation conditions and revealed differences in the particle size[98]. Other studies characterised debris from the synovial aspirate[24,291] and revealed particles as small as 5 nm, forming clusters as large as 50 nm[291]. Nevertheless, these studies reported metal debris in the micrometre size range, which were likely particle aggregates rather than individual particles[274,277,286].

The investigation techniques used in the studies play an important factor which determines the accuracy of the study's outcomes[286]. The wider particle size ranges reported by others using different characterisation techniques (LM, SEM, TEM, FEF-SEM) reflect the difficulty in resolving the small particles which form the clusters, which are regarded instead as large, individual particles. An important limitation of the present study is the lack of information about the physicochemical properties of debris from the CoCrMo bearing surfaces, achieved with the same techniques used to characterise taper and stem debris. The comparison between the size distributions of the particles found in this study and characterised by STEM, and debris from the bearing surfaces reported in other studies using other characterisation techniques may be irrelevant. The differences in size may be attributed to the use of different techniques, rather than to the different origin and wear mechanisms.

The chemical characterisation of debris released from tapers and cement-stem interfaces revealed mainly Cr_2O_3, traces of $CrPO_4$ and TiO_2 released from the dissimilar taper junctions. The composition and speciation results are in agreement with most of the previous studies which reported metal debris from the bearings[100,288,295] or taper junctions[39,100,338]. Besides Cr_2O_3, other studies also reported CoCr debris, which was not identified in the present study. According to Catelas et al., the particles characterised by a higher amount of Cr compared to Co, and a significant C peak can originate from carbides. Carbides are formed during the manufacturing of the CoCrMo bearings, incorporating C and various proportions of Co, Cr and Mo, of which Cr is predominant[111]. The particles with higher Co over Cr concentrations are believed to originate from the bulk alloy[281]. Beside CoCrMo particles, Cr and O rich particles were also reported and were believed to be chromium oxides released from the passivating oxide layer[21,111,281]. Others reported Cr and O rich amorphous structures believed to form after the corrosion of the CoCrMo particles released *in vivo,* which resulted in the dissolution of Co and the remaining of the Cr rich amorphous debris[36,274]. Cr oxide particles with minimal or no Co were found in periprosthetic tissue regardless of the implantation time, while the CoCr particles, believed to originate from the bulk alloy, were mainly reported in patients with longer implantation times.

The speciation analysis of debris from the CoCrMo hip resurfacings using STXM/XAS[100,295] and STEM/EELS/EDX[288] revealed mainly oxidised Cr (Cr^{3+}) with less Co (Co^{2+}), found highly packed in macrophages within the periprosthetic tissue. Other particles showed a metallic core, comprised of Co, Cr and Mo, surrounded by a Cr_2O_3 shell[288]. According to the authors of the study, the oxidised Cr particles potentially resulted from the corrosion of the metallic debris which released the more soluble Co, believed to have implications on the changes observed at the sub-cellular level in macrophages. The metallic particles, believed to be partially corroded debris, were less frequent in tissue. These fragments were suggested to be released in the body later than the fully oxidised fragments, which were lacking Co and indicated a complete *in vivo* transformation. The evidence of

high Co levels in the serum suggested that Co is more soluble than Cr and is more easily released from the CoCrMo particles and exposed CoCrMo alloy.

Other authors reported different types of CoCrMo particles released from the bearing surfaces in total hip replacements. They reported amorphous Cr and O rich structures with crystalline regions rich in Co, and both small and large particles containing only Cr and O[28]. The small particles revealed the lattice structure of Cr_2O_3 and were believed to flake off the surface of the larger particles. The study also revealed lattice defects of the small chromium oxide particles which are believed to result from the high stresses experienced by the particle in the nano crystalline layer of the hip bearings, which provided them with increased energy and reactivity[28]. The non-crystalline regions reported in some of the particles are believed to be triggered by a reversible phase transition experienced by nanoparticles under load.

At equal doses, debris released from tapers can trigger more severe adverse reactions than debris released from the bearing surfaces[6,7]. The reason remains unknown, but the characteristics of the debris, including the size, morphology and composition are believed to be responsible for the different *in vivo* particles toxicity[48]. Although the purpose of the present study was not to directly compare debris from the bearing surfaces and debris from tapers or stem, it can easily identify some differences which may result in the onset of different adverse body reactions. The discussion regarding the size differences between the taper debris, reported in this study, and bearing debris, reported by others, would not be fair, because of the different techniques used to assess the PSDs, and the associated technical limitations. The electrochemical conditions at the taper crevice, however, are believed to shape the particulate debris, potentially resulting in particles with altered size, morphology and composition, from their native state. The dissolution of Co from the wearing taper interfaces and particulate debris can be a consequence of the corrosive environment at the crevice which results in increased Co systemic concentrations. This mechanism of debris alteration is supported by the increased Co blood levels[2,4,169], commonly reported with failing CoCrMo taper junctions and by the signs of the Co rich corrosion products localised at the surface of the as-retrieved wear and corrosion flakes investigated in the present study. The investigation of debris from the bearing surfaces, reported in the previous studies, revealed Cr oxides, $CrPO_4$, as well as CoCr debris in which Co was metallic (Co^0)[288,295]. The conditions at the bearings, therefore, may not favour the leach of the Co ions from the particles, although some Co may be released from the corrosion of the exposed bearing surfaces or the particulate debris. The open space, however, means that particles can leave the joint area, getting entrapped in the periprosthetic tissue or traveling within the body, resulting in a rapid dilution/excretion of the released ions. The severe adverse reactions to taper debris can therefore be a consequence of the high levels of systemic Co which is believed to be the initiator of the ALTRs to CoCrMo debris[34]. The theory is further supported by the *in vitro* studies assessing the toxicity of the main products released from the hip replacements. The toxicity of the Cr_2O_3 particles, which is the main phase revealed after the cleaning of the taper wear and corrosion flakes,

was not proven by the previous studies[330]. One study, however, reported the *in vitro* release of Cr^{6+} ions when cells were treated with Cr_2O_3 debris and it was associated with severe cytotoxicity[329]. Similarly, the cells fed with $CrPO_4$, reported by others around the failing tapers and bearings, experienced low cytotoxic effects and therefore could not explain the severe reactions observed with the taper debris[331].

5.6 Summary

The comprehensive characterisation of the stem and taper debris in this study, revealed for the first time the structure and composition of the wear and corrosion flakes from the micron-scale down to the nano-level. The results demonstrate that the flakes consist of mechanically mixed oxide nanoparticles, corrosion products and biological material, which is in agreement with the mechanisms proposed by others to explain the release of debris from tapers[224], cement-stem interface[29] and MoM bearing surfaces[130]. The use of the high-resolution STEM revealed the structure of the crystalline nanoparticles originating from the CoCrMo taper junctions, cement-stem interface and CoCrMo/Ti tapers, which, according to our knowledge, has never been shown before. The size, morphology and composition analysis revealed the original nature of the metal particles released from the various interfaces, which have not been altered by macrophage internalisation. In contrast to the previous studies, the wear and corrosion flakes in this study were collected from around the site of material loss and are representative of the debris released at these interfaces. The study also stands ahead by revealing both the physico-chemical properties of particles cleaned by the use of two alternative treatments, and by providing speciation information about the various types of debris in relation to the origin. For the first time, the study compares the characteristics and speciation of debris released from mixed and matched material taper junctions, and shows that larger particles originate from the CoCrMo/Ti tapers. The results can have implications on particle reactivity which can trigger different local adverse reactions. Finally, the study compares the effects of the cleaning treatments on the particles characteristics and provides useful guidelines on how to isolate and characterise nanoparticles, which can have applications in various fields. The results of the study aim to serve as reference for *in vitro* studies which assess the particle toxicity, and have previously used mainly commercially available CoCrMo particles or debris generated from tribotests with an unrealistic composition or size distribution[156].

Chapter 6 Conclusions and Future Work

6.1 Conclusions

The present study provided the first comprehensive characterisation of the wear and corrosion flakes released *in vivo* from the taper junctions and cement-stem interfaces of total hip replacements. The study had a different research approach which used complementary characterisation techniques to reveal the structure, composition and speciation of wear and corrosion products from the mixed and matched materials tapers and cement-stem interfaces. The products originating from these secondary interfaces have never before been investigated to such an extent, despite the evidence of the increased potential of the taper debris to trigger ALTRs, in comparison to the equivalent amount of debris from the MoM bearing surfaces. Furthermore, the study assessed and compared the efficiency of two cleaning treatments which were used to revel the smallest building blocks that make up the wear and corrosion flakes. This allowed for a complete investigation of the wear and corrosion flakes from the micron scale down to the nano level.

The main conclusions of the study are listed below:

- The study reported the elemental composition of the *in vivo* released wear and corrosion flakes and demonstrated the heterogeneous nature of these products, which resulted from a mechanical mixing process. The ICP-MS analysis revealed mainly Co, Cr and Mo in debris released from the CoCrMo alloy tapers and cement-stem interfaces, and Co, Cr, Mo and Ti in debris originating from the mixed material taper junctions (CoCrMo/Ti alloy).
- The SEM and EDX characterisation demonstrated the preferential distribution of the main elements of the CoCrMo alloy, confirming that these products are subjected to changes in the body. Although it was not confirmed by chemical analysis, the SEM and EDX characterisation of the as retrieved flakes provided for the first time evidence of $Co_3(PO_4)_2$ whose toxicity has not been assessed in relation to hip related debris.
- The study used for the first time an alkaline and an enzymatic treatment to digest and clean wear and corrosion products released from the secondary interfaces of total hip replacements. The cleaning treatments revealed the smallest building blocks which make up the wear and corrosion flakes and made them available for the in-depth structural characterisation.
- The individual nanoparticles were characterised by a state-of-the-art atomic resolution electron microscope fitted with EDX and EELS capabilities, which revealed the size, morphology, lattice structure, composition and speciation of the nano-sized debris. To the knowledge of the authors, the study is the first to provide microscopic evidence of particles as small as 3-5 nm originating from the tapers and cement-stem interfaces, which has

important health implications concerning the potential of the particles to travel systemically and dissolve at distant organs.

- The study is the first to perform the speciation analysis of taper and stem debris which was not found in periprosthetic tissue and was not internalised by macrophages, being subjected to minimal alterations from their original nature.
- The XANES, EELS and SAED investigations revealed mainly Cr_2O_3 nanoparticles from the CoCrMo tapers and cement-stem interfaces, and Cr_2O_3 and TiO_2 nanoparticles from the mixed CoCrMo/Ti alloy tapers, and provided evidence of the highly toxic Co^{2+} ions, most likely in the form of oxides.
- The comparison between the CoCrMo taper and stem debris, showed that smaller particles are released from the cement-stem interface, although debris from both wear sites are in the nanometre size range. The speciation analysis, however, did not reveal any differences between the species released from CoCrMo tapers and stems. The assessment included taper and stem debris from both different and same retrievals.
- The study provided a comparison between debris released from mixed and matched material taper junctions and revealed that larger particles originate from the CoCrMo/Ti alloy tapers. The size difference may be justified by the presence of both Cr_2O_3 and TiO_2 nanoparticles released from the mixed material taper interface.
- The speciation of the particulate debris with XANES and EELS was confirmed by complementary techniques, such as SAED, which indicated that mainly Cr_2O_3 and TiO_2 nanoparticles, with traces of Co^{2+} are released from the mixed and matched tapers and cement-stem interfaces.
- The study provided two alternative methods to clean and isolate particulate debris from the mechanically mixed wear and corrosion flakes. The comparison between debris cleaned with the alkaline and enzymatic treatment revealed that smaller and generally cleaner nanoparticles are released from the alkaline treatment. The selection of the isolation treatment should be made based on the study objectives and taking into account the strengths and limitations of each technique.
- Finally, the study provides a guideline on how to clean, isolate and characterise nanoparticles, which may have applications in various research fields, other than the field of debris characterisation.

6.2 Future Work

- The results of the present study show that the majority of the particles release from the mixed and matched tapers and cement-stem interface are smaller than 140 nm. The *in vitro* studies, which assess the toxicity of the hip related debris should use nanoparticles which are representative of what is being released in the body, both size and composition wise. Future work should focus therefore on understanding the toxicity of Cr_2O_3 and TiO_2 nanoparticles smaller than 140 nm.
- Further work should better understand the chemistry of the Co and P rich patches reported in this study, to understand the processes that lead to it being produced in the body, although Co was only present as a trace element in the Cr oxide nanoparticles. The *in vitro* toxicity of the Co and P rich product, should also be assessed.
- The authors acknowledge the small number of retrievals used in the study. For more powerful comparisons between debris from various wear and corrosion sites, debris from more retrievals should be investigated.
- In order to allow for the direct comparison of debris from secondary interfaces (taper and stem) and primary articulating surfaces (hip bearings), identical treatments and characterisation techniques must be used. Future studies should apply the cleaning treatments and characterisation steps described here to reveal the nature of the wear particles originating from the MoM CoCrMo bearing surfaces and assess how their characteristics compare to those of the particles originating from the secondary interfaces.

Appendix A

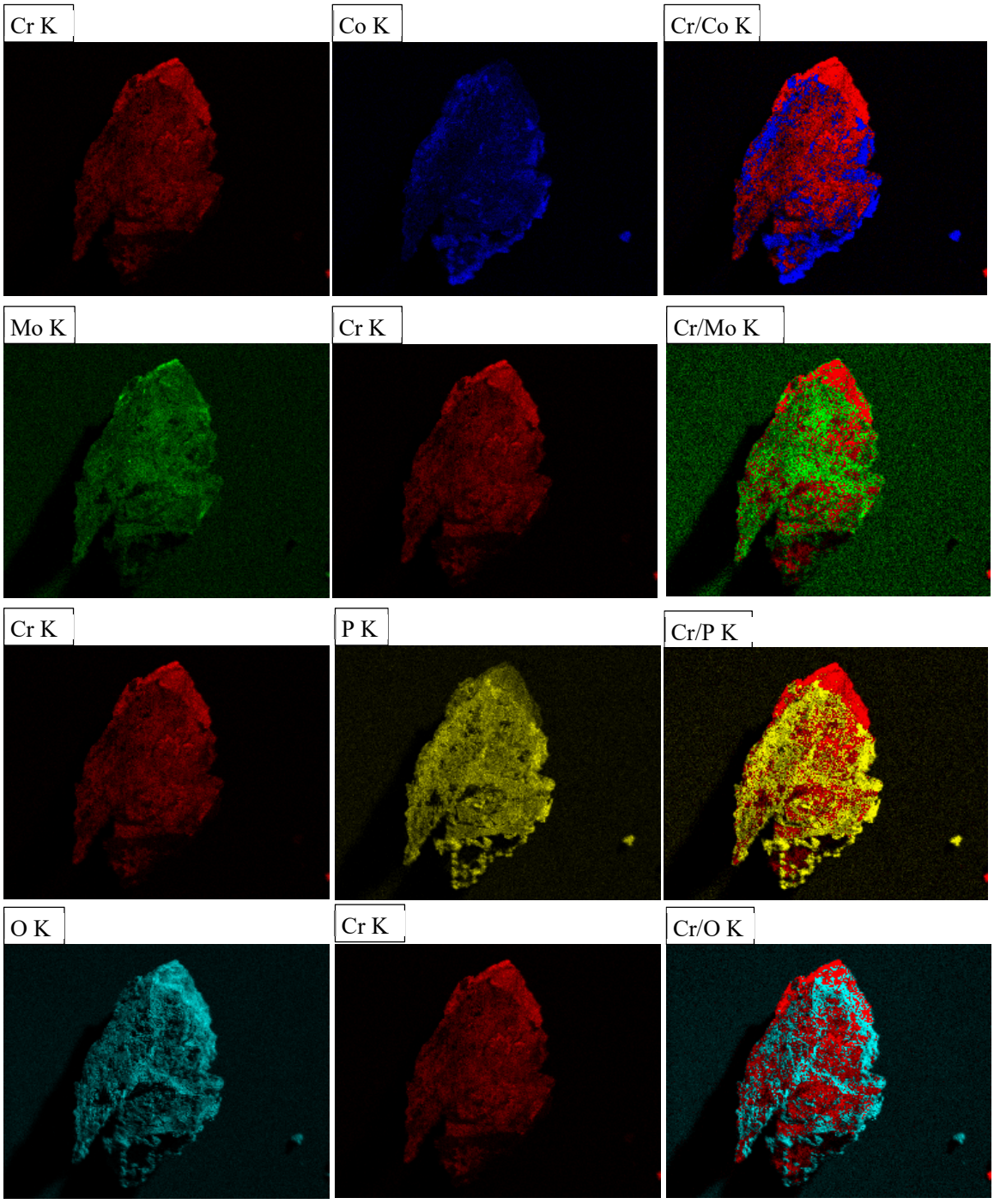

The SEM/EDX maps of a fragment of debris from taper 1.

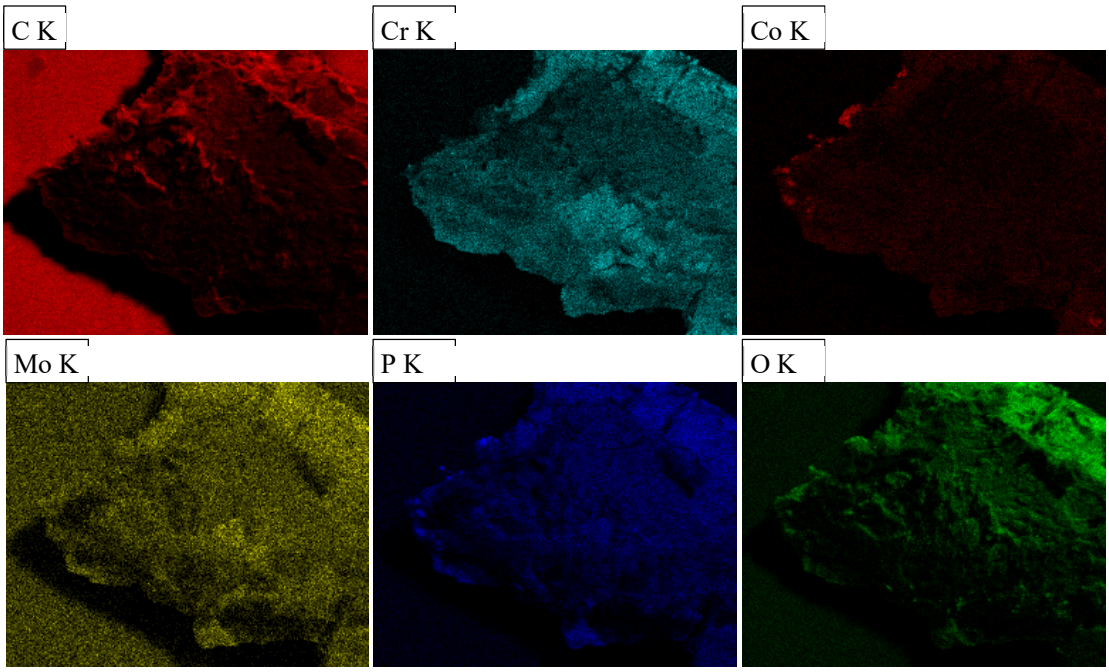

The SEM/EDX maps of a fragment of debris from taper 2.

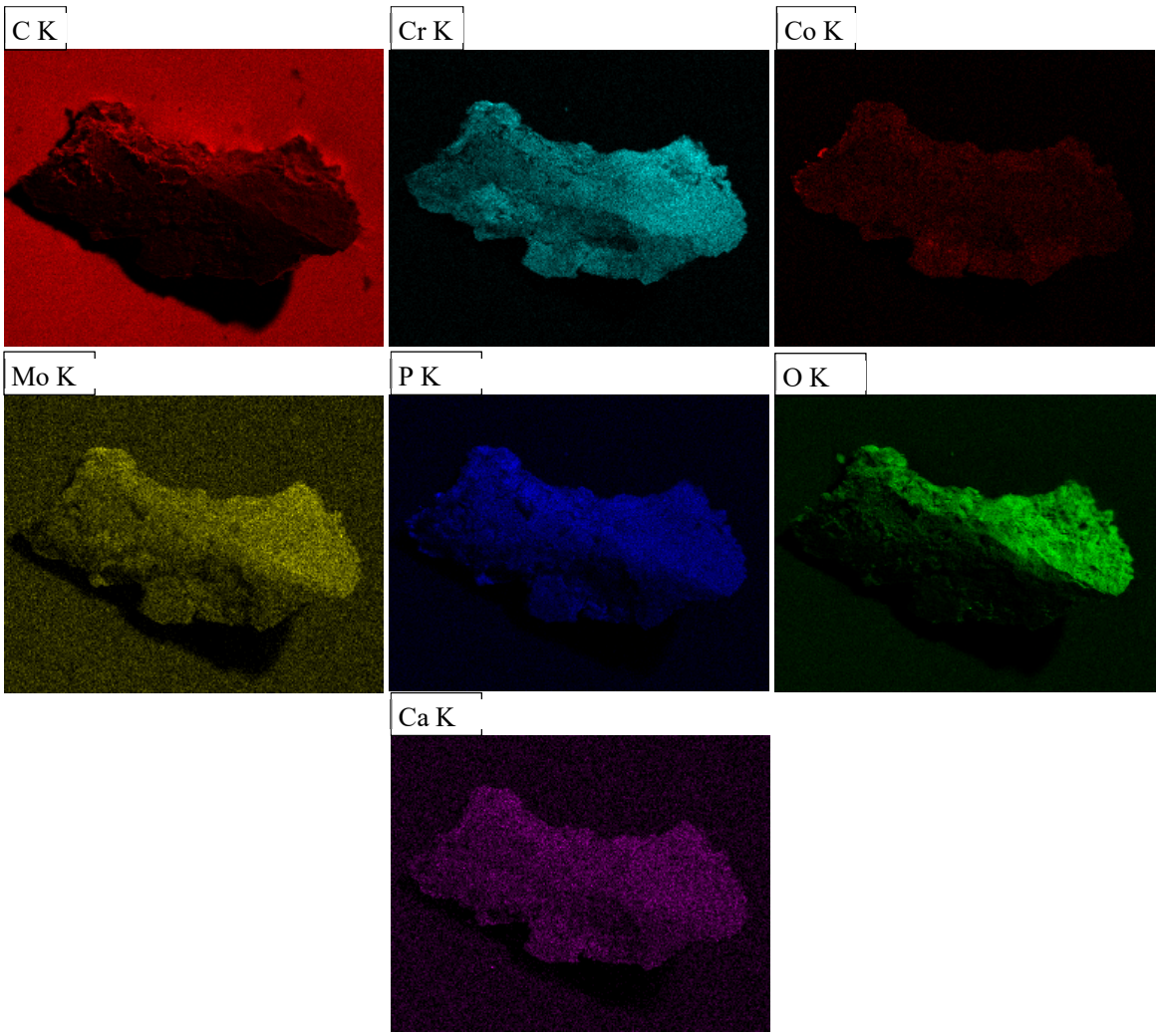

The SEM/EDX maps of a fragment of debris from taper 2.

Appendix B

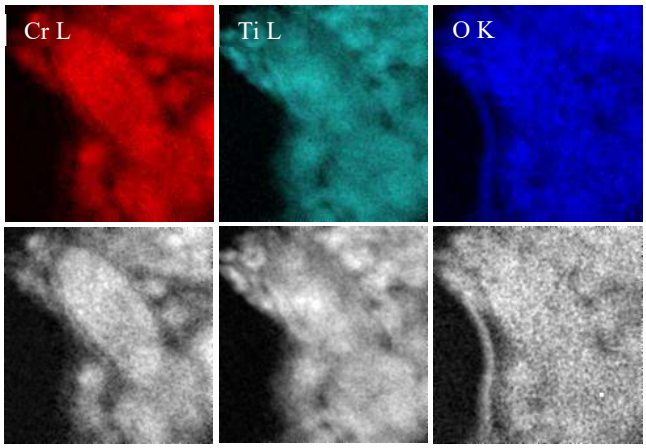

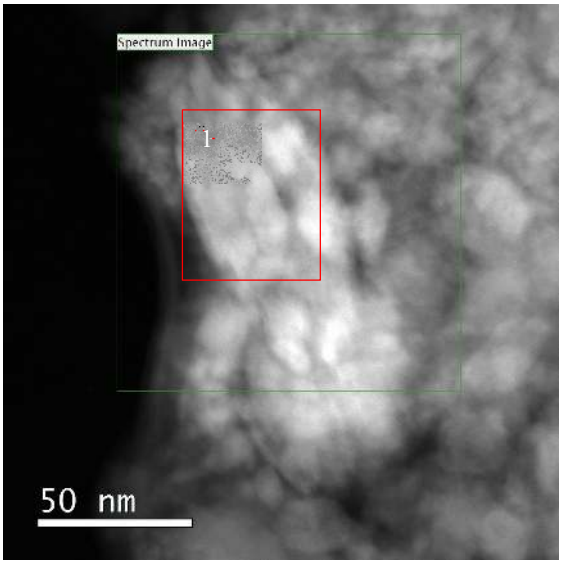

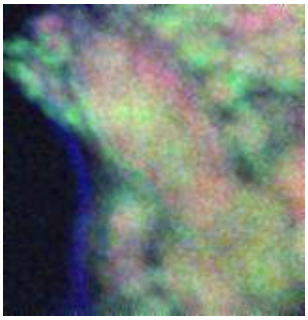

Red – Cr; Green – Ti; Blue – O.

Cluster	**Atomic ratio (/O)**	**At %**
Ti	0.27 (±0.04)	16.31
O	1.00 (±0.00)	59.57
Cr	0.40 (±0.06)	24.12

Reg 1	**Atomic ratio (/O)**	**At %**
Ti	0.26 (±0.04)	15.14
O	1.00 (±0.00)	58.13
Cr	0.46 (±0.06)	26.73

The STEM/EELS maps and quantification results of a fragment of debris from taper 7.

Appendix C

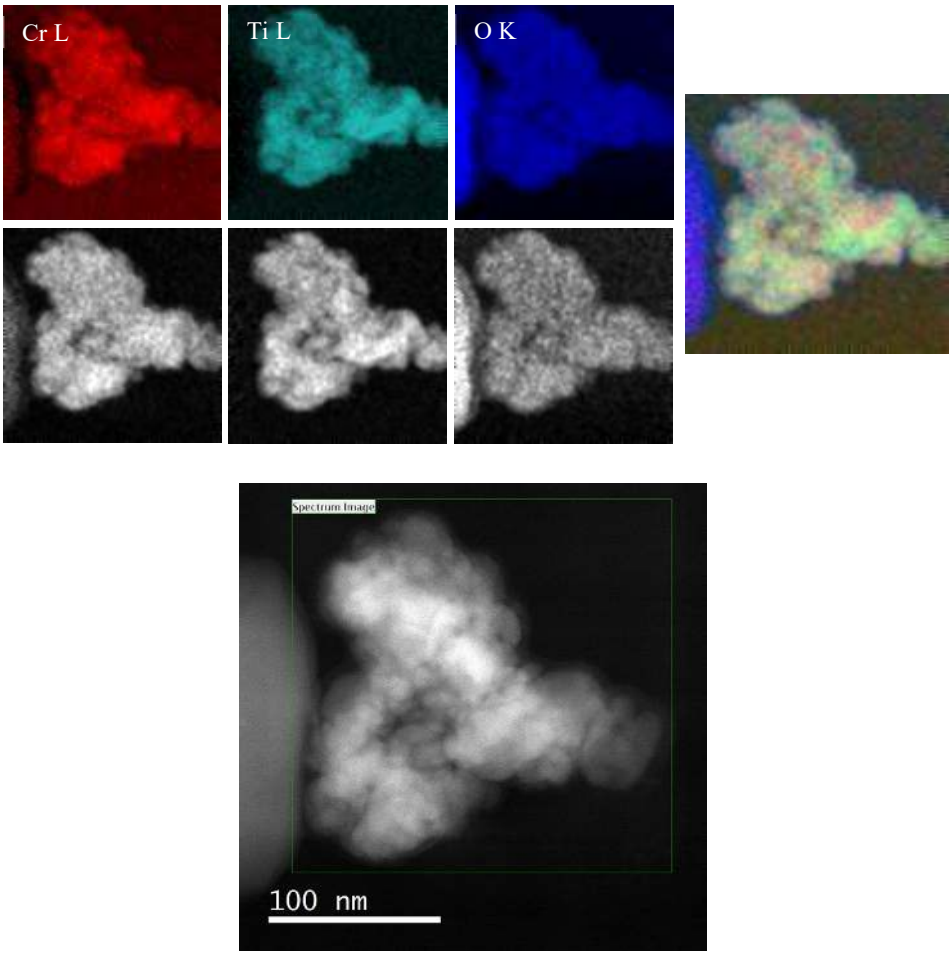

Cluster	**Atomic ratio (/O)**	**At %**
Ti	0.19 (±0.03)	13.03
O	1.00 (±0.00)	68.38
Cr	0.27 (±0.04)	18.59

Reg 1	**Atomic ratio (/O)**	**At %**
Ti	0.24 (±0.03)	15.94
O	1.00 (±0.00)	65.12
Cr	0.29 (±0.04)	18.94

The STEM/EELS maps and quantification results of a fragment of debris from taper 8.

Appendix D – Publications and Awards

- Publications

Investigation of nano-sized debris released from CoCrMo secondary interfaces in total hip replacements: Digestion of the flakes

Alina M. Crainic, Mauro Callisti, Martin R. Palmer, Richard B. Cook
J Biomed Mater Res Part B, 2018:00B:000–000 (https://doi.org/10.1002/jbm.b.34134)

A comparative study on the physicochemical characteristics of nanoparticles released *in vivo* from CoCrMo tapers and cement-stem interfaces of total hip replacements

Alina M. Crainic, Mauro Callisti, Arjen van Veelen, Agnes Michalik, James A. Milton, Martin R. Palmer, Richard .B. Cook

Finalised manuscript intended to be submitted to Biomaterials in the next months

What provides the increased *in vivo* reactivity of CoCrMo taper debris?

Alina M. Crainic, Mauro Callisti, Arjen van Veelen, Agnes Michalik, James A. Milton, Martin R. Palmer, Richard .B. Cook

Manuscript intended to be submitted to Nature Biotechnology in the next months

- Conference Proceedings

A comparison between debris from CoCrMo tapers, cement-stem interfaces and CoCrMo/Ti tapers

Alina M. Crainic, Mauro Callisti, Arjen van Veelen, Martin R. Palmer, Richard B. Cook
Orthopaedic Research Society (ORS) Annual Meeting, New Orleans, Louisiana (US)
10-13 March 2018. Contribution: Poster

Characterisation of wear and corrosion products from around a retrieved CoCrMo taper junction

Alina M. Crainic, Mauro Callisti, Martin R. Palmer, Richard B. Cook
Orthopaedic Research Society (ORS) Annual Meeting, San Diego, California (US)
19-22 March 2017. Contribution: Poster

Investigation of wear and corrosion products from the cement-stem interface of explanted hip replacements

Alina M. Crainic, Mauro Callisti, Agnes Michalik, James A. Milton, Martin R. Palmer, Richard B. Cook
British Hip Society (BHA) Annual Meeting, London (UK)
1-3 March 2017. Contribution: Oral

- Awards

£50 000 research grant from 'Arthroplasty for Arthritis Charity', UK

References

1. Bradberry, S. M., Wilkinson, J. M. & Ferner, R. E. Systemic toxicity related to metal hip prostheses. *Clinical Toxicology* **52,** 837–847 (2014).

2. Cook, R. B. *et al.* Pseudotumour formation due to tribocorrosion at the taper interface of large diameter metal on polymer modular total hip replacements. *J. Arthroplasty* **28,** 1430–1436 (2013).

3. Messana, J., Adelani, M. & Goodman, S. B. Case report: Pseudotumor associated with corrosion of a femoral component with a modular neck and a ceramic-on-polyethylene bearing. *J. Long. Term. Eff. Med. Implants* **24,** 1–5 (2014).

4. John Cooper, H. *et al.* Corrosion at the Head-Neck Taper as a Cause for Adverse Local Tissue Reactions After Total Hip Arthroplasty. *J. Bone Jt. Surgery-American Vol.* **94,** 1655–1661 (2012).

5. Goodman, S. B., Barrena, E. G., Takagi, M. & Konttinen, Y. T. Biocompatibility of total joint replacements: A review. *Journal of Biomedical Materials Research - Part A* **90,** 603–618 (2009).

6. Sidaginamale, R. P. *et al.* The clinical implications of metal debris release from the taper junctions and bearing surfaces of metal-on-metal hip arthroplasty. *Bone Jt. J.* **98B,** 925–933 (2016).

7. Langton, D. *et al.* Metal debris release from taper junctions appears to have a greater clinical impact than debris released from metal on metal bearing surfaces. *Bone Jt. J. Orthop. Proc. Suppl.* **95–B,** 28 LP-28 (2013).

8. Grover, M. L. Controversial topics in orthopaedics: metal-on-polyethylene. *Ann. R. Coll. Surg. England.* **87,** 416–418 (2005).

9. Billi, F. *et al.* Metal wear particles: What we know, what we do not know, and why. *SAS J.* **3,** 133–142 (2009).

10. Hussenbocus, S., Kosuge, D., Solomon, L. B., Howie, D. W. & Oskouei, R. H. Head-neck taper corrosion in hip arthroplasty. *Biomed Res. Int.* **2015,** (2015).

11. Meyer, H. *et al.* Corrosion at the cone/taper interface leads to failure of large-diameter metal-on-metal total hip arthroplasties. *Clin. Orthop. Relat. Res.* **470,** 3101–3108 (2012).

12. Zhang, H. Y., Blunt, L. A., Jiang, X. Q., Fleming, L. T. & Barrans, S. M. The influence of bone cement type on production of fretting wear on the femoral stem surface: A preliminary

study. *Clin. Biomech.* **27,** 666–672 (2012).

13. Urban, R. M., Tomlinson, M. J., Hall, D. J. & Jacobs, J. J. Accumulation in liver and spleen of metal particles generated at nonbearing surfaces in hip arthroplasty. in *Journal of Arthroplasty* **19,** 94–101 (2004).

14. Swiatkowska, I. *et al.* Synchrotron analysis of human organ tissue exposed to implant material. *J. Trace Elem. Med. Biol.* **46,** 128–137 (2018).

15. Matusiewicz, H. Potential release of in vivo trace metals from metallic medical implants in the human body: From ions to nanoparticles - A systematic analytical review. *Acta Biomaterialia* **10,** 2379–2403 (2014).

16. Tower, S. S. Arthroprosthetic cobaltism: Neurological and cardiac manifestations in two patients with metal-on-metal arthroplasty: A case report. *J. Bone Jt. Surg. - Ser. A* **92,** 2847–2851 (2010).

17. Akbar, M., Brewer, J. M. & Grant, M. H. Effect of chromium and cobalt ions on primary human lymphocytes in vitro. *J. Immunotoxicol.* **8,** 140–149 (2011).

18. Jomova, K. & Valko, M. Advances in metal-induced oxidative stress and human disease. *Toxicology* **283,** 65–87 (2011).

19. De Smet, K. a *et al.* Revisions of metal-on-metal hip resurfacing: lessons learned and improved outcome. *Orthop. Clin. North Am.* **42,** 259–69, ix (2011).

20. Catelas, I., Medley, J. B., Campbell, P. A., Huk, O. L. & Bobyn, J. D. Comparison ofin vitro within vivo characteristics of wear particles from metal-metal hip implants. *J. Biomed. Mater. Res.* **70B,** 167–178 (2004).

21. Billi, F. *et al.* The John Charnley award: An accurate and sensitive method to separate, display, and characterize wear debris: Part 1: Polyethylene particles. *Clin. Orthop. Relat. Res.* **470,** 329–338 (2012).

22. Billi, F. *et al.* The John Charnley Award: an accurate and extremely sensitive method to separate, display, and characterize wear debris: part 2: metal and ceramic particles. *Clin. Orthop. Relat. Res.* **470,** 339–350 (2012).

23. Lu, F. *et al.* Simple isolation method for the bulk isolation of wear particles from metal on metal bearing surfaces generated in a hip simulator test. *J. Mater. Sci. Mater. Med.* **23,** 891–901 (2012).

24. Kavanaugh, A. E., Benya, P. & Billi, F. A method to isolate and characterize wear debris from synovial fluid and tissues. in *ASTM Special Technical Publication* **1560 STP,** (2013).

25. De Pasquale, D. *et al.* Metal-on-metal hip prostheses: Correlation between debris in the synovial fluid and levels of cobalt and chromium ions in the bloodstream. *Int. Orthop.* **38,** 469–475 (2014).

26. Campbell, P., RM, U., Catelas, I., AK, S. & TP, S. Autopsy analysis thirty years after metal-on-metal total hip replacements. *J Bone Joint Surg Am* **85–A,** 2218–2222 (2003).

27. Nine, M., Choudhury, D., Hee, A., Mootanah, R. & Osman, N. Wear Debris Characterization and Corresponding Biological Response: Artificial Hip and Knee Joints. *Materials (Basel).* **7,** 980–1016 (2014).

28. Pourzal, R., Catelas, I., Theissmann, R., Kaddick, C. & Fischer, A. Characterization of wear particles generated from CoCrMo alloy under sliding wear conditions. *Wear* **271,** 1658–1666 (2011).

29. Bryant, M. *et al.* Characterisation of the surface topography, tomography and chemistry of fretting corrosion product found on retrieved polished femoral stems. *J. Mech. Behav. Biomed. Mater.* **32,** 321–334 (2014).

30. National Joint Registry. National Joint Registry 13th Annual report. *Natl. Jt. Regist. Reports* (2016).

31. Chana, R., Esposito, C., Campbell, P. A., Walter, W. K. & Walter, W. L. Mixing and matching causing taper wear: Corrosion associated with pseudotumour formation. *Bone Joint J.* **94–B,** 281–286 (2012).

32. Cooper, H. J. *et al.* Adverse local tissue reaction arising from corrosion at the femoral neck-body junction in a dual-taper stem with a cobalt-chromium modular neck. *J. Bone Joint Surg. Am.* **95,** 865–72 (2013).

33. Bosker, B. H. *et al.* High incidence of pseudotumour formation after large-diameter metal-on-metal total hip replacement: A prospective cohort study. *J. Bone Jt. Surg. - Br. Vol.* **94–B,** 755–761 (2012).

34. Bradberry, S. M., Wilkinson, J. M. & Ferner, R. E. Systemic toxicity related to metal hip prostheses. *Clin. Toxicol.* **52,** 837–847 (2014).

35. Keegan, G. M., Learmonth, I. D. & Case, C. P. A systematic comparison of the actual, potential, and theoretical health effects of cobalt and chromium exposures from industry and surgical implants. *Critical Reviews in Toxicology* **38,** 645–674 (2008).

36. Doorn, P. F. *et al.* Metal wear particle characterization from metal on metal total hip replacements: Transmission electron microscopy study of periprosthetic tissues and isolated

particles. *J. Biomed. Mater. Res.* **42,** 103–111 (1998).

37. Crainic, A. M., Callisti, M., Palmer, M. R. & Cook, R. B. Investigation of nano-sized debris released from CoCrMo secondary interfaces in total hip replacements: Digestion of the flakes. *J. Biomed. Mater. Res. Part B Appl. Biomater.* 1–11 (2017). doi:10.1002/jbm.b.34134

38. Xia, Z. *et al.* Characterization of metal-wear nanoparticles in pseudotumor following metal-on-metal hip resurfacing. *Nanomedicine Nanotechnology, Biol. Med.* **7,** 674–681 (2011).

39. Xia, Z. *et al.* Nano-analyses of wear particles from metal-on-metal and non-metal-on-metal dual modular neck hip arthroplasty. *Nanomedicine Nanotechnology, Biol. Med.* **13,** 1205–1217 (2017).

40. Urban, R. M. *et al.* Dissemination of wear particles to the liver, spleen, and abdominal lymph nodes of patients with hip or knee replacement. *J. Bone Joint Surg. Am.* **82,** 457–476 (2000).

41. Urban, R. M., Jacobs, J. J., Gilbert, J. L. & Galante, J. O. Migration of corrosion products from modular hip prostheses. Particle microanalysis and histopathological findings. *J Bone Jt. Surg Am* **76,** 1345–1359 (1994).

42. De Smet, K. *et al.* Metal ion measurement as a diagnostic tool to identify problems with metal-on-metal hip resurfacing. *J. Bone Joint Surg. Am.* **90 Suppl 4,** 202–208 (2008).

43. Altamirano-Lozano, M. *et al.* Cobalt in hard metals and cobalt sulfate, gallium arsenide, indium phosphide and vanadium pentoxide. in *IARC Monographs on the Evaluation of Carcinogenic Risks to Humans* **86,** (2006).

44. Kwon, Y.-M. *et al.* Dose-dependent cytotoxicity of clinically relevant cobalt nanoparticles and ions on macrophages *in vitro*. *Biomed. Mater.* **4,** 25018 (2009).

45. Germain, M. A. *et al.* Comparison of the cytotoxicity of clinically relevant cobalt-chromium and alumina ceramic wear particles in vitro. *Biomaterials* **24,** 469–479 (2003).

46. Drummond, J., Tran, P. & Fary, C. Metal-on-metal hip arthroplasty: A review of adverse reactions and patient management. *J. Funct. Biomater.* **6,** 486–499 (2015).

47. Glyn-Jones, S. *et al.* Risk factors for inflammatory pseudotumour formation following hip resurfacing. in *The Journal of bone and joint surgery. British volume* **91,** 1566–74 (2009).

48. Gill, H. S., Grammatopoulos, G., Adshead, S., Tsialogiannis, E. & Tsiridis, E. Molecular and immune toxicity of CoCr nanoparticles in MoM hip arthroplasty. *Trends in Molecular Medicine* **18,** 145–155 (2012).

49. Fricka, K. B., Ho, H., Peace, W. J. & Engh, C. A. Metal-on-Metal local tissue reaction is

associated with corrosion of the head taper junction. *J. Arthroplasty* **27,** (2012).

50. Van Der Straeten, C. *et al.* The 2012 Otto Aufranc Award: The interpretation of metal ion levels in unilateral and bilateral hip resurfacing. *Clin. Orthop. Relat. Res.* **471,** 377–385 (2013).

51. Fillingham, Y. A. *et al.* Serum Metal Levels for Diagnosis of Adverse Local Tissue Reactions Secondary to Corrosion in Metal-on-Polyethylene Total Hip Arthroplasty. *J. Arthroplasty* **32,** S272–S277 (2017).

52. Matziolis, G., Perka, C. & Disch, A. Massive metallosis after revision of a fractured ceramic head onto a metal head. *Arch. Orthop. Trauma Surg.* **123,** 48–50 (2003).

53. Oldenburg, M., Wegner, R. & Baur, X. Severe Cobalt Intoxication Due to Prosthesis Wear in Repeated Total Hip Arthroplasty. *J. Arthroplasty* **24,** (2009).

54. Gilbert, C. J. *et al.* Hip pain and heart failure: the missing link. *Can. J. Cardiol.* **29,** 639.e1-2 (2013).

55. Catelas, I. *et al.* Effects of digestion protocols on the isolation and characterization of metal-metal wear particles. I. Analysis of particle size and shape. *J. Biomed. Mater. Res.* **55,** 320–329 (2001).

56. Brown, C., Fisher, J. & Ingham, E. Biological effects of clinically relevant wear particles from metal-on-metal hip prostheses. *Proc. Inst. Mech. Eng. Part H J. Eng. Med.* **220,** 355–369 (2006).

57. Beaule, P. E., Campbell, P., Mirra, J., Hooper, J. C. & Schmalzried, T. P. Osteolysis in a cementless, second generation metal-on-metal hip replacement. *Clin. Orthop. Relat. Res.* 159–165 (2001).

58. Park, Y. S. *et al.* Early osteolysis following second-generation metal-on-metal hip replacement. *J. Bone Jt. Surg. - Ser. A* **87,** 1515–1521 (2005).

59. Carr, A. M. & DeSteiger, R. Osteolysis in patients with a metal-on-metal hip arthroplasty. *ANZ J. Surg.* **78,** 144–147 (2008).

60. Szuszczewicz, E. S., Schmalzried, T. P. & Petersen, T. D. Progressive bilateral pelvic osteolysis in a patient with McKee-Farrar metal-metal total hip prostheses. *J. Arthroplasty* **12,** 819–824 (1997).

61. Klapperich, C., Graham, J., Pruitt, L. & Ries, M. D. Failure of a metal-on-metal total hip arthroplasty from progressive osteolysis. *J. Arthroplasty* **14,** 877–881 (1999).

62. Holloway, I., Walter, W. L., Zicat, B. & Walter, W. K. Osteolysis with a cementless second generation metal-on-metal cup in total hip replacement. *Int. Orthop.* **33,** 1537–1542 (2009).

63. Dorr, L. D., Wan, Z., Sirianni, L. E., Boutary, M. & Chandran, S. Fixation and osteolysis with Metasul metal-on-metal articulation. *J. Arthroplasty* **19,** 951–955 (2004).

64. Howie, D. W. Tissue response in relation to type of wear particles around failed hip arthroplasties. *J. Arthroplasty* **5,** 337–348 (1990).

65. Willert, H. G. *et al.* Metal-on-metal bearings and hypersensitivity in patients with artificial hip joints: A clinical and histomorphological study. *J. Bone Jt. Surg. - Ser. A* **87,** 28–36 (2005).

66. Campbell, P. *et al.* Histological features of pseudotumor-like tissues from metal-on-metal hips. in *Clinical Orthopaedics and Related Research* **468,** 2321–2327 (2010).

67. De Haan, R. *et al.* Correlation between inclination of the acetabular component and metal ion levels in metal-on-metal hip resurfacing replacement. *J. Bone Jt. Surg. - Br. Vol.* **90–B,** 1291–1297 (2008).

68. Zeng, Y. & Feng, W. Metal allergy in patients with total hip replacement: A review. *J. Int. Med. Res.* **41,** 247–252 (2013).

69. Halwani, D. O. *et al.* In-vivo corrosion and local release of metallic ions from vascular stents into surrounding tissue. *J. Invasive Cardiol.* **22,** 528–535 (2010).

70. Yamazoe, M. Study of corrosion of combinations of titanium/Ti-6Al-4V implants and dental alloys. *Dent. Mater. J.* **29,** 542–553 (2010).

71. Posada, O. M., Gilmour, D., Tate, R. J. & Grant, M. H. CoCr wear particles generated from CoCr alloy metal-on-metal hip replacements, and cobalt ions stimulate apoptosis and expression of general toxicology-related genes in monocyte-like U937 cells. *Toxicol. Appl. Pharmacol.* **281,** 125–135 (2014).

72. Hallab, N., Merritt, K. & Jacobs, J. J. Metal sensitivity in patients with orthopaedic implants. *J. Bone Joint Surg. Am.* **83–A,** 428–36 (2001).

73. Münch, H. J. *et al.* The association between metal allergy, total knee arthroplasty, and revision. *Acta Orthop.* **86,** 378–383 (2015).

74. Basko-Plluska, J., Thyssen, J. & Schalock, P. Cutaneous and systemic hypersensitivity reactions to metallic implants. *Dermatitis* **22,** 65–79 (2011).

75. Langkamer, V. G. *et al.* Systemic distribution of wear debris after hip replacement. A cause

for concern? *J. Bone Joint Surg. Br.* **74,** 831–9 (1992).

76. Case, C. P. *et al.* Widespread dissemination of metal debris from implants. *J. Bone Joint Surg. Br.* **76,** 701–12 (1994).

77. Revell, P. A. The combined role of wear particles, macrophages and lymphocytes in the loosening of total joint prostheses. *J. R. Soc. Interface* **5,** 1263–1278 (2008).

78. Charette, R. S., Neuwirth, A. L. & Nelson, C. L. Arthroprosthetic cobaltism associated with cardiomyopathy. *Arthroplast. Today* **3,** 225–228 (2017).

79. Steens, W., Von Foerster, G. & Katzer, A. Severe cobalt poisoning with loss of sight after ceramic-metal pairing in a hip - A case report. *Acta Orthop.* **77,** 830–832 (2006).

80. Tower, S. Arthroprosthetic cobaltism: identification of the at-risk patient. *Alaska Med.* **52,** 28–32 (2010).

81. Stephen, S. Arthroprosthetic cobaltism associated with metal on metal hip implants. *BMJ (Online)* **344,** (2012).

82. Dahms, K., Sharkova, Y., Heitland, P., Pankuweit, S. & Schaefer, J. R. Cobalt intoxication diagnosed with the help of Dr House. *The Lancet* **383,** 574 (2014).

83. Leikin, J. B. *et al.* Outpatient toxicology clinic experience of patients with hip implants. *Clin. Toxicol. (Phila).* **51,** 230–6 (2013).

84. Cohen, D. Medical devices - Out of joint: The story of the ASR. *BMJ* **342,** (2011).

85. Machado, C., Appelbe, A. & Wood, R. Arthroprosthetic Cobaltism and Cardiomyopathy. *Hear. Lung Circ.* **21,** 759–760 (2012).

86. Wolfel, E. E. Missing Elements of the History. **370,** 559–566 (2015).

87. Nordberg, G. Assessment of risks in occupational cobalt exposures. *Sci. Total Environ.* **150,** 201–207 (1994).

88. Yu, R. Cobalt Toxicity, An overlooked Cause of Hypothyroidism. *J. Endocrinol. Thyroid Res.* **1,** 1–4 (2017).

89. Zywiel, M. G. *et al.* Fatal cardiomyopathy after revision total hip replacement for fracture of a ceramic liner. *Bone Joint J.* **95–B,** 31–37 (2013).

90. Witzleb, W.-C., Ziegler, J., Krummenauer, F., Neumeister, V. & Guenther, K.-P. Exposure to chromium, cobalt and molybdenum from metal-on-metal total hip replacement and hip resurfacing arthroplasty. *Acta Orthop.* **77,** 697–705 (2006).

91. Antoniou, J. *et al.* Metal ion levels in the blood of patients after hip resurfacing: a comparison between twenty-eight and thirty-six-millimeter-head metal-on-metal prostheses. *J. Bone Joint Surg. Am.* **90 Suppl 3,** 142–148 (2008).

92. Vyskočil, A. & Viau, C. Assessment of molybdenum toxicity in humans. *Journal of Applied Toxicology* **19,** 185–192 (1999).

93. Puleo, D. A. & Huh, W. W. Acute toxicity of metal ions in cultures of osteogenic cells derived from bone marrow stromal cells. *J. Appl. Biomater.* **6,** 109–116 (1995).

94. Scharf, B. *et al.* Molecular analysis of chromium and cobalt-related toxicity. *Sci. Rep.* **4,** 5729 (2015).

95. Anissian, H. L., Stark, A., Gustafson, A., Good, V. & Clarke, I. C. Metal-on-metal bearing in hip prosthesis generates 100-fold less wear debris than metal-on-polyethylene. *Acta Orthop. Scand.* **70,** 578–582 (1999).

96. Kamali, A. *et al.* Tribological performance of various CoCr microstructures in metal-on-metal bearings: THE DEVELOPMENT OF A MORE PHYSIOLOGICAL PROTOCOL IN VITRO. *J. Bone Jt. Surg. - Br. Vol.* **92–B,** 717–725 (2010).

97. Milošev, I. & Remškar, M. In vivo production of nanosized metal wear debris formed by tribochemical reaction as confirmed by high-resolution TEM and XPS analyses. *J. Biomed. Mater. Res. - Part A* **91,** 1100–1110 (2009).

98. Brown, C., Williams, S., Tipper, J. L., Fisher, J. & Ingham, E. Characterisation of wear particles produced by metal on metal and ceramic on metal hip prostheses under standard and microseparation simulation. *J. Mater. Sci. Mater. Med.* **18,** 819–827 (2007).

99. Kwon, Y.-M. *et al.* Analysis of wear of retrieved metal-on-metal hip resurfacing implants revised due to pseudotumours. *J. Bone Jt. Surg. - Br. Vol.* **92–B,** 356–361 (2010).

100. Di Laura, A. *et al.* The Chemical Form of Metal Species Released from Corroded Taper Junctions of Hip 2 Implants: Synchrotron Analysis of Patient Tissue. *Sci. Rep.* 1–13 (2017). doi:10.1038/s41598-017-11225-w

101. Wilburg, S., Ingerman, L., Citra, M. Osier, M., Wohlers, D. Toxicological Profile for Chromium. *Public Health* 421 (2000).

102. Simonsen, L. O., Harbak, H. & Bennekou, P. Cobalt metabolism and toxicology-A brief update. *Science of the Total Environment* **432,** 210–215 (2012).

103. Cheung, A. C. *et al.* Systemic cobalt toxicity from total hip arthroplasties: review of a rare condition Part 1 - history, mechanism, measurements, and pathophysiology. *Bone Joint J.* **98–**

B, 6–13 (2016).

104. Zywiel, M. G. *et al.* Systemic cobalt toxicity from total hip arthroplasties. *Bone Jt. J.* **98B,** 14–20 (2016).

105. Keegan, G. M., Learmonth, I. D. & Case, C. P. Orthopaedic metals and their potential toxicity in the arthroplasty patient: A review of current knowledge and future strategies. *J. Bone Joint Surg. Br.* **89,** 567–573 (2007).

106. Billi, F. & Campbell, P. Nanotoxicology of metal wear particles in total joint arthroplasty: a review of current concepts. *J. Appl. Biomater. Biomech.* **8,** 1–6 (2010).

107. Harris, H. H. *et al.* Time-dependent uptake, distribution and biotransformation of chromium(VI) in individual and bulk human lung cells: Application of synchrotron radiation techniques. *J. Biol. Inorg. Chem.* **10,** 105–118 (2005).

108. Geiser, M. *et al.* Ultrafine particles cross cellular membranes by nonphagocytic mechanisms in lungs and in cultured cells. *Environ. Health Perspect.* **113,** 1555–1560 (2005).

109. Colognato, R. *et al.* Comparative genotoxicity of cobalt nanoparticles and ions on human peripheral leukocytes in vitro. *Mutagenesis* **23,** 377–382 (2008).

110. Yue, H. *et al.* Particle size affects the cellular response in macrophages. *Eur. J. Pharm. Sci.* **41,** 650–657 (2010).

111. Catelas, I. *et al.* Size, shape, and composition of wear particles from metal-metal hip simulator testing: Effects of alloy and number of loading cycles. *J. Biomed. Mater. Res.* **67A,** 312–327 (2003).

112. Papageorgiou, I. *et al.* The effect of nano- and micron-sized particles of cobalt-chromium alloy on human fibroblasts in vitro. *Biomaterials* **28,** 2946–2958 (2007).

113. Pandit, H. *et al.* Pseudotumours associated with metal-on-metal hip resurfacings. *J. Bone Jt. Surg. - Br. Vol.* **90–B,** 847–851 (2008).

114. Reynolds, M. F. *et al.* Rapid DNA double-strand breaks resulting from processing of Cr-DNA cross-links by both MutS dimers. *Cancer Res.* **69,** 1071–1079 (2009).

115. Zhitkovich, A. Importance of chromium-DNA adducts in mutagenicity and toxicity of chromium(VI). *Chemical Research in Toxicology* **18,** 3–11 (2005).

116. Visuri, T. I., Pukkala, E., Pulkkinen, P. & Paavolainen, P. Cancer incidence and causes of death among total hip replacement patients: a review based on Nordic cohorts with a special emphasis on metal-on-metal bearings. *Proc. Inst. Mech. Eng. Part H J. Eng. Med.* **220,** 399–

407 (2006).

117. Levašič, V., Milošev, I. & Zadnik, V. Risk of cancer after primary total hip replacement : The influence of bearings , cementation and the material of the stem Risk of cancer after primary total hip replacement : The infl u- ence of bearings , cementation and the material of the stem A retros. **3674,** (2018).

118. Visuri, T., Pulkkinen, P., Paavolainen, P. & Pukkala, E. Cancer risk is not increased after conventional hip arthroplasty: A nationwide study from the Finnish Arthroplasty Register with follow-up of 24,636 patients for a mean of 13 years. *Acta Orthop.* **81,** 77–81 (2010).

119. Jiang, J., Oberdörster, G. & Biswas, P. Characterization of size, surface charge, and agglomeration state of nanoparticle dispersions for toxicological studies. *J. Nanoparticle Res.* **11,** 77–89 (2009).

120. Williams, J. *Engineering tribology*. *Engineering Tribology* **9780521609,** (2005).

121. Schmidt, T. A. & Sah, R. L. Effect of synovial fluid on boundary lubrication of articular cartilage. *Osteoarthr. Cartil.* **15,** 35–47 (2007).

122. Schmidt, T. A., Gastelum, N. S., Nguyen, Q. T., Schumacher, B. L. & Sah, R. L. Boundary lubrication of articular cartilage: Role of synovial fluid constituents. *Arthritis Rheum.* **56,** 882–891 (2007).

123. Katta, J., Jin, Z., Ingham, E. & Fisher, J. Biotribology of articular cartilage-A review of the recent advances. *Med. Eng. Phys.* **30,** 1349–1363 (2008).

124. Hui, A. Y., McCarty, W. J., Masuda, K., Firestein, G. S. & Sah, R. L. A systems biology approach to synovial joint lubrication in health, injury, and disease. *Wiley Interdisciplinary Reviews: Systems Biology and Medicine* **4,** 15–37 (2012).

125. Sophia Fox, A. J., Bedi, A. & Rodeo, S. A. The basic science of articular cartilage: Structure, composition, and function. *Sports Health* **1,** 461–468 (2009).

126. Di Puccio, F. & Mattei, L. Biotribology of artificial hip joints. *World J. Orthop.* **6,** 77–94 (2015).

127. Wimmer, M. A., Loos, J., Nassutt, R., Heitkemper, M. & Fischer, A. The acting wear mechanisms on metal-on-metal hip joint bearings: In vitro results. *Wear* **250–251,** 129–139 (2001).

128. McKellop, H., Shen, F., Lu, B., Campbell, P. & Salovey, R. Development of an extremely wear-resistant ultra high molecular weight polythylene for total hip replacements. *J. Orthop. Res.* **17,** 157–167 (1999).

129. Wimmer, M. A., Sprecher, C., Hauert, R., Täger, G. & Fischer, A. Tribochemical reaction on metal-on-metal hip joint bearings. *Wear* **255,** 1007–1014 (2003).

130. Wimmer, M. A. *et al.* Wear mechanisms in metal-on-metal bearings: The importance of tribochemical reaction layers. *J. Orthop. Res.* **28,** 436–443 (2010).

131. Büscher, R. *et al.* Subsurface microstructure of metal-on-metal hip joints and its relationship to wear particle generation. *J. Biomed. Mater. Res. - Part B Appl. Biomater.* **72,** 206–214 (2005).

132. Mathew, M. T. *et al.* Tribolayer formation in a metal-on-metal (MoM) hip joint: An electrochemical investigation. *J. Mech. Behav. Biomed. Mater.* **29,** 199–212 (2014).

133. Fischer, A., Weiß, S. & Wimmer, M. A. The tribological difference between biomedical steels and CoCrMo-alloys. *J. Mech. Behav. Biomed. Mater.* **9,** 50–62 (2012).

134. Scholes, S. C. & Unsworth, A. Comparison of friction and lubrication of different hip prostheses. *Proc. Inst. Mech. Eng. Part H J. Eng. Med.* **214,** 49–57 (2000).

135. Mattei, L., Di Puccio, F., Piccigallo, B. & Ciulli, E. Lubrication and wear modelling of artificial hip joints: A review. *Tribol. Int.* **44,** 532–549 (2011).

136. Liu, F., Jin, Z., Roberts, P. & Grigoris, P. Importance of head diameter, clearance, and cup wall thickness in elastohydrodynamic lubrication analysis of metal-on-metal hip resurfacing prostheses. *Proc. Inst. Mech. Eng. Part H J. Eng. Med.* **220,** 695–704 (2006).

137. Liu, F., Leslie, I., Williams, S., Fisher, J. & Jin, Z. Development of computational wear simulation of metal-on-metal hip resurfacing replacements. *J. Biomech.* **41,** 686–694 (2008).

138. Brockett, C. L., Williams, S., Jin, Z. M., Isaac, G. & Fisher, J. A comparison of friction in 28 mm conventional and 55 mm resurfacing metal-on-metal hip replacements. in *Proceedings of the Institution of Mechanical Engineers, Part J: Journal of Engineering Tribology* **221,** 391–398 (2007).

139. Meng, Q., Liu, F., Fisher, J. & Jin, Z. Contact mechanics and lubrication analyses of ceramic-on-metal total hip replacements. in *Tribology International* **63,** 51–60 (2013).

140. Hardaker, C., Dowson, D. & Isaac, G. H. Head replacement, head rotation, and surface damage effects on metal-on-metal total hip replacements: A hip simulator study. *Proc. Inst. Mech. Eng. Part H J. Eng. Med.* **220,** 209–217 (2006).

141. Lee, R., Essner, A. & Wang, A. Tribological Considerations in Primary and Revision Metal-on-Metal Arthroplasty. *J. Bone Jt. Surgery-American Vol.* **90,** 118–124 (2008).

142. Vassiliou, K., Elfick, A. P. D., Scholes, S. C. & Unsworth, A. The effect of 'running-in' on the tribology and surface morphology of metal-on-metal Birmingham hip resurfacing device in simulator studies. *Proc. Inst. Mech. Eng. Part H J. Eng. Med.* **220,** 269–277 (2006).

143. Underwood, R. J., Zografos, A., Sayles, R. S., Hart, A. & Cann, P. Edge loading in metal-on-metal hips: Low clearance is a new risk factor. in *Proceedings of the Institution of Mechanical Engineers, Part H: Journal of Engineering in Medicine* **226,** 217–226 (2012).

144. De Haan, R., Campbell, P. A., Su, E. P. & De Smet, K. A. Revision of metal-on-metal resurfacing arthroplasty of the hip: THE INFLUENCE OF MALPOSITIONING OF THE COMPONENTS. *J. Bone Jt. Surg. - Br. Vol.* **90–B,** 1158–1163 (2008).

145. Morlock, M. M. *et al.* Modes of implant failure after hip resurfacing: morphological and wear analysis of 267 retrieval specimens. *J. Bone Joint Surg. Am.* **90 Suppl 3,** 89–95 (2008).

146. Langton, D. J. *et al.* Adverse reaction to metal debris following hip resurfacing: THE INFLUENCE OF COMPONENT TYPE, ORIENTATION AND VOLUMETRIC WEAR. *J. Bone Jt. Surg. - Br. Vol.* **93–B,** 164–171 (2011).

147. Kwon, Y.-M., Mellon, S. J., Monk, P., Murray, D. W. & Gill, H. S. In vivo evaluation of edge-loading in metal-on-metal hip resurfacing patients with pseudotumours. *Bone Joint Res.* **1,** 42–9 (2012).

148. Liao, Y. *et al.* Graphitic tribological layers in metal-on-metal hip replacements. *Science (80-.).* **334,** 1687–1690 (2011).

149. Hallab, N. J., Mikecz, K., Vermes, C., Skipor, A. & Jacobs, J. J. Differential lymphocyte reactivity to serum-derived metal-protein complexes produced from cobalt-based and titanium-based implant alloy degradation. *J. Biomed. Mater. Res.* **56,** 427–436 (2001).

150. Yan, Y., Neville, A. & Dowson, D. Biotribocorrosion—an appraisal of the time dependence of wear and corrosion interactions: II. Surface analysis. *J. Phys. D. Appl. Phys.* **39,** 3206–3212 (2006).

151. Huang, P. & López, H. F. Athermal ε-martensite in a Co-Cr-Mo alloy: Grain size effects. *Mater. Lett.* **39,** 249–253 (1999).

152. Wang, Z. W., Yan, Y. & Qiao, L. J. Nanocrystalline layer on the bearing surfaces of artificial hip implants induced by biotribocorrosion processes. *Biosurface and Biotribology* **1,** 130–134 (2015).

153. Afolaranmi, G. A., Akbar, M., Brewer, J. & Grant, M. H. Distribution of metal released from cobalt-chromium alloy orthopaedic wear particles implanted into air pouches in mice. *J.*

Biomed. Mater. Res. - Part A **100 A,** 1529–1538 (2012).

154. Akbar, M., Fraser, A. R., Graham, G. J., Brewer, J. M. & Grant, M. H. Acute inflammatory response to cobalt chromium orthopaedic wear debris in a rodent air-pouch model. *J. R. Soc. Interface* **9,** 2109–2119 (2012).

155. Lewis, A. C. *et al.* The entrapment of corrosion products from CoCr implant alloys in the deposits of calcium phosphate: A comparison of serum, synovial fluid, albumin, EDTA, and water. *J. Orthop. Res.* **24,** 1587–1596 (2006).

156. Madl, A. K. *et al.* Toxicology of wear particles of cobalt-chromium alloy metal-on-metal hip implants Part II: Importance of physicochemical properties and dose in animal and in vitro studies as a basis for risk assessment. *Nanomedicine: Nanotechnology, Biology, and Medicine* **11,** 1285–1298 (2015).

157. Hanawa, T. Metal ion release from metal implants. *Mater. Sci. Eng. C-Biomimetic Supramol. Syst.* **24,** 745–752 (2004).

158. Hodgson, A. W. E. *et al.* Passive and transpassive behaviour of CoCrMo in simulated biological solutions. *Electrochim. Acta* **49,** 2167–2178 (2004).

159. Rashidi, N., Alavi-soltani, S. & Asmatulu, R. Crevice Corrosion Theory, Mechanisms and Prevention Methods. *Proc. 3rd Annu. GRASP Symp.* 215–216 (2007).

160. Molloy, D. O. *et al.* Fretting and corrosion in modular-neck total hip arthroplasty femoral stems. *J. Bone Joint Surg. Am.* **96,** 488–93 (2014).

161. Srinivasan, A., Jung, E. & Levine, B. R. Modularity of the femoral component in total hip arthroplasty. *J. Am. Acad. Orthop. Surg.* **20,** 214–222 (2012).

162. Yan, Y., Neville, A. & Dowson, D. Understanding the role of corrosion in the degradation of metal-on-metal implants. *Proc. Inst. Mech. Eng. Part H J. Eng. Med.* **220,** 173–180 (2006).

163. Yan, Y., Dowson, D. & Neville, A. In-situ electrochemical study of interaction of tribology and corrosion in artificial hip prosthesis simulators. *J. Mech. Behav. Biomed. Mater.* **18,** 191–199 (2013).

164. Kwon, Y. M. Evaluation of the Painful Dual Taper Modular Neck Stem Total Hip Arthroplasty: Do They All Require Revision? *J. Arthroplasty* **31,** 1385–1389 (2016).

165. Lucas, L. C., Buchanan, R. A. & Lemons, J. E. Investigations on the galvanic corrosion of multialloy total hip prostheses. *J. Biomed. Mater. Res.* **15,** 731–747 (1981).

166. Collier, J. P., Surprenant, V. A., Jensen, R. E. & Mayor, M. B. Corrosion at the interface of

cobalt-alloy heads on titanium-alloy stems. *Clin. Orthop. Relat. Res.* 305–12 (1991). doi:10.1097/00003086-199110000-00042

167. Collier, J. P., Surprenant, V. a, Jensen, R. E., Mayor, M. B. & Surprenant, H. P. Corrosion between the components of modular femoral hip prostheses. *J. Bone Joint Surg. Br.* **74,** 511–517 (1992).

168. Brown, S. A. *et al.* Fretting corrosion accelerates crevice corrosion of modular hip tapers. *J. Appl. Biomater.* **6,** 19–26 (1995).

169. Gill, I. P. S., Webb, J., Sloan, K. & Beaver, R. J. Corrosion at the neck-stem junction as a cause of metal ion release and pseudotumour formation. *Bone Joint J.* **94–B,** 895–900 (2012).

170. Kop, A. M. & Swarts, E. Corrosion of a Hip Stem With a Modular Neck Taper Junction. A Retrieval Study of 16 Cases. *J. Arthroplasty* **24,** 1019–1023 (2009).

171. Wilson, D. A. J., Dunbar, M. J., Amirault, J. D. & Farhat, Z. Early failure of a modular femoral neck total hip arthroplasty component: A case report. *J. Bone Jt. Surg. - Ser. A* **92,** 1514–1517 (2010).

172. Wright, C. G., Sporer, S., Urban, R. & Jacobs, J. Fracture of a Modular Femoral Neck After Total Hip Arthroplasty. *J. Bone Jt. Surgery-American Vol.* **92,** 1518–1521 (2010).

173. Sporer, S. M., DellaValle, C., Jacobs, J. & Wimmer, M. A Case of Disassociation of a Modular Femoral Neck Trunion After Total Hip Arthroplasty. *J. Arthroplasty* **21,** 918–921 (2006).

174. Huber, M., Reinisch, G., Trettenhahn, G., Zweymüller, K. & Lintner, F. Presence of corrosion products and hypersensitivity-associated reactions in periprosthetic tissue after aseptic loosening of total hip replacements with metal bearing surfaces. *Acta Biomater.* **5,** 172–180 (2009).

175. Matthies, A. K. *et al.* Material loss at the taper junction of retrieved large head metal-on-metal total hip replacements. *J. Orthop. Res.* **31,** 1677–1685 (2013).

176. Hsu, A. R., Gross, C. E. & Levine, B. R. Pseudotumor from modular neck corrosion after ceramic-on-polyethylene total hip arthroplasty. *Am. J. Orthop. (Belle Mead. NJ).* **41,** 422–6 (2012).

177. Lindgren, J. U., Brismar, B. H. & Wikstrom, A. C. Adverse reaction to metal release from a modular metal-on-polyethylene hip prosthesis. *Bone Joint J.* **93–B,** 1427–1430 (2011).

178. Van Erve, R. H. G. P. V. The absence of a metal-on-metal bearing does not preclude the formation of a destructive pseudotumor in the hip - A case report. *Acta Orthop.* **84,** 598–599

(2013).

179. Mistry, J. B. *et al.* Trunnionosis in total hip arthroplasty: a review. *Journal of Orthopaedics and Traumatology* **17,** (2016).

180. Gilbert, J. L., Buckley, C. A. & Jacobs, J. J. In vivo corrosion of modular hip prosthesis components in mixed and similar metal combinations. The effect of crevice, stress, motion, and alloy coupling. *J. Biomed. Mater. Res.* **27,** 1533–1544 (1993).

181. Cook, S. D., Barrack, R. L. & Clemow, a J. Corrosion and wear at the modular interface of uncemented femoral stems. *J. Bone Joint Surg. Br.* **76,** 68–72 (1994).

182. Goldberg, J. R. *et al.* A Multicenter Retrieval Study of the Taper Interfaces of Modular Hip Prostheses. *Clin. Orthop. Relat. Res.* **401,** 149–161 (2002).

183. Langton, D. J. *et al.* Accelerating failure rate of the ASR total hip replacement. *Bone Joint J.* **93–B,** 1011–1016 (2011).

184. Bishop, N. *et al.* Wear patterns of taper connections in retrieved large diameter metal-on-metal bearings. *J. Orthop. Res.* **31,** 1116–1122 (2013).

185. Munir, S., Walter, W. L. & Walsh, W. R. Variations in the trunnion surface topography between different commercially available hip replacement stems. *J. Orthop. Res.* **33,** 98–105 (2015).

186. Panagiotidou, A. *et al.* Enhanced wear and corrosion in modular tapers in total hip replacement is associated with the contact area and surface topography. *J. Orthop. Res.* **31,** 2032–2039 (2013).

187. Kocagöz, S. B. *et al.* Does taper angle clearance influence fretting and corrosion damage at the head-stem interface? A matched cohort retrieval study. *Semin. Arthroplasty* **24,** 246–254 (2013).

188. Witt, F., Gührs, J., Morlock, M. M. & Bishop, N. E. Quantification of the contact area at the head-stem taper interface of modular hip prostheses. *PLoS One* **10,** (2015).

189. Higgs, G. B. *et al.* Is increased modularity associated with increased fretting and corrosion damage in metal-on-metal total hip arthroplasty devices? A retrieval study. *J. Arthroplasty* **28,** 2–6 (2013).

190. Werner, S. D., Bono, J. V., Nandi, S., Ward, D. M. & Talmo, C. T. Adverse Tissue Reactions in Modular Exchangeable Neck Implants: A Report of Two Cases. *J. Arthroplasty* **28,** (2013).

191. Malik, A., Maheshwari, A. & Dorr, L. D. Impingement with total hip replacement. *J. Bone*

Joint Surg. Am. **89,** 1832–1842 (2007).

192. Nassif, N. A. *et al.* Taper design affects failure of large-head metal-on-metal total hip replacements. in *Clinical Orthopaedics and Related Research* **472,** 564–571 (2014).

193. Tan, S. C., Teeter, M. G., Del Balso, C., Howard, J. L. & Lanting, B. A. Effect of Taper Design on Trunnionosis in Metal on Polyethylene Total Hip Arthroplasty. *J. Arthroplasty* **30,** 1269–1272 (2015).

194. Langton, D. J., Sidaginamale, R., Lord, J. K., Nargol, A. V. F. & Joyce, T. J. Taper junction failure in large-diameter metal-on-metal bearings. *Bone Joint Res.* **1,** 56–63 (2012).

195. Esposito, C. I., Wright, T. M., Goodman, S. B. & Berry, D. J. What is the Trouble With Trunnions? *Clin. Orthop. Relat. Res.* **472,** 3652–3658 (2014).

196. Bishop, N. E., Waldow, F. & Morlock, M. M. Friction moments of large metal-on-metal hip joint bearings and other modern designs. *Med. Eng. Phys.* **30,** 1057–1064 (2008).

197. Higgs, G. B. *et al.* Does Taper Size Have an Effect on Taper Damage in Retrieved Metal-on-Polyethylene Total Hip Devices? *J. Arthroplasty* **31,** 277–281 (2016).

198. Bishop, N. E., Hothan, A. & Morlock, M. M. High friction moments in large hard-on-hard hip replacement bearings in conditions of poor lubrication. *J. Orthop. Res.* **31,** 807–813 (2013).

199. Parekh, J., Jones, H., Chan, N. & Noble, P. Effect of Angular Mismatch Tolerance on Trunnion Micro-Motion in Metal-on-Metal THA Designs. *Bone & Jt. J. Orthop. Proc. Suppl.* **95–B,** 261 LP-261 (2013).

200. Donaldson, F. E., Coburn, J. C. & Siegel, K. L. Total hip arthroplasty head-neck contact mechanics: A stochastic investigation of key parameters. *J. Biomech.* **47,** 1634–1641 (2014).

201. Hallab, N. J., Messina, C., Skipor, A. & Jacobs, J. J. Differences in the fretting corrosion of metal-metal and ceramic-metal modular junctions of total hip replacements. *J. Orthop. Res.* **22,** 250–259 (2004).

202. Kurtz, S. M. *et al.* Do ceramic femoral heads reduce taper fretting corrosion in hip arthroplasty? A retrieval study. *Clin. Orthop. Relat. Res.* **471,** 3270–3282 (2013).

203. Kocagoz, S. B., Underwood, R. J., Macdonald, D. W., Gilbert, J. L. & Kurtz, S. M. Ceramic heads decrease metal release caused by head-taper fretting and corrosion. *Clin. Orthop. Relat. Res.* **474,** 985–994 (2016).

204. Hannouche, D. *et al.* Fractures of Ceramic Bearings: History and Present Status. *Clin. Orthop.*

Relat. Res. **417,** 19–26 (2003).

205. Tateiwa, T. *et al.* Ceramic Total Hip Arthroplasty in the United States: Safety and Risk Issues Revisited. *Am. J. Orthop.* **37,** E26–E31 (2008).

206. Allain, J. *et al.* Revision total hip arthroplasty performed after fracture of a ceramic femoral head: A multicenter survivorship study. *J. Bone Jt. Surg. - Ser. A* **85,** 825–830 (2003).

207. Koo, K. H. *et al.* Isolated fracture of the ceramic head after third-generation alumina-on-alumina total hip arthroplasty. *J. Bone Jt. Surg. - Ser. A* **90,** 329–336 (2008).

208. Rhoads, D. P., Baker, K. C., Israel, R. & Greene, P. W. Fracture of an Alumina Femoral Head Used in Ceramic-on-Ceramic Total Hip Arthroplasty. *J. Arthroplasty* **23,** (2008).

209. Tai, S. M. M., Parker, L., de Roeck, N. J. & Skinner, J. A. Recurrent Catastrophic Ceramic Femoral Head Failure in Total Hip Arthroplasty. *Case Rep. Orthop.* **2014,** 1–4 (2014).

210. Huet, R., Sakona, A. & Kurtz, S. M. Strength and reliability of alumina ceramic femoral heads: Review of design, testing, and retrieval analysis. *Journal of the Mechanical Behavior of Biomedical Materials* **4,** 476–483 (2011).

211. Blunn, G., Meswania, J. & Hua, J. Enhanced Wear and Corrosion in Modular Tapers in Total Hip Replacement - An in-vitro biomechanical study . 2037 (2012).

212. Hart, A. *et al.* Head Diameter is Positively Correlated with Taper Corrosion in Retrieved Large Diameter Metal-on-Metal Total Hip Replacements. *Poster 2035, ORS Annu. Meet.* San Francisco, CA (2012).

213. Hannouche, D., Delambre, J., Zadegan, F., Sedel, L. & Nizard, R. Is there a risk in placing a ceramic head on a previously implanted trunion? in *Clinical Orthopaedics and Related Research* **468,** 3322–3327 (2010).

214. Hothi, H. S. *et al.* Clinical significance of corrosion of cemented femoral stems in metal-on-metal hips: a retrieval study. *Int. Orthop.* **40,** 2247–2254 (2016).

215. Pourzal, R. *et al.* Does Surface Topography Play a Role in Taper Damage in Head-neck Modular Junctions? *Clin. Orthop. Relat. Res.* **474,** 2232–2242 (2016).

216. Urban, R. *et al.* Are Fretting and Corrosion Reduced in Contemporary Head / Neck Modular Junctions ? *ORS poster* **80,** 39310 (2012).

217. Lavernia, C. J. *et al.* Trunnion-Head Stresses in THA: Are Big Heads Trouble? *Journal of Arthroplasty* **30,** 1085–1088 (2015).

218. Witt, F. *et al.* The relation between titanium taper corrosion and cobalt-chromium bearing

wear in large-head metal-on-metal total hip prostheses: A Retrieval Study. *J. Bone Jt. Surg. - Am. Vol.* **96,** e157 (2014).

219. Pereira, X. *et al.* Variables Influencing Tribo-Corrosion Of Modular Junctions In Metal-on-Polyethylene THR. *Poster 1832, ORS Annu. Meet.* New Orleans, LA (2014).

220. Bolland, B. J. R. F. *et al.* High failure rates with a large-diameter hybrid metal-on-metal total hip replacement: CLINICAL, RADIOLOGICAL AND RETRIEVAL ANALYSIS. *Bone Joint J.* **93–B,** 608–615 (2011).

221. Triantafyllopoulos, G. K. *et al.* Otto Aufranc Award: Large Heads Do Not Increase Damage at the Head-neck Taper of Metal-on-polyethylene Total Hip Arthroplasties. *Clin. Orthop. Relat. Res.* **474,** 330–338 (2016).

222. Mroczkowski, M. L., Hertzler, J. S., Humphrey, S. M., Johnson, T. & Blanchard, C. R. Effect of impact assembly on the fretting corrosion of modular hip tapers. *J. Orthop. Res.* **24,** 271–279 (2006).

223. Haschke, H., Jauch-Matt, S. Y., Sellenschloh, K., Huber, G. & Morlock, M. M. Assembly force and taper angle difference influence the relative motion at the stem-neck interface of bi-modular hip prostheses. *Proc. Inst. Mech. Eng. Part H J. Eng. Med.* **230,** 690–699 (2016).

224. Zeng, P., Rainforth, W. M. & Cook, R. B. Characterisation of the oxide film on the taper interface from retrieved large diameter metal on polymer modular total hip replacements. *Tribol. Int.* **89,** 86–96 (2015).

225. Bryant, M., Farrar, R., Freeman, R., Brummitt, K. & Neville, A. Fretting corrosion characteristics of polished collarless tapered stems in a simulated biological environment. in *Tribology International* **65,** 105–112 (2013).

226. Pourzal, R., Theissmann, R., Morlock, M. & Fischer, A. Micro-structural alterations within different areas of articulating surfaces of a metal-on-metal hip resurfacing system. *Wear* **267,** 689–694 (2009).

227. Rainforth, W. M., Zeng, P., Ma, L., Valdez, A. N. & Stewart, T. Dynamic surface microstructural changes during tribological contact that determine the wear behaviour of hip prostheses: metals and ceramics. *Faraday Discuss.* **156,** 41 (2012).

228. Brown, L., Zhang, H., Blunt, L. & Barrans, S. Reproduction of fretting wear at the stem-cement interface in total hip replacement. *Proc. Inst. Mech. Eng. Part H J. Eng. Med.* **221,** 963–971 (2007).

229. Pennington, M. *et al.* Cemented, cementless, and hybrid prostheses for total hip replacement:

Cost effectiveness analysis. *BMJ* **346,** 1–14 (2013).

230. Shearwood-Porter, N. *et al.* Damage mechanisms at the cement–implant interface of polished cemented femoral stems. *J. Biomed. Mater. Res. - Part B Appl. Biomater.* **105,** 2027–2033 (2017).

231. Ellison, P., Hallan, G., Johan, P., Gjerdet, N. R. & Havelin, L. I. Coordinating retrieval and register studies improves postmarket surveillance. in *Clinical Orthopaedics and Related Research* **470,** 2995–3002 (2012).

232. Bryant, M. *et al.* Failure analysis of cemented metal-on-metal total hip replacements from a single centre cohort. *Wear* **301,** 226–233 (2013).

233. Bryant, M., Farrar, R., Brummitt, K., Freeman, R. & Neville, A. Fretting corrosion of fully cemented polished collarless tapered stems: The influence of PMMA bone cement. *Wear* **301,** 290–299 (2013).

234. Huddleston, H. D. Femoral lysis after cemented hip arthroplasty. *J. Arthroplasty* **3,** 285–297 (1988).

235. Anthony, P. P., Gie, G. A., Howie, C. R. & Ling, R. S. Localised endosteal bone lysis in relation to the femoral components of cemented total hip arthroplasties. *J. Bone Joint Surg. Br.* **72,** 971–9 (1990).

236. Mohler, C. G., Callaghan, J. J., Collis, D. K. & Johnston, R. C. Early loosening of the femoral component at the cement-prosthesis interface after total hip replacement. *J. Bone Jt. Surg. - Ser. A* **77,** 1315–1322 (1995).

237. Verdonschot, N. & Huiskes, R. Cement debonding process of total hip arthroplasty stems. *Clin. Orthop. Relat. Res.* 297–307 (1997). doi:10.1097/00003086-199703000-00038

238. Donell, S. T. *et al.* Early failure of the Ultima metal-on-metal total hip replacement in the presence of normal plain radiographs. *J. Bone Jt. Surg. - Br. Vol.* **92–B,** 1501–1508 (2010).

239. Cook, R. B., Shearwood-Porter, N. R., Latham, J. M. & Wood, R. J. K. Volumetric assessment of material loss from retrieved cemented metal hip replacement stems. *Tribol. Int.* **89,** 105–108 (2015).

240. Massoud, S. N., Hunter, J. B., Holdsworth, B. J., Wallace, W. a & Juliusson, R. Early Femoral Loosening in One Design of Cemented Hip Replacement. *Br J Bone Jt Surg* **79–B,** 603–8 (1997).

241. Lichtinger, T. K., Schurmann, N. & Muller, R. T. [Early loosening of a cemented hip endoprosthesis stem of titanium]. *Unfallchirurg* **103,** 956–960 (2000).

242. Schöll, E., Eggli, S. & Ganz, R. Osteolysis in cemented titanium alloy hip prosthesis. *J. Arthroplasty* **15,** 570–574 (2000).

243. Willert, H. G. *et al.* Crevice corrosion of cemented titanium alloy stems in total hip replacements. *Clinical orthopaedics and related research* 51–75 (1996).

244. Jones, R. E., Willie, B. M., Hayes, H. & Bloebaum, R. D. Analysis of 16 retrieved proximally cemented femoral stems. *J. Arthroplasty* **20,** 84–93 (2005).

245. Zhang, H., Blunt, L., Jiang, X., Brown, L. & Barrans, S. The significance of the micropores at the stem-cement interface in total hip replacement. *Journal of Biomaterials Science, Polymer Edition* **22,** 845–856 (2011).

246. Zhang, H., Brown, L., Blunt, L., Jiang, X. & Barrans, S. The contribution of the micropores in bone cement surface to generation of femoral stem wear in total hip replacement. in *Tribology International* **44,** 1476–1482 (2011).

247. Bryant, M. *et al.* Crevice corrosion of biomedical alloys: A novel method of assessing the effects of bone cement and its chemistry. *J. Biomed. Mater. Res. - Part B Appl. Biomater.* **101 B,** 792–803 (2013).

248. Bader, R., Steinhauser, E., Holzwarth, U., Schmitt, M. & Mittelmeier, W. A novel test method for evaluation of the abrasive wear behaviour of total hip stems at the interface between implant surface and bone cement. **D,** 223–230 (2004).

249. Howell, J. R. *et al.* In Vivo Surface Wear Mechanisms of Femoral Components of Cemented Total Hip Arthroplasties: The Influence of Wear Mechanism on Clinical Outcome. *J. Arthroplasty* **19,** 88–101 (2004).

250. El-Fallal, A. A., Shams, M. & Abouelatta, O. B. Effect of roughness, porosity and wettability on release of gentamicin-loaded glass ionomer bone cement. *Egypt. Dent. J.* **55,** 625–637 (2009).

251. Lautenschlager, E. P., Marshall, G. W., Marks, K. E., Schwartz, J. & Nelson, C. L. Mechanical strength of acrylic bone cements impregnated with antibiotics. *J. Biomed. Mater. Res.* **10,** 837–845 (1976).

252. Van De Belt, H. *et al.* Surface roughness, porosity and wettability of gentamicin-loaded bone cements and their antibiotic release. *Biomaterials* **21,** 1981–1987 (2000).

253. Flis, J. & Kowalczyk, L. Effect of sulphate anions on tunnel etching of aluminium. *J. Appl. Electrochem.* **25,** 501–507 (1955).

254. Pistorius, P. C. & Burstein, G. T. Growth of corrosion pits on stainless steel in chloride

solution containing dilute sulphate. *Corros. Sci.* **33,** 1885–1897 (1992).

255. Wang, H., Zhao, J., Zuo, Y. & Xiong, J. The effects of some anions on metastable pitting of 316L stainless steel. *J. Chinese Soc. Corros. Prot.* **22,** 202–206 (2002).

256. Espehaug, B., Furnes, O., Havelin, L. I., Engesaeter, L. B. & Vollset, S. E. The type of cement and failure of total hip replacements. *J. Bone Jt. Surg.* **84,** 832–838 (2002).

257. Furnes, O., Lie, S. A., Havelin, L. I., Vollset, S. E. & Engesæter, L. B. Exeter and Charnley arthroplasties with Boneloc or high viscosity cement: Comparison of 1127 arthroplasties followed for 5 years in the Norwegian Arthroplasty Register. *Acta Orthop. Scand.* **68,** 515–520 (1997).

258. McGrath, L. R. *et al.* A retrieval study of capital hip prostheses with titanium alloy femoral stems. *J. Bone Jt. Surg. - Ser. B* **83,** 1195–1201 (2001).

259. Beake, B. D. & Liskiewicz, T. W. Comparison of nano-fretting and nano-scratch tests on biomedical materials. in *Tribology International* **63,** 123–131 (2013).

260. Zhang, H., Brown, L. & Blunt, L. Static shear strength between polished stem and seven commercial acrylic bone cements. *J. Mater. Sci. Mater. Med.* **19,** 591–599 (2008).

261. Endogan, T., Serbetci, K. & Hasirci, N. Effects of ingredients on thermal and mechanical properties of acrylic bone cements. *J. Appl. Polym. Sci.* **113,** 4077–4084 (2009).

262. Crowninshield, R., Jennings, J., Laurent, M. & Maloney, W. Cemented femoral component surface finish mechanics. *Clin. Orthop. Relat. Res.* 90–102 (1998).

263. Duffy, G. P. *et al.* A critical assessment of proximal macrotexturing on cemented femoral components. *J. Arthroplasty* **16,** 42–48 (2001).

264. Zhang, H. Y., Brown, L., Barrans, S., Blunt, L. & Jiang, X. Q. Investigation of relative micromotion at the stem-cement interface in total hip replacement. *Proc. Inst. Mech. Eng. Part H J. Eng. Med.* **223,** 955–964 (2009).

265. Zhang, H., Blunt, L., Jiang, X., Brown, L. & Barrans, S. The significance of the micropores at the stem-cement interface in total hip replacement. *J. Biomater. Sci. Polym. Ed.* **22,** 845–56 (2011).

266. Blunt, L. A., Zhang, H., Barrans, S. M., Jiang, X. & Brown, L. T. What results in fretting wear on polished femoral stems. *Tribol. Int.* **42,** 1605–1614 (2009).

267. Schmalzried, T. P., Jasty, M. & Harris, W. H. Periprosthetic bone loss in total hip arthroplasty. Polyethylene wear debris and the concept of the effective joint space. *J. Bone & Jt.*

Surg. **74,** 849 LP-863 (1992).

268. Hodgson, A. W., Mischler, S., Von Rechenberg, B. & Virtanen, S. An analysis of the in vivo deterioration of Co-Cr-Mo implants through wear and corrosion. *Proc. Inst. Mech. Eng. Part H J. Eng. Med.* **221,** 291–303 (2007).

269. Goldberg, J. R. & Gilbert, J. L. Electrochemical response of CoCrMo to high-speed fracture of its metal oxide using an electrochemical scratch test method. *J. Biomed. Mater. Res.* **37,** 421–431 (1997).

270. Crawford, R. W., Evans, M., Ling, R. S. & Murray, D. W. Fluid flow around model femoral components of differing surface finishes: In vitro investigations. *Acta Orthop. Scand.* **70,** 589–595 (1999).

271. Zhang, L. F. *et al.* Bond strength analysis of the bone cement- stem interface of hip arthroplasties. *Asian Pac. J. Trop. Med.* **7,** 153–159 (2014).

272. Witt, J. D. & Swann, M. Metal wear and tissue response in failed titanium alloy total hip replacements. *J. Bone Jt. Surgery, Br. Vol.* **73–B,** 559–563 (1991).

273. Buly, R. L., Huo, M. H., Salvati, E., Brien, W. & Bansal, M. Titanium wear debris in failed cemented total hip arthroplasty. *J. Arthroplasty* **7,** 315–323 (1992).

274. Shanbhag, a S. *et al.* Composition and morphology of wear debris in failed uncemented total hip replacement. *J. Bone Joint Surg. Br.* **76,** 60–67 (1994).

275. Oberdörster, G., Oberdörster, E. & Oberdörster, J. Nanotoxicology: An emerging discipline evolving from studies of ultrafine particles. *Environmental Health Perspectives* **113,** 823–839 (2005).

276. Catelas, I. *et al.* Effects of digestion protocols on the isolation and characterization of metal-metal wear particles. II. Analysis of ion release and particle composition. *J. Biomed. Mater. Res.* **55,** 330–337 (2001).

277. Margevicius, K. J., Bauer, T. W., McMahon, J. T., Brown, S. a & Merritt, K. Isolation and characterization of debris in membranes around total joint prostheses. *J. Bone Joint Surg. Am.* **76,** 1664–1675 (1994).

278. Hirakawa, K., Bauer, T. W., Stulberg, B. N., Wilde, A. H. & Secic, M. Characterization and comparison of wear debris from failed total hip implants of different types. *J. Bone Jt. Surgery-American Vol.* **78A,** 1235–1243 (1996).

279. Firkins, P. J. *et al.* Quantitative analysis of wear and wear debris from metal-on-metal hip prostheses tested in a physiological hip joint simulator. *Biomed. Mater. Eng.* **11,** 143–157

(2001).

280. Campbell, P., Ma, S., Schmalzried, T. & Amstutz, H. C. Tissue digestion for wear debris particle isolation. *J. Biomed. Mater. Res.* **28,** 523–526 (1994).

281. Catelas, I., Campbell, P. A., Bobyn, J. D., Medley, J. B. & Huk, O. L. Wear particles from metal-on-metal total hip replacements: Effects of implant design and implantation time. *Proc. Inst. Mech. Eng. Part H J. Eng. Med.* **220,** 195–208 (2006).

282. Kavanaugh, A. A New Method for the Isolation of Metallic Debris from Synovial Fluid Poster No . 2265 • 56th Annual Meeting of the Orthopaedic Research Society. 2265 (2008).

283. Simoes, T. A. *et al.* Microstructural characterization of low and high carbon CoCrMo alloy nanoparticles produced by mechanical milling. in *Journal of Physics: Conference Series* **522,** (2014).

284. Tipper, J. L. *et al.* Quantitative analysis of polyethylene wear debris, wear rate and head damage in retrieved Charnley hip prostheses. *J. Mater. Sci. Mater. Med.* **11,** 117–124 (2000).

285. Tipper, J. L. *et al.* Quantitative analysis of the wear and wear debris from low and high carbon content cobalt chrome alloys used in metal on metal total hip replacements. *J. Mater. Sci. Mater. Med.* **10,** 353–362 (1999).

286. Lee, J. *et al.* Size of metallic and polyethylene debris particles in failed cemented total hip replacements. *J. bone Jt. surgery. Birtish Vol.* **74–B,** 380–384 (1992).

287. Catelas, I., Medley, J. B., Campbell, P. A., Huk, O. L. & Bobyn, J. D. Comparison of in vitro with in vivo characteristics of wear particles from metal-metal hip implants. *J. Biomed. Mater. Res. - Part B Appl. Biomater.* **70,** 167–178 (2004).

288. Goode, A. E. *et al.* Chemical speciation of nanoparticles surrounding metal-on-metal hips. *Chem. Commun.* **48,** 8335 (2012).

289. Loeschner, K., Harrington, C. F., Kearney, J. L., Langton, D. J. & Larsen, E. H. Feasibility of asymmetric flow field-flow fractionation coupled to ICP-MS for the characterization of wear metal particles and metalloproteins in biofluids from hip replacement patients. *Anal. Bioanal. Chem.* **407,** 4541–4554 (2015).

290. Simoes, T. A. *et al.* Evidence for the dissolution of molybdenum during tribocorrosion of CoCrMo hip implants in the presence of serum protein. *Acta Biomater.* **45,** 410–418 (2016).

291. Ward, M. B., Brown, A. P., Cox, A., Curry, A. & Denton, J. Microscopical analysis of synovial fluid wear debris from failing CoCr hip prostheses. in *Journal of Physics: Conference Series* **241,** (2010).

292. Minoda, Y. *et al.* Polyethylene wear particles in synovial fluid after total knee arthroplasty. *Clin. Orthop. Relat. Res.* 165–72 (2003). doi:10.1097/01.blo.0000063122.39522.c2

293. Minoda, Y. *et al.* Characteristics of polyethylene wear particles isolated from synovial fluid after mobile-bearing and posterior-stabilized total knee arthroplasties. *J. Biomed. Mater. Res. B. Appl. Biomater.* **71,** 1–6 (2004).

294. Benz, E. B. *et al.* Transmission electron microscopy of intracellular particles of polyethylene from joint replacement prostheses: Size distribution and cellular response. *Biomaterials* **22,** 2835–2842 (2001).

295. Hart, A. J. *et al.* The chemical form of metallic debris in tissues surrounding metal-on-metal hips with unexplained failure. *Acta Biomater.* **6,** 4439–4446 (2010).

296. Myant, C. & Cann, P. On the matter of synovial fluid lubrication: Implications for Metal-on-Metal hip tribology. *Journal of the Mechanical Behavior of Biomedical Materials* **34,** 338–348 (2014).

297. Gale, L. R., Chen, Y., Hills, B. A. & Crawford, R. Boundary lubrication of joints: Characterization of surface-active phospholipids found on retrieved implants. *Acta Orthop.* **78,** 309–314 (2007).

298. Slouf, M. *et al.* Isolation, characterization and quantification of polyethylene wear debris from periprosthetic tissues around total joint replacements. *Wear* **262,** 1171–1181 (2007).

299. Punt, I. *et al.* Submicron sized ultra-high molecular weight polyethylene wear particle analysis from revised SB Charité III total disc replacements. *Acta Biomater.* **7,** 3404–3411 (2011).

300. Baxter, R. M. *et al.* Comparison of periprosthetic tissue digestion methods for ultra-high molecular weight polyethylene wear debris extraction. *J. Biomed. Mater. Res. B. Appl. Biomater.* **91,** 409–18 (2009).

301. Scott, M., Widding, K. & Jani, S. Do current wear particle isolation procedures underestimate the number of particles generated by prosthetic bearing components? *Wear* **251,** 1213–1217 (2001).

302. Geringer, J., Pellier, J., Cleymand, F. & Forest, B. Atomic force microscopy investigations on pits and debris related to fretting-corrosion between 316L SS and PMMA. *Wear* **292–293,** 207–217 (2012).

303. Scott, M., Morrison, M., Mishra, S. R. & Jani, S. Particle analysis for the determination of UHMWPE wear. *J. Biomed. Mater. Res. - Part B Appl. Biomater.* **73,** 325–337 (2005).

304. Ingham, E. & Fisher, J. Biological reactions to wear debris in total joint replacement. *Proc. Inst. Mech. Eng. Part H J. Eng. Med.* **214,** 21–37 (2000).

305. Tuke, M., Taylor, A., Roques, A. & Maul, C. 3D linear and volumetric wear measurement on artificial hip joints - Validation of a new methodology. *Precis. Eng.* **34,** 777–783 (2010).

306. De Castro, V., Rodrigo, P., Marquis, E. A. & Lozano-Perez, S. Oxide dispersion strengthened Fe-12Cr steel in three dimensions: An electron tomography study. *J. Nucl. Mater.* **444,** 416–420 (2014).

307. Meyers, D. *et al.* Zhang-Rice physics and anomalous copper states in A-site ordered perovskites. *Sci. Rep.* **3,** 1834 (2013).

308. Sharma, A. *et al.* XANES, EXAFS and photocatalytic investigations on copper oxide nanoparticles and nanocomposites. *RSC Adv.* **5,** 21762–21771 (2015).

309. Si, P. Z. *et al.* Structure and Magnetic Properties of Cr 2 O 3 / CrO 2 Nanoparticles Prepared by Reactive Laser Ablation and Oxidation under High Pressure of Oxygen. **20,** 211–214 (2015).

310. Canham, C. D., Muradov, P. I., Simpson, J. B. & Incavo, S. J. Corrosion and adverse local tissue reaction after total hip arthroplasty with a modular titanium alloy femoral neck. *Arthroplast. Today* **3,** 211–214 (2017).

311. Moore, B. F. & Lachiewicz, P. F. Corrosion and adverse tissue reaction after modular unipolar hip hemiarthroplasty. *Arthroplasty Today* (2016). doi:10.1016/j.artd.2017.01.002

312. Hall, D. J. *et al.* Mechanical, chemical and biological damage modes within head-neck tapers of CoCrMo and Ti6Al4V contemporary hip replacements. *Journal of Biomedical Materials Research - Part B Applied Biomaterials* (2017). doi:10.1002/jbm.b.33972

313. dos Santos, C. T. *et al.* Characterization of the fretting corrosion behavior, surface and debris from head-taper interface of two different modular hip prostheses. *J. Mech. Behav. Biomed. Mater.* **62,** 71–82 (2016).

314. Urban, R., Gilbert, J. & Jacobs, J. Corrosion of Modular Titanium Alloy Stems in Cementless Hip Replacement. *J. ASTM Int.* **2,** 12810 (2005).

315. Gilbert, J. L., Mali, S., Urban, R. M., Silverton, C. D. & Jacobs, J. J. In vivo oxide-induced stress corrosion cracking of Ti-6Al-4V in a neck-stem modular taper: Emergent behavior in a new mechanism of in vivo corrosion. *J. Biomed. Mater. Res. - Part B Appl. Biomater.* **100 B,** 584–594 (2012).

316. Fan, J., Myant, C., Underwood, R. & Cann, P. Synovial fluid lubrication of artificial joints:

protein film formation and composition. *Faraday Discuss.* **156,** 69 (2012).

317. Mucalo, M. R. *Hydroxyapatite (HAp) for Biomedical Applications*. *Hydroxyapatite (HAp) for Biomedical Applications* (2015). doi:10.1016/C2013-0-16440-9

318. Haynes, D. R., Rogers, S. D., Howie, D. W., Pearcy, M. J. & Vernon-Roberts, B. Drug inhibition of the macrophage response to metal wear particles in vitro. *Clin. Orthop. Relat. Res.* 316–26 (1996).

319. Deng, M. J. *et al.* Low cost facile synthesis of large-area cobalt hydroxide nanorods with remarkable pseudocapacitance. *ACS Appl. Mater. Interfaces* **7,** 9147–9156 (2015).

320. Chen, L. *et al.* Facile synthesis of Cu doped cobalt hydroxide (Cu–Co(OH) $_2$) nano-sheets for efficient electrocatalytic oxygen evolution. *J. Mater. Chem. A* **5,** 22568–22575 (2017).

321. Caicedo, M. S., Samelko, L., McAllister, K., Jacobs, J. J. & Hallab, N. J. Increasing both CoCrMo-alloy particle size and surface irregularity induces increased macrophage inflammasome activation in vitro potentially through lysosomal destabilization mechanisms. *J. Orthop. Res.* **31,** 1633–1642 (2013).

322. Warheit, D. B. How meaningful are the results of nanotoxicity studies in the absence of adequate material characterization? *Toxicological Sciences* **101,** 183–185 (2008).

323. Veiseh, O. *et al.* Size- and shape-dependent foreign body immune response to materials implanted in rodents and non-human primates. *Nat. Mater.* **14,** 643–651 (2015).

324. Chikaura, H. *et al.* Effect of particle size on biological response by human monocyte-derived macrophages. *Biosurface and Biotribology* **2,** 18–25 (2016).

325. Prokopovich, P. Interactions between mammalian cells and nano- or micro-sized wear particles: Physico-chemical views against biological approaches. *Adv. Colloid Interface Sci.* **213,** 36–47 (2014).

326. Jacobs, J. J., Gilbert, J. L. & Urban, R. M. Corrosion of metal orthopaedic implants. *J. Bone Jt. Surg. - Ser. A* **80,** 268–282 (1998).

327. Koronfel, M. A. *et al.* Understanding the reactivity of CoCrMo-implant wear particles. *npj Mater. Degrad.* **2,** 8 (2018).

328. Atapour, M., Pilchak, A. L., Frankel, G. S. & Williams, J. C. Corrosion behavior of β titanium alloys for biomedical applications. *Mater. Sci. Eng. C* **31,** 885–891 (2011).

329. Horie, M. *et al.* Chromium(III) oxide nanoparticles induced remarkable oxidative stress and apoptosis on culture cells. *Environ. Toxicol.* **28,** 61–75 (2013).

330. Vanos, R., Lildhar, L. L., Lehoux, E. A., Beaulé, P. E. & Catelas, I. In vitro macrophage response to nanometer-size chromium oxide particles. *J. Biomed. Mater. Res. - Part B Appl. Biomater.* **102,** 149–159 (2014).

331. Lee, S. H. *et al.* Human monocyte/macrophage response to cobalt-chromium corrosion products and titanium particles in patients with total joint replacements. *J. Orthop. Res.* **15,** 40–49 (1997).

332. Revell, P. a, AL-Saffar, N. & Kobayashi, A. Biological reaction to debris in relation to joint prostheses. *Proc. Inst. Mech. Eng. Part H J. Eng. Med.* **211,** 187–197 (1997).

333. Christensen, M. M., Ernst, E. & Ellermann-Eriksen, S. Cytotoxic effects of hexavalent chromium in cultured murine macrophages. *Arch. Toxicol.* **66,** 347–353 (1992).

334. Moniz, S., Hodgkinson, S. & Yates, P. Cardiac transplant due to metal toxicity associated with hip arthroplasty. *Arthroplast. Today* **3,** 151–153 (2017).

335. Martin, J. R., Spencer-Gardner, L., Camp, C. L., Stulak, J. M. & Sierra, R. J. Cardiac cobaltism: A rare complication after bilateral metal-on-metal total hip arthroplasty. *Arthroplast. Today* **1,** 99–102 (2015).

336. Grosse, S. *et al.* Wear particles and ions from cemented and uncemented titanium-based hip prostheses - A histological and chemical analysis of retrieval material. *J. Biomed. Mater. Res. - Part B Appl. Biomater.* **103,** 709–717 (2015).

337. Yao, J. J. *et al.* Local Cellular Responses to Titanium Dioxide from Orthopedic Implants. *Biores. Open Access* **6,** 94–103 (2017).

338. Munir, S. *et al.* The histological and elemental characterisation of corrosion particles from taper junctions. *Bone Jt. Res.* **5,** 370 LP-378 (2016).

References